

NAVAL POSTGRADUATE SCHOOL
Monterey, California



DISSERTATION

**SENSITIVITY STUDIES USING MULTI-REGION AND
OPEN BOUNDARY CONDITIONS FOR TERRAIN
BOTTOM-FOLLOWING OCEAN MODELS**

by

Antonio S. Martinho

March 2003

Dissertation Supervisor:

Mary L. Batteen

Approved for public release; distribution is unlimited

THIS PAGE INTENTIONALLY LEFT BLANK

REPORT DOCUMENTATION PAGE			<i>Form Approved OMB No. 0704-0188</i>	
Public reporting burden for this collection of information is estimated to average 1 hour per response, including the time for reviewing instruction, searching existing data sources, gathering and maintaining the data needed, and completing and reviewing the collection of information. Send comments regarding this burden estimate or any other aspect of this collection of information, including suggestions for reducing this burden, to Washington headquarters Services, Directorate for Information Operations and Reports, 1215 Jefferson Davis Highway, Suite 1204, Arlington, VA 22202-4302, and to the Office of Management and Budget, Paperwork Reduction Project (0704-0188) Washington DC 20503.				
1. AGENCY USE ONLY (Leave blank)		2. REPORT DATE March 2003	3. REPORT TYPE AND DATES COVERED Dissertation	
4. TITLE AND SUBTITLE: Sensitivity Studies Using Multi-Region and Open Boundary Conditions for Terrain Bottom-Following Ocean Models			5. FUNDING NUMBERS	
6. AUTHOR(S) Antonio Santos Martinho				
7. PERFORMING ORGANIZATION NAME(S) AND ADDRESS(ES) Naval Postgraduate School Monterey, CA 93943-5000			8. PERFORMING ORGANIZATION REPORT NUMBER	
9. SPONSORING / MONITORING AGENCY NAME(S) AND ADDRESS(ES) N/A			10. SPONSORING / MONITORING AGENCY REPORT NUMBER	
11. SUPPLEMENTARY NOTES The views expressed in this thesis are those of the author and do not reflect the official policy or position of the Department of Defense or the U.S. Government.				
12a. DISTRIBUTION / AVAILABILITY STATEMENT Approved for public release; distribution is unlimited			12b. DISTRIBUTION CODE	
13. ABSTRACT (maximum 200 words) The objective of this thesis is to develop a prognostic model of the Northern Canary Current System (NCCS) based on the Princeton Ocean Model with parallel processing capabilities on a cluster of workstations and improved boundary conditions. A one-way coupling with a z-level basin scale model, a North Atlantic version of the Parallel Ocean Program, will also be executed. The development of this model will allow the investigation of coastal processes and the development of numerical models in order to improve the results of sigma coordinate bottom-following ocean models. The roles of wind forcing, bottom topography and thermohaline gradients in coastal processes will be investigated. In order to reduce the Pressure Gradient Force Error while maintaining a realistic topography, a new topographic smoothing technique will be developed. Modified Marchesiello boundary conditions will be applied to a version of POM model one-way coupled with a North Atlantic version of POP. Finally, a automatic multi-region parallelization will be developed, applying minimal changed to the serial POM code. It is shown that a prognostic sigma-coordinate model can be successfully developed for the NCCS, with more realistic topography, improved boundary conditions and with parallel processing capabilities.				
14. SUBJECT TERMS Sigma Coordinate Model, Parallelization, MPI, Boundary Conditions, Multi-Region			15. NUMBER OF PAGES 230	
			16. PRICE CODE	
17. SECURITY CLASSIFICATION OF REPORT Unclassified	18. SECURITY CLASSIFICATION OF THIS PAGE Unclassified	19. SECURITY CLASSIFICATION OF ABSTRACT Unclassified	20. LIMITATION OF ABSTRACT UL	

THIS PAGE INTENTIONALLY LEFT BLANK

Approved for public release; distribution is unlimited

**SENSITIVITY STUDIES USING MULTI-REGION AND OPEN BOUNDARY
CONDITIONS FOR TERRAIN BOTTOM FOLLOWING OCEAN MODELS**

Antonio S. Martinho
Lieutenant, Portuguese Navy
B.S., Portuguese Naval Academy, 1992
M.S., Naval Postgraduate School, 2001

Submitted in partial fulfillment of the
requirements for the degree of

DOCTOR OF PHILOSOPHY IN PHYSICAL OCEANOGRAPHY

from the

**NAVAL POSTGRADUATE SCHOOL
March 2003**

Author:

Antonio S. Martinho

Approved by:

Mary Batteen
Associate Professor of Oceanography
Dissertation Supervisor

Albert Semtner
Professor of Oceanography

Julie McClean
Research Associate Professor
of Oceanography

Roger Williams
Professor of Meteorology

Julie Pullen
Research Scientist
Naval Research Lab

Approved by:

Mary Batteen, Chair, Department of Oceanography

Approved by:

Carson K. Eoyang, Associate Provost for Academic Affairs

THIS PAGE INTENTIONALLY LEFT BLANK

ABSTRACT

The objective of this thesis is to develop a prognostic model of the Northern Canary Current System (NCCS) based on the Princeton Ocean Model (POM) with parallel processing capabilities on a cluster of workstations and improved boundary conditions. A one-way coupling with a z-level basin scale model, a North Atlantic version of the Parallel Ocean Program (POP), will also be executed. The development of this model will allow the investigation of coastal processes and the development of numerical models in order to improve the results of sigma coordinate bottom-following ocean models.

The roles of wind forcing, bottom topography and thermohaline gradients in coastal processes will be investigated. In order to reduce the pressure gradient force error while maintaining a realistic topography, a new topographic smoothing technique will be developed. Modified Marchesiello boundary conditions will be applied to a version of POM model one-way coupled with a North Atlantic version of POP. Finally, an automatic multi-region parallelization will be developed, applying minimal changes to the serial POM code. It is shown that a prognostic sigma-coordinate model can be successfully developed for the NCCS, with more realistic topography, improved boundary conditions and with parallel processing capabilities.

THIS PAGE INTENTIONALLY LEFT BLANK

TABLE OF CONTENTS

I.	INTRODUCTION.....	1
II.	ON THE EFFECTS OF WIND FORCING, TOPOGRAPHY, AND THERMOHALINE EFFECTS IN THE EASTERN BOUNDARY CURRENT SYSTEM OFF IBERIA AND MOROCCO.....	3
A.	ABSTRACT.....	3
B.	INTRODUCTION.....	3
C.	MODEL DESCRIPTION.....	6
1.	Data Sets	6
2.	Pre-Processing	6
3.	Brief Model Description	7
4.	Initialization, Forcing and Boundary Conditions	8
D.	RESULTS	10
1.	Experiment 1 – Pressure Gradient Force Error	10
2.	Experiment 2 – Effects of Wind Forcing	11
3.	Experiment 3 – Effects of Bottom Topography	12
4.	Experiment 4 – Effects of Full Climatology	15
E.	SUMMARY	17
F.	REFERENCES.....	18
III.	ON REDUCING THE SLOPE PARAMETER IN TERRAIN BOTTOM-FOLLOWING NUMERICAL OCEAN MODELS.....	39
A.	ABSTRACT.....	39
B.	INTRODUCTION.....	39
C.	A PRACTICAL EXAMPLE.....	41
D.	TOPOGRAPHY COMPARISONS.....	42
E.	COASTAL CIRCULATION EFFECTS	44
F.	CONCLUSIONS	45
G.	REFERENCES.....	45
IV.	COUPLING THE PARALLEL OCEAN PROGRAM (POP) WITH THE PRINCETON OCEAN MODEL (POM) AND OPEN BOUNDARY CONDITION INVESTIGATIONS IN HIGH RESOLUTION SIGMA COORDINATE OCEAN MODELS.....	71
A.	ABSTRACT.....	71
B.	INTRODUCTION.....	72
C.	MODEL OUTPUT	72
D.	BOUNDARY CONDITIONS.....	74

1.	Radiation Condition	76
2.	Radiation Condition Algorithm.....	77
3.	Adaptivity	78
4.	Volume Constraint.....	79
4.	Sponge Layer	80
5.	Nudging Layer.....	80
E.	BOUNDARY CONDITIONS FOR HIGH RESOLUTION DATA	81
F.	RESULTS	83
1.	Barotropic Velocity and Elevation Results.....	83
2.	Mean Sea Level and Kinetic Energy Results.....	86
G.	SEASONAL STUDY	88
1.	Monthly Model Output.....	88
2.	Three Day Average Model Output.....	90
H.	CONCLUSIONS	91
I.	REFERENCES.....	93
V.	THE DEVELOPMENT OF THE AUTOMATIC PARALLELIZATION OF THE PRINCETON OCEAN MODEL USING THE MULTI-REGION PARALLELIZATION SCHEME WITH MESSAGE PASSING INTERFACE	153
A.	ABSTRACT.....	153
B.	INTRODUCTION.....	153
C.	MULTI-REGION PARALLELIZATION	154
D.	MESSAGE PASSING INTERFACE (MPI) DETAILS	155
E.	PRACTICAL DETERMINATION OF THE MESSAGE PASSING INTERFACE EXCHANGE REGION (MPIER).....	156
F.	MESSAGE PASSING INTERFACE (MPI) EXPERIMENTS	159
G.	AUTOMATIC MULTI-REGION PARALLELIZATION.....	165
H.	CONCLUSIONS	166
I.	REFERENCES.....	167
VI.	SUMMARY	199
	APPENDIX A.....	203
	APPENDIX B. SELECTION OF THE MESSAGE PASSING INTERFACE (MPI) LIBRARY.....	205
	APPENDIX 5.C. STANDARD PARALLELIZATION.....	207
	INITIAL DISTRIBUTION LIST	209

LIST OF FIGURES

Figure 2.1a. Model domain for the Northern Canary Current System (NCCS) is bounded by 31.5N to 41.5N, 16.5W to 6W. Geographical locations are labeled.....	22
Figure 2.1b. Smoothed topography, depths in m, obtained from Sandwell and Smith (1996) after applying a linear two-dimensional low-pass filter.....	23
Figure 2.2. Wind stress vector and magnitude (in color) in Pascals Calculated from annual climatological ECMWF winds obtained from Trenberth et al. (1990).	24
Figure 2.3a. Levitus annual climatological surface temperature ($^{\circ}\text{C}$).	25
Figure 2.3b. Cross-Section at 36N of Levitus annual climatological salinity.	26
Figure 2.4. Pressure gradient force error at day 10. Meridional component of the horizontal velocity (m/s) (in color).	27
Figure 2.5a. Surface temperature ($^{\circ}\text{C}$) (in color) and velocity vectors (m/s) (arrows) for Experiment 2 on day 40.	28
Figure 2.5b. Cross-section of meridional velocity (m/s) at 37.4N for Experiment 2 on day 40.....	29
Figure 2.6a. Temperature ($^{\circ}\text{C}$) (in color) and velocity (m/s) (arrows) for Experiment 2 at day 40 at 1200 m Depth.	30
Figure 2.6b. Cross-section at 37.4N of salinity for Experiment 2 at day 40.	31
Figure 2.7a. Surface temperature ($^{\circ}\text{C}$) (in color) and velocity vectors (m/s) (arrows) for Experiment 3 at day 40. Contour at 200 m depth is shown.	32
Figure 2.7b. Cross-section of meridional velocity (m/s) at 37.4N for Experiment 3 on day 40.....	33
Figure 2.7c. Temperature ($^{\circ}\text{C}$) (color) and velocity (m/s) (arrows) for Experiment 3 at day 40 at 1200 m depth. Contour represents the coastline.	34
Figure 2.8a. Meridional component of the velocity (m/s) (in color) and velocity vectors (m/s) (arrows) for Experiment 4a at day 40.....	35
Figure 2.8b. Cross-section of meridional velocity (m/s) at 37.4N for Experiment 4a on day 40.....	36
Figure 2.9a. Surface temperature ($^{\circ}\text{C}$) (in color) and velocity vectors (m/s) (arrows) for Experiment 4b at day 40. Contour at 200 m Depth is shown.	37
Figure 2.9b. Cross-section of meridional velocity (m/s) at 37.4N for Experiment 4b on day 40.....	38
Figure 3.1a. Initial signed slope parameter in the X-Direction (SSPX). Contour lines for -0.2 and 0.2	48
Figure 3.1b. Signed slope parameter in the X-Direction (SSPX) after the execution of the smoothing algorithm targeting SSPX values less than -0.2 . Contour line for 0.2	49
Figure 3.1c. Signed slope parameter in the X-Direction (SSPX) after the execution of the smoothing algorithm targeting SSPX values less than -0.2 and SSPY values greater than 0.2 . Contour lines for -0.2 and 0.2	50
Figure 3.1d. Signed slope parameter in the X-Direction (SSPX) after the execution of the smoothing algorithm targeting SSPX values less than -0.2 and greater than 0.2 and SSPY values greater than 0.2	51

Figure 3.1e. Signed slope parameter in the X-Direction (SSPX) after the execution of the smoothing algorithm targeting SSPX values less than -0.2 and greater than 0.2 and SSPY values greater than 0.2 and Less than -0.2 . This is the result after the end of the first iteration. Contour lines for -0.2 and 0.2	52
Figure 3.1f. Signed slope parameter in the X-Direction (SSPX) after the execution of two complete iterations.	53
Figure 3.2a. Initial signed slope parameter in the Y-Direction (SSPY). Contour lines for -0.2 and 0.2	54
Figure 3.2b. Signed slope parameter in the Y-Direction (SSPY) after the execution of the smoothing algorithm targeting SSPX values less than -0.2 . . Contour lines for -0.2 and 0.2	55
Figure 3.2c. Signed slope parameter in the Y-Direction (SSPY) after the execution of the smoothing algorithm targeting SSPX values less than -0.2 and SSPY values greater than 0.2 . Contour lines for -0.2	56
Figure 3.2d. Signed slope parameter in the Y-Direction (SSPY) after the execution of the smoothing algorithm targeting SSPX values less than -0.2 and greater than 0.2 and SSPY values greater than 0.2 . Contour lines for -0.2	57
Figure 3.2e. Signed slope parameter in the Y-Direction (SSPY) after the execution of the smoothing algorithm targeting SSPX values less than -0.2 and greater than 0.2 and SSPY values greater than 0.2 and less than -0.2 . This is the result after the end of the first iteration.	58
Figure 3.2f. Signed slope parameter in the Y-Direction (SSPY) after the execution of two complete iterations.	59
Figure 3.3a. Raw topography for the Northern Canary Current System, depths in meters. Contour lines at 100, 200, 500 and 1000 m depth.	60
Figure 3.3b. Topography smoothed with the direct iterative method for the Northern Canary Current System, depths in meters. Contour lines at 100, 200, 500 and 1000 m depth.....	61
Figure 3.3c. Topography smoothed with a Gaussian two-dimensional filter method for the Northern Canary Current System, depths in meters. Contour lines at 100, 200, 500 and 1000 m depth.....	62
Figure 3.4a. Raw topography for the California Current System, depths in meters. Contour lines at 100, 200, 500 and 1000m depth.	63
Figure 3.4b. Topography smoothed with the direct iterative method for the California Current System, depths in meters. Contour lines at 100, 200, -00 and 1000 m depth.....	64
Figure 3.4c. Topography smoothed with a Gaussian two-dimensional filter method for the California Current System, depths in meters. Contour lines at 100, 200, 500 and 1000 m depth.....	65
Figure 3.4d. Raw topography as surface, depths in meters. Difference in depths between raw and smoothed topography with two-dimensional Gaussian filter scaled by the raw topography in Color. Contour lines at 100, 200, 500 and 1000 m depth.....	66
Figure 3.4e. Raw topography as surface, depths in meters. Difference in depths between raw and smoothed topography with one-dimensional direct method scaled by the raw topography in color. Contour lines at 100, 200, 500 and 1000 m depth.....	67

Figure 3.4f. Raw topography as surface, depths in meters. Difference in depths between raw and an alternative smoothing method provided to POM users scaled by the raw topography in Color. Contour lines at 100, 200, 500 and 1000 m depth.....	68
Figure 3.5a. Cross-section of meridional velocity for the experiment with the topography smoothed with the one-dimensional direct iterative method.	69
Figure 3.5b. Cross-section of meridional velocity for the experiment with the topography smoothed with a two-dimensional Gaussian filter.....	70
Figure 4.1a. Bottom topography in color, depths in meters. Every fifth grid line for the POP model is represented.	97
Figure 4.1b. Bottom topography in color, depths in meters. Every fifth grid line for the POM model is represented.....	98
Figure 4.2a. Initial surface temperature ($^{\circ}\text{C}$) fields interpolated for the NCCS POM model. Initial surface velocity (m/s) (arrows).....	99
Figure 4.2b. Initial salinity field interpolated to the NCCS POM.	100
Figure 4.2c. Initial Elevation (m) field interpolated to the NCCS POM.	101
Figure 4.3a Mean wind stress (Pa) from March to May (arrows). Standard deviation of the magnitude of the wind stress from March to May (in color).	102
Figure 4.3b Mean wind Stress (Pa) from June to August (arrows). Standard deviation of the Magnitude of the Wind Stress from June to August (in color).	103
Figure 4.4a Monthly surface temperature ($^{\circ}\text{C}$) from Levitus 94 on March.....	104
Figure 4.4b Monthly surface salinity from Levitus 94 on March.....	105
Figure 4.4c Monthly surface temperature ($^{\circ}\text{C}$) from Levitus 94 on August.....	106
Figure 4.4d Monthly surface salinity from Levitus 94 on August.....	107
Figure 4.6b. Difference in Elevation (m) (in color) and in the barotropic velocity (m/s) (arrows) at day 30 between the boundary condition study with the inflow nudging time scale for velocities (tracers) equal to 3 (1) days (Experiment 1 in Table 4.4) and the reference model.	110
Figure 4.6c. Difference in Elevation (m) (in color) and in the barotropic velocity (m/s) (arrows) at day 30 between the boundary condition study with the inflow nudging time scale for velocities (tracers) equal to 1 (0.5) days (Experiment 2 in Table 4.4) and the reference model.	111
Figure 4.6e. Difference in Elevation (m) (in color) and in the barotropic velocity (m/s) (arrows) at day 30 between the boundary condition study with the inflow nudging time scale for velocities (tracers) equal to 3 (3) days (Experiment 4 in Table 4.4) and the reference model.	113
Figure 4.6f. Difference in Elevation (m) (in color) and in the barotropic velocity (m/s) (arrows) at day 30 between the boundary condition study with the inflow nudging time scale for velocities (tracers) equal to 3 (1) days with no active sponge layer (Experiment 5 in Table 4.4) and the reference model.	114
Figure 4.8a. Monthly wind stress vector (Pa) (arrows) and intensity (Pa) (in color) for March 1996.	118
Figure 4.8b. Monthly wind stress vector (Pa) (arrows) and intensity (Pa) (in color) for April 1996.	119

Figure 4.8c. Monthly wind stress vector (Pa) (arrows) and intensity (Pa) (in color) for May 1996.	120
Figure 4.8d. Monthly wind stress vector (Pa) (arrows) and intensity (Pa) (in color) for June 1996.	121
Figure 4.8e. Monthly wind stress vector (Pa) (arrows) and intensity (Pa) (in color) for July 1996.	122
Figure 4.8f. Monthly wind stress vector (Pa) (arrows) and intensity (Pa) (in color) for August 1996.	123
Figure 4.8g. Monthly wind stress vector (Pa) (arrows) and intensity (Pa) (in color) for September 1996.	124
Figure 4.9a. Monthly surface temperature (°C) (in color) and velocity vectors (m/s) (arrows) for March 1996. Contour at 200 m depth is shown.	125
Figure 4.9b. Monthly surface temperature (°C) (in color) and velocity vectors (m/s) (arrows) for April 1996. Contour at 200 m depth is shown.	126
Figure 4.9c. Monthly surface temperature (°C) (in color) and velocity vectors (m/s) (arrows) for May 1996. Contour at 200 m depth is shown.	127
Figure 4.9d. Monthly surface temperature (°C) (in color) and velocity vectors (m/s) (arrows) for June 1996. Contour at 200 m depth is shown.	128
Figure 4.9e. Monthly surface temperature (°C) (in color) and velocity vectors (m/s) (arrows) for July 1996. Contour at 200 m depth is shown.	129
Figure 4.9f. Monthly surface temperature (°C) (in color) and velocity vectors (m/s) (arrows) for August 1996. Contour at 200 m depth is shown.	130
Figure 4.9g. Monthly surface temperature (°C) (in color) and velocity vectors (m/s) (arrows) for September 1996. Contour at 200 m depth is shown.	131
Figure 4.10a. Salinity (in color) and velocity vectors (m/s) (arrows) at 1000 m depth at simulation day 65.	132
Figure 4.10b. Salinity (in color) and velocity vectors (m/s) (arrows) at 1000 m depth at simulation day 70.	133
Figure 4.10c. Salinity (in color) and velocity vectors (m/s) (arrows) at 1000 m depth at simulation day 75.	134
Figure 4.10d. Observed Salinity (in color) and geostrophic velocity (cm/s) field at 1200m referenced to 2000m, September 1997 (from Johnson et al., 2002).	135
Figure 4.11a. Average wind stress vector (Pa) (arrows) and intensity (Pa) (in color) for 21-24 July.	136
Figure 4.11b. Average wind stress vector (Pa) (arrows) and intensity (Pa) (in color) for 24-27 July.	137
Figure 4.11c. Average wind stress vector (Pa) (arrows) and intensity (Pa) (in color) for 27-30 July.	138
Figure 4.11d. Average wind stress vector (Pa) (arrows) and intensity (Pa) (in color) for 30July-02August.	139
Figure 4.11e. Average wind stress vector (Pa) (arrows) and intensity (Pa) (in color) for 02-05August.	140
Figure 4.11f. Average wind stress vector (Pa) (arrows) and intensity (Pa) (in color) for 05-08August.	141

Figure 4.12a. Average surface temperature ($^{\circ}\text{C}$) (in color) and velocity vectors (m/s) (arrows) for 21-24 July. Contour at 200 m depth is shown.	142
Figure 4.12b. Average surface temperature ($^{\circ}\text{C}$) (in color) and velocity vectors (m/s) (arrows) for 24-27 July. Contour at 200 m depth is shown.	143
Figure 4.12c. Average surface temperature ($^{\circ}\text{C}$) (in color) and velocity vectors (m/s) (arrows) for 27-30 July. Contour at 200 m depth is shown.	144
Figure 4.12d. Average surface temperature ($^{\circ}\text{C}$) (in color) and velocity vectors (m/s) (arrows) for 30 July-02 August. Contour at 200 m depth is shown.	145
Figure 4.12e. Average surface temperature ($^{\circ}\text{C}$) (in color) and velocity vectors (m/s) (arrows) for 02-05 August. Contour at 200 m depth is shown.	146
Figure 4.12f. Average surface temperature ($^{\circ}\text{C}$) (in color) and velocity vectors (m/s) (arrows) for 05-08 August. Contour at 200 m depth is shown.	147
Figure 4.13a. Average surface temperature ($^{\circ}\text{C}$) (in color) for 03-06 July.....	148
Figure 4.13b. Averaged AVHRR surface temperature for 05Sep to 05 Oct ($^{\circ}\text{C}$) (in color) and bottom topography contours (m). From Hagen and al., 1996.....	149
Figure 4.14a. Average wind stress vector (Pa) (arrows) and intensity (Pa) (in color) for 20-23 March.....	150
Figure 4.14b. Average surface temperature ($^{\circ}\text{C}$) (in color) and velocity vectors (m/s) (arrows) for 20-23 March. Iberian Current enclosed by red polygon. Contour at 200 m depth is shown.	151
Figure 5.1a. Illustration of how an adjacent dependence causes out-of-bounds data references on processes P2 and P3 (from SMS Users Guide).	169
Figure 5.1b. Halo regions eliminate the out-of-bounds array references. Notice the distinction between interior points (in white) and halo points (in gray). The local indices of the halo points on the domain edges actually lie outside the serial domain range (1 to 10). These edge halo points are only used for problems that have periodic boundary conditions (from SMS Users Guide).....	170
Figure 5.1c. Halo regions are updated by exchanging data between adjacent processes (from SMS Users Guide).	171
Figure 5.2a. Topography, Depths in Meters.	172
Figure 5.2b. Slope parameter defined as the absolute value of the difference in depths between adjacent points scaled by their mean. In this case it can be seen the simulation of the continental shelf with a slope parameter of around 0.09 and the continental slope with a value of 0.2 (the maximum suggested for sigma coordinate models).....	173
Figure 5.4. Representation of the Arakawa C-Grid. Squares represent the meridional component of the velocities, triangles the zonal component of the velocities and circles represent the elevation, temperature, salinity, and magnitude and length scale of the turbulent kinetic energy. In red, points not used, in magenta, boundary conditions and in blue, points fully calculated by the non-linear equations.	175
Figure 5.5a. Cyclic boundary conditions with three common points are shown in green and orange. In blue points fully calculated by the non-linear equations.	176
Figure 5.5b. Surface meridional velocity (m/s) component at day 25.....	177
Figure 5.5c. Surface meridional velocity (m/s) component at day 43.....	178

Figure 5.5d. Surface meridional velocity (m/s) component at day 80.....	179
Figure 5.5e. Surface zonal velocity (m/s) component at day 80.....	180
Figure 5.5f. Surface velocity (m/s) (vectors) and surface temperatures (°C) (in color) at day 80. Highest vector magnitude is 1.25 m/s.....	181
Figure 5.5g. Surface temperature (°C) at day 80.....	182
Figure 5.6a. Cyclic boundary conditions with four common points shown in green and orange.....	183
Figure 5.6b. Surface meridional velocity (m/s) component at day 80.....	184
Figure 5.6c. Surface zonal velocity (m/s) component at day 80.....	185
Figure 5.6d. Surface temperature (°C) at day 80.....	186
Figure 5.6e. Surface velocity (m/s) (vectors) and surface temperature (°C) (in color) at day 80. Highest vector magnitude is 0.95 m/s.....	187
Figure 5.7. Exchange of information between the two processes running at the same time represented by the red arrows.....	188
Figure 5.8a. Exchange of information between the two processes running at the same time represented by the red arrows. In green, orange and red the points common to both processes. In green and orange the cyclic boundary conditions.....	189
Figure 5.8b. Subdivision of the main region in three zonal sub-regions, running on different processors. Common points between the models in orange, green and red. In green and orange the cyclic boundary conditions. Exchange of data between processes not shown.....	190
Figure 5.8c. Subdivision of the main region in four zonal sub-regions, running on different processors. Common points between the models in orange, green and red. In green and orange the cyclic boundary conditions. Exchange of data between processes not shown.....	191
Figure 5.9a. Subdivision of the Northern Canary Current System model in two zonal sub-regions.....	192
Figure 5.9b. Subdivision of the Northern Canary Current System model in three zonal sub-regions.....	193
Figure 5.9c. Subdivision of the Northern Canary Current System model in four zonal sub-regions.....	194
Figure 5.9d. Subdivision of the Northern Canary Current System model in four rectangular sub-regions.....	195
Figure 5.9e. Subdivision of the Northern Canary Current System model in four rectangular sub-regions avoiding most of the land points.....	196
Figure 5.10a. Time step one of data exchange. Representation of a model subdivided in 16 sub-regions with the processes of the same color exchanging information simultaneously.....	197

LIST OF TABLES

Table 2.1. Summary of experimental design.	5
Table 4.1 Marchesiello (2001) Boundary Conditions.....	76
Table 4.2 Boundary Conditions with High Resolution Data.	81
Table 4.3 Alternative Boundary Conditions (for the variables not specified, the formulation in Table 4.2 was used).	83
Table 4.4 Time Scales for Boundary Condition Nudging (for boundary condition formulations see Table 4.2).	85
Table 5.1. Running times for north-south channel (model 1) with 100 by 70 by 21 points and cyclic boundary conditions.	160
Table 5.2. Running Times for the Northern Canary Current System (model 2) (see Chapter II) with 287 by 241 by 21 Points.	162

THIS PAGE INTENTIONALLY LEFT BLANK

ACKNOWLEDGMENTS

The completion of this research effort represents the end of a long but very rewarding journey. In the first place, I would like to thank my committee. Without the guidance, encouragement and patience of professors M. Batteen, A. Semtner, J. McClean, R. Williams and J. Pullen, this work would not be possible.

Each person fulfilled a critical role towards my success: Prof. Batteen, for supporting my desire to pursue this degree, for her guidance and for the countless advice and effort spent on thesis revisions; Prof. Semtner for the computer time that made available and helpful insights; Prof. McClean for the POP output and for reading my drafts, and gave valuable advice on POP. Prof. Williams is thanked for helpful discussions. Finally, to Dr. Pullen provided valuable suggestions to improve my thesis.

The POP simulation was performed at the Army Research Laboratory as part of a Department of Defense High Performance Grand Challenge project. Pam Rosey (NRL) provided the NOGAPS wind fields.

I also have to thank a former Ph.D. Naval Postgraduate School alumni, Dr. Breno Moura Castro, of the Brazilian Navy. He introduced me to the Message Passing Interface and because of him, the direction of my thesis changed substantially.

I have to thank my advisor in Portugal, LCDR Ventura Soares, for his guidance and support during these four years. I also have to thank the support given by the Hydrographic Institute in Portugal, Direccao de Servico de Formacao and Naval Attache in Washington.

I have to thank the Portuguese NPS students and their families. Their encouragement and support sustained me throughout my thesis. I also wish to thank my family and friends in Portugal, who endured my absence during these four years. Their encouragement, support, trust and love made me feel as though I had never left!

THIS PAGE INTENTIONALLY LEFT BLANK

I. INTRODUCTION

The main objectives of this thesis are to investigate coastal processes and to develop numerical methods in order to improve the capabilities of sigma coordinate bottom-following models, such as the Princeton Ocean Model (POM) community model. Although most of the improvements will be tested in a Northern Canary Current System (NCCS) model, the results should be applicable to other coastal models such as other Eastern Boundary Current (EBC) models.

In the following chapter coastal processes are systematically investigated in order to explore the roles of wind forcing, bottom topography and thermohaline gradients using the POM model in the NCCS. Several experiments of increasing complexity are conducted with annual forcing and initialization in order to isolate their effects on the generation, evolution and maintenance of classical as well as unique features in the NCCS.

In Chapters III to V, new numerical methods are developed to improve the modeling capabilities of sigma coordinate bottom-following models. In Chapter III an alternative numerical method of reducing the slope parameter is developed. This one-dimensional robust direct iterative technique efficiently smoothes the bottom topography so that the pressure gradient force errors, which are common to all sigma coordinate models, are reduced to acceptable values.

In Chapter IV, the regional NCCS Princeton Ocean Model is one-way coupled to a North Atlantic configuration of the Parallel Ocean Program (POP) model. New boundary condition formulations are developed to be able to handle high spatial and temporal resolution data input necessary for the initialization and forcing.

In Chapter V a new automatic parallelization scheme of the POM is developed using a multi-region parallelization in order to achieve superior model performances without having to incorporate major changes to the POM code. In this multi-region scheme, each sub-region acts as a completely independent model, with each running in a

different processor simultaneously. In the boundary condition region, data is exchanged between processes where needed.

II. ON THE EFFECTS OF WIND FORCING, TOPOGRAPHY, AND THERMOHALINE EFFECTS IN THE EASTERN BOUNDARY CURRENT SYSTEM OFF IBERIA AND MOROCCO

A. ABSTRACT

To investigate the role of wind forcing, bottom topography and thermohaline gradients on classical as well as unique features in the northern Canary Current system (NCCS), four process-oriented experiments are conducted with a sigma coordinate primitive equation model. The first experiment, which investigates the pressure gradient force error, shows that velocity errors inherent in three-dimensional sigma coordinate models can be reduced from ~ 100 cm/s to less than 0.5 cm/s in the NCCS. The second experiment, which investigates the effect of annual wind forcing on a flat bottom, accurately portrays classical eastern boundary current (EBC) features. Unique NCCS features associated with a large embayment (i.e., the Gulf of Cadiz), poleward spreading of Mediterranean Outflow, and the generation of Meddies are also discernible. The additional effect of bottom topography in Experiment 3 shows that topography plays important roles in intensifying and trapping the equatorward current near the coast, in weakening the subsurface poleward current, in intensifying eddies off the capes of Iberia and in producing eddies off Figueira da Foz. The use of full instead of horizontally averaged thermohaline gradients in Experiment 4 highlights the development of the Iberian Current off the Portugal west coast, a feature not seen in the previous experiments. This shows that thermohaline gradients are essential to the formation of the Iberian Current. Overall, these results show that while wind forcing is the primary mechanism for generating classical EBC features, bottom topography and thermohaline gradients also play important roles in the generation, evolution, and maintenance of classical as well as unique features in the NCCS.

B. INTRODUCTION

The Canary Current System (CCS) on the eastern boundary of the central North Atlantic is a classical eastern boundary current (EBC) system. Stretching from $\sim 10^\circ\text{N}$ to

~45°N along the coasts of northwest Africa and the Iberian Peninsula (IP), it marks the closing eastern boundary of the North Atlantic Gyre. Typical of other EBCs, there is a mean equatorward Canary Current (CC) and a poleward undercurrent beneath the CC (e.g., Meincke *et al.*, 1975; Fiuza, 1982) near Cabo da Roca (see Figure 2.1a for geographic locations, and Figure 2.1b for bathymetric contours and coastline geometry for the region). Unique to this region is a poleward surface current, referred to as the Iberian Current (IC) (Haynes and Barton, 1993), which has been seen as far south as Cabo de Sao Vicente (Batteen *et al.*, 2000).

Another unique feature that distinguishes the NCCS from other EBCs is the existence of Mediterranean Outflow (MO) through the Strait of Gibraltar into the adjacent Gulf of Cadiz. A large embayment, the Gulf of Cadiz's pronounced east-west coastline orientation results in weaker upwelling in the Gulf of Cadiz than to the north or south of the Gulf of Cadiz, due to the dominant equatorward trade wind direction. The Gulf of Cadiz also creates a large separation between the two west coast upwelling regimes so that no continuous flow between the two appears to exist (Barton, 1998).

Like other classical EBCs, observations of the sea surface in the NCCS region have shown highly energetic mesoscale features such as jet-like surface currents, meanders, eddies and filaments over the broad climatological mean flow of the CC. Satellite sea surface images have shown nearshore upwelling during periods of upwelling favorable winds with several narrow filaments of cooler water extending off the coast of the Iberian Peninsula (Fiuza and Sousa, 1989) and Cape Ghir in northwest Africa (Van Camp *et al.*, 1991; Hagen *et al.*, 1996). Observations have also shown mesoscale eddies on the order of 100 km off the IP coast (Fiuza, 1984; Stammer *et al.*, 1991). These mesoscale features have been observed during periods of predominantly upwelling favorable winds and appear to be located near prominent coastline irregularities such as capes.

Unique to the NCCS is the generation of anticyclonic submesoscale coherent vortices or Meddies. Numerical studies suggest that baroclinic instability of the northward dense plume of salty MO along the IP continental slope leads to the generation

of Meddies (Kase *et al.*, 1989). As a result of numerous observations over the past decade, the primary generation region of Meddies is widely accepted to be off Iberia.

The objective of this study is to investigate the role of wind forcing, bottom topography and thermohaline gradients on classical as well as unique features in the NCCS. The Princeton Ocean Model (POM), a bottom following sigma coordinate model, was chosen for this study because it has been widely used to simulate coastal processes associated with continental shelf flows and bottom boundary layer dynamics. The results of several numerical experiments (see Table 2.1) are explored.

Experiment Number	Annual Wind	Annual Climatology	Bottom Topography
1	No	Horizontally Averaged	Yes
2	Yes	Horizontally Averaged	No
3	Yes	Horizontally Averaged	Yes
4a	No	Full	Yes
4b	Yes	Full	Yes

Table 2.1. Summary of experimental design.

In Experiment 1 velocity errors produced by the pressure gradient force error, an error inherent in all three-dimensional sigma coordinate models, are investigated using the horizontally averaged climatology with bottom topography and no wind forcing. In Experiment 2 the horizontally averaged annual climatology is used with annual wind forcing (see Figure 2.2) on a flat bottom. Experiment 3 is the same as Experiment 2 except that bottom topography (see Figure 2.1b) has been incorporated. To explore the role of bottom topography on the NCCS, the results of Experiment 3 are compared with the results of Experiment 2. Experiment 4b is the same as Experiment 3 except that full

annual climatology (see Figure 2.3a and 2.3b) is used instead of the horizontally averaged annual climatology. To determine the role of the full climatology, the results of Experiment 4 are compared with the results of Experiment 3. To isolate the effect of wind forcing from the joint effects of full climatology and bottom topography, a no wind version of the experiment with full climatology (Experiment 4a) is compared with the same version with wind forcing added (Experiment 4b).

This study is organized as follows. In section 2 we describe the numerical model and the specific experimental conditions. The results of the numerical experiments are presented in section 3. A summary is presented in section 4.

C. MODEL DESCRIPTION

1. Data Sets

The topographic data of the study region were obtained from the Institute of Geophysics and Planetary Physics, University of California San Diego (Sandwell and Smith, 1996). The data set has a resolution of 2 minutes (1/30 of a degree) based upon 30 years compilation of bottom echo soundings obtained by ships. Where the ship data is sparse, altimetry information was used to interpolate soundings.

Annual temperature and salinity values were obtained from Levitus and Boyer (1994) and Levitus et al. (1994). These data sets incorporate a 1 by 1 degree horizontal resolution and have 33 vertical levels.

For wind forcing, climatological wind fields were obtained from the European Centre for Medium Range Weather Forecasts (ECMWF) near-surface wind analyses (Trenberth et al., 1990). The wind data are formulated on a 2.5 by 2.5 degree grid.

2. Pre-Processing

The original topography was interpolated with a two-dimensional (2D) linear interpolation filter to the resolution used in the POM model, i. e., 3 by 3.7 km near the coast and 6 by 7.4 km away from the coast, with a total of 287 by 241 points. The highest resolution was used where the values of the ‘slope parameter’ (defined by Mellor et al.,

1998, as $\frac{|\delta H|}{2 * \bar{H}}$, where \bar{H} is the average depth and δH is the difference in depth between two adjacent cells), were the largest in both the latitude and longitude directions. Since over much of the topography the slope parameter was larger than 0.2, which is the suggested maximum value to be used in sigma coordinate models (Mellor et al., 1998), the topography was smoothed with a linear 2D low-pass filter in order to meet this criterium. The new depth of each point calculated with this filter was a non-weighted average of 15 by 15 points surrounding the point. Subsequently depths greater than 2500 m were reassigned to depths of 2500 m, land was assigned the depth of 10 m (to avoid divisions by zero in the model) and the Strait of Gibraltar was closed. The resulting topography is shown in Figure 2.1b.

The annual temperature and salinity values were interpolated for the horizontal spatial resolution of the model and for the 21 vertical sigma levels using a three-dimensional (3D) linear interpolation scheme. The interpolation had to be done separately for smoothed topography and flat bottom experiments. The temperature field at the near-surface (sigma level one) is shown in Figure 2.3a, while a typical cross-section of salinity is shown in Figure 2.3b.

The daily seasonal winds were averaged over time in order to obtain the annual non-weighted average wind vector field (Figure 2.2). The wind vectors were interpolated for the horizontal spatial resolution of the model with a 2D linear interpolation scheme. The components of the wind stress were then calculated.

3. Brief Model Description

The POM, a well documented model (e.g., Blumberg and Mellor, 1987; Mellor, 1996), was used in the model studies. POM is a primitive equation, free surface model with a second-moment turbulence closure scheme (Mellor and Yamada, 1982) that, through the use of bottom-following sigma levels, can realistically simulate processes associated with continental shelf flows and bottom boundary layer dynamics in local domains (e.g, bays, estuaries and coastal regions). Recently, the model has been used

successfully to simulate decadal processes in entire ocean basins (see Ezer and Mellor, 1994, 1997).

As described earlier, the resolution of the horizontal orthogonal grid varies between 3 by 3.7 km and 6 by 7.4 km. The variable grid allows the use of more (less) points in regions of large (small) gradients.

The 21 sigma level values range from zero at the surface to minus one at the bottom with the vertical grid spacing proportional to the ocean depth. The vertical resolution has been chosen to be higher near the surface and the bottom in order to resolve both the surface boundary layer and the bottom boundary layer, which are important in coastal regions. To eliminate the time constraints for the vertical grid related to the higher resolution near the surface, bottom and shallow waters, an implicit vertical time differencing scheme is used.

The prognostic variables of the model are potential temperature, salinity, density, the three components of velocity, surface elevation, turbulence kinetic energy and length scale. The model uses a split time step for the external and internal modes. The external mode solves the equations for the vertically integrated momentum equations. It also provides the sea surface and barotropic velocity components, and has a time step of 6 seconds. The internal mode solves the complete 3D (baroclinic) equations and has a time step of 180 seconds.

A Smagorinsky formulation (Smagorinsky et al., 1965) is used for the horizontal diffusion in which the horizontal viscosity coefficients depend on the grid size, the horizontal velocity gradients and a Smagorinsky coefficient. In this study a value of 0.2 was assigned to this coefficient, consistent with other POM studies (e.g, Ezer and Mellor, 1997).

4. Initialization, Forcing and Boundary Conditions

The model was initialized with annual temperature and salinity values obtained from Levitus and Boyer (1994) and Levitus et al. (1994). Since the model runs reached a quasi-equilibrium state in a relatively short time (~40 days, not shown), zero salinity and

temperature fluxes have been prescribed at the ocean surface. The climatological surface temperature (Figure 2.3a) shows a latitudinal decrease in temperature. The gradient increases to the north (which will be shown to be important for the formation of the Iberian Current). A cross-section for salinity at 36°N (Figure 2.3b) shows the Mediterranean Water signature at ~1200 m depth with salinity values of ~36.1 psu. In the upper 300 m the North Atlantic Ocean waters are found, with the characteristic high salinity values. A cross-section for temperature at the same location (not shown) shows below ~1000 m depth a downward sloping of the isotherms approaching the coast, which is consistent with the presence of warm Mediterranean Water and of a poleward flow.

In all experiments, the model was run on a beta-plane and forced from rest with the annual ECMWF wind fields, which were interpolated for the model grid. As expected, the wind stress is stronger in the southern region of the model domain and weaker off Iberia and in the Gulf of Cadiz (Figure 2.2).

Correct specification of the open boundary conditions (BC) is important to achieve realistic results, with no reflections, clamping, spurious currents or numerical alteration of the total volume of water in the model. No general criteria can provide the answer to what boundary conditions are the best for a specific model or study. For models with a free surface, such as used here, one of the important criterion is that the BCs should be transparent to the waves. In this model, a gradient boundary condition (Chapman, 1985) which allows geostrophic flow normal to the boundary worked best for the elevation. For the baroclinic velocity components normal to the boundary, an explicit wave radiation scheme based on the Sommerfeld radiation condition was used. For inflow situations, the model was forced with annual temperature and salinity values obtained from Levitus and Boyer (1994) and Levitus et al. (1994), while in outflow situations an advection scheme was used.

For the barotropic velocity components, a Flather radiation plus Roed local solution (FRO) was used. Palma and Matano (2000) showed good results with the FRO during BC tests to determine the BCs response to an alongshelf wind stress. Palma and Matano (1998) also showed that the FRO BC demonstrated good reflection properties and results in a test that determined the BC response to the combined action of wind

forcing and wave radiation. Their tests were executed with the barotropic version of POM and compared well with benchmark results (no boundary conditions).

D. RESULTS

1. Experiment 1 – Pressure Gradient Force Error

In Experiment 1 (see Table 2.1), the model was initialized with the horizontally averaged annual climatological temperatures and salinities. A realistic coastline and realistic topography were used, and there was no wind or thermohaline forcing.

With the horizontal averages of the climatology and no forcing, we should expect that nothing will happen, i.e., the initial state of rest should be maintained with time. Due to pressure gradient force errors, however, this will not be the case and there will be resultant velocities as the result of these errors on the order of 100 cm/s in the NCCS.

Velocity errors induced by the pressure gradient force are unavoidable in three-dimensional (3D) sigma coordinate models. There are two types of sigma coordinate errors, the sigma error of the first kind (SEFK) and of the second kind (SESK), as defined by Mellor et al. (1998). The first one goes to zero prognostically by advecting the density field to a new state of equilibrium. The second one, a vorticity error, is the most important because it does not vanish with time, and is present in both two-dimensional (2D) and three-dimensional (3D) cases.

There are several techniques to reduce the pressure gradient errors:

1 – Smoothing the topography can reduce both SEFK and SESK. In particular, the slope parameter should not be greater than 0.2 (Mellor et al., 1998). Greater values of this parameter can induce currents over 100 cm/s.

2 – Using the highest possible resolution can reduce the errors, since, the pressure gradient error decreases with the square of the horizontal and vertical grid size (Mellor et al., 1994).

3 – Subtracting the horizontally averaged density before the computation of the baroclinic integral reduces the SESK (Mellor et al., 1998).

4 - Using a curvilinear grid that follows the bathymetry reduces the SESK (Mellor et al., 1998).

In this study the first three techniques were used. The last technique, the use of a curvilinear grid, could not be used, because the geography of the Gulf of Cadiz would have given rise to singularity points.

The results of Experiment 1 show that the pressure gradient force error is reduced to less than 0.5 cm/s by day 10 (see Figure 2.4). As expected, maximum velocities of ~ 0.5 cm/s are found within ~ 30 km from the coast where the slope parameter is the largest. Experiment 1 has shown that with the use of the three techniques, the pressure gradient error has been considerably reduced. Before the use of these techniques, model runs showed pressure gradient errors of ~ 100 cm/s in the coastal regions (not shown).

2. Experiment 2 – Effects of Wind Forcing

In Experiment 2 (see Table 2.1), the model was initialized with the horizontally averaged annual climatological temperatures and salinities. A realistic coastline and flat bottom (constant depth of 2500 m) were used, and the model was forced with annual climatological winds.

As expected, the stronger winds at the southward end of the model result in cooler temperatures associated with relatively strong upwelling in the coastal region south of Cape Beddouzza (Figure 2.5a). For example, the offshore extent of the 17°C isotherm is at ~ 300 km off Cape Ghir and at ~ 60 km off Cabo de Sao Vicente. The minimum offshore extent of ~ 25 km is in the Gulf of Cadiz region and north of Cabo da Roca where the wind stress is weaker.

Throughout the model domain, there are predominantly southward surface currents (Figure 2.5a). The stronger currents tend to be found near coastline features, e.g., off Cabo da Roca and off Cape Ghir, with maximum speeds of ~ 60 cm/s in the coastal region between Cape Beddouzza and Cape Ghir. Below the surface flow, the coastal current is predominantly poleward, in the opposite direction of the surface flow (Figure 2.5b).

There is evidence of filament activity off Cabo da Roca, the southwest tip of Iberia, and off Cape Ghir (Figure 2.5a). The development of mesoscale features is also evident in almost all of the coastal domain with the more developed features near coastline irregularities, i.e., Cabo da Roca, Cabo de Sao Vicente, Cape Ghir and Cape Beddouzza. The development of some smaller mesoscale features in the region of the Gulf of Cadiz is also discernible (Figure 2.5a).

Also apparent in the model results is the development of subsurface anticyclonic eddies (i.e., Meddies) centered at ~ 1000 m depth (Figures 2.5b and 2.6a), off Cabo de Sao Vicente and one off Cabo da Roca. A cross-section of salinity at 37.4°N off Cabo de Sao Vicente (see Figure 2.6b) shows a salty core with a maximum of 35.87 psu at 1100 m depth, which is associated with the signature of Mediterranean Water. It has been suggested (e.g., Kase et al., 1989) that the Meddies are generated by the basic instability of the equatorward coastal jet and the poleward undercurrent. The deep origin, salty signature and anticyclonic rotation of the eddy west of Cabo de Sao Vicente are consistent with observations of Meddies in this region (e.g., Richardson and Tychensky, 1998). The Meddy observed off Cabo da Roca (see Figure 2.6a) is consistent with the results of Kase et al., (1989), who observed eddies in the MO off northern Iberia.

3. Experiment 3 – Effects of Bottom Topography

In Experiment 3 (see Table 2.1), the model was initialized with the horizontally averaged annual climatological temperatures and salinities. A realistic coastline and bottom topography were used along with forcing by the annual climatological winds.

The velocities in the coastal areas in Experiment 3 (Figure 2.7a) are roughly 50% higher than the ones in Experiment 2 (e.g., compare with Figure 2.5a). The velocities in Experiment 3 also have the highest magnitudes at ~ 15 km offshore (near the shelf break) instead of at the coast as in Experiment 2. A comparison of the 16°C isotherm in both experiments (Figures 2.5a and 2.7a) shows that the extent of the upwelled waters to the south in Experiment 3 is much less than in Experiment 2, particularly off Cape Ghir. This can be explained by the presence of bottom topography which traps the flow and opposes the tendency for westward propagation due to the planetary beta effect. This is not the

case, however, in the Gulf of Cadiz where the continental shelf is much wider with the result that in the Gulf of Cadiz, Experiment 3 shows a wider spreading of the upwelled waters than in Experiment 2.

Unlike Experiment 2, which had extensive meanders and filaments (Figure 2.5a), the only evidence of mesoscale phenomena in Experiment 3 are two relatively strong eddies, one off Cabo da Roca and another off Figueira da Foz (Figure 2.7a). The eddy off Figueira da Foz, which was not seen in Experiment 2, is associated with a prominent topographic feature off an almost straight coastline which shows that bottom topography can play an important role in the development of mesoscale features.

Note that the core of the undercurrent in Experiment 3 is deeper than in Experiment 2 (compare Figures 2.5b and 2.7b). In Experiment 3 the undercurrent is below ~600 m while in Experiment 2 it is shallower. This is a likely cause for the decrease of mesoscale activity in Experiment 3, since the deepening of the undercurrent results in weaker vertical and horizontal shears, which causes a reduction in the baroclinic and barotropic instabilities responsible for the generation of mesoscale features.

Meddy formation also occurs in Experiment 3 off Cabo da Roca and off Figueira da Foz (not shown); however, unlike Experiment 2, no Meddy forms off Cabo de Sao Vicente. The reason for the lack of formation will now be discussed.

Boundary layer separation is necessary for the formation of Meddies and occurs when a nearly inviscid fluid lying just outside the boundary layer encounters an adverse pressure gradient and undergoes an appreciable deceleration (Batchelor, 1967). Marshall (2001) shows that the downstream pressure variations are determined by three large-scale dynamical processes: the beta effect, vortex stretching and changes in the streamline curvature.

To show this, consider the quasi-adiabatic, steady-state equations of motion with density as a vertical coordinate:

$$\vec{u} \cdot \nabla \vec{u} + f \vec{k} \times \vec{u} + \frac{\nabla(M)}{\rho} = 0 \quad (2.1)$$

$$\nabla \cdot (h\vec{u}) = 0 \quad (2.2)$$

where \vec{u} is the isopycnal velocity, ∇ is the lateral gradient operator, f is the Coriolis parameter, $M = p + \rho g z$ is the Montgomery potential, p is the pressure, ρ is density, g is the gravitational acceleration, z is height and $h = \frac{\partial z}{\partial \rho}$ is the isopycnal thickness. The absolute vorticity equation obtained by taking the curl of (2.1) is:

$$\nabla \cdot (\zeta \vec{u}) + \vec{u} \cdot \nabla f = \frac{f}{h} \vec{u} \cdot \nabla h \quad (2.3)$$

where ζ is the vertical component of the relative vorticity. If we assume that the coastline is to the left of the boundary current, then after the integration over an rectangular area ABCD and some scaling we obtain :

$$\iint_{ABCD} \beta^* v dA - \iint_{ABCD} \frac{f}{h} \vec{u} \cdot \nabla h dA + \left[\int \frac{v^2}{R} dn \right]_{BA}^{CD} \quad (2.4)$$

where $\beta^* = \frac{\partial f}{\partial s}$, s and n are the natural coordinates, R is the radius of curvature of the streamlines and v is the velocity in natural coordinates. The first term in Equation (2.4) is the beta effect, the second the vortex stretching and the third the coastline curvature. In the case studied by Marshall (2001) with the coast on the left side of the boundary current and an anticyclonic current (corresponding to the case of the Gulf Stream), in order to have separation it is necessary that Equation (2.4) be negative. In this case, the beta term works to stabilize the current and to inhibit separation, while the vortex stretching acts to decelerate the current, thus helping the separation. For the coastline to induce separation it is necessary to overcome the stabilizing effects of the beta term and/or vortex stretching. In the case of flat bottom, the implicit (i.e., a priori knowledge of the boundary current path is assumed) relation that gives the separation condition is:

$$R = \left(\frac{v}{\beta^*} \right)^{1/2} \quad (2.5)$$

For the new case considered here where the coastline is to the right of the boundary current (as off Iberia), the condition for boundary current separation is that

Equation (2.4) be positive. In this case, the beta term works to decelerate the boundary current and helps the separation, while the vortex stretching acts to accelerate the currents, thus inhibiting the separation of the current. In order to have separation it is necessary that the changes in streamline curvature (i.e., the last term in Equation (2.4)) overcome the effects of both beta effect and vortex stretching. Noting that the first two terms in Equation (2.4) are roughly linearly dependent on the velocity while the coastline curvature term is roughly proportional to the square of the velocity, separation can still occur if the velocity is very high. Since the coastline curvature term is inversely proportional to the radius of curvature, if the radius approaches zero there can also be separation. Except for these two limiting situations, no guarantees of separation where the coastline is to the right of the boundary current exists. In general, for this case, the generation of Meddies will be dependent on all three terms of Equation (2.4), the beta, vortex stretching and streamline curvature terms.

Applying this criteria to Experiment 3 (bottom topography), we can explain the lack of formation of Meddies off Cabo de Sao Vicente. Bottom topography can inhibit separation in two ways, first because vortex stretching inhibits the separation of boundary currents and second because in the case with bottom topography (experiment 3) the radius of curvature of the land at ~1000 m depth is much larger than in the flat bottom case (Experiment 2). At Cabo de Sao Vicente in Figures 2.6a (flat bottom) and 2.7c (topography), the increase of the radius of curvature in the topography case is an inhibiting factor for the separation of the boundary current; thus no Meddy was formed. In contrast off Cabo da Roca because there is no significant change in the radius of curvature at Cabo da Roca from Experiment 2 to Experiment 3, Meddies do occur in this location for both the flat bottom (Experiment 2) and the topography (Experiment 3) cases.

4. Experiment 4 – Effects of Full Climatology

In Experiments 4a (no wind forcing) and 4b (wind forcing), the model was initialized with the full annual climatological temperatures and salinities (see Table 2.1). A realistic coastline and bottom topography were used in both experiments.

In Experiment 4a, which has no wind forcing, a density-driven poleward coastal current is generated (Figure 2.8a). This current is strongest near the shelf break with maximum speeds of ~ 40 cm/s, and in the northern region of the model where the horizontal variation of temperature is the highest. Due to the horizontal gradient of temperature the current advects warmer waters from south to north with a subsequent, increase of the poleward velocity to the north. A cross-section of the meridional component of the velocity at 37.4°N shows the presence of a weak and very deep equatorward undercurrent (Figure 2.8b). The core of the undercurrent is located at ~ 1700 m depth. The resulting weak vertical and horizontal shear between the surface current and undercurrent is responsible for the almost total absence of mesoscale features (see Figure 2.8a).

When wind forcing is added (Experiment 4b), similar patterns are discernible for Experiments 3 and 4b; however, the equatorward coastal jet in Experiment 4b is weaker and narrower than in Experiment 3 (compare Figures 2.7a and 2.7b with Figures 2.9a and 2.9b). The surface coastal current in Experiment 4b is weaker because the thermohaline forcing opposes the wind forcing; it is also narrower because the opposing poleward surface current (i.e., the Iberian Current) present in Experiment 4b traps the equatorward surface current near the coast. Since the Iberian Current is only present when full climatological temperatures and salinities are used (Experiments 4a and 4b), this shows that the horizontal thermohaline gradients play an important role in the formation and maintenance of this current. In particular, the surface poleward Iberian Current present in the northern region of the model is formed due to the effect of the strong horizontal thermohaline gradients (Figure 2.3a) which oppose and overcome the forcing by the weaker equatorward wind stress (Figure 2.2) to the north. Note that even though the Gulf of Cadiz is also an area of weak wind stress, the horizontal thermohaline gradient is not strong enough to overcome the effects of the wind stress in this region.

A cross-section of the meridional velocity at 37.4°N shows that Experiment 4b has the shallowest (at ~ 700 m core depth), and strongest undercurrent ($\sim 20 - 30$ cm/s) of all the experiments (Figure 2.9b). The resulting increase in the vertical and horizontal shear is responsible for the subsequent increase in barotropic and baroclinic instabilities and

resulting increased mesoscale activity (see Figure 2.9a). Note that the surface poleward Iberian Current is also discernible at ~ 80 km offshore.

E. SUMMARY

The objective of this study was to investigate the roles of wind forcing, bottom topography and thermohaline gradients on classical as well as unique features in the NCCS. Toward this end, four numerical experiments were run, all on a beta-plane, with a sigma coordinate numerical model, i.e., the Princeton Ocean Model. The first experiment investigated the pressure gradient force error. The second experiment studied the effect of annual wind forcing on a flat bottom. The third experiment investigated the additional effect of topography. The fourth experiment examined the additional role of the full annual climatology.

Experiment 1, used to evaluate the pressure gradient force error, showed that velocity errors inherent in three-dimensional sigma coordinate models could be successfully reduced from ~ 100 cm/s to ~ 0.5 cm/s using three techniques: smoothing the topography, using the highest possible resolution, and subtracting the area-averaged density before the computation of the baroclinic integral. The results showed that the highest velocities (~ 0.5 cm/s) were concentrated near the coast where the values of the slope parameter were the highest.

Experiment 2 produced classical features of the NCCS, an offshore surface equatorward meandering jet, realistic surface and subsurface poleward currents, upwelling, meanders, eddies and filaments. In addition, these experiments depicted unique NCCS features, including the geographical separation of the Gulf of Cadiz region from the west coast upwelling regimes, poleward spreading of the MO, and the development and propagation of Meddies from the Cabo de Sao Vicente and Cabo da Roca regions.

A comparison between Experiments 2 and 3 showed that bottom topography plays an important role in trapping and intensifying the equatorward current near the coast, in weakening and deepening the poleward undercurrent and in producing eddies off Figueira da Foz. Stronger eddies occurred off Cabo da Roca and off Figueira da Foz

in Experiment 3. Unlike Experiment 2 no formation of Meddies off Cabo Sao Vicente in Experiment 3 occurred. It was shown that the lack of formation was primarily due to both vortex stretching and increased radius of curvature of the smoothed topography, which inhibited boundary current separation.

In Experiment 4, the additional effect of the full annual climatology produced the tightening of currents near the coast and slightly weaker currents due to the opposing effects of thermohaline gradients and wind forcing. As in Experiment 3, there was no development of Meddies of Cabo de Sao Vicente. Only Experiment 4 showed the Iberian Current off the Portugal coast showing that horizontal thermohaline gradients are essential to the formation of this current. Overall, the results of these experiments show that while wind forcing is the primary mechanism for generating classical EBC features, bottom topography and thermohaline gradients also play important roles in the generation, evolution, and maintenance of classical as well as unique features in the NCCS.

F. REFERENCES

Barton, E.D., Eastern Boundary of the North Atlantic: Northwest Africa and Iberia. In *The Sea, Vol. 11, The Global Coastal Ocean: Regional Studies and Syntheses*, K.H. Brink and A.R. Robinson, eds., Wiley, New York, Chap.22, 633-657, 1998.

Batchelor, G.K., An Introduction to Fluid Dynamics, *Cambridge University Press*, 615pp, 1967.

Batteen, M. L., J. R. Martinez, D. W. Bryan, and E. J. Buch, A Modeling Study of the Coastal Eastern Boundary Current System off Iberia and Morocco, *Journal of Geophysical Research* , 105 (C6), 14,173-14,195, 2000.

Blumberg, A. F., and G. L. Mellor, A Description of a Three-Dimensional Coastal Ocean Circulation Model, *Three-Dimensional Coastal Ocean Models, Coastal Estuarine Sciences.*, 4, edited by N. Heaps, pp 1-16, AGU, Washington, D. C., 1987.

Chapman, D. C., Numerical Treatment of Cross-Shelf Open Boundaries in a Barotropic Coastal Ocean Model, *Journal of Physical Oceanography*, 25, 1060-1075, 1985.

Ezer, T. and G. L. Mellor, Diagnostic and Prognostic Calculations of the North Atlantic Circulation and Sea Level Using a Sigma Coordinate Ocean Model, *Journal of Geophysical Research*, 99 (C7), 14,159-14,171, 1994.

Ezer, T. and G. L. Mellor, Simulations of the Atlantic Ocean With a Free Surface Sigma Coordinate Ocean Model, *Journal of Geophysical Research*, 102 (C7), 15,647-15,657, 1997.

Fiuza, A. F. de G., M. E. de Macedo, and M. R. Guerreiro, Climatological Space and Time Variation of the Portuguese Coastal Upwelling, *Oceanologica Acta*, Vol. 5, No. 1, 31-40, 1982.

Fiuza, A. F. de G., Hidrologia e Dinamica das Aguas Costeiras de Portugal. Dissertacao apresentada a Universidade de Lisboa para obtencao do grau de Doutor em Fisica, especializacao em Ciencias Geofisicas Universidade de Lisboa, 294pp, 1984.

Fiuza, A. F. de G. and F. M. Sousa, Preliminary Results of a CTD Survey in the Coastal Transition Zone off Portugal During 1-9 September 1988, *Coastal Transition Zone Newsletter*, 4, 2-9, 1989.

Haynes, R., E. D. Barton, and I. Pilling, Development, Persistence and Variability of Upwelling Filaments off the Atlantic Coast of Iberia, *Journal of Geophysical Research*, 98, 22681-22692, 1993.

Kase, R. H., A. Beckman, and H. H. Hinrichsen, Observational Evidence of Salt Lens Formation in the Iberian Peninsula, *Journal of Geophysical Research*, 94, 4905-4912, 1989.

Levitus, S., and T. P. Boyer, World Ocean Atlas 1994, Vol. 4: Temperature, *NOAA Atlas NESDI 4*, 117 pp., U. S. Department of Commerce, Washington, D.C., 1994.

Levitus, S., R. Burgett, and T.P. Boyer, World Ocean Atlas, 1994, Vol. 3: Salinity, *NOAA Atlas NESDI 3*, 99 pp., U.S. Department of Commerce, Washington, D.C., 1994.

Marshall, David P. and Claire E. Tansley, An Implicit Formula for Boundary Current Separation, *American Meteorological Society*, 1633-1638, 2001.

Meincke, J., G. Siedler, and W. Zenk, Some Current Observations Near the Continental Slope off Portugal, *"Meteor" Forsch.-Ergebn.*, A, 16, 15-22, 1975.

Mellor, G.L., User's Guide for a Three-Dimensional, Primitive Equation, Numerical Ocean Model, 40 pp, Program in Atmospheric and Ocean Sciences Report, Princeton Univ., Princeton, N. J., 1996.

Mellor, G.L., L.Y. Oey, and T. Ezer, Sigma Coordinate Pressure Gradient Errors and the Seamount Problem, *Journal of Atmospheric and Ocean Technology*, 15, 1122-1131, 1998.

Mellor, G. L., and T. Yamada, Development of a Turbulence Closure Model for Geophysical Fluid Problems, *Review Geophysics Space Physics*, 20, 851-875, 1982.

Palma E.D., and R. P. Matano, On the Implementation of Passive Open Boundary Conditions for a General Circulation Model: the Barotropic Mode, *Journal of Geophysical Research*, 103 (C1), 1319-1341, 1998.

Palma, E. D., and R. P. Matano, On the Implementation of Open Boundary Conditions for a General Circulation Model: the Three-Dimensional Case, *Journal of Geophysical Research*, 105 (C4), 8605-8627, 2000.

Richardson, P. L. and A. Tychensky, Meddy Trajectories in the Canary Basin Measured During the SEMAPHORE Experiment, 1993-1995, *Journal of Geophysical Research*, 103, 25029-25045, 1998.

Sandwell, D.T., and W. F. Smith, Global Bathymetric Prediction for Ocean Modelling and Marine Geophysics, 1996.

Smagorinsky, J., S. Manabe and J.L. Holloway, Numerical Results from a Nine-Level General Circulation Model of the Atmosphere, *Monthly Weather Review*, 93, 727-765, 1965.

Stammer, D., H. H. Hinrichsen, and R. H. Kase, Can Meddies Be Detected By Satellite Altimetry?, *Journal of Geophysical Research*, 96, 7005-7014, 1991.

Trenberth, K. E., W. G. Large, J. G. Olsen, The Mean Annual Cycle in Global Ocean Wind Stress, *Journal of Physical Oceanography*, 20, 1742-1760, 1990.

Van Camp, L., L. Nykjaer, E. Mittelstaedt, and P. Schlittenhardt, Upwelling and Boundary Circulation off Northwest Africa as Depicted by Infrared and Visible Satellite Observations, *Progress in Oceanography*, 26, 357-402, 1991.

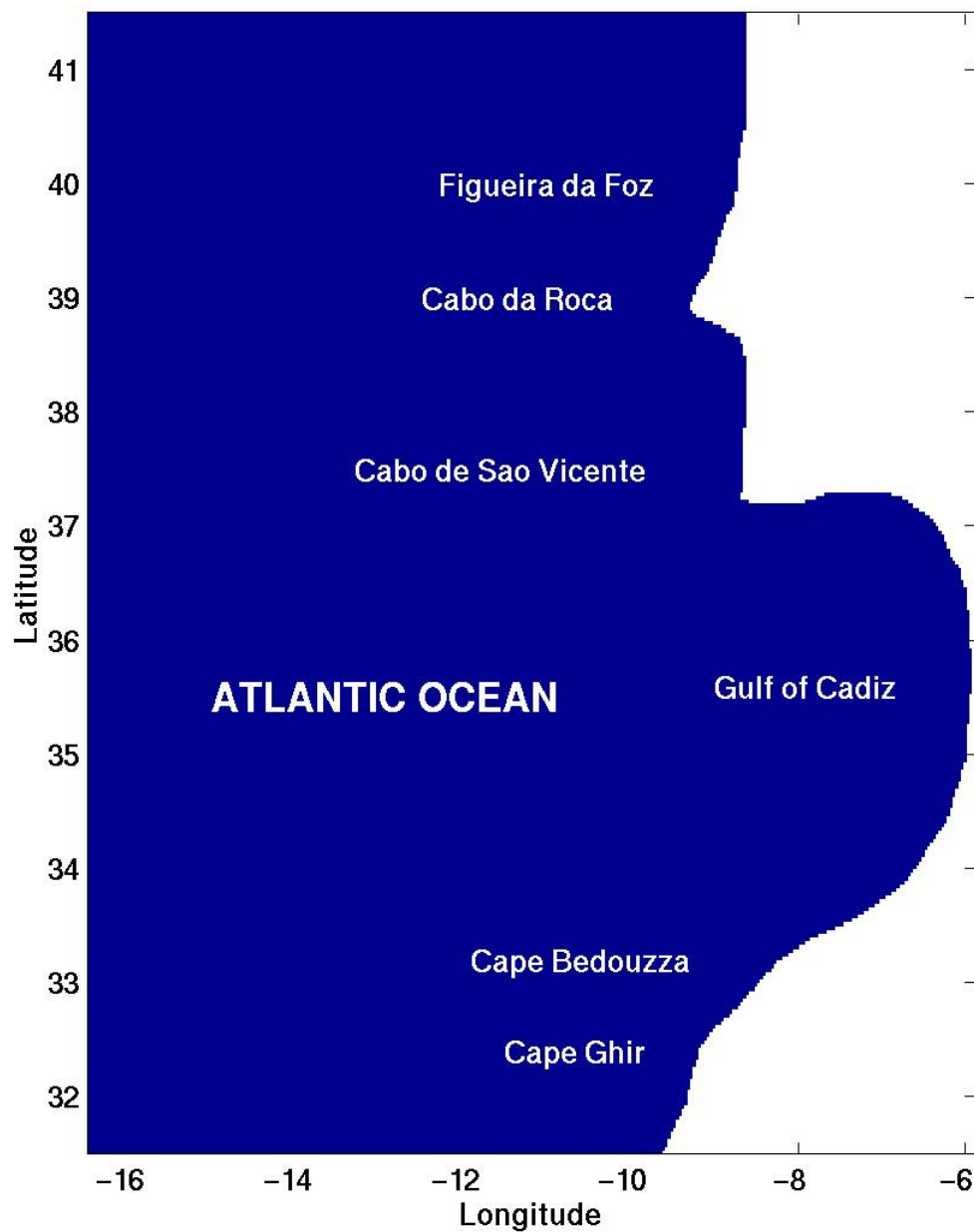


Figure 2.1a. Model domain for the Northern Canary Current System (NCCS) is bounded by 31.5N to 41.5N, 16.5W to 6W. Geographical locations are labeled.

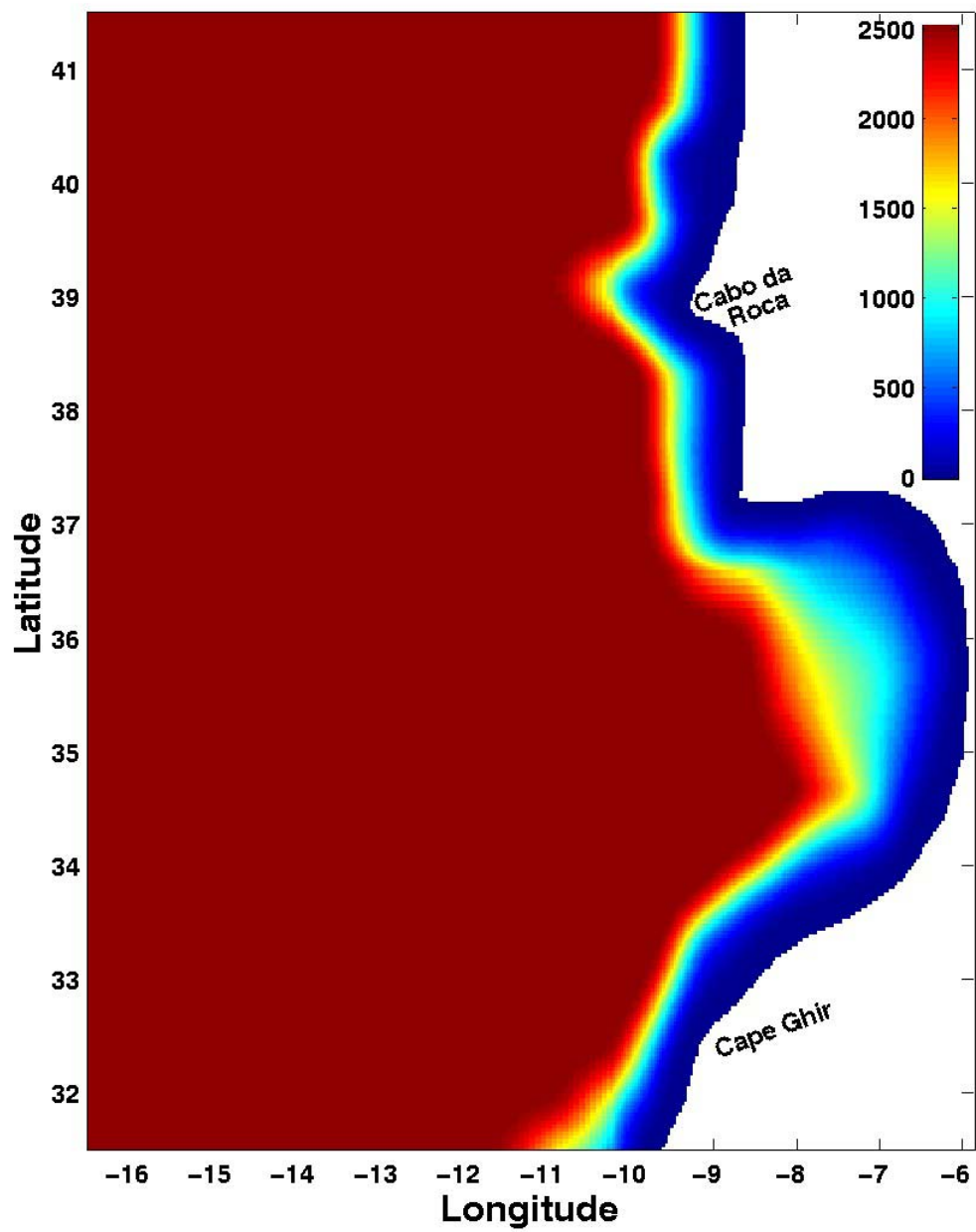


Figure 2.1b. Smoothed topography, depths in m, obtained from Sandwell and Smith (1996) after applying a linear two-dimensional low-pass filter.

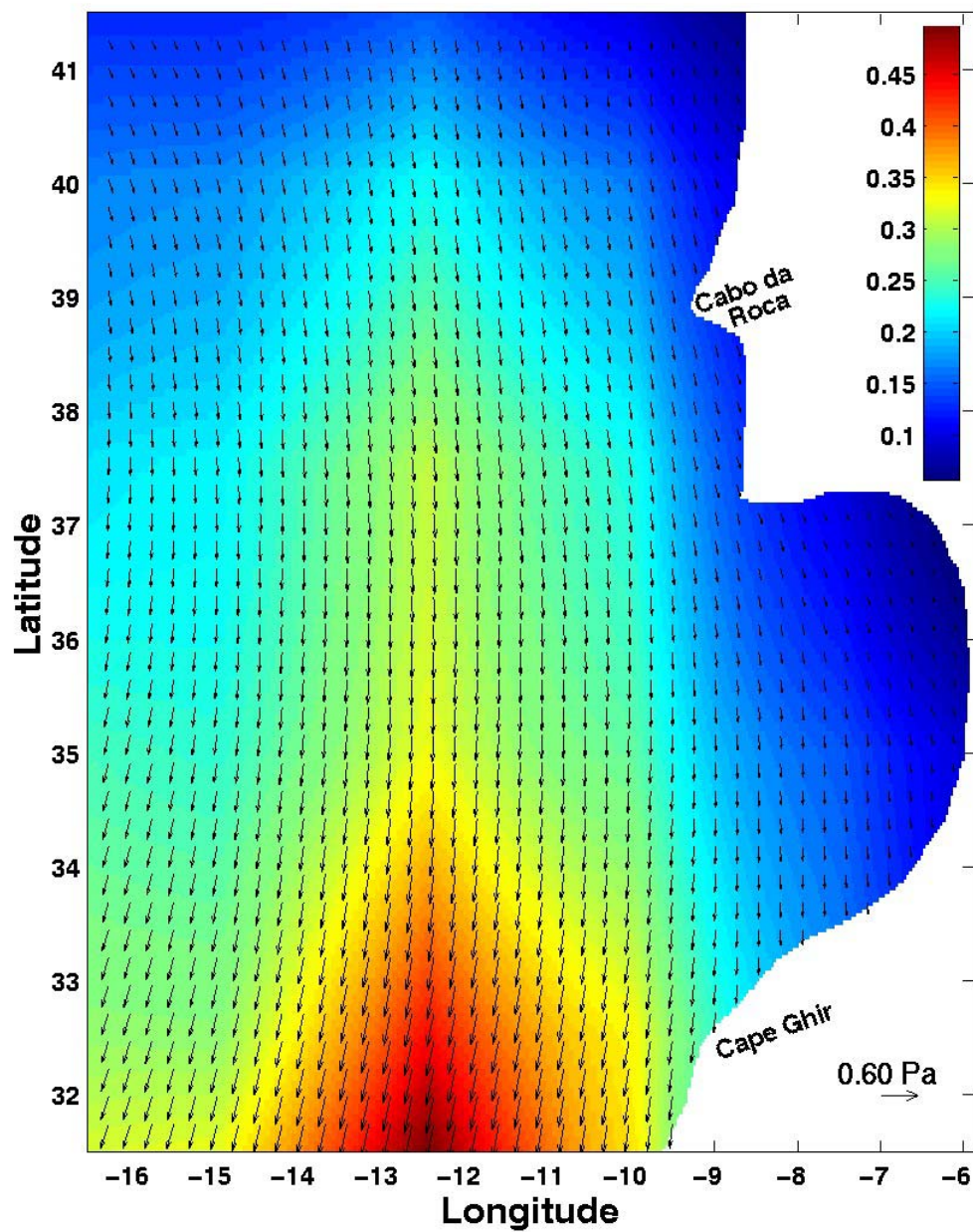


Figure 2.2. Wind stress vector and magnitude (in color) in Pascals Calculated from annual climatological ECMWF winds obtained from Trenberth et al. (1990).

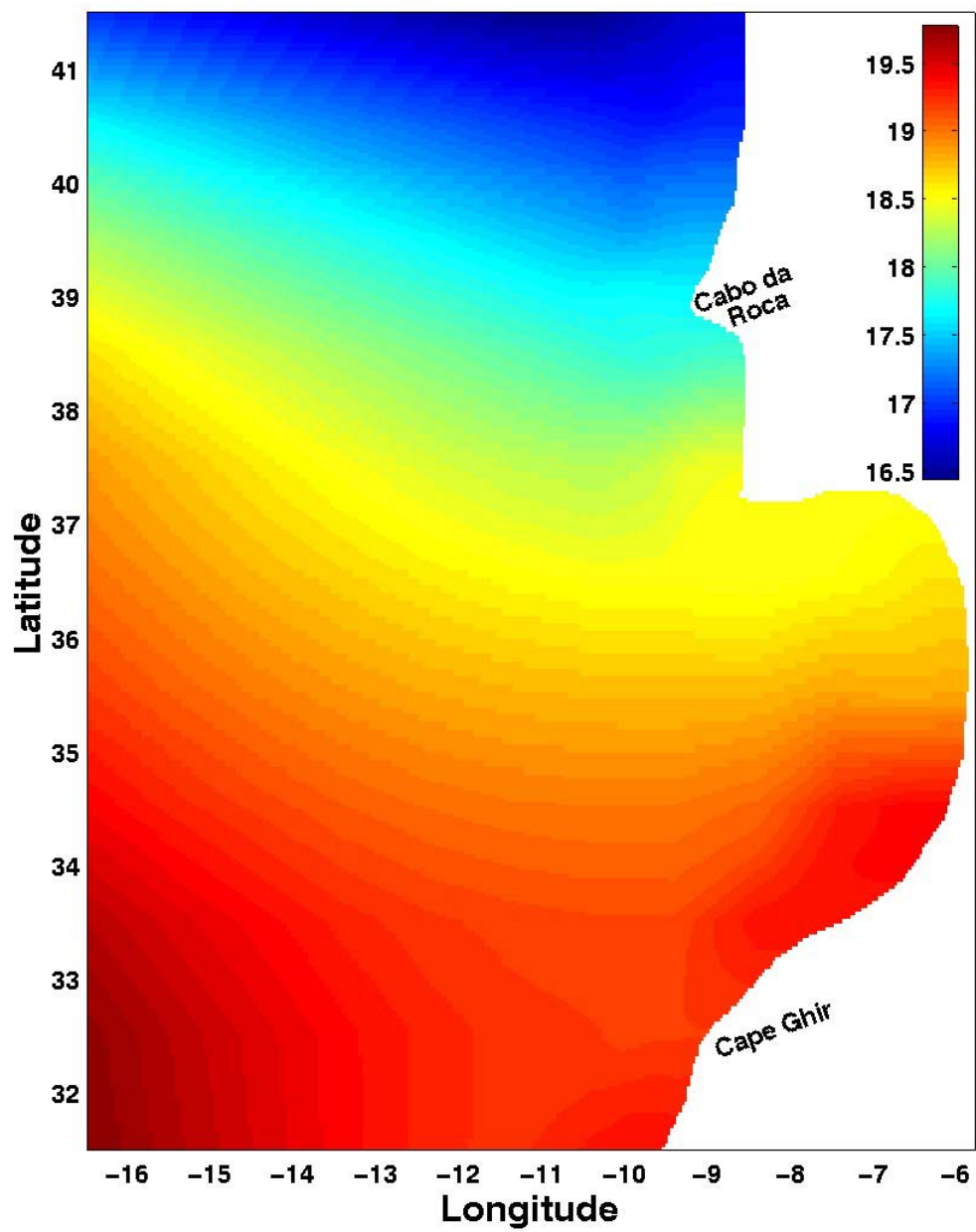


Figure 2.3a. Levitus annual climatological surface temperature (°C).

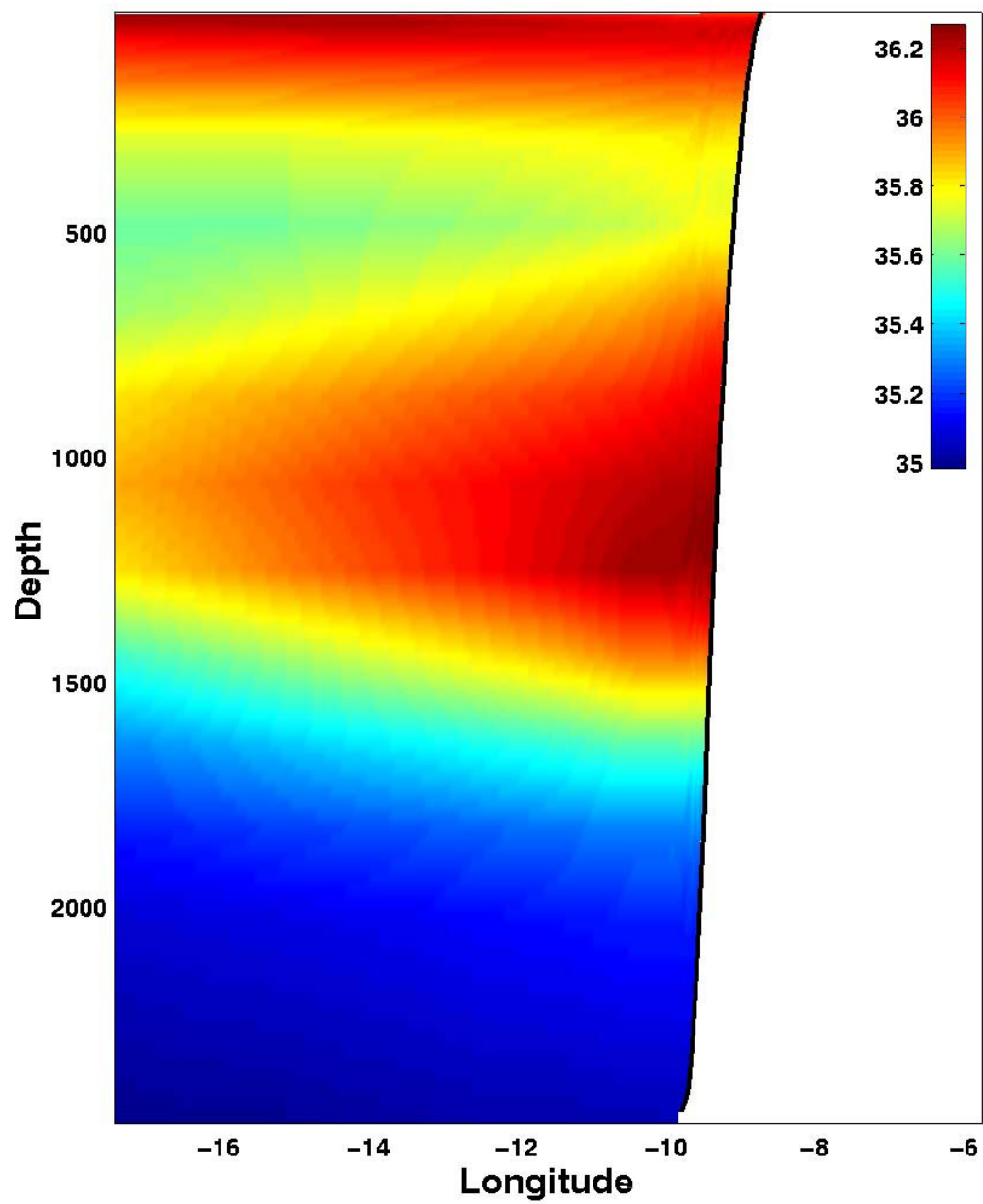


Figure 2.3b. Cross-Section at 36N of Levitus annual climatological salinity.

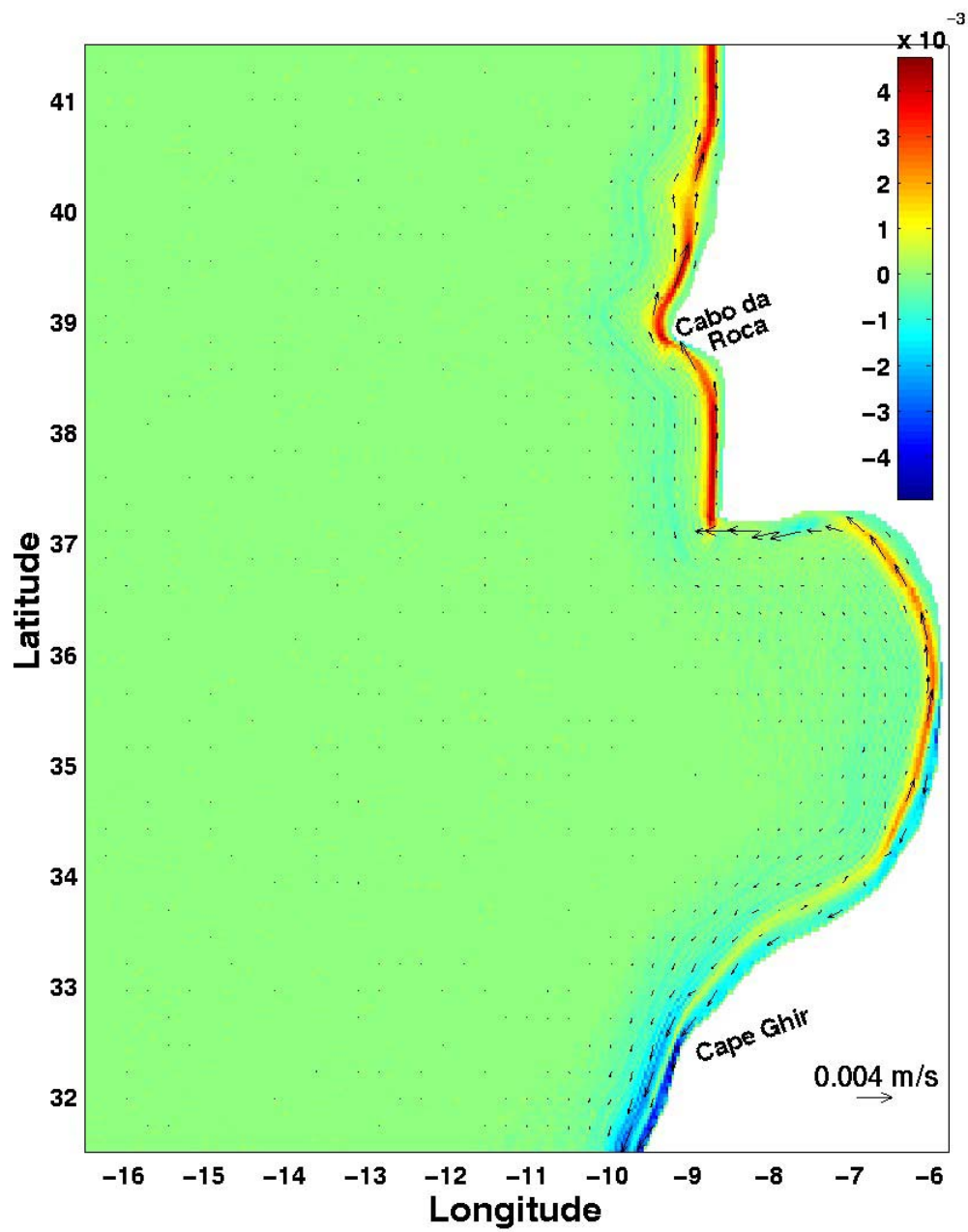


Figure 2.4. Pressure gradient force error at day 10. Meridional component of the horizontal velocity (m/s) (in color).

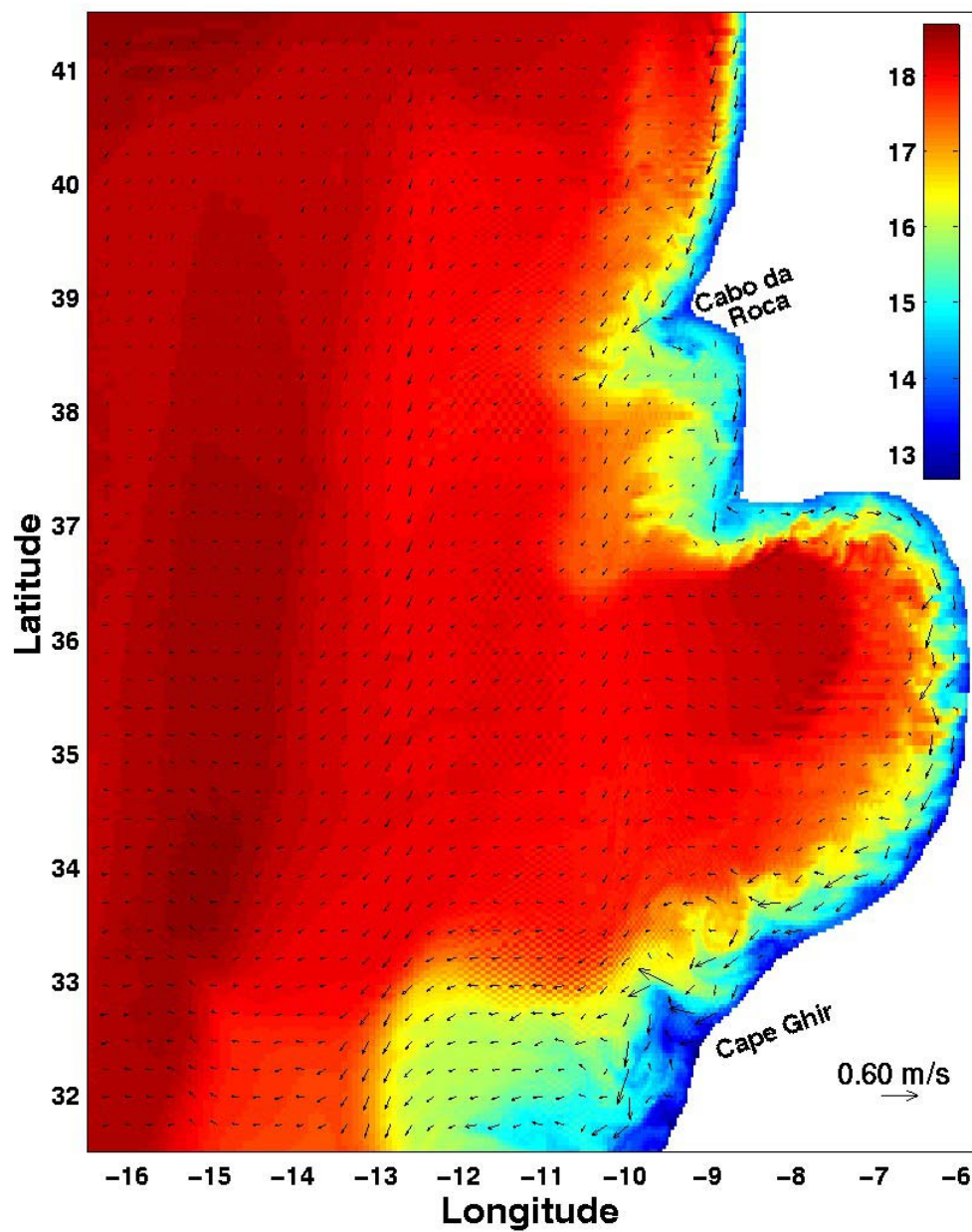


Figure 2.5a. Surface temperature (°C) (in color) and velocity vectors (m/s) (arrows) for Experiment 2 on day 40.

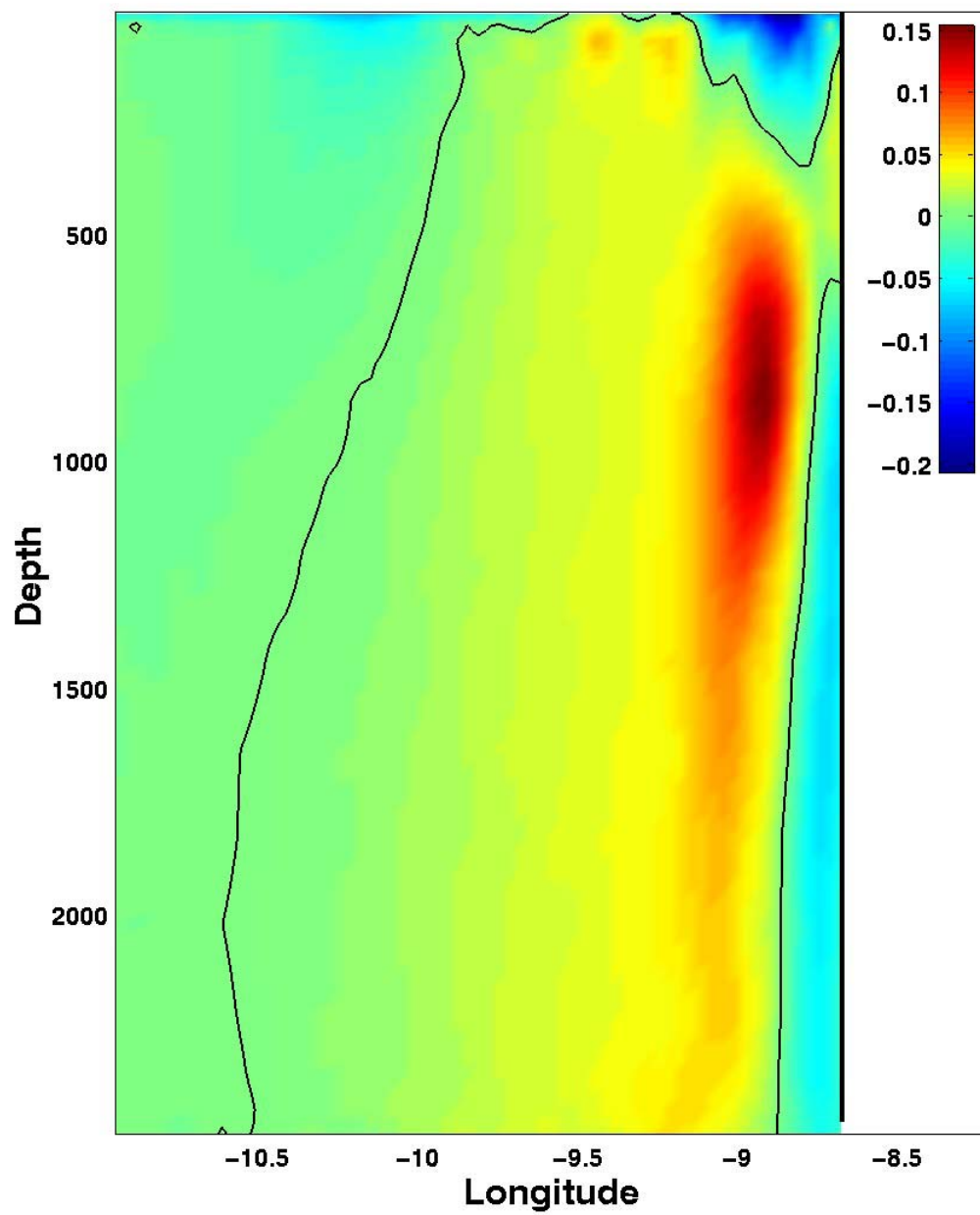


Figure 2.5b. Cross-section of meridional velocity (m/s) at 37.4N for Experiment 2 on day 40.

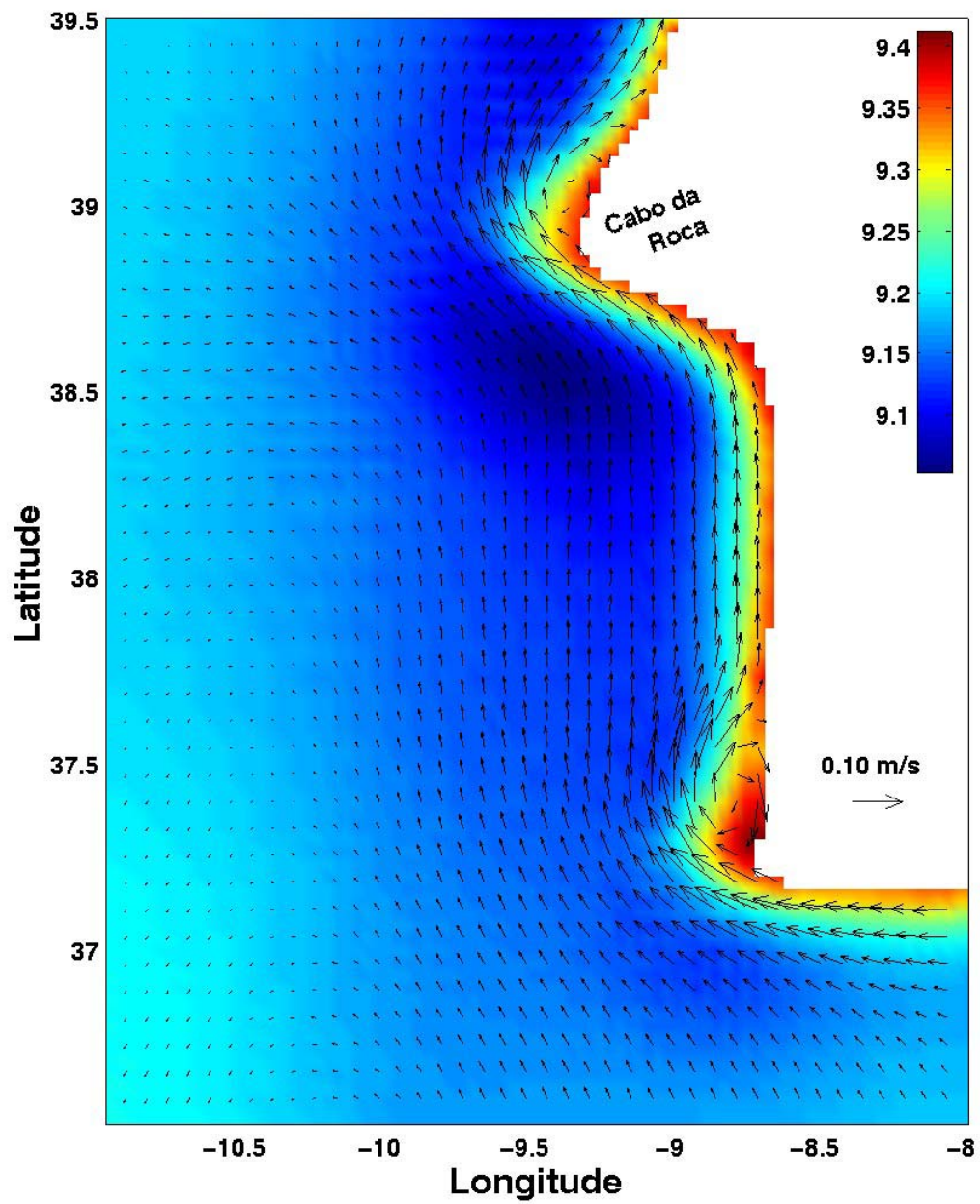


Figure 2.6a. Temperature (°C) (in color) and velocity (m/s) (arrows) for Experiment 2 at day 40 at 1200 m Depth.

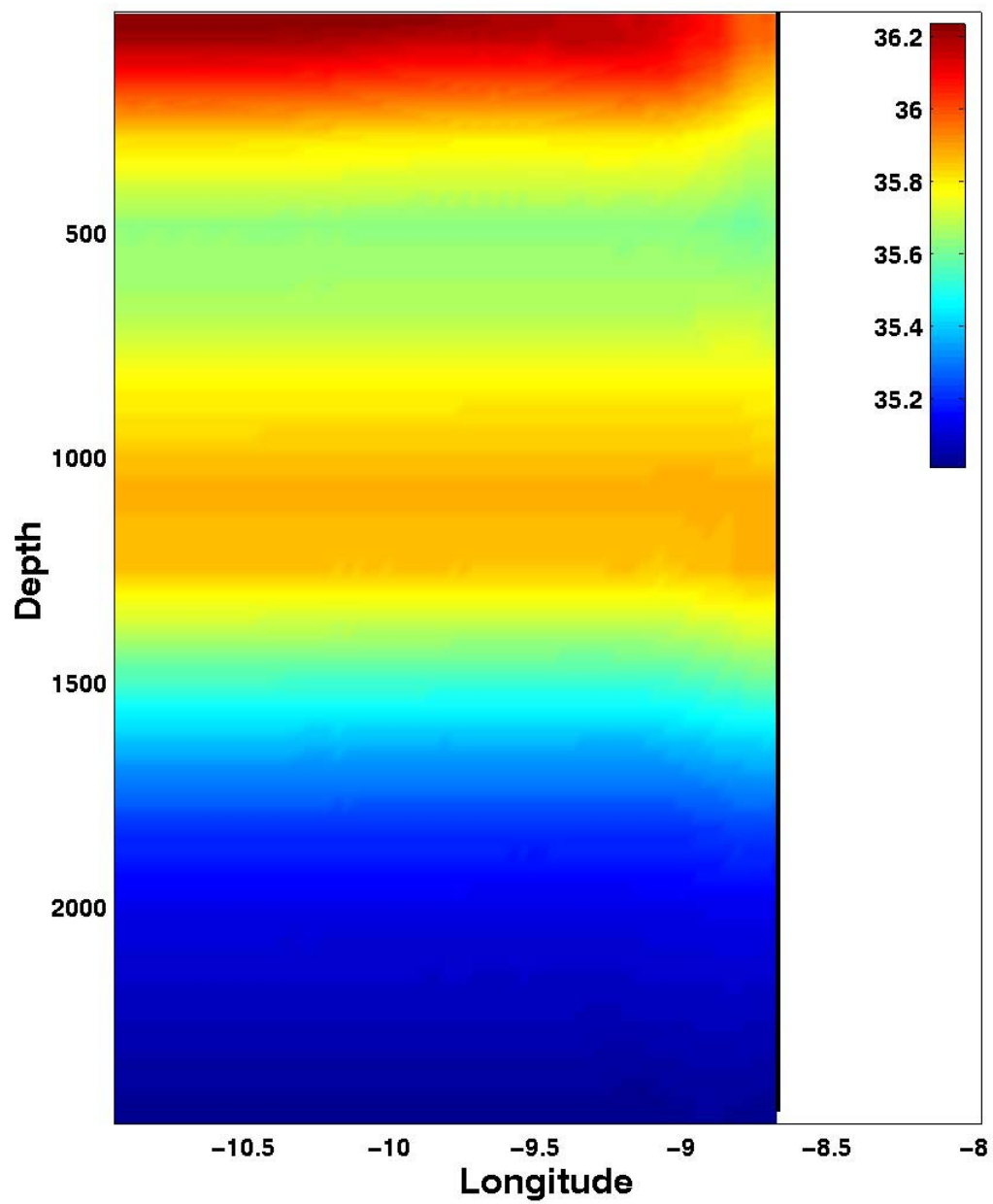


Figure 2.6b. Cross-section at 37.4N of salinity for Experiment 2 at day 40.

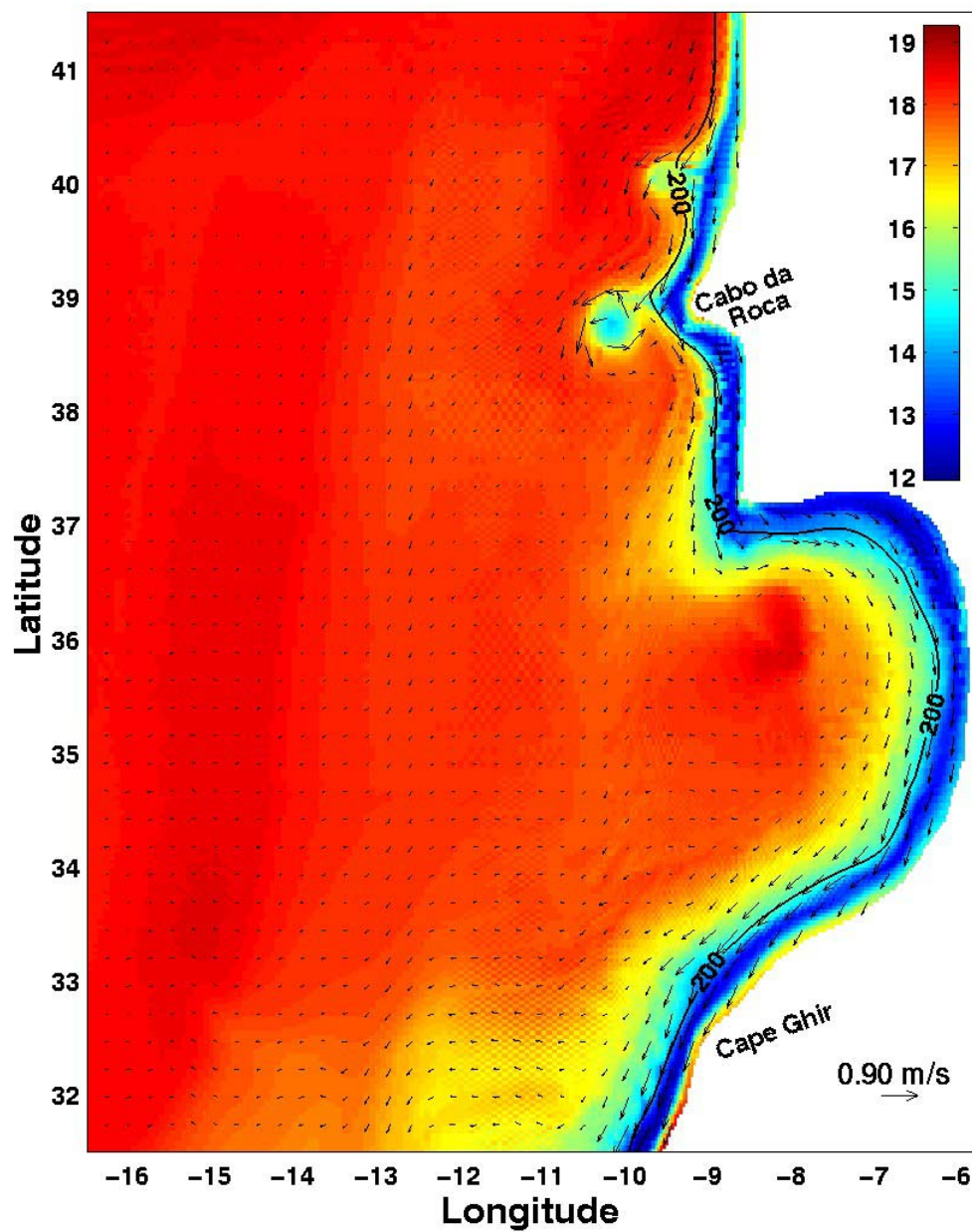


Figure 2.7a. Surface temperature ($^{\circ}\text{C}$) (in color) and velocity vectors (m/s) (arrows) for Experiment 3 at day 40. Contour at 200 m depth is shown.

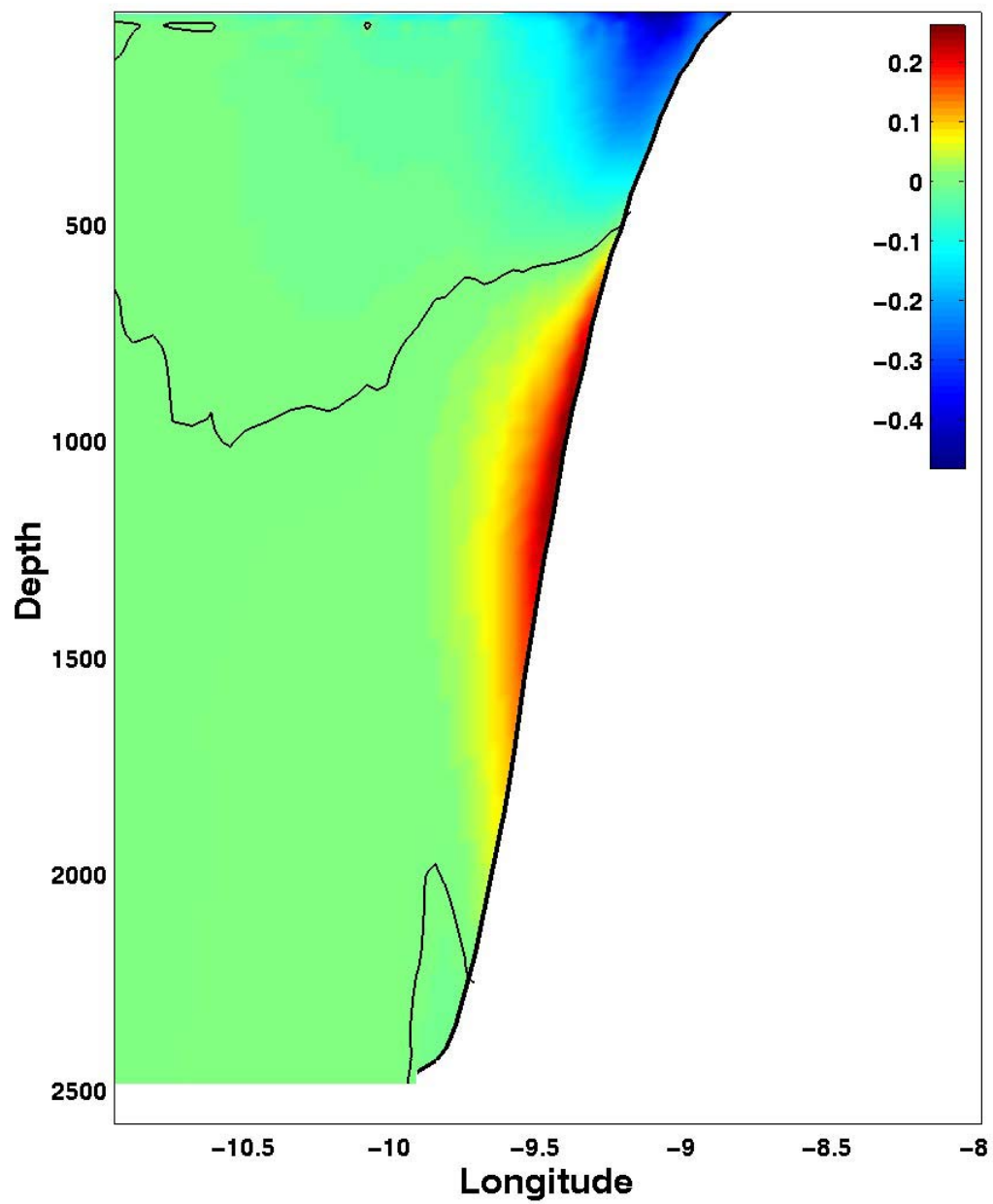


Figure 2.7b. Cross-section of meridional velocity (m/s) at 37.4N for Experiment 3 on day 40.

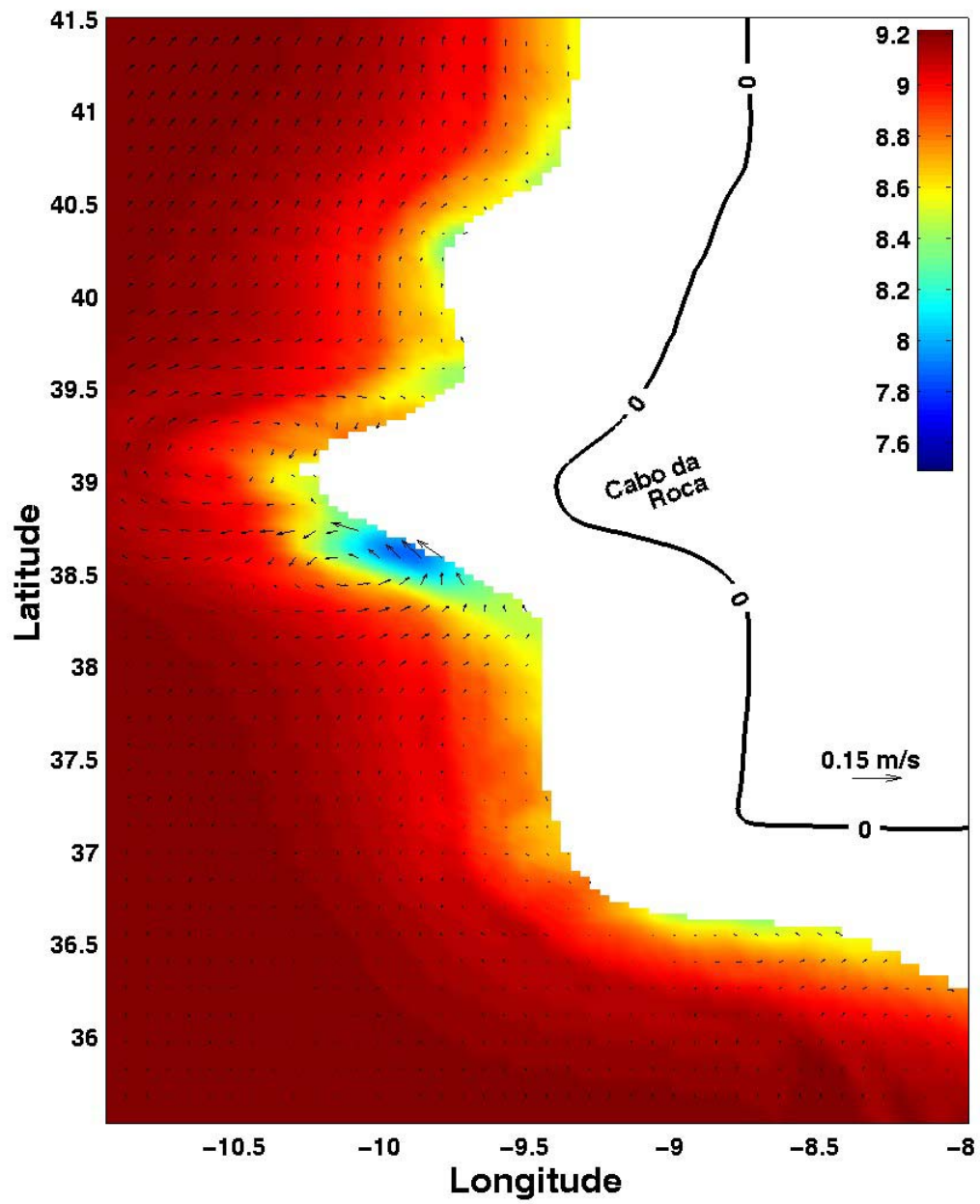


Figure 2.7c. Temperature (°C) (color) and velocity (m/s) (arrows) for Experiment 3 at day 40 at 1200 m depth. Contour represents the coastline.

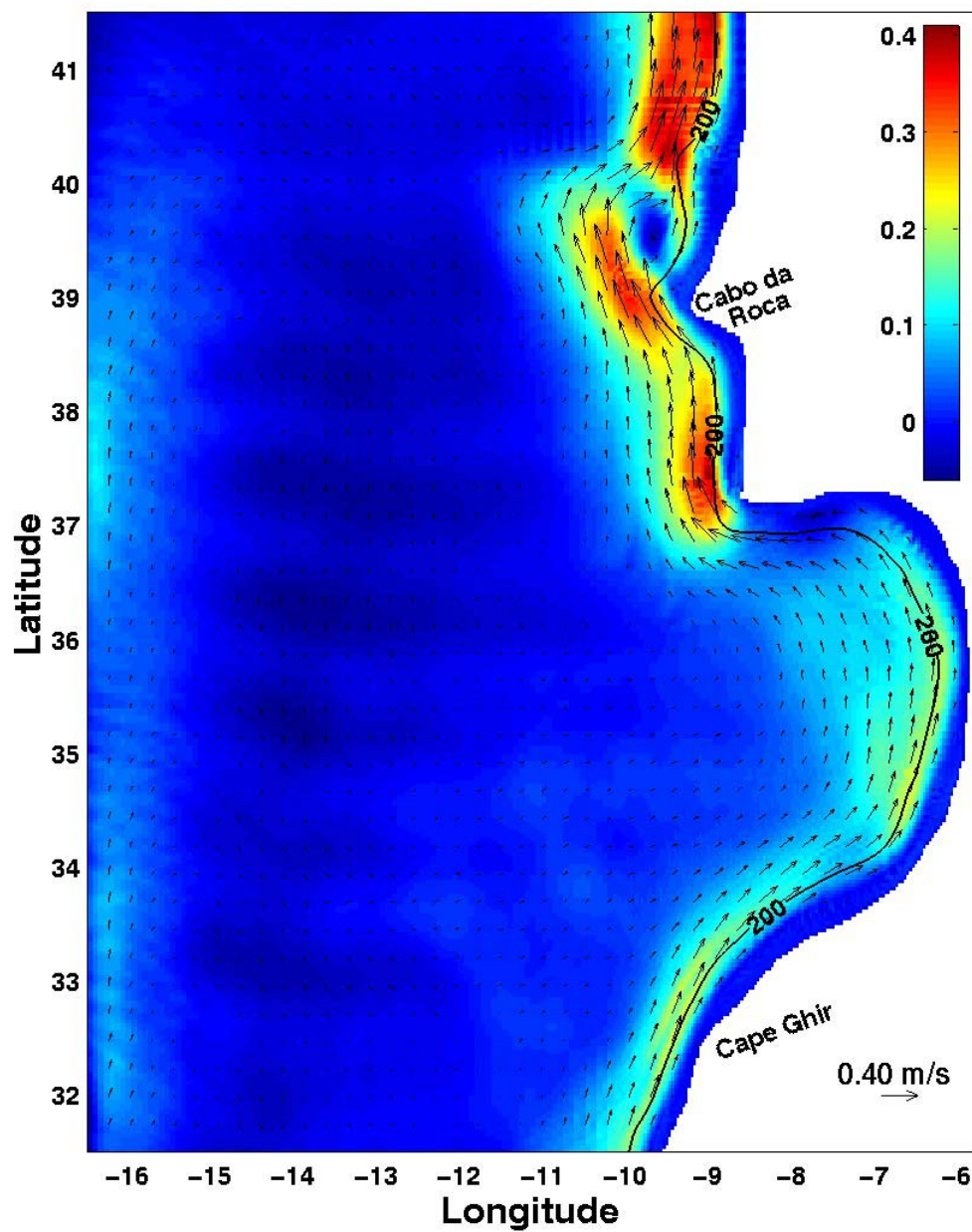


Figure 2.8a. Meridional component of the velocity (m/s) (in color) and velocity vectors (m/s) (arrows) for Experiment 4a at day 40.

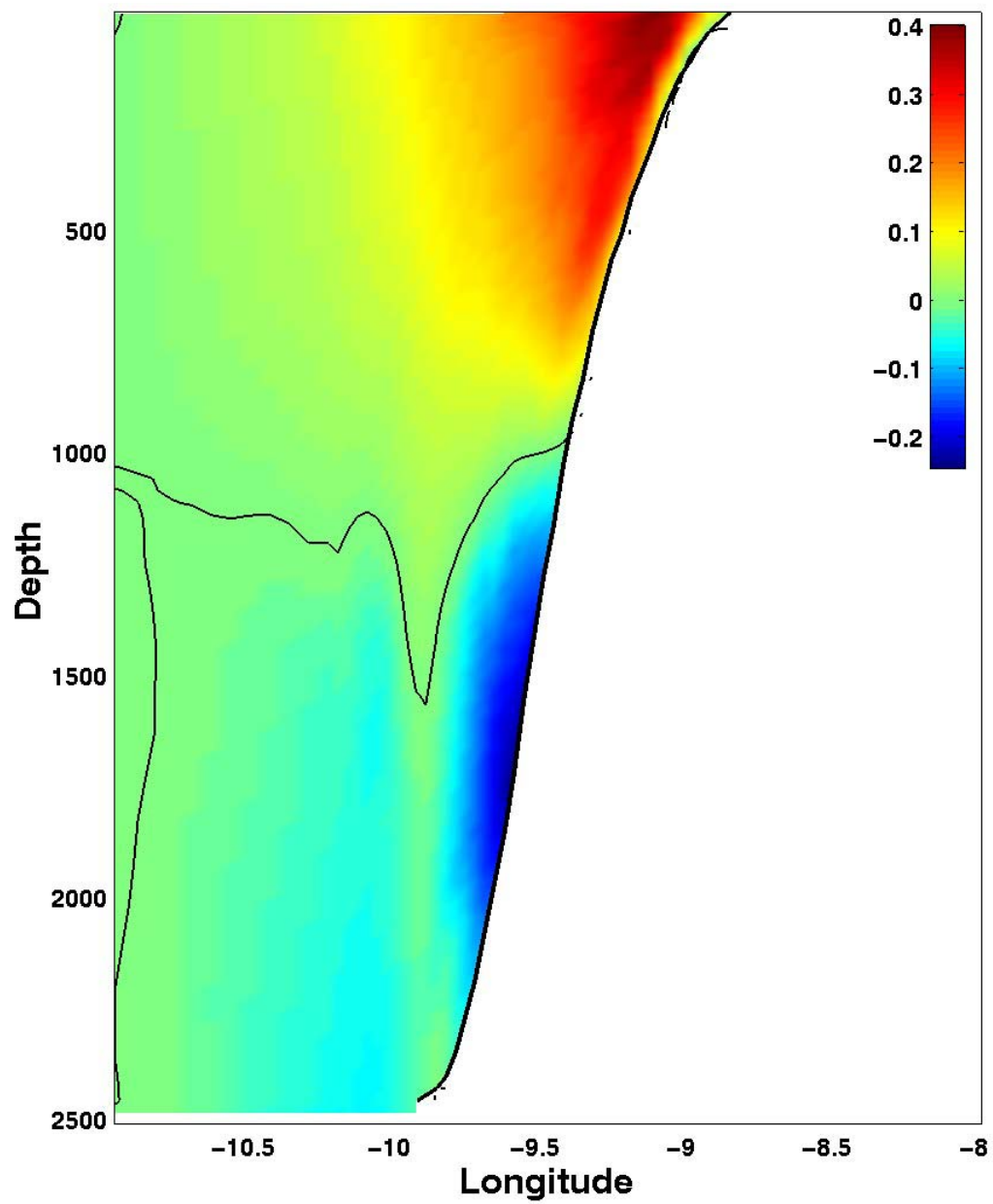


Figure 2.8b. Cross-section of meridional velocity (m/s) at 37.4N for Experiment 4a on day 40.

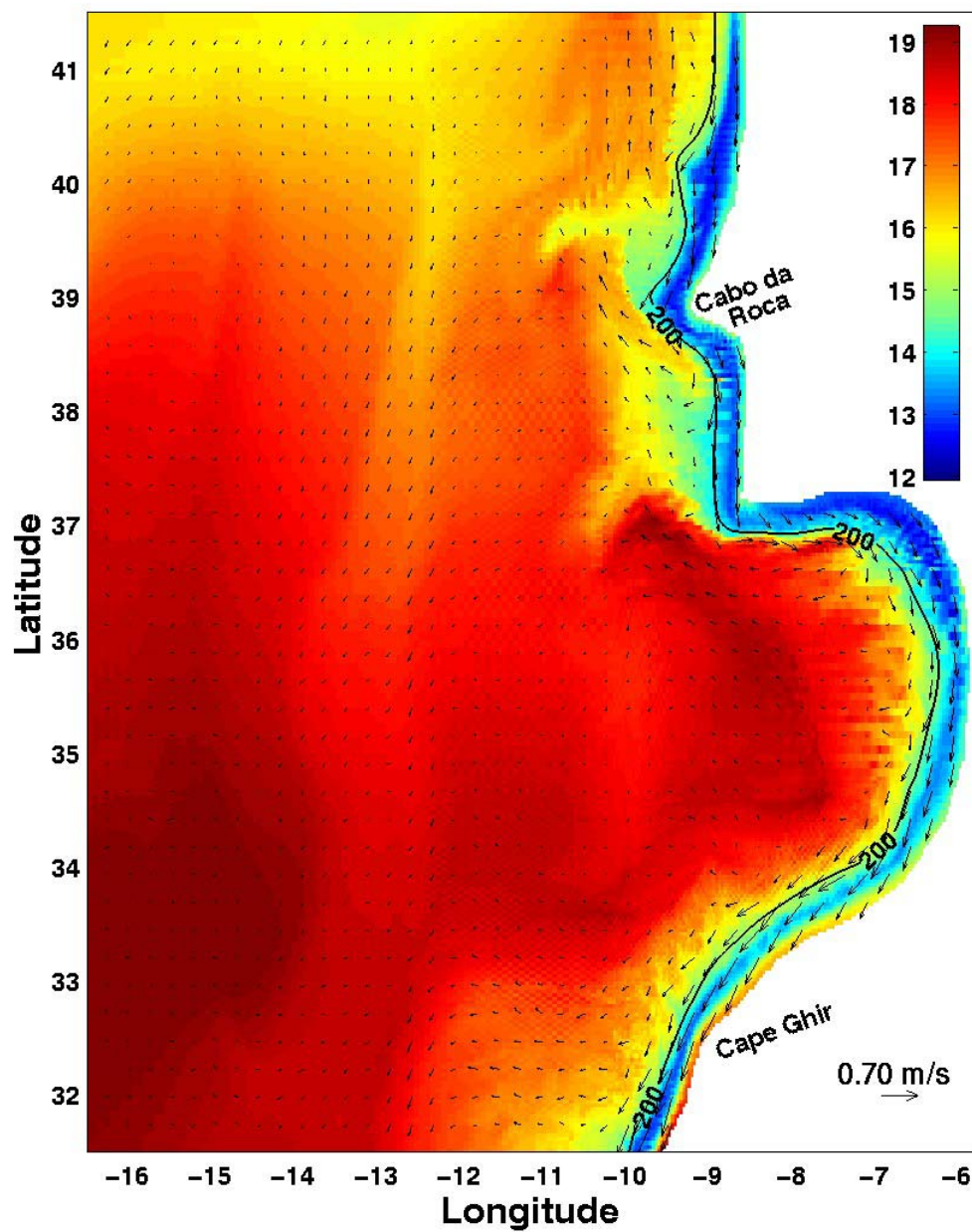


Figure 2.9a. Surface temperature ($^{\circ}\text{C}$) (in color) and velocity vectors (m/s) (arrows) for Experiment 4b at day 40. Contour at 200 m Depth is shown.

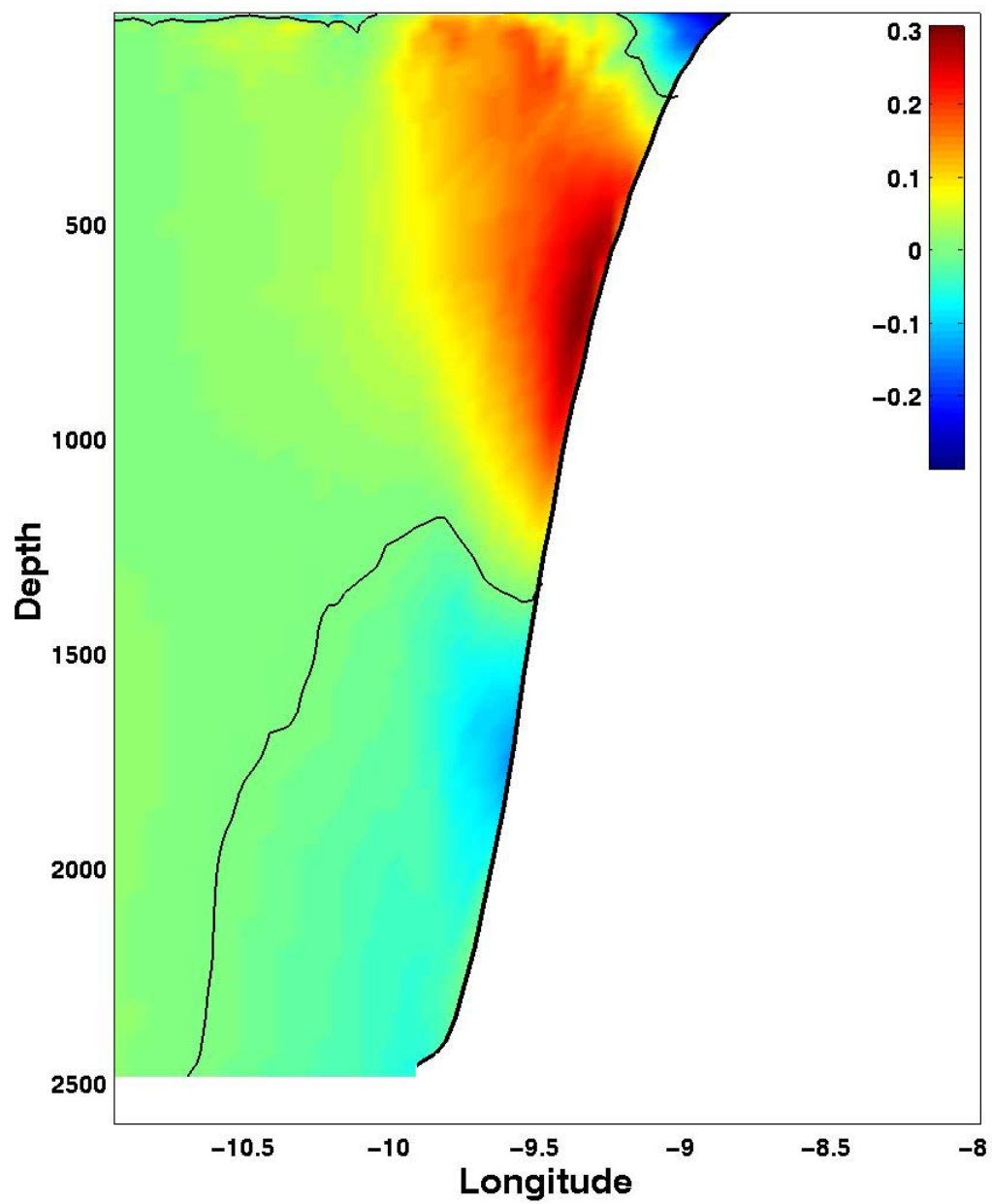


Figure 2.9b. Cross-section of meridional velocity (m/s) at 37.4N for Experiment 4b on day 40.

III. ON REDUCING THE SLOPE PARAMETER IN TERRAIN BOTTOM-FOLLOWING NUMERICAL OCEAN MODELS

A. ABSTRACT

Sigma coordinate ocean models are a type of terrain bottom-following model which are currently being used in regions with large topographic variability such as entire ocean basins, shelf breaks, continental shelves, estuaries and bays. The main concern when using a terrain bottom-following ocean model is to reduce the pressure gradient force error. One approach for reducing the error is to reduce the slope parameter, defined by the absolute value of the ratio of the difference between two adjacent cell depths and their mean depth. Here an alternative method to reducing the slope parameter, i.e., with the traditional two-dimensional smoothing with Gaussian filters, is detailed. In particular, a one-dimensional robust direct iterative technique is introduced. This method is shown to have the unique advantage of maintaining coastline irregularities, continental shelves, and relative maxima such as seamounts and islands.

B. INTRODUCTION

When reducing the pressure gradient force error (PGFE) in sigma coordinate models (Haney, 1991; Mellor et al., 1994, 1998), two types of sigma coordinate errors must be considered, namely, the sigma error of the first kind (SEFK) and the sigma error of the second kind (SESK), as defined by Mellor (1998). The SEFK is readily corrected because it goes to zero prognostically by advecting the density field to a new state of equilibrium.

The second one, a vorticity error, is of greater concern because the error does not vanish with time, and is present in both two and three-dimensional calculations (Mellor, 1998). One PGFE technique to reduce this error is to use a curvilinear grid that follows the bathymetry. Another technique, subtracting the horizontally averaged density before the computation of the baroclinic integral also reduces the SESK (Mellor, 1998). Other SESK reduction techniques are the use of high-order schemes (fourth and sixth) (McCalpin, 1994; Chu and Fan, 1997, 1998) interpolation of the pressure gradient to z-

levels (Kliem and Pietrzak, 1999), and reconstruction of pressure density fields using parabolic splines (Shchepetkin and McWilliams, 2000 a and b).

Note that, regardless of the method of calculation of the pressure gradient, the PGFE will not be reduced to an acceptable value without first reducing the slope parameter.

The slope parameter (SP) is defined as:

$$SP = \frac{|h_B - h_A|}{h_B + h_A} \quad (2.1)$$

where h_B and h_A are the depths of adjacent grid points. According to Mellor (1998), the SP must be less than 0.2 because greater values can induce high PGFEs. Since the numerator in (3.1) decreases faster than the denominator, the slope parameter can also be reduced by increasing the horizontal resolution of the model. In particular the increase in horizontal resolution necessary to change the slope parameter can be determined by

$$R = \frac{SP_i \times (1 - SP_f)}{SP_f \times (1 - SP_i)} \quad (2.2)$$

where R is the ratio of increase in resolution, SP_i is the raw slope parameter and SP_f is the final slope parameter. Using topography from Sandwell and Smith (1996) interpolated for a regional model grid, a conservative value for SP_i is 0.6. To obtain values of the slope parameter less than 0.2, it would be necessary to increase the horizontal resolution by a factor of 6. Note that this higher resolution in latitudinal and longitudinal directions would end up increasing the number of computational points by 36. For the Princeton Ocean Model (POM), a typical sigma coordinate ocean model, the increase in horizontal resolution would imply a decrease in the internal and external time steps by a factor of 6 (this is necessary to maintain the computational stability condition of Courant-Friedrichs-Levy). If all the algorithms in the model had a computational effort proportional to N, where N is the total amount of points in the model, the computational effort would be increased by a factor of 216.

Since the increase in resolution to solve the slope parameter is usually too expensive computationally, an alternative method is suggested to reduce the PGFE in coastal areas. In many coastal regions, the initial topography (without smoothing) already

interpolated to the model grid (usually between 4 and 20 km for a regional model) can have typical maximum slope parameter values between 0.6 and 0.8 over the shelf break.

Typical two-dimensional Gaussian filters used in the smoothing of bottom topography can have the disadvantage of smoothing topographic features that could be of great importance in coastal regions. For example, these filters can smooth coastline irregularities, and may not maintain continental shelves and relative maxima (i.e., they may sink small islands and seamounts). In addition the corrections to the depths can be negative or positive. If negative, additional problems can result because there is usually no initialization or forcing data available below the initial depth values.

Here an alternative method to reducing the slope parameter, i.e., with the traditional two-dimensional smoothing with Gaussian filters is detailed. In particular, a one-dimensional robust iterative technique is introduced. This method is shown to have the unique advantage of maintaining coastline irregularities, continental shelves, and relative maxima such as seamounts and islands. A detailed description of the algorithm is given in Section F, but here we describe the process.

C. A PRACTICAL EXAMPLE

Here an advanced method to reduce the slope parameter, a one-dimensional robust iterative method, is introduced. First, the signed slope parameter is calculated along each grid line in a particular direction over the domain. Where the slope parameter between two adjacent cells is greater than the limit, it is adjusted to the limit value and then the signed slope parameter is recalculated. After each line in the domain has been adjusted for that particular direction, the topography matrix is then rotated by 90 degrees. Each process is repeated until the topography has been adjusted for all the directions (rotated by 360 degrees). This is an iterative process since a change in the topography necessary to reduce the slope parameter in one direction may alter the slope parameter in the perpendicular direction to values greater than the limit, usually 0.2.

Figures 3.1a-f and 3.2a-f show the evolution of the values of the signed slope parameter in the x-direction (SSPX) and in the y-direction (SSPY), respectively, for ETOPO 5 topography interpolated to 4.1 to 9.6 km horizontal resolution for use in a

typical terrain sigma coordinate bottom-following ocean model (e.g. POM, Mellor, 1996). Note that the topography has relatively high slope parameter values of ~ 0.8 . Here the results of using the algorithm to successfully reduce the slope parameter from 0.8 to 0.2 are shown. The initial values of SSP have a range between -0.86 and 0.81 for SSPY (Figure 3.2a) and between -0.74 and 0.60 for SSPX (Figure 3.1a). The application of the smoothing algorithm in the x-direction (which targets negative SSPX values less than -0.2 and each patch of those values individually) changes the minimum value of SSPX from -0.74 to -0.2 (Figure 3.1b). Note that the change in topography necessary to reduce SSPX also changes SSPY values (Figure 3.2b). A comparison of the contour lines in Figures 3.2a and 3.2b shows differences in almost all the continental shelf regions and near Madeira Island.

To target values of SSPY larger than 0.2, the topography is rotated 90 degrees counter-clockwise and the algorithm is applied again. Figure 3.2c shows that SSPY values have been reduced to less than 0.2. The subsequent changes in SSPX due to the change in topography can be seen by comparing Figures 3.1b and 3.1c. Note in particular the differences between both figures near the northern coast of Madeira Island.

When the topography is rotated another 90 degrees counter-clockwise, the values of SSPX larger than 0.2 are targeted. The final result for SSPX (Figure 3.1d) shows that SSPX is now reduced to an acceptable range (between -0.2 and 0.2). However, the values for SSPY show that there are still values of the slope parameter larger than 0.2.

The rotation and cleaning process shown in Figures 3.1a (3.2a) through 3.1e (3.2e), targeting successively four different directions separated by 90 degrees, is called an iteration, and corresponds to the rotation of the topography by 360 degrees. To reduce the remaining values of SSPX to the intended range (-0.2 to 0.2), there is the necessity to do another complete iteration. The result of the second iteration for SSPX (SSPY) is shown in Figure 3.1f (3.2f). Also, all the values of the slope parameter have been successfully reduced to values less than or equal to 0.2.

D. TOPOGRAPHY COMPARISONS

The application of the iterative method to two different regional models of complex bathymetry (Canary Current System and California Current System) showed

that only two iterations were necessary to reduce the slope parameter from around 0.8 to less than 0.2. To test the robustness of the one-dimensional iterative method, it was also applied for the western and southern coastal regions of Australia, where similar results were obtained.

For example, the raw and final topography (after direct reduction of slope parameter) for the Canary Current System is shown in Figures 3.3a and 3.3b, respectively. No discernible differences are seen between the two figures except for a slightly widening of the most prominent seamounts. In contrast, when two-dimensional Gaussian smoothing is used, a significant widening of topographic features can be seen (Figure 3.3c). In addition there is a clear deepening of seamounts and islands. Figure 3.3c also shows that there is significant smoothing of coastline irregularities, a decrease of the shelf width and a shallowing of the Strait of Gibraltar.

As another example, the raw topography, the topography smoothed with the one-dimensional direct method and the topography smoothed with the two-dimensional Gaussian filter are shown in Figures 3.4a through 3.4c, respectively, for the California Current System. Since it is difficult to notice differences between the topographies in coastal areas, the difference between the raw and smoothed topographies was calculated and is shown in Figures 3.4d through 3.4f, respectively to the one-dimensional direct method, to the topography smoothed with the two-dimensional Gaussian filter and to an alternative smoothing method provided to POM users. The surface in the Figures 3.4d to 3.4f represents the raw topography, where scaled differences are in color. Figure 3.4d shows the difference between raw and smoothed topography after the application of a two-dimensional Gaussian filter, scaled by the raw data, showing that seamounts are again highly smoothed (blue areas indicate negative corrections) and have corrections on the same order of magnitude as the initial depths (Figure 3.4d). There is also a change in the coastline, represented by the red areas (indicating positive corrections), just near the coast. In addition there is a relatively large change in depths for the continental slope and rise regions.

In Figure 3.4e, the difference between the raw topography and the smoothed with the one-dimensional direct algorithm, scaled by the raw topography, is shown. A comparison of Figures 3.4d and 3.4e shows that the algorithm has the effect of making

changes in much fewer points than when traditional smoothing is used. Also the minimum depth of the seamounts is maintained (zero value for the difference in green), preserving coastline irregularities and the continental shelf and rise. The only places where this algorithm changes the topography is in areas near the upper continental slope and around seamounts where there are relatively high slopes and shallow depths.

The difference between raw and the topography smoothed with an alternative method provided to POM users is shown in Figure 3.4f. A comparison of Figures 3.4e and 3.4f shows that the one-dimensional direct iterative method changes much fewer points than the POM method. In addition almost all the corrections made by the POM method are negative. Note that if there is no initialization and forcing data beyond the initial topography values, there will be problems. Lastly, since the POM smoothing method is not maxima conservative, topographic features such as seamounts and islands will be deepened and the changes to the coastline geometry will be made, represented by the blue areas near at the coast.

E. COASTAL CIRCULATION EFFECTS

To determine if the different types of smoothing (i.e., Gaussian and direct interactive methods) can significantly influence the coastal circulation, the same NCCS ocean model experiment as in Chapter II was run using different types of smoothed topographies. In particular, the POM for the Northern Canary Current System was run with annual wind forcing and annual climatological forcing of temperature and salinity at the boundaries (Experiment 4 in Chapter II). The model was initialized with the full annual climatology for the smoothed topography with the traditional Gaussian smoothing and then for the topography smoothed with the direct interactive method described earlier.

In Figure 3.5a (Figure 3.5b) the results for day 40 of the meridional velocity are shown in a cross-section at 37.4N for the direct interactive (Gaussian) smoothing of topography. In the direct interactive smoothing method the continental shelf remains very similar to the raw topography, while in the regular smoothing the continental shelf almost disappears. The frictional layer that develops due to the presence of the continental shelf in the direct interactive smoothing results is responsible for the smaller surface equatorward current magnitude (Figure 3.5a) relatively to the Gaussian smoothing results (Figure

3.5b). The smaller surface current in the direct iterative case allows the development of a higher magnitude poleward current off Iberia (i.e., the Iberian Current). The development of the Iberian Current in the direct iterative method constrains even further the coastal equatorward current near the coast with increased friction values. The poleward undercurrent also shows a well-defined friction boundary layer for the direct iterative method results (Figure 3.5a) compared with Gaussian smoothing results (Figure 3.5b), recall that the parametrization of POM is in between no-slip and free-slip. The differences in the results in the two models are solely due to the methods for smoothing the topography.

F. CONCLUSIONS

In this chapter a one-dimensional direct iterative method for reducing the slope parameter was developed. A comparison with Gaussian and POM smoothing showed that the use of the direct iterative technique resulted in a more realistic topography and coastline geometry for use in terrain bottom-following ocean models. The method was tested for three different coastal regions with complex topography. In all the different regions, the slope parameter was successfully reduced from maximum values of ~ 0.8 to acceptable values of less than 0.2. This reduction was obtained by changing the depth of relatively few grid points and with only two iterations. This method was shown to have the unique advantage of maintaining coastline irregularities, continental shelves, and relative maxima such as seamounts and islands.

G. REFERENCES

- Chu, P.C., Fan, C., Sixth-order Difference Scheme for Sigma Coordinate Ocean Models. *Journal of Physical Oceanography* 27, 2064-2071, 1997.
- Chu, P.C., Fan, C., A Three-point Combined Compact Difference Scheme. *Journal of Computational Physics* 140, 370-399, 1998.

- Haney, R.L., On the Pressure Gradient Force Over Steep Topography in Sigma Coordinate Ocean Models. *Journal of Physical Oceanography* 21, 610-619, 1991.
- Kliem, N. and J.D. Pietrzak, On the Pressure Gradient Error in Sigma Coordinate Models: a Comparison with Laboratory Experiment. *Journal of Geophysical Research* 104, 29,781-29,799, 1999.
- McCalpin, J.D., A Comparison of Second-order and Fourth-order Pressure Gradient Algorithms in a Sigma Coordinate Ocean Model. *International Journal of Numerical Methods in Fluids* 18, 361-363, 1994.
- Mellor, G.L., User's Guide for a Three-dimensional, Primitive Equation, Numerical Ocean Model. Program in Atmospheric and Ocean Sciences, Princeton University, Princeton, NJ, 40 pp, 1996.
- Mellor, G.L., T. Ezer, and L.-Y. Oey, The Pressure Gradient Conundrum of Sigma Coordinate Ocean Models. *Journal of Atmospheric and Ocean Technology* 11 (Part 2), 1126-1134, 1994.
- Mellor, G.L., L.-Y. Oey, and T. Ezer, Sigma Coordinate Pressure Gradient Errors and the Seamount Problem. *Journal of Atmospheric and Ocean Technology* 15, 1122-1131, 1998.
- Sandwell, D.T., and W.F. Smith, Global Bathymetric prediction for Ocean Modelling and Marine geophysics, 1996.
- Shchepetkin, A.F. and J.C. McWilliams, The Regional Ocean Modeling System: a Split-explicit, Free Surface, Topography-following Coordinate Ocean Model, submitted, 2000.
- Shchepetkin, A.F., and J.C. McWilliams, A Method for Computing Horizontal Pressure Gradient Force in an Ocean Model with Non-aligned Vertical Coordinate, submitted, 2000.

Smith, R.D., M.E. Maltrud, F.O. Bryan and R.W. Hecht, Numerical Simulation of the North Atlantic Ocean at 1/10-degree, *Journal of Physical oceanography*, 30, 1532-1561, 2000.

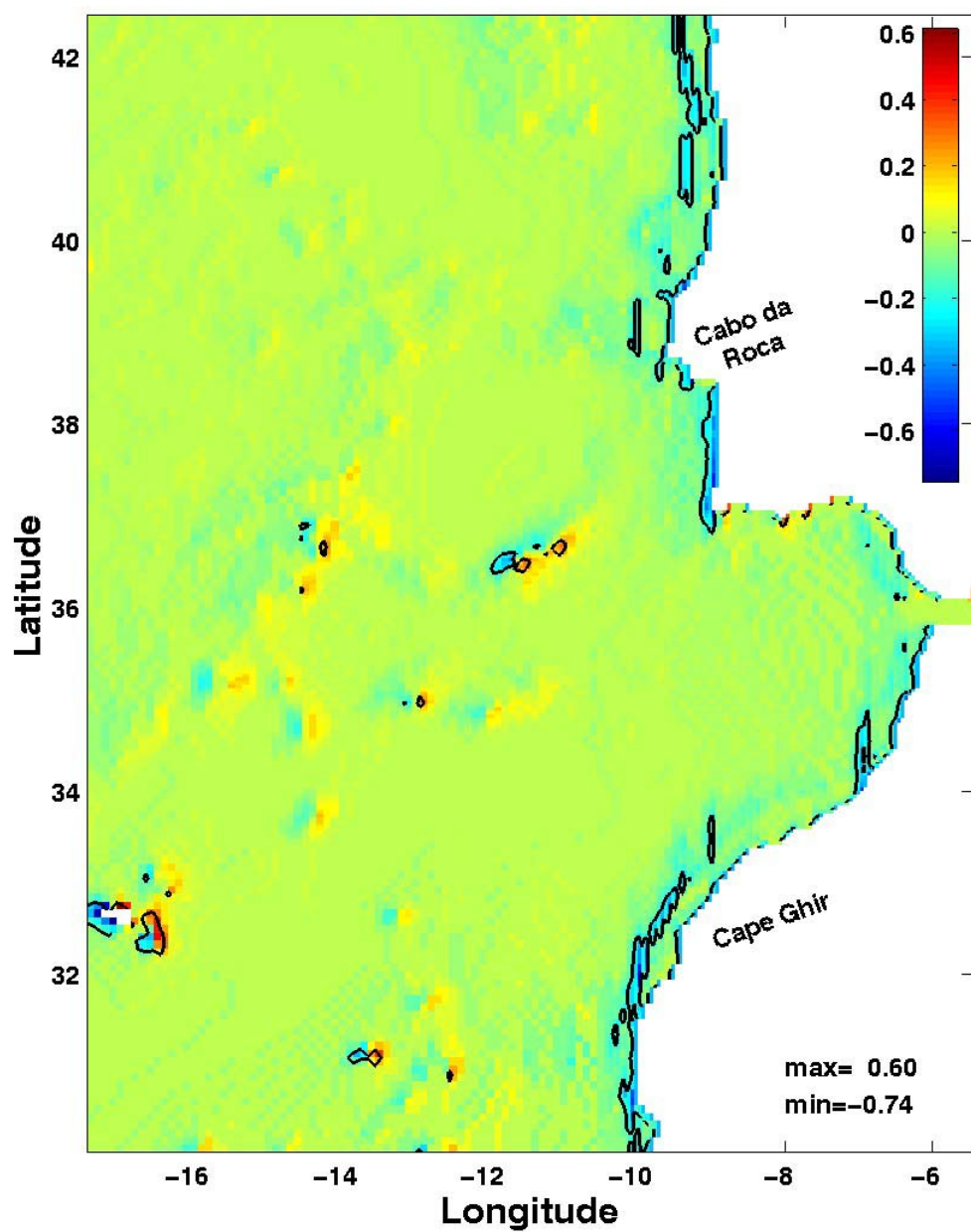


Figure 3.1a. Initial signed slope parameter in the X-Direction (SSPX). Contour lines for -0.2 and 0.2 .

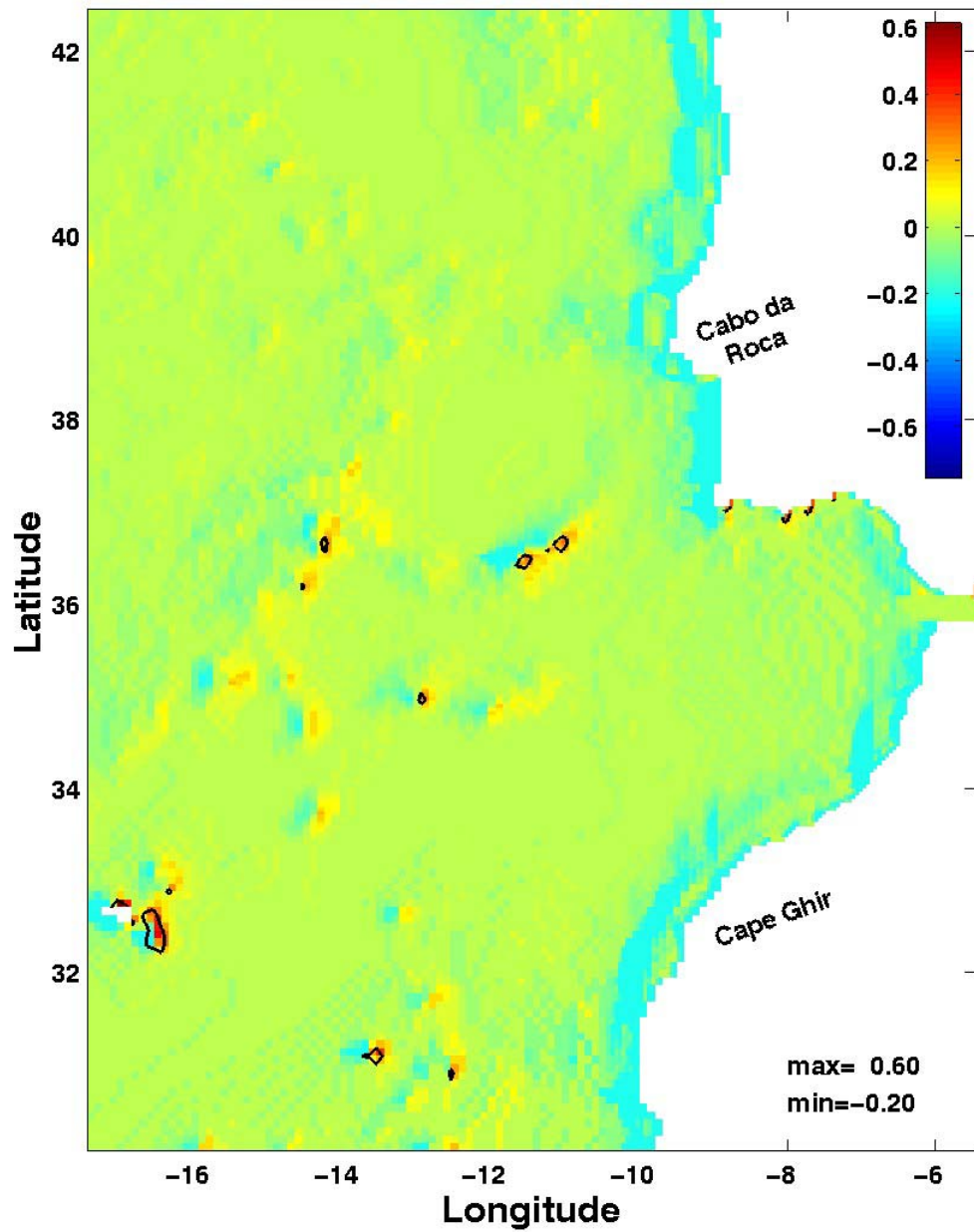


Figure 3.1b. Signed slope parameter in the X-Direction (SSPX) after the execution of the smoothing algorithm targeting SSPX values less than -0.2 . Contour line for 0.2 .

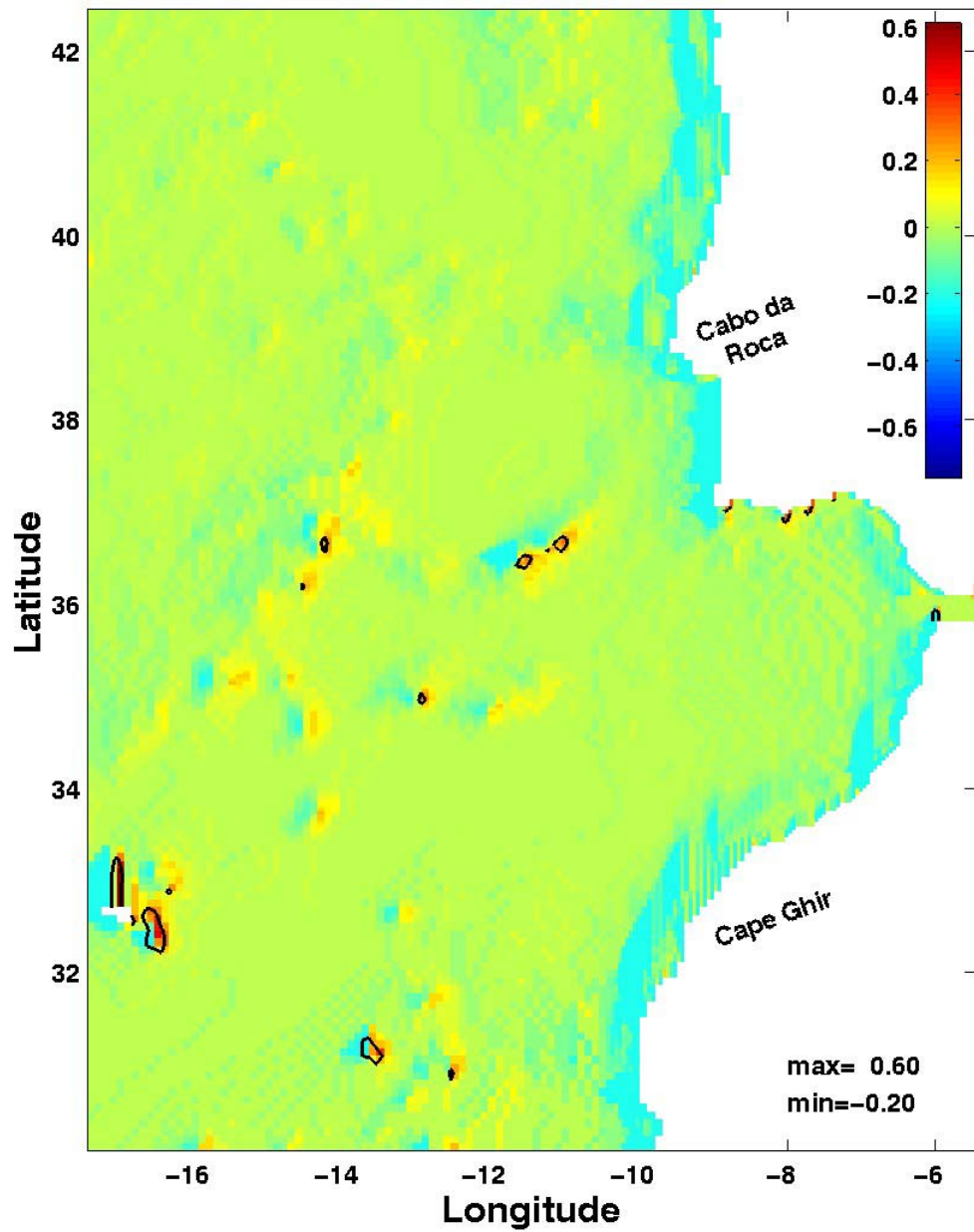


Figure 3.1c. Signed slope parameter in the X-Direction (SSPX) after the execution of the smoothing algorithm targeting SSPX values less than -0.2 and SSPY values greater than 0.2 . Contour lines for -0.2 and 0.2 .

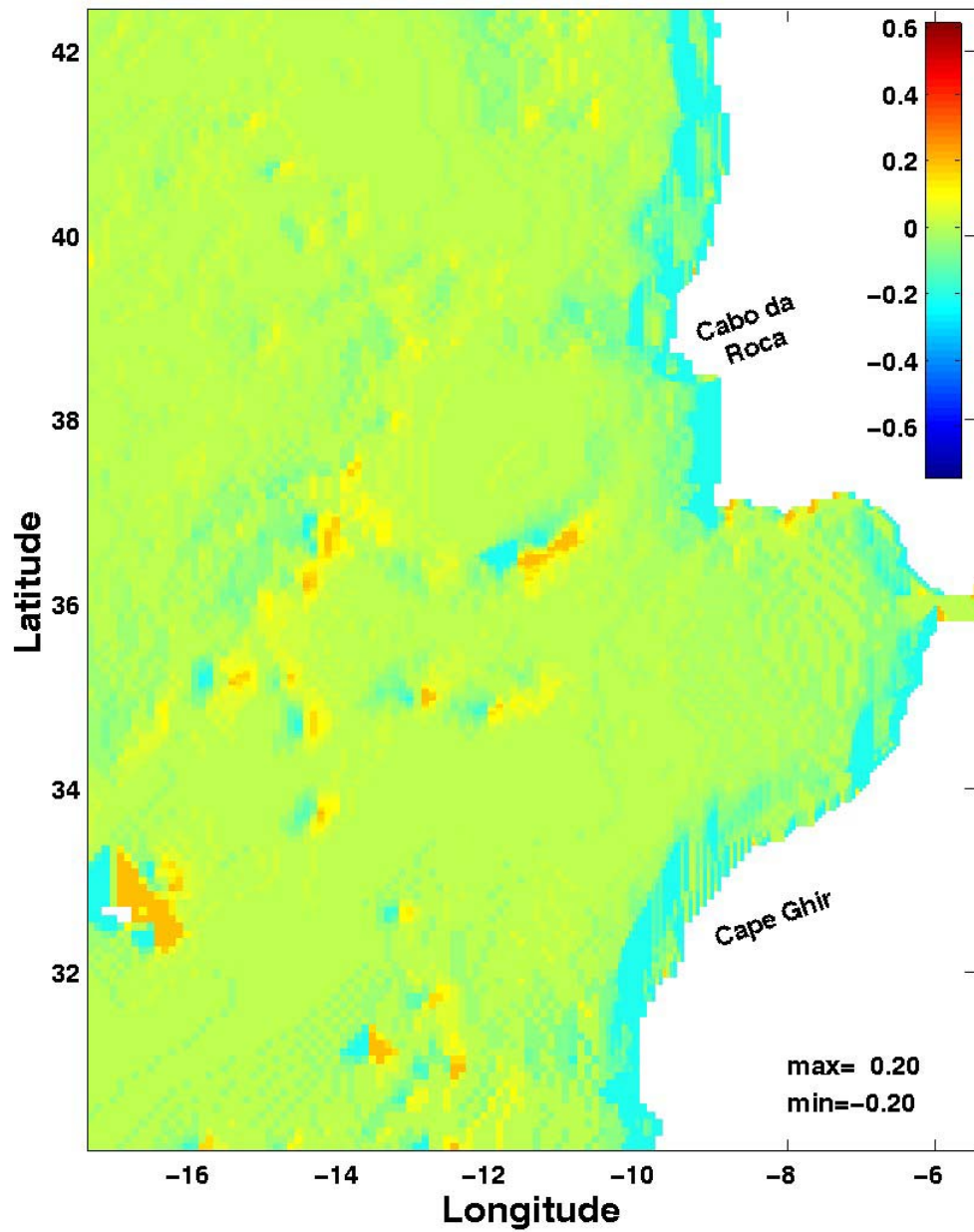


Figure 3.1d. Signed slope parameter in the X-Direction (SSPX) after the execution of the smoothing algorithm targeting SSPX values less than -0.2 and greater than 0.2 and SSPY values greater than 0.2 .

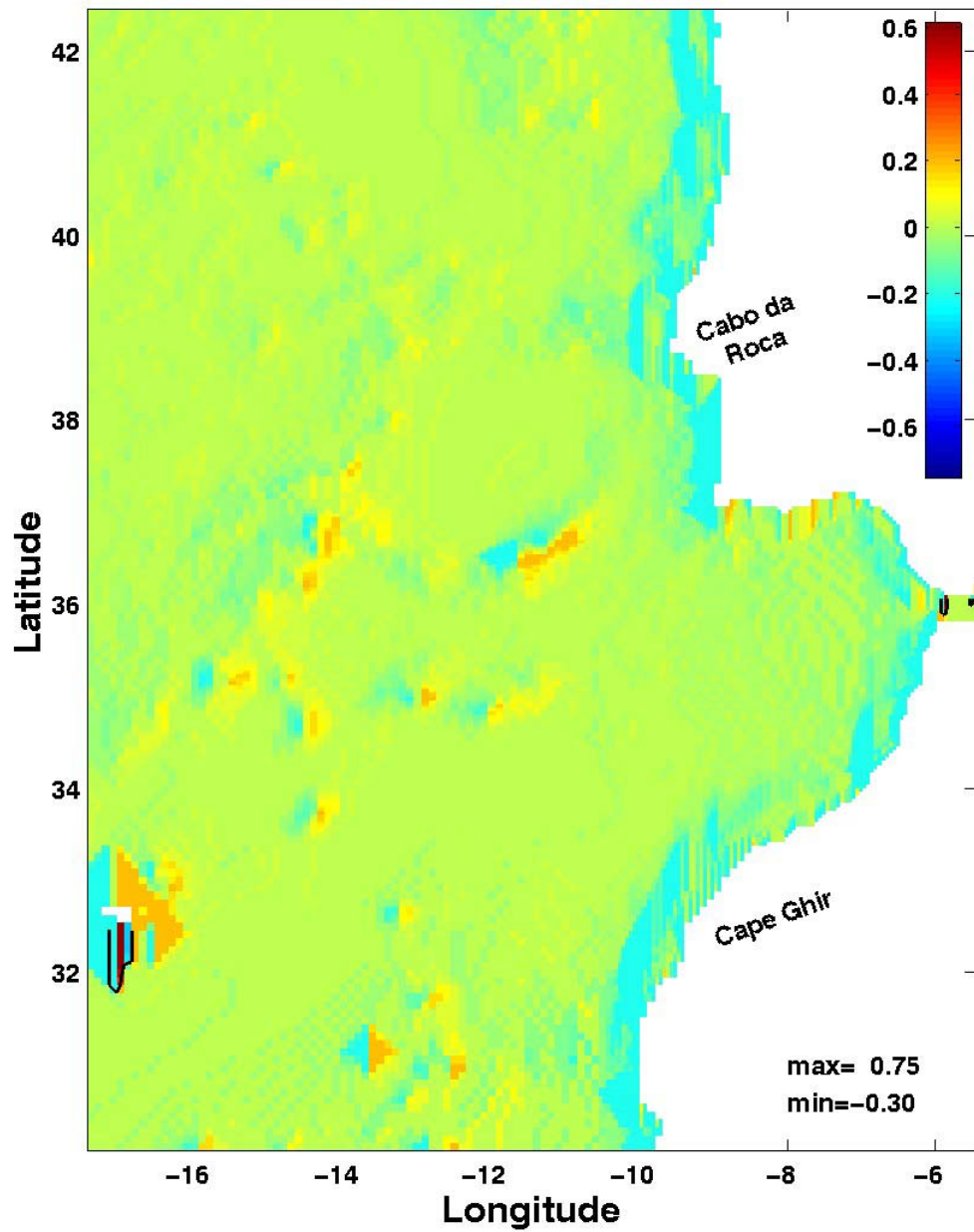


Figure 3.1e. Signed slope parameter in the X-Direction (SSPX) after the execution of the smoothing algorithm targeting SSPX values less than -0.2 and greater than 0.2 and SSPY values greater than 0.2 and Less than -0.2 . This is the result after the end of the first iteration. Contour lines for -0.2 and 0.2 .

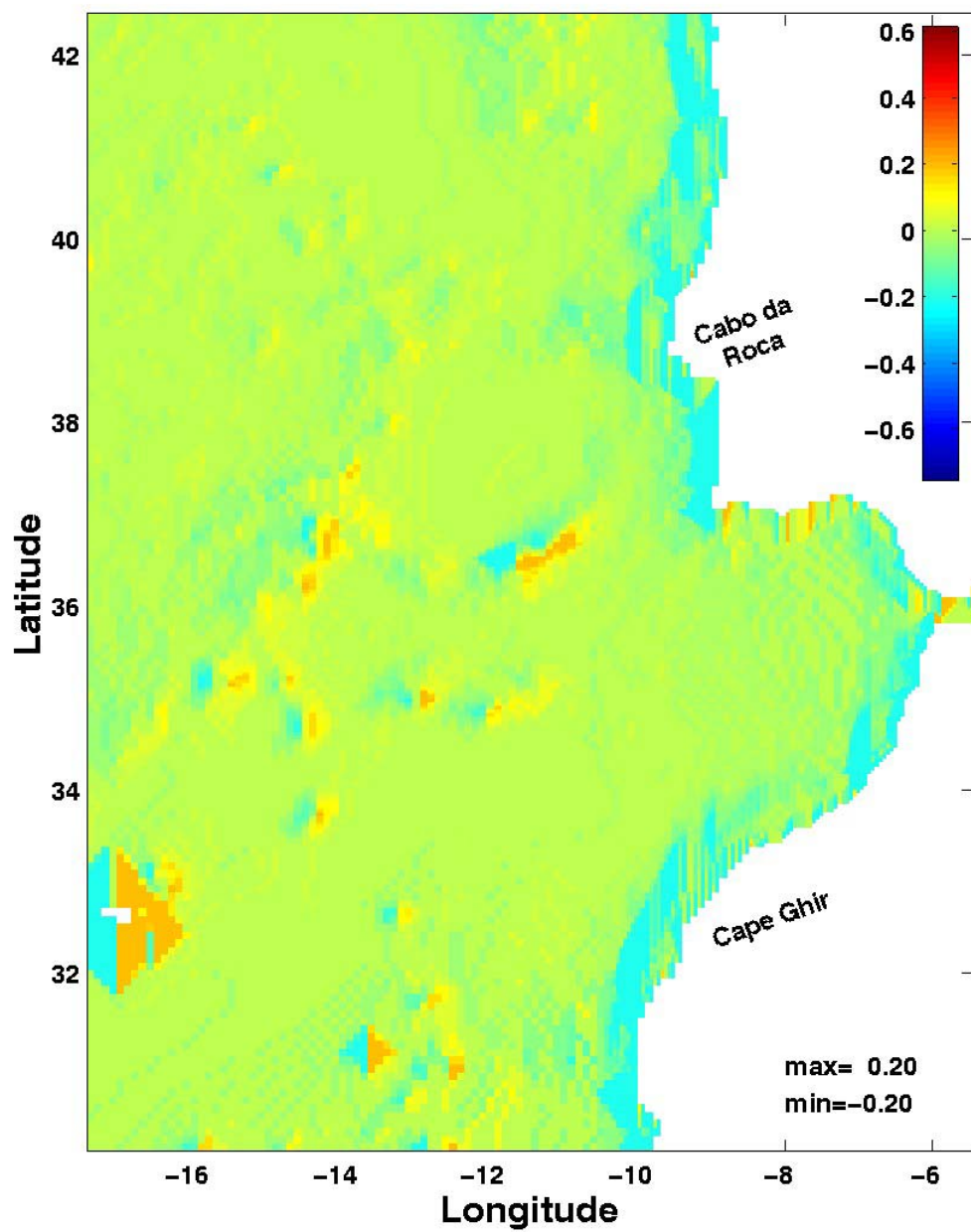


Figure 3.1f. Signed slope parameter in the X-Direction (SSPX) after the execution of two complete iterations.

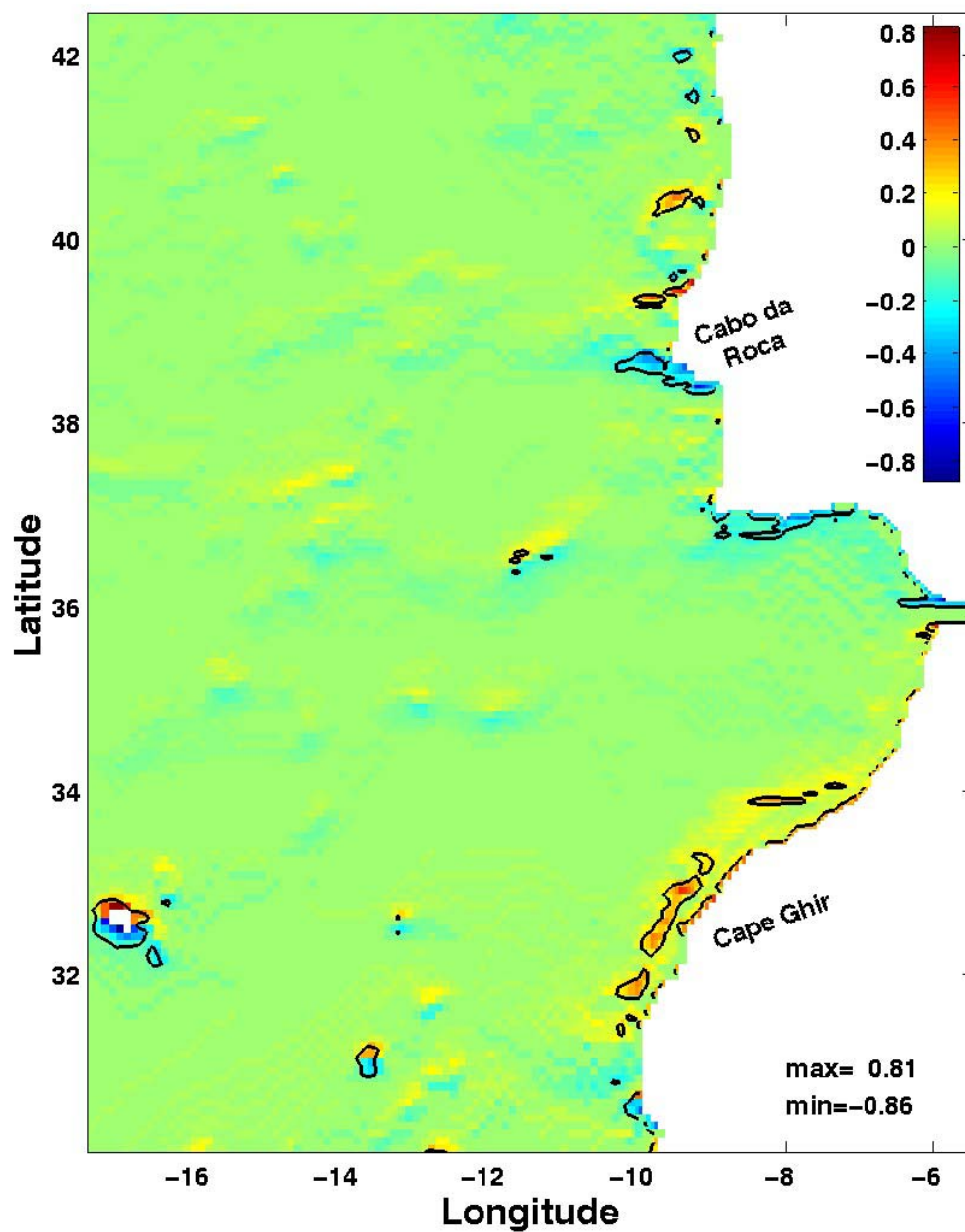


Figure 3.2a. Initial signed slope parameter in the Y-Direction (SSPY). Contour lines for -0.2 and 0.2 .

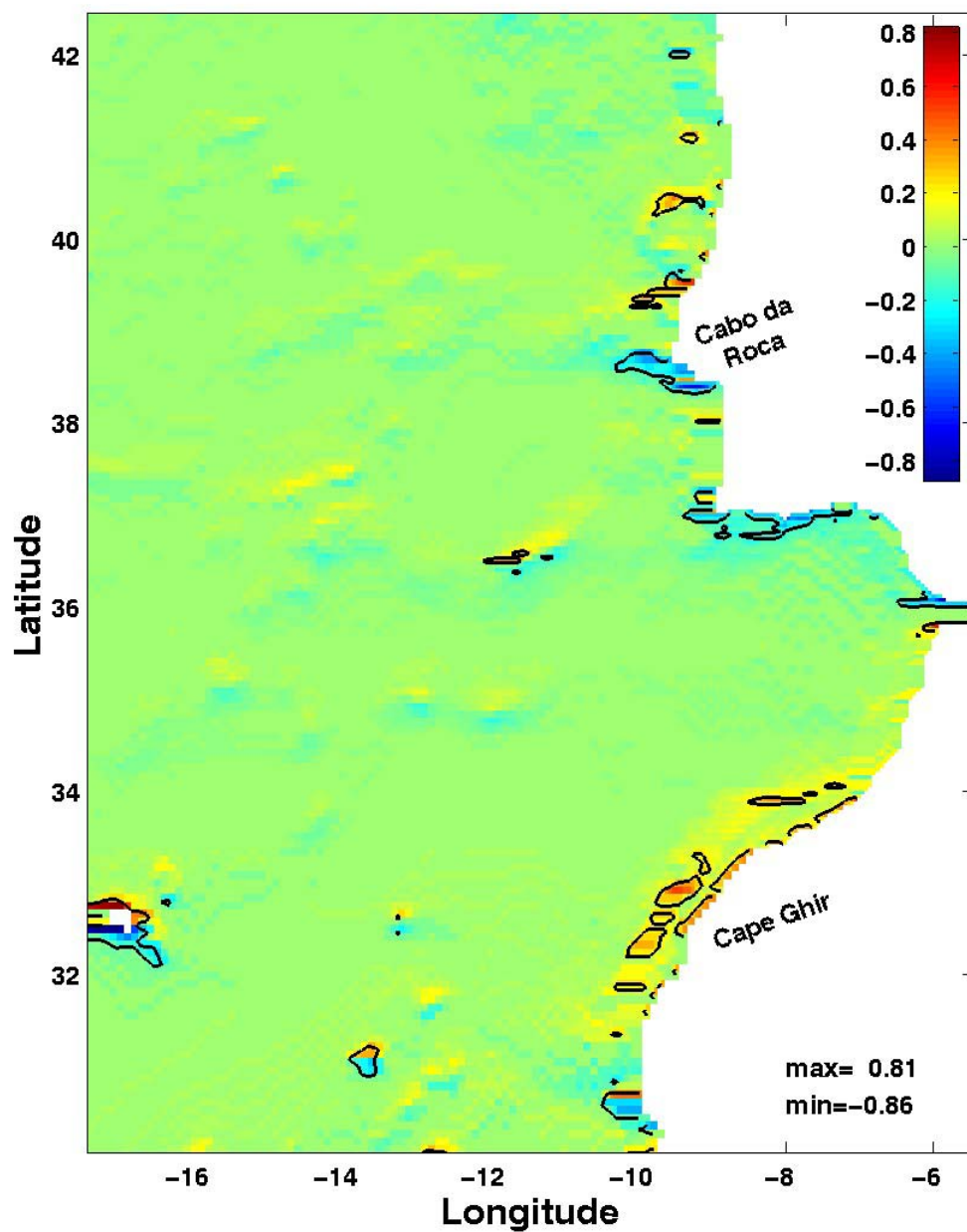


Figure 3.2b. Signed slope parameter in the Y-Direction (SSPY) after the execution of the smoothing algorithm targeting SSPX values less than -0.2 . . Contour lines for -0.2 and 0.2 .

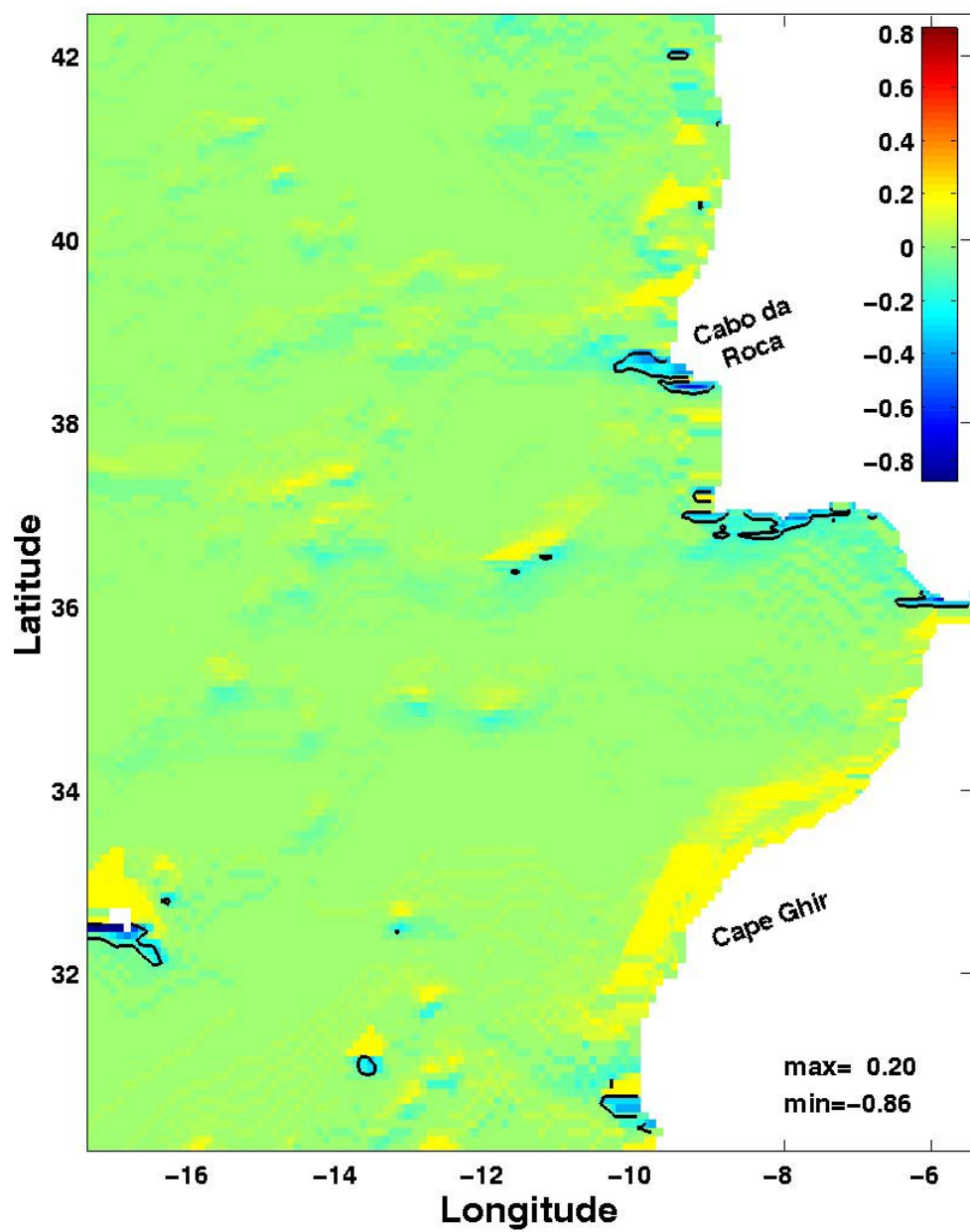


Figure 3.2c. Signed slope parameter in the Y-Direction (SSPY) after the execution of the smoothing algorithm targeting SSPX values less than -0.2 and SSPY values greater than 0.2 . Contour lines for -0.2 .

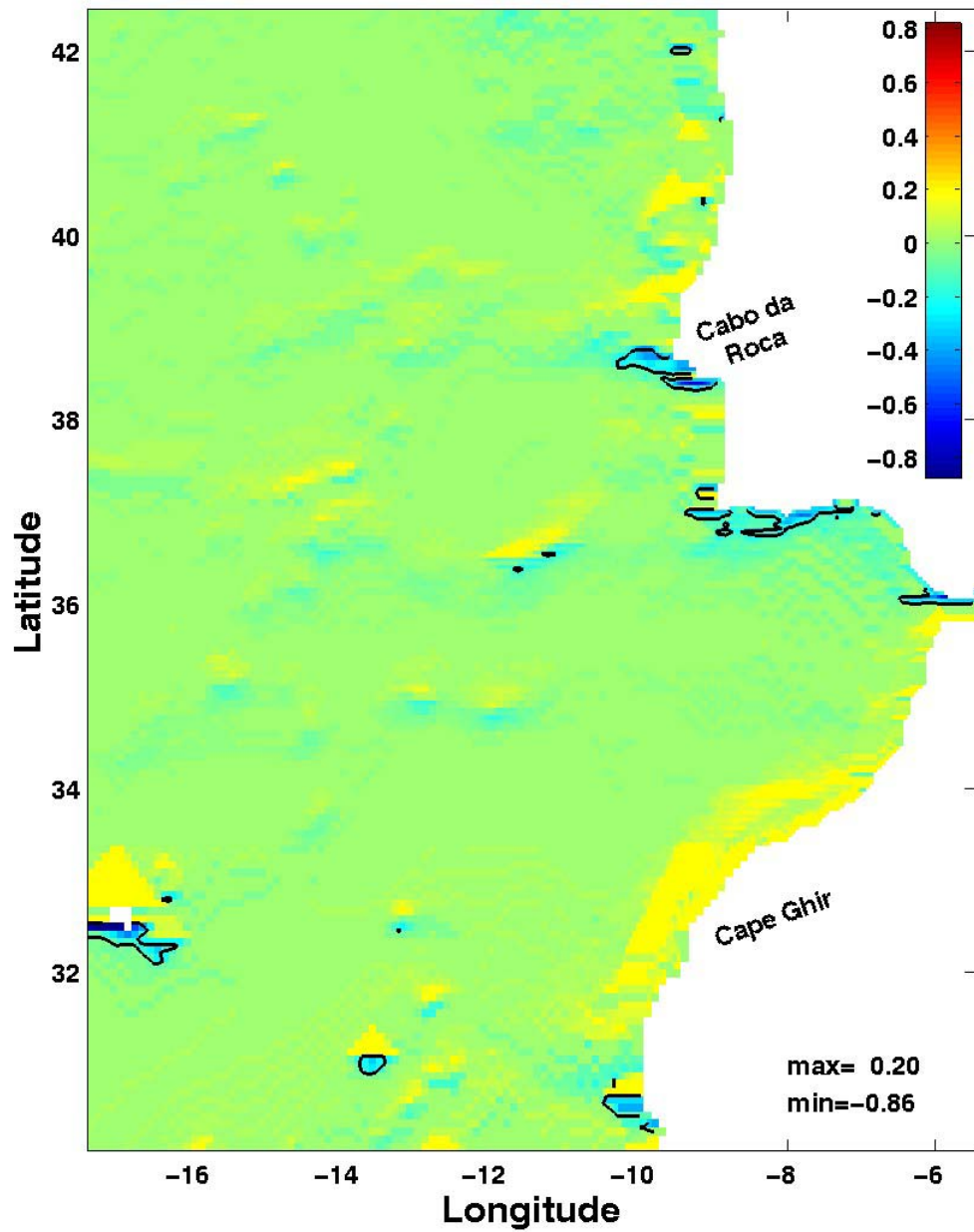


Figure 3.2d. Signed slope parameter in the Y-Direction (SSPY) after the execution of the smoothing algorithm targeting SSPX values less than -0.2 and greater than 0.2 and SSPY values greater than 0.2 . Contour lines for -0.2 .

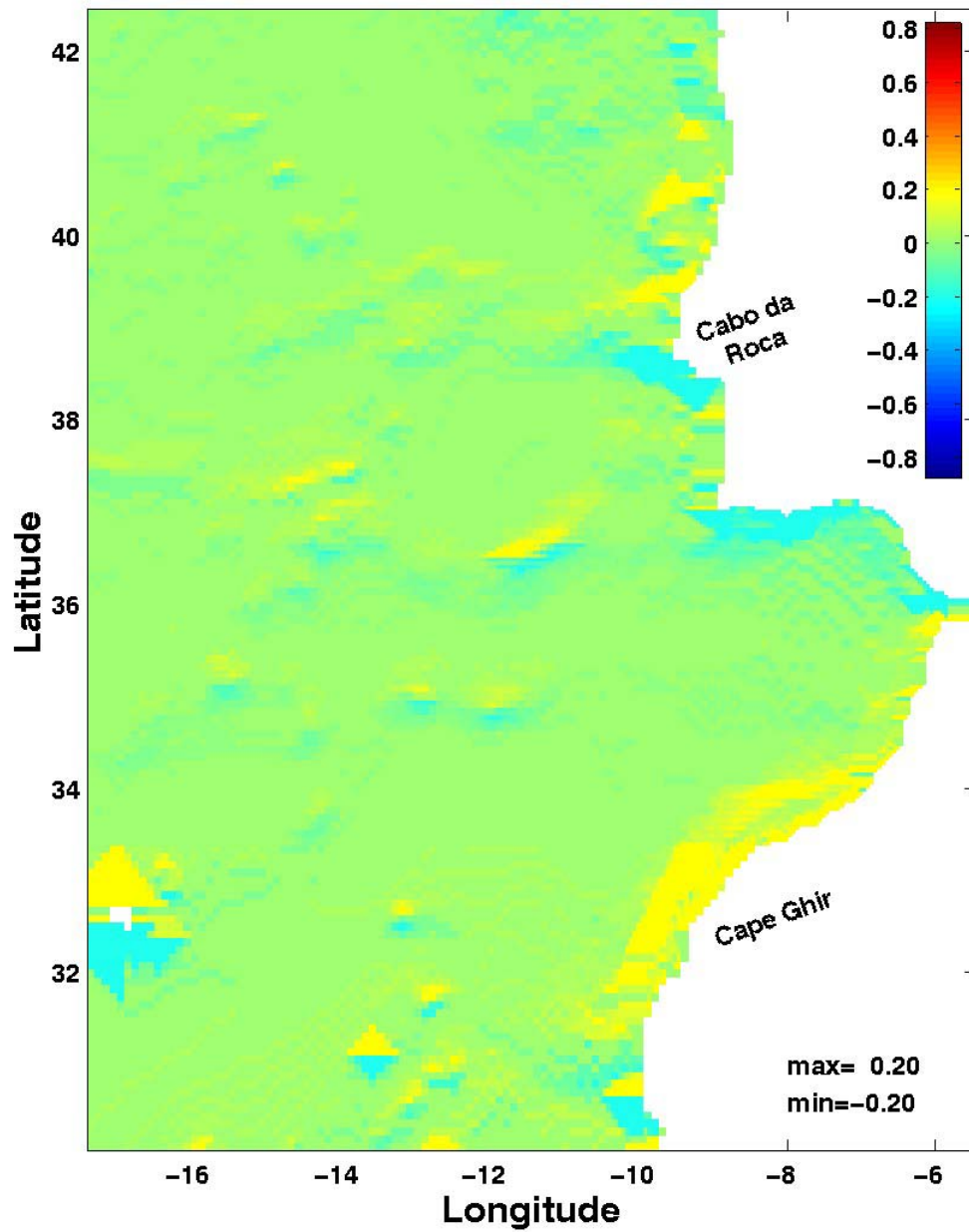


Figure 3.2e. Signed slope parameter in the Y-Direction (SSPY) after the execution of the smoothing algorithm targeting SSPX values less than -0.2 and greater than 0.2 and SSPY values greater than 0.2 and less than -0.2 . This is the result after the end of the first iteration.

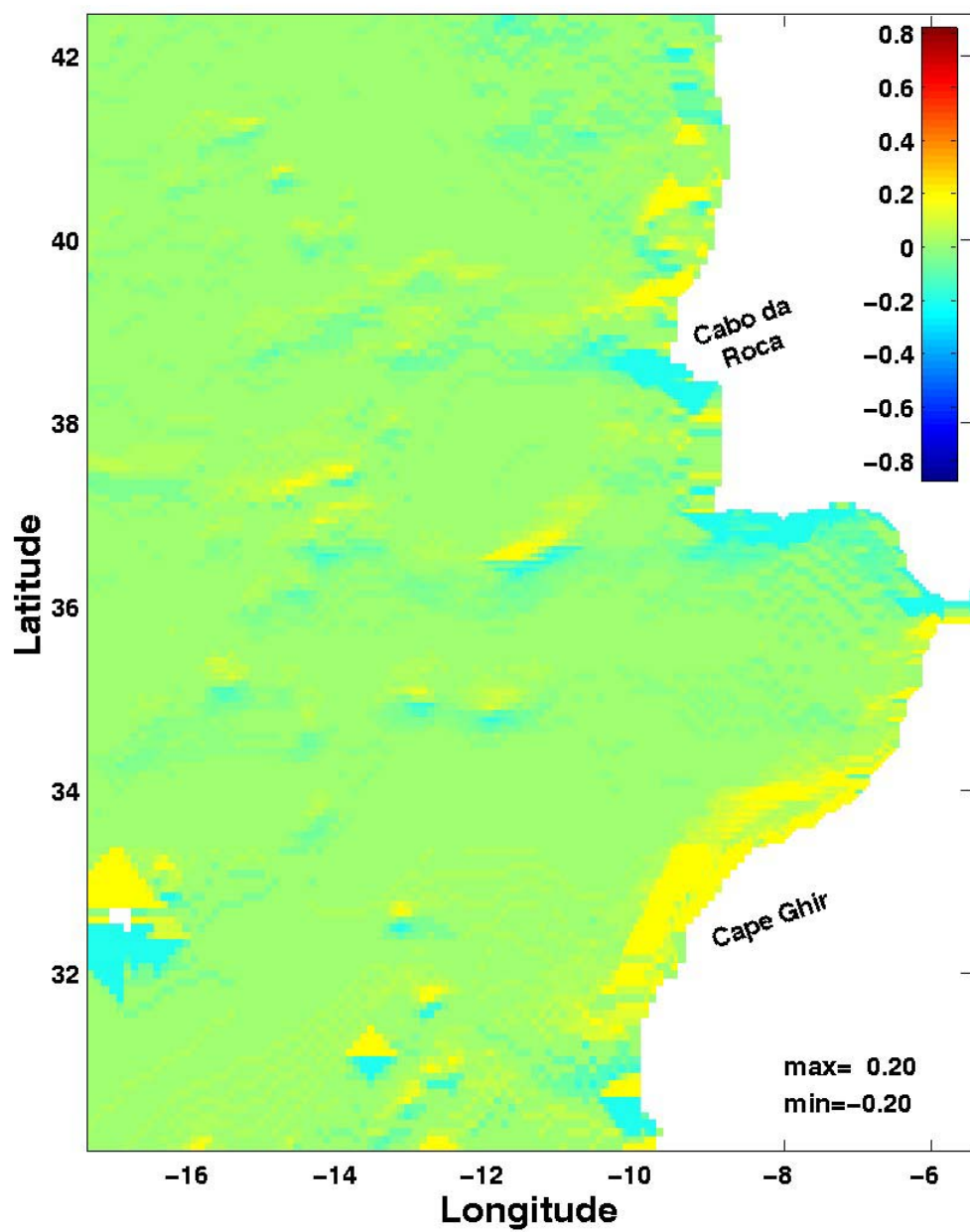


Figure 3.2f. Signed slope parameter in the Y-Direction (SSPY) after the execution of two complete iterations.

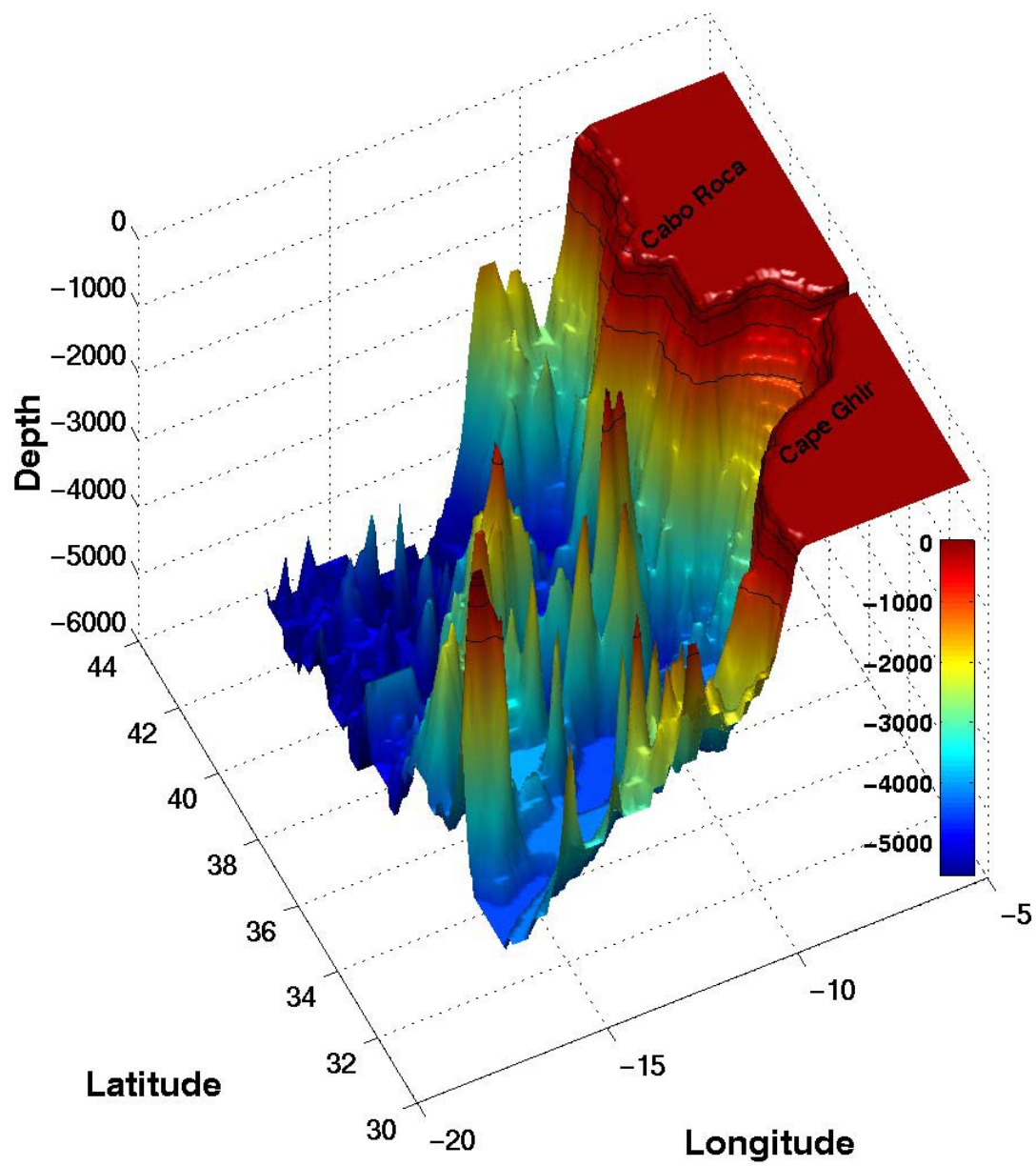


Figure 3.3a. Raw topography for the Northern Canary Current System, depths in meters. Contour lines at 100, 200, 500 and 1000 m depth.

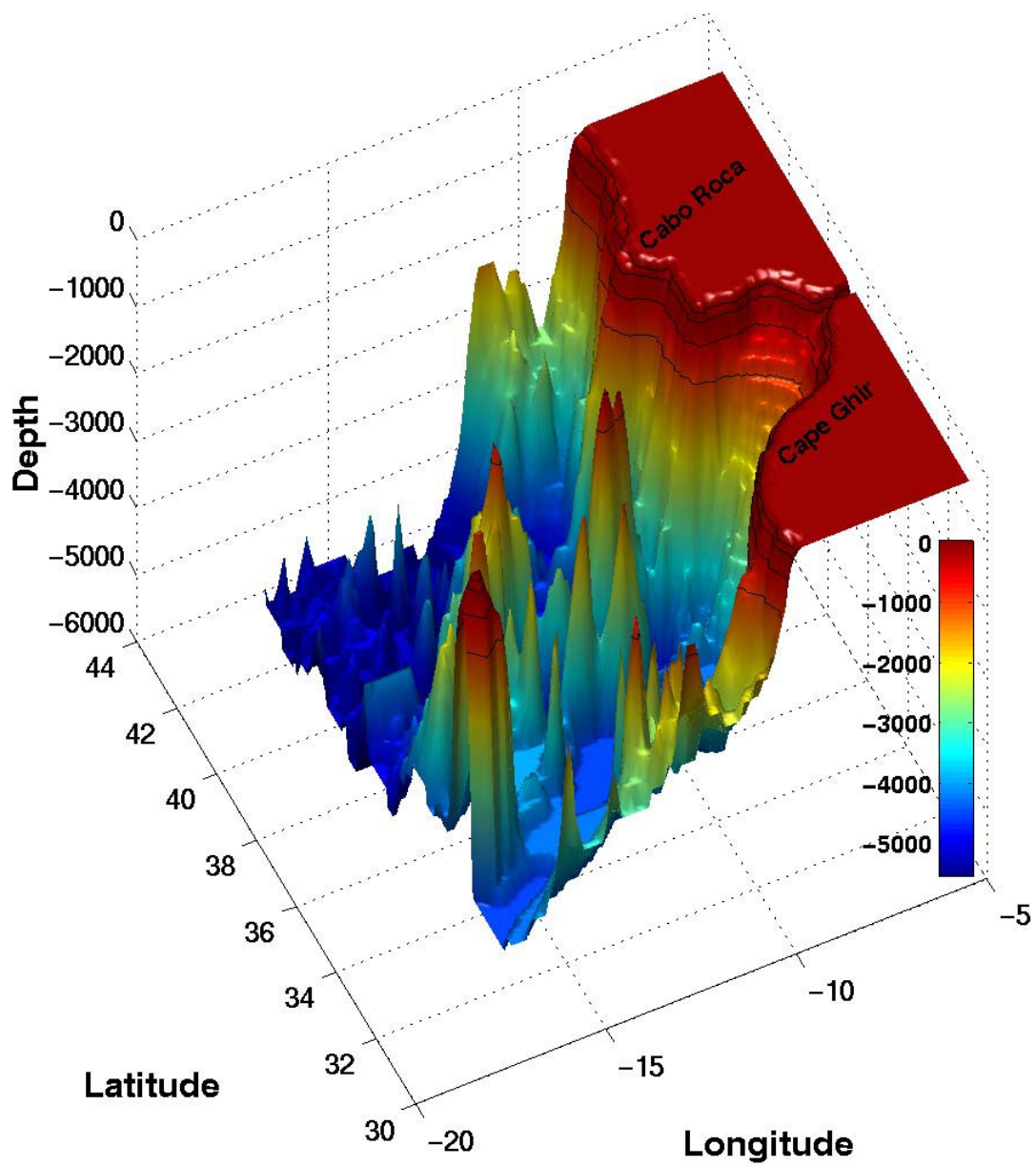


Figure 3.3b. Topography smoothed with the direct iterative method for the Northern Canary Current System, depths in meters. Contour lines at 100, 200, 500 and 1000 m depth.

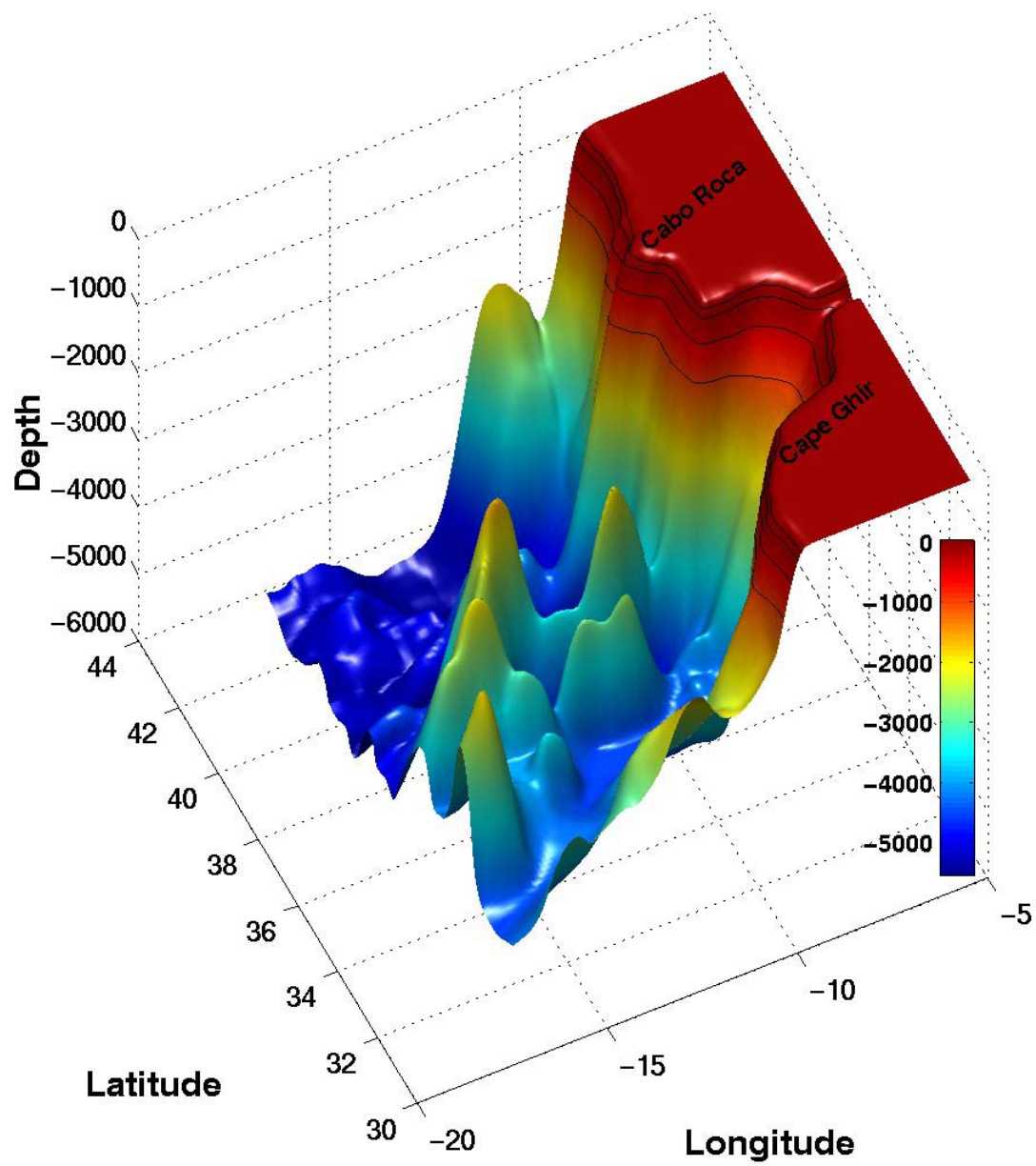


Figure 3.3c. Topography smoothed with a Gaussian two-dimensional filter method for the Northern Canary Current System, depths in meters. Contour lines at 100, 200, 500 and 1000 m depth.

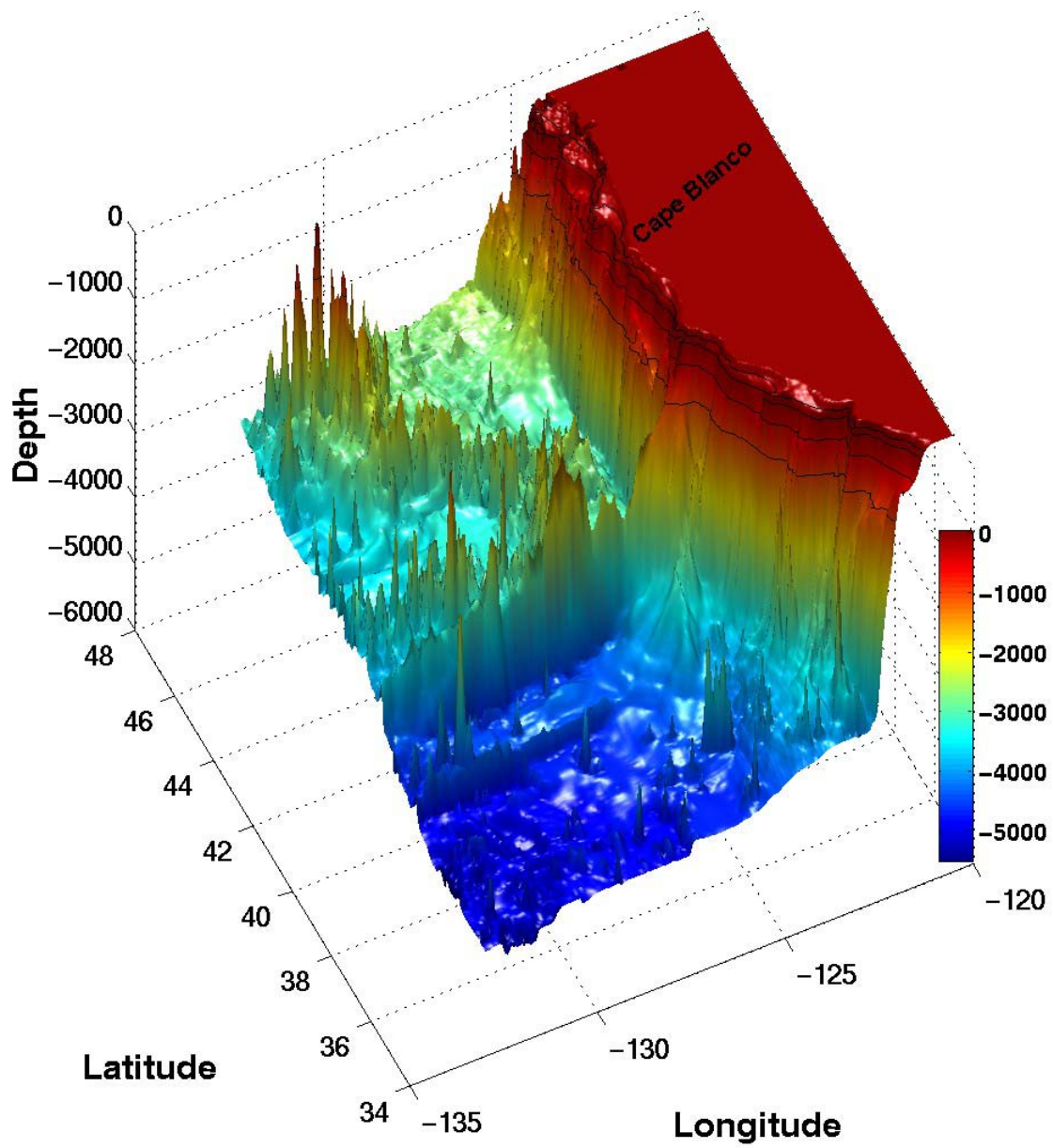


Figure 3.4a. Raw topography for the California Current System, depths in meters. Contour lines at 100, 200, 500 and 1000m depth.

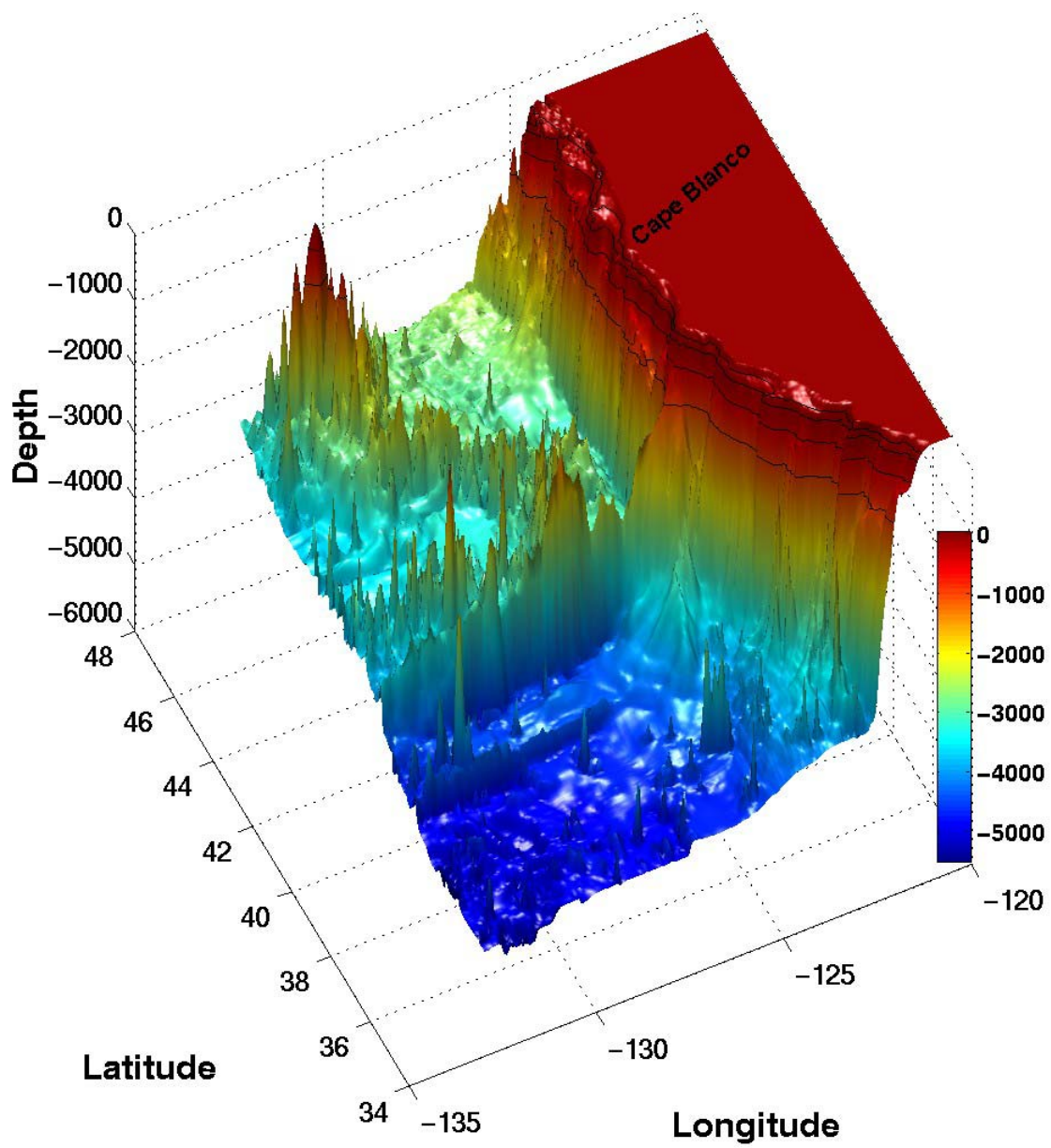


Figure 3.4b. Topography smoothed with the direct iterative method for the California Current System, depths in meters. Contour lines at 100, 200, -00 and 1000 m depth.

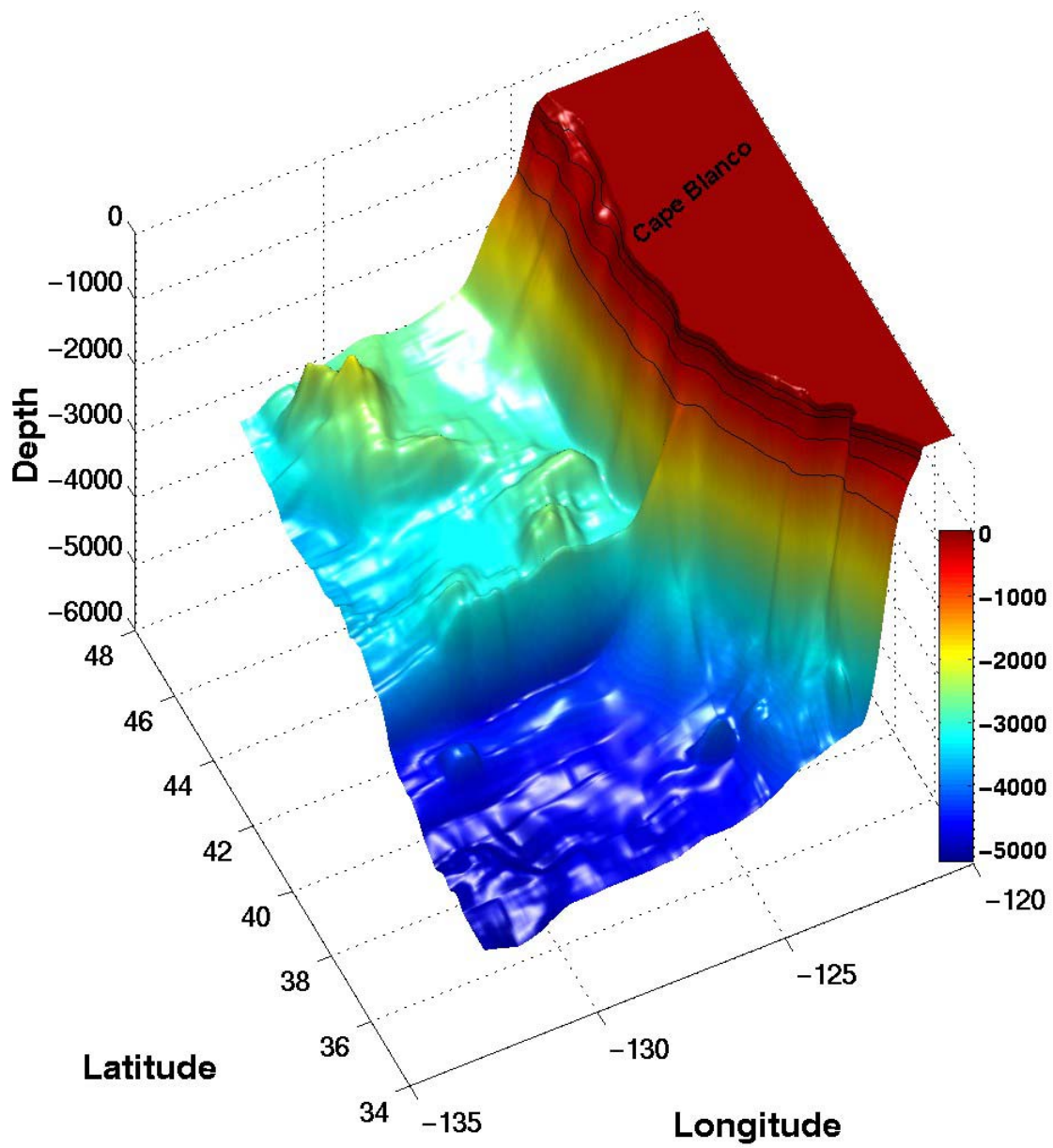


Figure 3.4c. Topography smoothed with a Gaussian two-dimensional filter method for the California Current System, depths in meters. Contour lines at 100, 200, 500 and 1000 m depth.

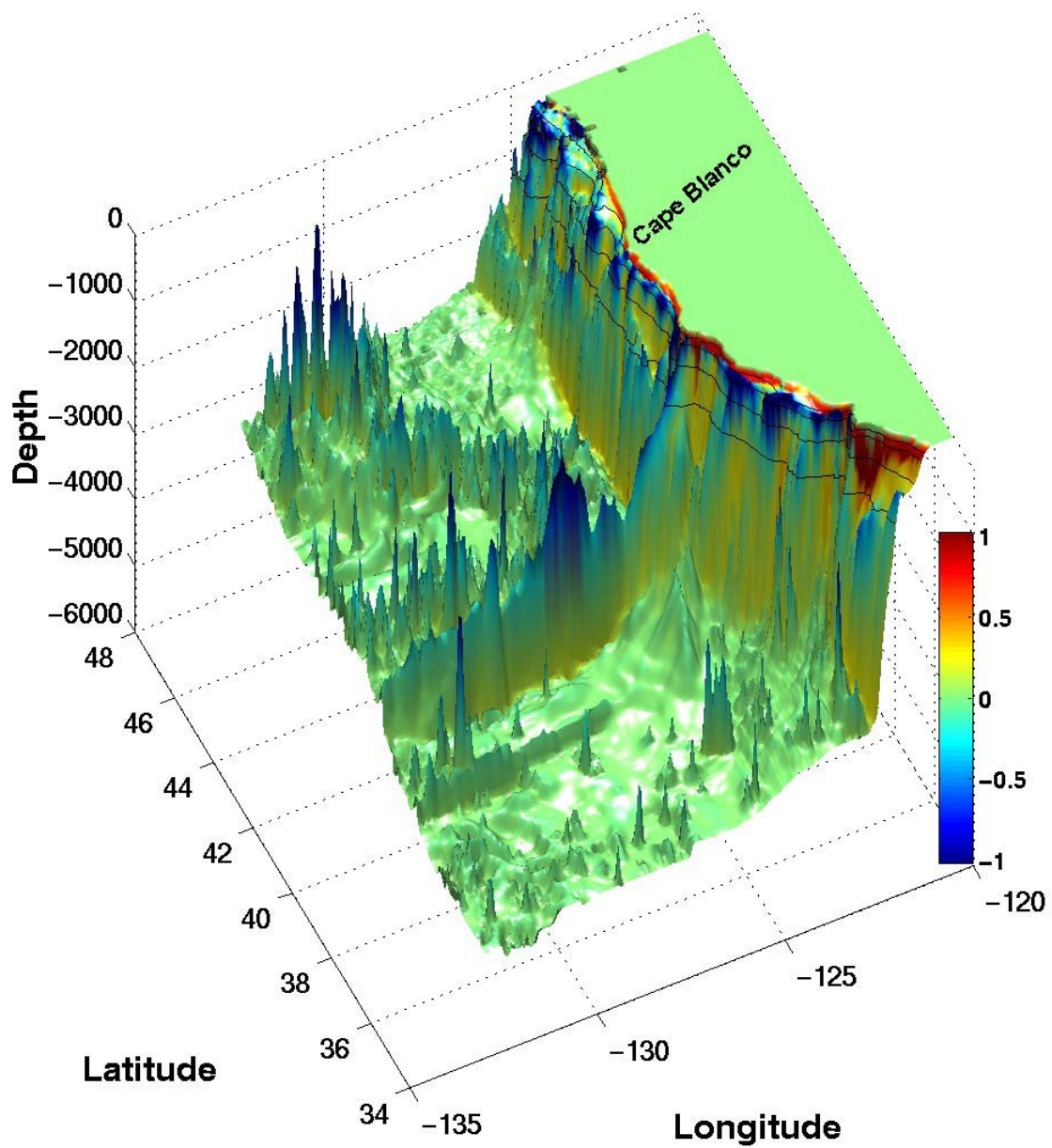


Figure 3.4d. Raw topography as surface, depths in meters. Difference in depths between raw and smoothed topography with two-dimensional Gaussian filter scaled by the raw topography in Color. Contour lines at 100, 200, 500 and 1000 m depth.

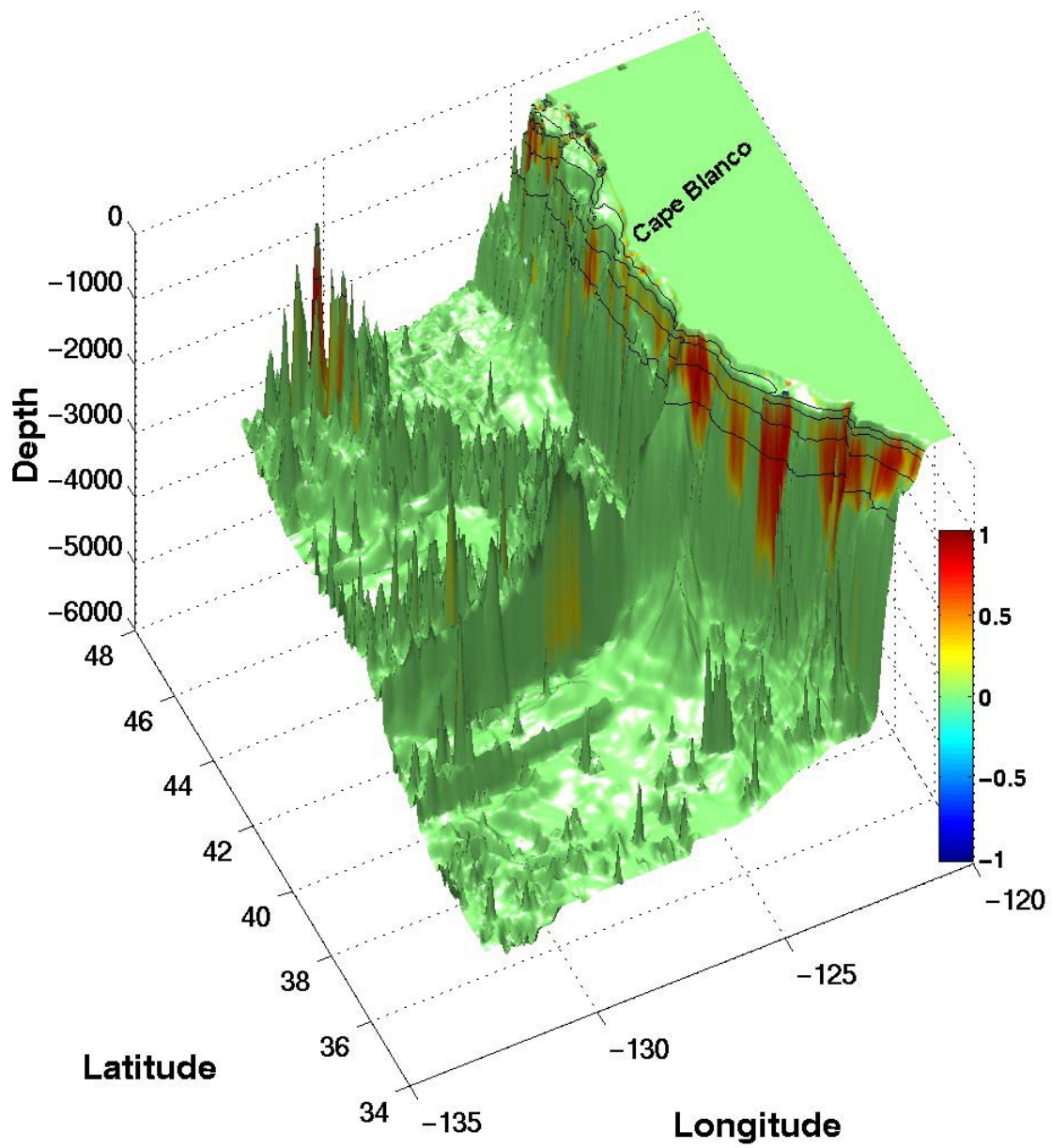


Figure 3.4e. Raw topography as surface, depths in meters. Difference in depths between raw and smoothed topography with one-dimensional direct method scaled by the raw topography in color. Contour lines at 100, 200, 500 and 1000 m depth.

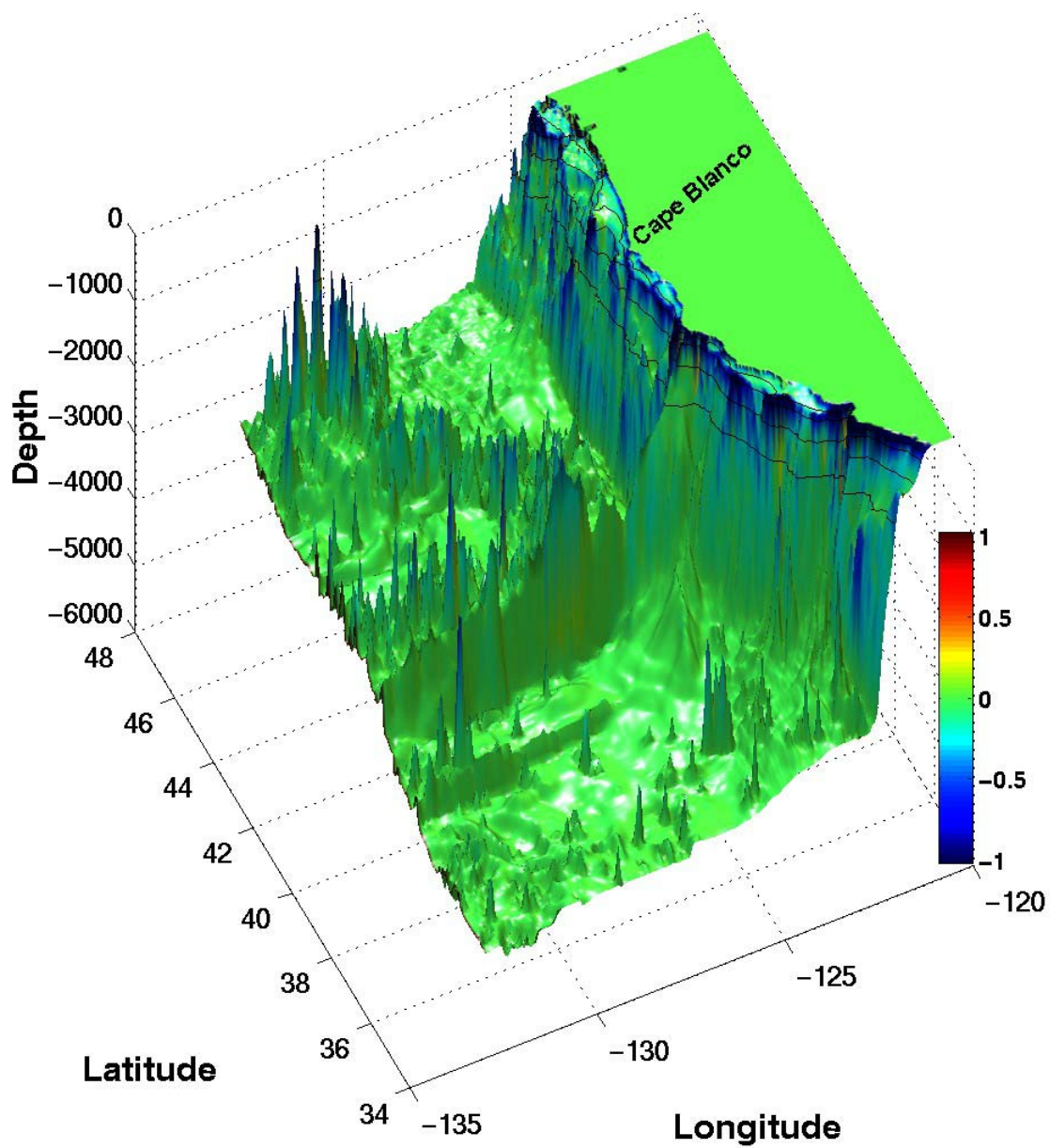


Figure 3.4f. Raw topography as surface, depths in meters. Difference in depths between raw and an alternative smoothing method provided to POM users scaled by the raw topography in Color. Contour lines at 100, 200, 500 and 1000 m depth.

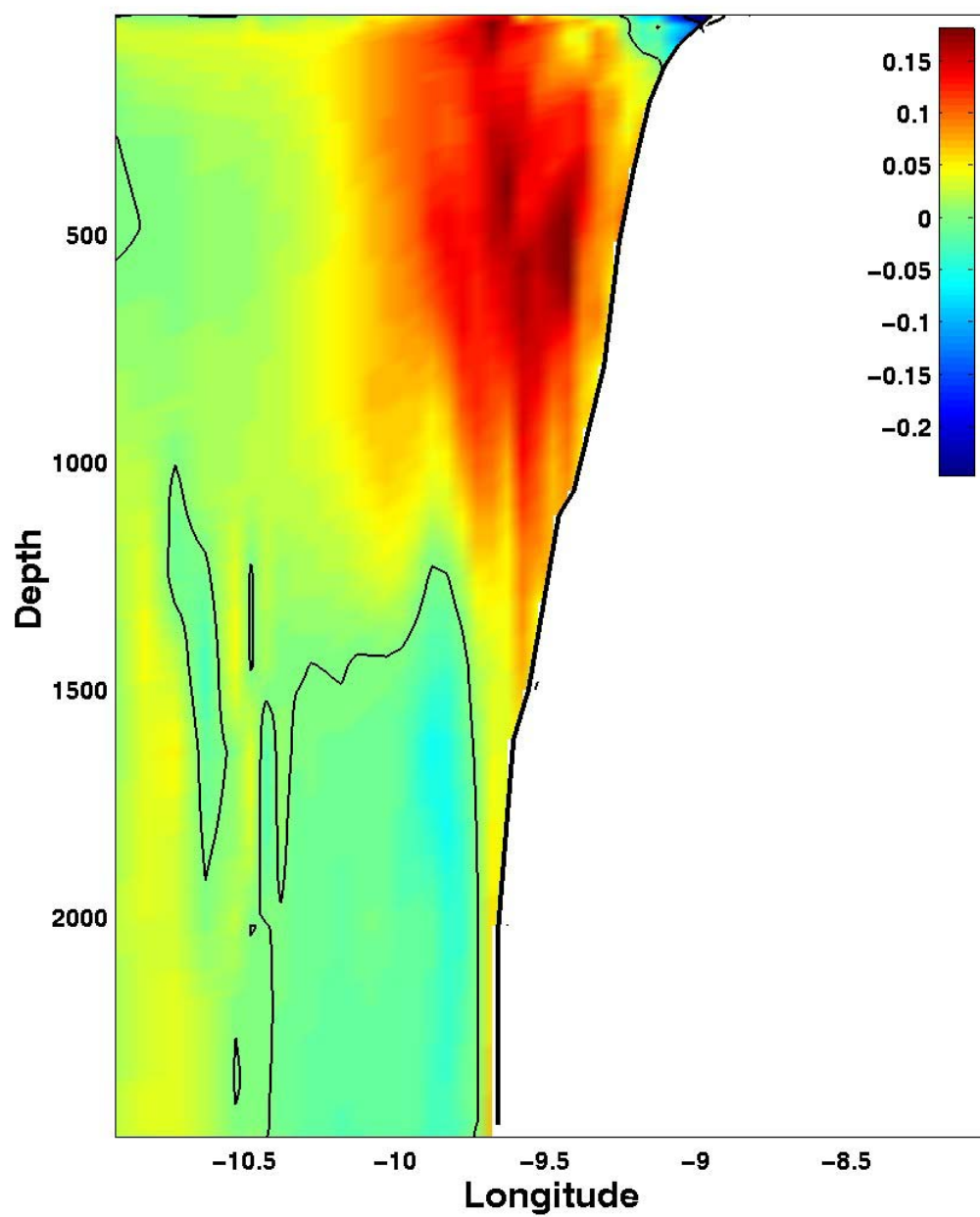


Figure 3.5a. Cross-section of meridional velocity for the experiment with the topography smoothed with the one-dimensional direct iterative method.

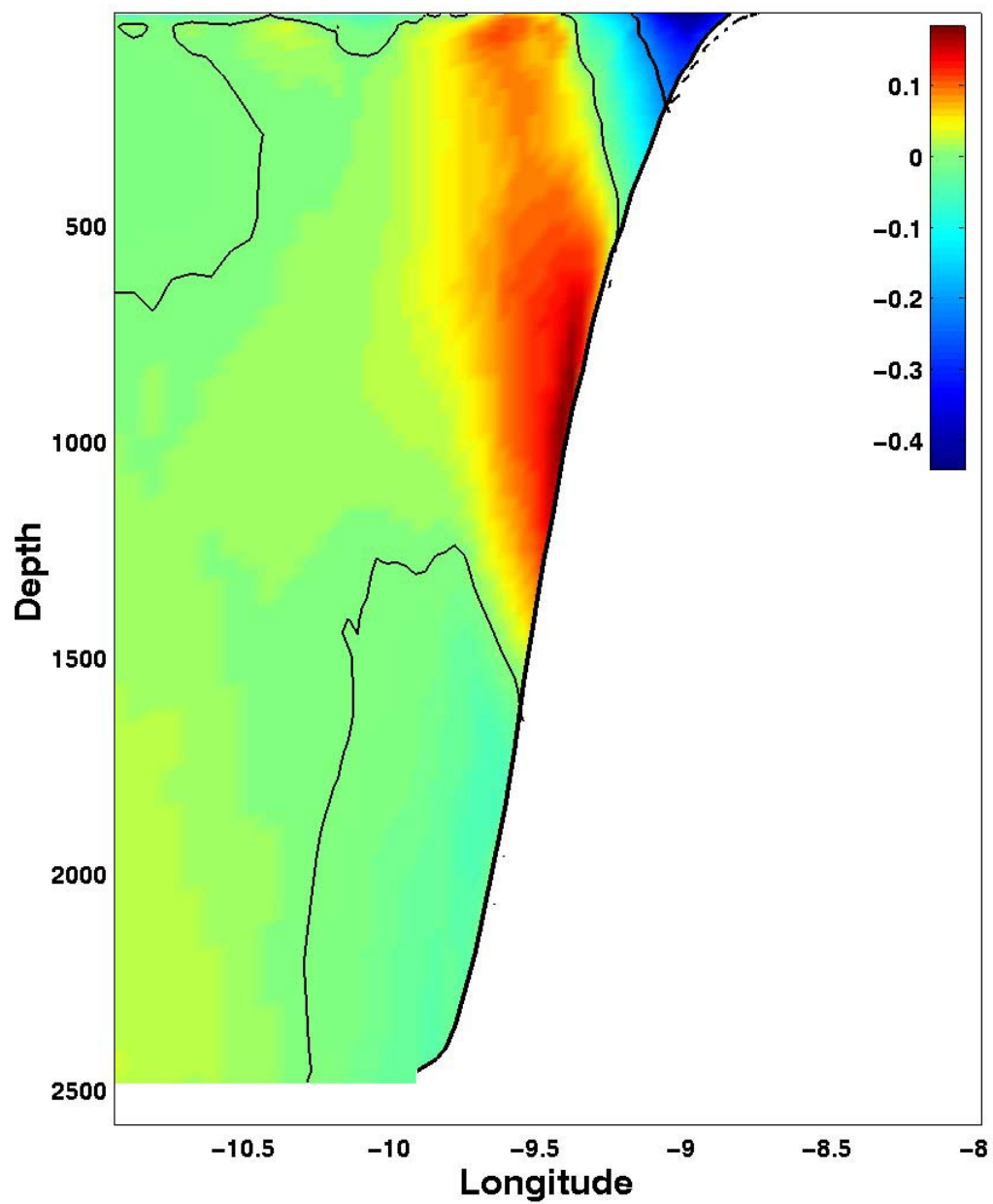


Figure 3.5b. Cross-section of meridional velocity for the experiment with the topography smoothed with a two-dimensional Gaussian filter.

IV. COUPLING THE PARALLEL OCEAN PROGRAM (POP) WITH THE PRINCETON OCEAN MODEL (POM) AND OPEN BOUNDARY CONDITION INVESTIGATIONS IN HIGH RESOLUTION SIGMA COORDINATE OCEAN MODELS

A. ABSTRACT

To properly one-way couple a basin-scale z -level coordinate model, in this case, the Parallel Ocean Program (POP) model, with a sigma-coordinate regional model, here, the Princeton Ocean Model (POM) model, a new set of boundary conditions was developed. These boundary conditions were then applied to the Northern Canary Current System (NCCS), a typical Eastern Boundary Current (EBC) system. Several experiments were performed to explore different boundary condition formulations that remain stable when using high spatial/temporal resolution forcing. Normal Projection of Oblique (NPO) radiation conditions were used for all the prognostic variables, with a sponge layer and a nudging layer that were shown to be stable. Several sensitivity studies were performed with this set of boundary conditions with different values of the inflow time scales for velocities and tracers. Model results with this new set of boundary conditions showed good agreement with the results from a wider reference model in the NCCS. The change in mean sea level between a test model and the reference model showed that the mean sea level adjustment time is proportional to the inflow time scale for the velocities, and that larger values for the inflow time scales give the best results over time. Best results are obtained with inflow time scales of three days for the velocities and one day for the tracers. The total kinetic energy demonstrates that a sponge layer, besides absorbing disturbances and suppressing computational noise, also has the effect of helping to conserve the total kinetic energy of the model. The results of the seasonal study of the NCCS shows that the model is able to reproduce the basic characteristics of the NCCS.

B. INTRODUCTION

Standard boundary conditions (BC) (see Chapter II) provided by the POM community model (Mellor, 1996) induce spurious currents near the boundaries and propagate noisy density fields into the interior, particularly when high temporal/spatial resolution fields are used or long term integrations are performed. Since the region to be modeled (the Northern Canary Current System) has three extensive ocean boundaries at the northern, southern and western limits of the model domain, and the Strait of Gibraltar in the eastern part, it is essential to determine a new set of robust boundary conditions that will be transparent to perturbations generated inside the model (Roed and Cooper, 1986), as well as being stable and convergent.

A large number of open boundary conditions (OBCs) have been proposed (e.g., see Palma and Matano, 1998, 2000, for a review). Here, a variation of the version of the OBCs described by Marchesiello et al. (2001), are described and tested in the Northern Canary Current System. Marchesiello et al. (2001) were the first to implement BCs where independent calculations of phase speed are made for all prognostic three-dimensional variables.

To achieve a more realistic model solution than obtained using standard climatological data, high temporal and spatial resolution POP output was used to initialize and force the lateral boundaries of POM. This simulation was run for the period March 1996 to September 1996.

C. MODEL OUTPUT

The topography used in POP is ETOPO 5 interpolated to the model grid (Figure 4.1). In turn, this topography was interpolated to the higher resolution of the POM grid (i.e., compare the grids in Figures 4.1 and 4.2). Note that even with higher resolution, the slope parameter was outside the range allowed for sigma coordinate models (recall that the slope parameter decreases with increasing resolution and smoothing). As a result, the direct interactive method (described in Chapter III) was used to decrease the slope

parameter to values less than 0.2, applying always a positive correction. The final topography is shown in Figure 4.2.

The model output used to initialize and force the lateral boundary conditions of POM are from a high-resolution North Atlantic basin configuration of the POP model (McClean et al., 2002). The spatial domain of the POP model is 20S-72N, 98W-17E, which includes the Gulf of Mexico and the Western Mediterranean. It is configured on a Mercator grid, producing horizontal resolutions varying from 11.1 km at the equator to 3.2 km at the northern boundary. There are 40 vertical levels.

It was run from 1993 through 2000 and was forced with daily NOGAPS (Navy Operational Global Atmospheric Prediction System) wind stresses and Barnier (1995) climatological heat fluxes. The Large et al. (1994) mixed layer formulation K-profile parameterization was active. Surface salinity was restored to monthly Levitus values (1982) using a time scale of 30 days. At the lateral boundaries temperature and salinity values were restored to monthly Levitus values (1982). The POP output consists of three-day averages of temperature, salinity, the horizontal components of velocity, and sea surface height.

Since the smoothing applied to the topography always has positive corrections, the POP fields can be used without vertical extrapolation of the model fields. This is an important consideration since vertical extrapolations can induce significant errors in the models. It is necessary, however, to extrapolate the POP fields horizontally at the points adjacent to land (coastline and bottom), since POP assigns the value zero to any field that is over land and POM has higher horizontal resolution than POP. Recall that since the variation of the horizontal fields is much less than of the vertical fields, models are usually less sensitive to horizontal extrapolations than vertical ones.

An extrapolation subroutine that automatically distinguishes between land points and ocean data points was used to fill points adjacent to land. Note that, if this extrapolation is not used, the resulting data fields interpolated to the POM grid (a sigma coordinate grid) will be very noisy not only near the coast but also where there is depth

variation between adjacent points. This noise can be sufficient to make the model unstable.

The POM model was initialized with POP temperature, salinity, horizontal velocity components and elevation fields from 02 March, 1996 (Figures 4.2a to 4.2c). The horizontal 3D velocity components were vertically averaged in order to obtain the initial 2D velocity component fields. The data was then re-interpolated to the POM horizontal grid (Figure 4.2) and to the 21 vertical sigma levels (Recall that the sigma levels are bottom following and have highest resolution near the surface and the bottom in order to resolve the surface and bottom boundary layers).

The lateral boundary forcing fields (temperature, salinity, velocity components and elevation) were interpolated to the boundary grid points of POM. The velocities were then averaged to obtain a 2D velocity field. The lateral boundary conditions were ingested every three days (the same frequency as the POP averages); while the boundary condition POM fields were updated at every internal time step by linear interpolation.

Daily wind stresses from NOGAPS (Figures 4.3a-b), were re-interpolated to the horizontal POM grid and updated at every internal time step producing smoothly varying surface forcing fields. The use of the time interpolated forcing reduces the likelihood of exciting inertial oscillations in the model solution (Jayne and Tokmakian, 1997; McClean, 2002). The temperature and salinity of the near-surface sigma level were restored to LEVITUS 94 climatology (Levitus, 94; Levitus and Boyer, 1994) with a relaxation time scale of 30 days.

D. BOUNDARY CONDITIONS

The POM boundary conditions are stable when climatological data are used because climatological data have lower variance than data with high temporal/spatial resolution. The lower variance of climatological data is not only due to the averaging over time (acting as a temporal smoother) but also because of the typical lower resolution (acting as a spatial smoother). As a result, highly smoothed temperature and salinity

fields have less stored energy and are consequently less capable of inducing density-driven currents. However, in long term integrations noise can still be created at the boundaries which then propagates to the model interior. The initial calculations with the boundary condition formulation provided with POM proved to be unstable when using high spatial-temporal resolution initialization and forcing.

Marchesiello et al. (2001), developed a set of boundary conditions that were tested in the California Current System (CCS), another eastern boundary current system. They initialized POM with temperature and salinity fields from Levitus and Boyer (1994) and Levitus et al. (1994) from a state of rest. The surface forcing consisted of mean seasonal wind stresses, and heat and freshwater fluxes derived from COADS (da Silva et al., 1994) that included a thermal feedback (Barnier et al., 1995). The external data used in the lateral boundary condition forcing were the temperature and salinity fields from Levitus and Boyer (1994) and Levitus et al. (1994), and the climatological values for the geostrophic and Ekman components of the velocity fields estimated from the climatological winds and density fields (this boundary condition formulation requires external data for temperature, salinity and the horizontal components of the velocity field).

Marchesiello et al. (2001) were the first to use boundary conditions where independent phase speed calculations were made for all 3-D prognostic variables (temperature, salinity and horizontal components of the velocity). The boundary conditions used in their study are shown in Table 4.1; the different conditions are explained in greater detail below.

Variables	Passive Regime	Active regime	Active and Passive
T,S ⁽¹⁾	Oblique Radiation	No Radiation	Sponge Layer
	Weak Nudging	Strong Nudging	Nudging Layer

Variables	Passive Regime	Active regime	Active and Passive
$u,v^{(1)}$	Oblique Radiation Weak Nudging	No Radiation Strong Nudging	Sponge Layer
$ua,va^{(1)}$	Oblique Radiation Weak Nudging	No Radiation Strong Nudging	Sponge Layer Volume Constraint
$\eta^{(1)}$			Zero Gradient Nudging layer

⁽¹⁾ T,S – temperature and salinity.

⁽¹⁾ u,v – 3D horizontal components of velocity.

⁽¹⁾ ua, va – 2D components of velocity.

⁽¹⁾ η - surface elevation.

Table 4.1 Marchesiello (2001) Boundary Conditions.

1. Radiation Condition

A variation of the radiation condition based on Raymond and Kuo (1984) where phase speed components are normal and tangential to the boundary is described by:

$$\frac{\partial \phi}{\partial t} + C_x \frac{\partial \phi}{\partial x} + C_y \frac{\partial \phi}{\partial y} = 0 \quad (4.1)$$

where ϕ is the prognostic variable, t is time, x is the normal direction to the boundary and y is the tangential direction to the boundary. C_x and C_y are the normal and tangential phase speeds calculated from interior points, defined as:

$$C_x = -\frac{\frac{\partial \phi}{\partial t} \frac{\partial \phi}{\partial x}}{\left(\frac{\partial \phi}{\partial x}\right)^2 + \left(\frac{\partial \phi}{\partial y}\right)^2} \quad (4.2)$$

$$C_y = -\frac{\frac{\partial \phi}{\partial y}}{\frac{\partial \phi}{\partial t} \left(\left(\frac{\partial \phi}{\partial x} \right)^2 + \left(\frac{\partial \phi}{\partial y} \right)^2 \right)} \quad (4.3)$$

Equation (4.1) is the oblique radiation condition. When used with high resolution initialization and forcing in the NCSS it was found to be unstable. Barnier (1998) and Marchesiello et al. (2001) also mentioned that under certain conditions even when climatological data is used, the oblique radiation condition can be unstable. As a result, to prevent instabilities, a simplification of this radiation condition called Normal Projection of Oblique radiation (NPO) (Marchesiello et al., 2001) is used where $C_y = 0$ but the component $\frac{\partial \phi}{\partial y} \neq 0$ in the calculation of C_x . It is important to note that NPO differs from the traditional normal radiation condition (Orlanski, 1976), because in the latest case not only $C_y = 0$ but also $\frac{\partial \phi}{\partial y}$ is set to zero in the calculation of C_x . Marchesiello et al. (2001) show that the NPO produces results that are close to the ones obtained by the oblique radiation condition, however rather than being unstable, NPO is very stable.

2. Radiation Condition Algorithm

The NPO radiation condition uses an extrapolation based on interior values. This extrapolation is only valid if the phase speeds are positive, where positive indicates outward propagation. When the phase speed is negative, nudging to external values is used.

The numerical scheme was implemented with implicit time differencing for normal propagation, and with first order forward time differencing, which is a very simple and accurate scheme (Stevens, 1990). Upstream spatial differencing for both

normal and tangential gradients and the phase speed calculated at the current time, are shown to have the best performance (Chapman, 1985).

The resulting algorithm is:

$$\phi_{b,j}^{n+1} = \frac{1}{1+r_x} \left[\phi_{b,j}^n + r_x \phi_{b-1,j}^{n+1} \right]$$

with

$$r_x = - \frac{\Delta \phi_t \Delta \phi_x}{(\Delta \phi_x)^2 + (\Delta \phi_t)^2 + 2.22 \times 10^{-16}}$$

$$\Delta \phi_t = \phi_{b-1,j}^{n+1} - \phi_{b-1,j}^n$$

$$\Delta \phi_x = \phi_{b-1,j}^{n+1} - \phi_{b-2,j}^{n+1}$$

$$\Delta \phi_y = \phi_{b-1,j}^n - \phi_{b-1,j-1}^n \quad \text{if } \left[\Delta \phi_t \times (\phi_{b-1,j+1}^n - \phi_{b-1,j-1}^n) \right] \geq 0$$

$$\Delta \phi_y = \phi_{b-1,j+1}^n - \phi_{b-1,j}^n \quad \text{if } \left[\Delta \phi_t \times (\phi_{b-1,j+1}^n - \phi_{b-1,j-1}^n) \right] < 0$$

where n indicates time, subscript b indicates the normal position of the boundary point, and the subscript j indicates the tangential position of the boundary point.

3. Adaptivity

When the phase speed remains positive for a long duration, boundary condition values can be quite different from the prescribed external values. If the phase speed changes to become negative, numerical instabilities can arise. To overcome this potential problem a nudging term is used at the boundary, regardless of the sign of the phase speed. The resulting radiation condition is:

$$\frac{\partial \phi}{\partial t} + C_x \frac{\partial \phi}{\partial x} + C_y \frac{\partial \phi}{\partial y} = -\frac{1}{\tau} (\phi - \phi^{ext}) \quad (4.4)$$

with

$\tau = \tau^{out}$ if phase speed positive

$\tau = \tau^{in}$ and $C_x = C_y = 0$ if phase speed is negative or zero

τ is the time scale for nudging, and τ^{out} (τ^{in}) is the outflow (inflow) time scale for the nudging. When the phase speed is positive (i.e., outward propagation), weak nudging can prevent substantial drifts. When the phase speed is negative (i.e., inward propagation) relatively strong nudging is used to make the connection between the external data and the interior data model points. To avoid instabilities, typical values on the order of one year have been used for τ^{out} and on the order of 1 to 3 days for τ^{in} .

4. Volume Constraint

Unlike rigid-lid models, free surface models can lose or gain water through the boundaries. If the algorithm for the barotropic velocities is non-volume conservative, (which is the case when radiation boundary conditions are used for the barotropic velocities) it is necessary to apply an artificial volume constraint to the model. In this case, the total volume of water that is transported through the boundaries is calculated at every external time step. If there is a net volume outward or inward, a correction is applied at every boundary point in order to obtain a net change in volume equal to zero. Since the correction is always small and is applied at every open boundary condition point, there is no appreciable change discernible in the flow structures (Marchesiello et al., 2001).

The algorithm used is as follows:

$$\frac{dV}{dt} = \frac{d}{dt} \left[\iiint_V dV \right] = \iint_{Sb} \vec{u} \cdot \vec{n} dS = \int_{Lb} h \vec{u} \cdot \vec{n} dL$$

where V is the total volume, \vec{n} is the unit inward vector at the boundary, Sb is the surface of the open boundary, Lb is the perimeter of the open boundary and \vec{u} is the barotropic velocity. The new barotropic velocity at the boundaries will be

$$\vec{u}_{new} = \vec{u} - \bar{u}_c \vec{n}$$

where the velocity correction (\bar{u}_c) is:

$$\bar{u}_c = \frac{1}{Sb} \left(\int_{Lb} h \vec{u} \cdot \vec{n} dL \right).$$

4. Sponge Layer

A sponge layer is a region of increased viscosity near the boundaries. Its function is to absorb disturbances and suppress computational noise associated with the radiation condition (Palma and Matano, 1998). In this case a 15-point sponge layer is used where the viscosity decreases from $100 \text{ m}^2 / \text{s}^{-1}$ at the boundary to zero at the interior edge of the boundary layer, with a half-cosine variation.

5. Nudging Layer

This is a region near the boundary where the data is nudged to external data. Recall that nudging was applied in sub-section A3 – Adaptivity; to the boundary points for all the prognostic variables. Note that, the nudging layer is applied to the right hand side of the prognostic equations for elevation and tracers to points near the boundaries (not at boundaries):

$$\frac{\partial \phi}{\partial t} = r.h.s. - \frac{1}{\tau} (\phi - \phi^{ext})$$

where ϕ is the prognostic variable, τ is the time scale which varies from τ^{out} just near the boundary to infinity at about 100 km from the boundary. The nudging layer and the adaptivity act as a weak flow relaxation scheme (FRS), connecting spatially, as smoothly as possible, internal and external data.

E. BOUNDARY CONDITIONS FOR HIGH RESOLUTION DATA

The boundary conditions used for the high resolution cases are shown in Table 4.2. The biggest differences from those of Marchesiello (Table 4.1) are the use of the NPO radiation condition instead of the oblique radiation condition for tracers and velocities, and the use of the NPO radiation condition for the elevation instead of the gradient boundary condition; the latter proved to be unstable in the case of high resolution forcing.

Variables	Passive Regime	Active regime	Active and Passive
$T, S^{(1)}$	NPO	No Radiation	Sponge Layer
	Weak Nudging	Strong Nudging	Nudging Layer
$u, v^{(1)}$	NPO	No Radiation	Sponge Layer
	Weak Nudging	Strong Nudging	
$u_a, v_a^{(1)}$	NPO	No Radiation	Sponge Layer
	Weak Nudging	Strong Nudging	Volume Constraint
$\eta^{(1)}$	NPO	No Radiation	Sponge Layer
	Weak Nudging	Strong Nudging	Nudging layer

⁽¹⁾ T, S – temperature and salinity.

⁽¹⁾ u, v – 3D horizontal components of velocity.

⁽¹⁾ u_a, v_a – 2D components of velocity.

⁽¹⁾ η - surface elevation.

Table 4.2 Boundary Conditions with High Resolution Data.

Several experiments were conducted to try to assess the validity of the Marchesiello et al. (2001) boundary conditions in a high resolution setting. The basic test is defined in Table 4.2. Some changes to the initial boundary conditions are shown in Table 4.3. All the variations except the advection for tracers become unstable in a short period, in between a few internal time steps (400 sec) to a few days. This was the case even when all the prognostic variables were specified (assigned the external value) at the boundaries. When the advection was used for tracers the model become unstable after 10 days.

Variables	Active and Passive
$T, S^{(1)}$	Advection
$T, S^{(1)}$	Specified
$T, S^{(1)}$	Specified
$u, v^{(1)}$	Specified
$ua, va^{(1)}$	Specified
$\eta^{(1)}$	Specified
$u, v^{(1)}$	BK ⁽¹⁾ 3D
$ua, va^{(1)}$	Flather
$\eta^{(1)}$	Flather
$ua, va^{(1)}$	BK ⁽¹⁾ 2D
$u, v^{(1)}$	BK ⁽¹⁾ 3D
$ua, va^{(1)}$	BK ⁽¹⁾ 2D
$\eta^{(1)}$	Gradient

- ⁽¹⁾ T,S – temperature and salinity.
- ⁽¹⁾ u,v – horizontal baroclinic components of velocity.
- ⁽¹⁾ ua, va – barotropic components of velocity.
- ⁽¹⁾ η - surface elevation.
- ⁽¹⁾ BK – Blumberg and Kantha

Table 4.3 Alternative Boundary Conditions (for the variables not specified, the formulation in Table 4.2 was used).

F. RESULTS

In the analyses of the results it is important to note that the open boundary conditions for an incompressible, hydrostatic primitive equation model at large Reynolds number are inherently unstable (Oliger and Sundstrom, 1978; Miller and Bennett, 1988 and Bennett 1992). Even though the problem is ill-posed because the number of boundary conditions is over-specified, the solution can still be stable (Marchesiello et al., 2001). Note that this stable solution will not converge to the true solution (the solution obtained in a interior point of the model), but will be always be an approximation. This approximation will improve with more realistic boundary condition formulations (more transparent to outflow and inducing less noise).

1. Barotropic Velocity and Elevation Results

POM forced with POP output is now used to address the performance of the modified Marchesiello boundary conditions (see Table 4.2). The outer model (here Region A), shown in Figure 4.5, was forced with POP output at the boundaries and daily winds from NOGAPS; surface temperature and salinity were relaxed towards monthly Levitus 94. Next, temperature, salinity, the horizontal baroclinic components of the velocity and the elevation were extracted at the points coincident with the test model

(Region B, shown as the black box in Figure 4.5) every three days (the same time interval at which the POP BC was supplied). Note that the test model (Region B) located within the reference model (Region A), lies some distance from the reference model's sponge layer and defines the interior model that will be used to test the BCs. The evaluation region (Region C, Figure 4.5), located within the test model's sponge layer defines the region where fields from the test and reference models will be compared.

Figure 4.6a shows the barotropic velocity and elevation for day 30 (31 March 1996) for the reference model in the evaluation region. This will be considered the true solution with which all the other runs will be compared. The results show several mesoscale features in the model, mainly cyclonic and anti-cyclonic eddies off the Iberian Peninsula and off Morocco. Also seen is the equatorward flow off the Iberian Peninsula and the poleward Iberian Current off the coast of the Iberian Peninsula, which is characteristic of this region. The poleward flow discernible off the coast of Morocco is likely a density driven current since the wind stress is almost zero in this region (not shown).

Several sensitivity experiments were conducted with the modified Marchesiello et al. (2001) boundary conditions (Table 4.2) with the time scales for the boundary condition data nudging shown in Table 4.4. Several experiments were conducted where the outward time scales for the velocities and tracers was held constant with a value of 1 year, and the inward time scales for the velocities and tracers varied from 0.5 days to 3 days. An experiment was conducted without sponge and inward time scales of 3 days (1 day) for the velocities (tracers). Note that, the lower the values for the inflow time scales the faster the POM fields at the boundaries converge to POP forcing fields in the inflow situation.

Experiment	Velocities τ_{in} (Strong Nudging)	Velocities τ_{out} (Weak Nudging)	Tracers τ_{in} (Strong Nudging)	Tracers τ_{out} (Weak Nudging)	Sponge
1	3 days	1 year	1 day	1 year	Yes
2	1 day	1 year	0.5 days	1 year	Yes
3	0.5 days	1 year	0.5 days	1 year	Yes
4	3 days	1 year	3 days	1 year	Yes
5	3 days	1 year	1 day	1 year	No

Table 4.4 Time Scales for Boundary Condition Nudging (for boundary condition formulations see Table 4.2).

The difference in elevation and in the barotropic velocity between the reference and the test models is shown in Figures 4.6b-f. All the experiments show differences in the southern region of the western boundary. In particular, the cyclonic eddy located near latitude 36N was intensified and the same happens with the anti-cyclonic eddy located near the western boundary between latitudes 34N and 35N. This implies a change in the circulation that is reflected by barotropic velocities. Note that, the test models that have the best results in this area are the ones with the smallest time scales (Figures 4.6c-d). There is also in all the models, a eddy like feature induced by errors due to the boundary conditions at the southern boundary near longitude 9.5W.

In the coastal areas north of the Strait of Gibraltar, the elevation near the coast is generally lower in the test experiments than in the reference model, resulting in higher density driven currents and stronger upwelling. In this region, Experiment 5, the only experiment without a sponge, is the only one that shows good agreement with the

reference case (see Figure 4.6f). The absence of the sponge allows currents to be easily propagated from the boundaries to the interior of the model.

In the coastal areas south of the Strait of Gibraltar, the elevations are generally lower in the test experiments than in the reference case (see Figures 4.6b-f). Experiment 3 (Figure 4.6d, which has the lowest time scales for the velocities and tracers, most closely agrees with the reference case in this region. Experiment 5 (Figure 4.6f) with no sponge, has much higher values for the elevation and corresponding barotropic velocities in the southern coastal areas of the model than the reference case.

The Iberian Current, the surface coastal poleward current about 50 km offshore of the Iberian Peninsula, does not seem to be sensitive to the time scales of the nudging at the boundaries, since all the experiments show very similar results to the reference model. Generally there is a good agreement between the reference model results and the different test experiments in the evaluation region except for the southern region of the western boundary and off the Iberian Peninsula and Morocco.

2. Mean Sea Level and Kinetic Energy Results

In order to evaluate the performance of the BCs, statistics for the mean sea level, the surface kinetic energy and the total kinetic energy were calculated for the test and reference model simulations. These will give an overall idea of how well the BCs represent mass fluxes at the boundaries and impact the conservation of kinetic energy in the interior model domain. These results are shown in Figures 4.7 a-c.

Figure 4.7a shows the mean sea level for the test and reference models. The volume constraint has been applied over different regions, particularly, over that encompassed by the outer boundary of the reference model and for the black box (see Figure 4.5) in the test model. Since the reference model is not required to be volume conserving over the smaller perimeter of the test model, an artificial difference between both models can be induced. Figure 4.7a shows that all the test cases show a difference of mean sea level between 1 and 3 mm relative to the reference case. During the first three

days, all the test models have adjusted to the new location of the volume constraint calculation. As expected the test cases that adjust the fastest are the ones with the lower time scales (in green and blue in Figure 4.7a). They also have initially the smallest sea level differences relative to the reference model; however, in time they diverge from it. Overall, the best results are obtained for the simulations with inflow time scales of three days for the velocities (Experiments 1, 2 and 5), where the mean sea level difference between the test model and the reference model stays roughly constant over time following the initial adjustment. The model is more sensitive to the change in the inflow time scale for the velocities (see curves green and cyan, difference 0.5 days) than to the inflow time scale for the tracers (see curves red and magenta, difference 2 days). The comparison between two experiments with the same time scales, one with a sponge and the other with no sponge, shows that the mean sea level is not very sensitive to the presence of the sponge layer (compare Experiments 1 and 5 in Figure 4.7a).

The results for the surface kinetic energy (Figure 4.7b) are similar for all the model experiments. The best results are obtained for experiments with lower inflow time scales (1 and 0.5 days) for the velocities and for the test model with no sponge and the 3 days inflow time scale (experiment 5). The difference between curves with the same time scales, for example with a sponge (Experiment 1) and without a sponge (Experiment 5), is most discernible at day 25 and shows that the surface kinetic energy is more sensitive to the presence of the sponge than the mean sea level.

The total kinetic energy of Experiments 1, 2 and 4 (Figure 4.7c), with sponges and inflow time scales for the velocities between 1 and 3 days, show the best agreement with the reference experiment (blue line). In contrast, the total kinetic energy of the test case with inflow time scales equal to 0.5 days (Experiment 3) for both the velocities and the tracers, overshoots the total kinetic energy of the reference model. Likewise, the model without a sponge and inflow time scales of 3 days for velocities and 1 day for the tracers (Experiment 5), does not conserve the total kinetic energy of the model. In particular it overshoots the total energy of the reference model by about 10% after 30 days. As a result, the use of a sponge layer not only absorbs disturbances and suppresses

computational noise but also has additional effect of helping to conserve the total kinetic energy of the model.

Since the surface kinetic energy was conserved for Experiment 5, this means that the kinetic energy is gained mainly at depth. This is because the difference between the Smagorinsky viscosity values (Smagorinsky, 1965) and the ones prescribed at the sponge layer is larger at greater depths where the Smagorinsky viscosity has the lowest values. Recall that the sponge layer values are independent of the depth.

The optimal values of 3 days (1 day) for the velocity (temperature) nudging were then used to conduct the following seasonal study.

G. SEASONAL STUDY

1. Monthly Model Output

The evolution of the monthly wind stress in the NCCS region is shown from March to September 1996 (Figures 4.8a-g). In the northern region of the model there is an increase in the monthly wind stress from March to July (Figures 4.8 a-e) decreasing afterwards. In the southern region of the model the monthly wind stress increases from March to August (Figures 4.8 a-f) decreasing sharply from August to September (figures 4.8 f-g). Due to the positioning of the Azores High, the monthly wind stress intensity is generally higher in the southern region of the model. The monthly wind stress in the Gulf of Cadiz is usually very low.

Figures 4.9a through 4.9g show the monthly seasonal evolution of the surface temperature and currents for the same period (March to September 1996). The equatorward surface coastal currents off the west coasts of Morocco and the Iberian Peninsula are generally well correlated with the wind stress.

The surface current off the southern coast of Portugal flows generally eastward. When the wind stress has an eastward component this current reaches intensities greater than 30 cm/s (Figures 4.9b-c and 4.9f-g). The intensity decreases sharply if the wind stress has a significant southward or westward component. This current goes almost

entirely through the Strait of Gibraltar, giving rise to one of the unique characteristics of this region, the separation of the upwelling regimes.

To the south, the coastal current off Morocco is always equatorward, its intensity is strongest from June to September (Figures 4.9d-g). The strongest upwelling and the generation of filaments are found off Cape Ghir and Cape Bedouzza, demonstrating the importance of the coastline irregularities in the development of mesoscale features.

Between 34 and 36N, a relatively strong eastward jet ~ 100 km wide (Figures 4.9a-g), meanders toward the Gulf of Cadiz. This flow is consistent with observations of the Azores Current in this region (Pingree, 1997). Relatively strong thermohaline gradients are also discernible as well as the relatively high mesoscale activity and velocities (on the order of 40 cm/s), which are consistent with available observations (e.g., Pingree, 1997). The mean diameter of the eddies, which is on the order of 100-150 km, is also consistent with available observations (e.g., Le Traon and De Mey, 1994).

A time sequence of salinity and velocities at 1000 m depth is shown in Figures 4.10a through 4.10c. The Mediterranean Outflow is shown to follow the Iberian coast until it reaches Cabo da Roca where it subsequently separates from the coast. There is strong entrainment of the Mediterranean Outflow by North Atlantic Waters with the consequent reduction in the salinity. The Mediterranean Outflow arrives near Cabo de Sao Vicente with a salinity between 36.5 and 36.7 psu, consistent with observations (Baringer and Price, 1997). Note the development of a highly saline, clockwise eddy at day 65 (Figure 4.10a) southwest of Cabo da Roca. The relatively high salinity signal can be traced to a Mediterranean influence. Subsequent figures show the westward propagation of the eddy (see Figures 4.10a-c). This highly saline, clockwise eddy which subsequently propagates westward is consistent with available observations of Meddies, which are frequently observed south of Cabo da Roca (Johnson et al., 2002). The undercurrent results are also consistent with observations of Johnson et al. (2002, see Figure 4.10d) and Ambar et al., (2002). Note that the temperature and salinity values, originating in the Mediterranean Outflow, are kept against the continental slope (compare Figures 4.10a and 4.10d).

2. Three Day Average Model Output

Here, a more in-depth characterization of the variability of the Portuguese coastal upwelling system will be given. The upwelling along the west coast of Portugal is a seasonal event, reaching its maximum intensity from July to September (Fiuza, 1983, 1984; Frouin et al., 1990). The upwelling intensity presents a strong time correlation with the north-south wind stress. A more in-depth study by Fiuza (1983) also showed a strong spatial correlation between the favorable wind stress and upwelling intensity.

The wind stress vector and intensity is shown in Figures 4.11a-f for an upwelling event that occurred from 21 July to 08 August. The corresponding model surface temperature and velocity are shown in Figures 4.12a-f. Notice that this event occurred in an upwelling favorable season, and in Figures 4.12a-f it can be seen the flow off Iberia is generally equatorward, consistent with Wooster et al (1976). This equatorward coastal current (the Portugal Current) is apparently induced by the equatorward winds, prevailing during this time of year (Fiuza et al., 1982). The intensity of the Portugal Current (PC) increases sharply from 21-24 July to 24-27 July (compare Figure 4.12a and 4.12b). This is highly correlated with an increase of the wind stress in this region (compare Figures 4.11a and 4.11b). The intensity of the Portugal Current is relatively high (on the order of 20-30 cm/s) from 24-27 July to 30 July-02 August (Figures 4.12b-d), consistent with observations from Fiuza (1982) and highly correlated with the local wind stress (Figures 4.11b-d). After 30 July-02 August, the intensity of the Portugal current starts to decrease (Figures 4.12e-f) consistent with the relaxation of the wind stress (Figures 4.11e-f). As expected, the model results show a high correlation between the Portugal Current and the upwelling intensity. Also, the high correlation between the wind stress and the Portugal Current is consistent with observations of Fiuza (1983) and Sousa (1986), which show a delay of one day between the response of upwelled waters and wind stress.

Mesoscale features are typical of the west coast of Iberia in the upwelling season, such as filaments. Several filaments shown in Figure 4.13a (for 3-6 July) are in accordance with Sousa and Bricaud (1992). They are separated by ~ 120 km and have maximum extensions of ~ 200 km. A well-developed filament is also observed off Cape

Ghir. These filaments are shown in an averaged surface temperature AVHRR image (Figure 4.13b).

A feature typical of the fall-winter-spring time off Portugal is the Iberian Current (Frouin et al., 1990). The Iberian current develops when the local wind stress decreases intensity or/and its direction turns poleward. The Iberian Current is subsequently induced by onshore convergence of the poleward wind stress and by geostrophic adjustment of the eastward oceanic flow (which is driven by the large-scale meridional baroclinic pressure gradient as the flow reaches the continental slope, Frouin et al., 1990). Figure 4.14a shows the predominantly poleward wind stress vector fields 20-23 March, while Figure 4.14b shows the corresponding surface poleward velocity field (i.e., the Iberian Current). Note that the Iberian Current was also observed in other non-upwelling season periods, from 7-10 May and 7-10 September (not shown).

H. CONCLUSIONS

The results show that when a free-surface regional model is initialized and forced with high spatial and temporal resolution fields with strong variability there are just a few combinations of the boundary conditions that can remain stable (see Table 4.2). The oblique radiation condition was shown to be unstable, as well as all the alternatives shown in Table 4.3.

The modified Marchesiello et al. (2001) boundary conditions showed fairly good results all over the model domain. For example, the Iberian Current was well represented in all the models, and was not sensitive to the presence of the sponge or to the variation of the inflow time scales. The only discernible exception was in the southern region of the western boundary of the model.

The change in mean sea level over the evaluation region (in pink in Figure 4.5) was shown to be sensitive to changes in the inflow time scales for the velocities (Figure 4.7a). All the test model experiments adjusted to the new position of the volume constraint calculation in the first three days. Test models with lower inflow time scales for the velocities adjust faster and show the best results initially. In time, however, they

showed the worst results and diverged from the reference model. In contrast while the test models with the higher time scales maintained a constant difference to the reference model (except in the adjustment period).

The surface kinetic energy (Figure 4.7b), was shown to be the least sensitive of the statistical variables to the variation in the inflow time scales and to the sponge layer. The closest results were obtained by the no sponge test (Experiment 5) and with the test models with the lower inflow time scales (Experiments 2 and 3).

The total kinetic energy (Figure 4.7c) showed that the tests with the no sponge (Experiment 5) and with the lower inflow time scales for both tracers and velocities (experiment 3) overshoot and diverged from the reference model results. At day 9 the results of the no sponge diverged from the reference results. At day 30 the test model with no sponge shows a difference of 10 % relatively to the reference model. A comparison of Figures 4.7b and 4.7c showed that the kinetic energy was mainly gained at depth, since at the surface the test model showed good agreement with the reference model. This is because the main differences between the sponge viscosity values and the Smagorinsky (1965) viscosity values are higher where the horizontal shear is the least (usually at depth). Besides absorbing disturbances and suppressing computational noise the sponge layer was shown to have the effect of helping to conserve the kinetic energy of the model.

Based on this results, the inflow time scales for model runs were subsequently chosen to be 3 days for the velocities and 1 day for the tracers with a sponge layer. This combination was shown to maintain the mean sea level (after the initial adjustment) and conserve the kinetic energy.

Analysis of the monthly seasonal evolution of the surface currents showed that the currents were generally well correlated with the wind stress. In the spring and fall seasons the Iberian Current was detected. Mesoscale features were also well reproduced, the length and location of the filaments in the summer (upwelling) season were consistent with observations. The upwelling intensity was also weaker in the spring than in summer. The extent of the upwelled waters agree with observations. At depth, some Meddies were

generated off Cabo da Roca and the undercurrent was kept near the slope. As a result, it is shown that the model is able to reproduce the basic characteristics of the NCCS.

I. REFERENCES

Ambar, I., N. Serra, M.J. Nogueira, G. Cabecadas, F. Abrantes, P. Freitas, C. Goncalves and N. Gonzalez, Physical Chemical and Sedimentological Aspects of the Mediterranean Outflow off Iberia, *Deep Sea Research*, 49, 4163-4177, 2002.

Baringer, M. O. and J. F. Price, Mixing and Spreading of the Mediterranean Outflow, *Deep Sea Research*, 26, 555-568, 1997.

Barnier, B., L. Siefridt and P. Marchesiello, Thermal Forcing for a Global Ocean Model using a Three-year Climatology of ECMWF analyses, *Journal of Marine Systems*, 6, 363-380, 1995.

Bennett, A., Inverse Methods in Physical Oceanography. Cambridge University Press, Cambridge, 346pp, 1992.

Ezer, T., G. L. Mellor, Sensitivity Studies with the North Atlantic Sigma Coordinate Princeton Ocean Model, *Dynamics of Atmospheres and Oceans*, 32, 185-208, 2000.

Fiuza, A. F. G., Upwelling Patterns off Portugal, Coastal Upwelling: Its Sediment Record, part A, pp 85-97, Plenum, New York, 1983.

Fiuza, A. F. G., Hidrologia e Dinamica das Aguas Costeiras de Portugal (Hydrology and Dynamics of the Portuguese Coastal Waters), Ph.D. Thesis, 294 pp., Universidade de Lisboa, 1984.

Fiuza, A. F. G., M. E. Macedo and M. R. Guerreiro, Climatological Space and Time Variation of the Portuguese Coastal Upwelling, *Oceanologia Acta*, 5, 31-40, 1982.

Frouin, R., A. F. G. Fiuza, I. Ambar and T. J. Boyd, Observations of a Poleward Surface Current off Coasts of Portugal and Spain During Winter, *Journal of Geophysical Research*, 95, 679-691, 1990.

Hagen, E., C. Zulfick and R. Feistel, Near-Surface Structures in the Cape Ghir Filament off Morocco, *Oceanologica Acta*, 19 (6), 1996.

Jayne, S. R., and R. Tokmakian, Forcing and Sampling of Ocean General Circulation Models: Impact of High Frequency Motions, *Journal of Physical Oceanography*, 27, 1173-1179, 1997.

Johnson, J., I. Ambar, N. Serra and I. Stevens, Comparative Studies of the Spreading of the Mediterranean Water Through the Gulf of Cadiz, *Deep Sea Research*, 49, 4179-4193, 2002.

Large, W.G., J. C. Williams, and S. C. Doney, Oceanic Vertical Mixing: a Review and a Model with Nonlocal Boundary Layer parametrization, *Reviews of Geophysics*, 32, 363-403, 1994.

Levitus, S., and T.P. Boyer, World Ocean Atlas 1994, vol. 4: Temperature, NOAA Atlas NESDIS 4, US Government Printing Office, Washington, DC, 117 pp., 1994.

Levitus, S., R. Burgett and T.P. Boyer, World Ocean Atlas 1994, vol. 3: Salinity, NOAA Atlas NESDIS 3, US Government Printing Office, Washington, DC, 99 pp., 1994.

Marchesiello, P., J.C. McWilliams and A. Shchepetkin, Open Boundary Conditions for Long-term Integration of Regional Oceanic Models, *Ocean Modelling*, 3, 1-20, 2001.

McClean, Julie L., Pierre-Marie Poulain and Jimmy W. Pelton, Eulerian and Lagrangian Statistics from Surface Drifters and High-Resolution POP Simulation in the North Atlantic, *Journal of Physical Oceanography*, 2472-2491, 2002.

Oliger, J., Sundstrom, A., Theoretical and practical aspects of some initial boundary value problems in fluid dynamics. *SIAM Journal of Applied Mathematics* 35, 419-446, 1978.

Orlanski, I., A Simple Boundary Condition for Unbounded Hyperbolic Flows, *Journal of Computational Physics*, 21, 251-269, 1976.

Palma, E. D. and R. P. Matano, On the Implementation of Passive Open Boundary Conditions for a general Circulation Model: The Barotropic Mode, *Journal of Geophysical Research*, vol. 103 (C1), 1319-1341, 1998.

Palma, E. D. and R. P. Matano, On the Implementation of Passive Open Boundary Conditions for a general Circulation Model: The Three Dimensional Case, *Journal of Geophysical Research*, vol. 105 (C4), 8605-8627, 2000.

Pingree, R. D., The Eastern Subtropical Gyre (North Atlantic): Flow Rings Recirculation Structure and Subduction, *Journal of the Marine Biological Association of the United Kingdom*, 77, 573-624, 1997.

Roed, L. P. and C. Cooper, Open Boundary Conditions in Numerical Ocean Models, In: O'Brien, J.J. (Ed.), *Advanced Physical Oceanographic Numerical Modeling*, NATO ASI Series C, vol. 186, pp 411-436, 1986.

Shchepetkin, A. and J. C. McWilliams, Regional Ocean Model System: a Split-Explicit Ocean Model with a Free-surface and Topography-following vertical coordinate, 2000.

Smith, R.D., M.E. Maltrud, F.O. Bryan and R.W. Hecht, Numerical Simulation of the North Atlantic Ocean at 1/10-degree, *Journal of Physical oceanography*, 30, 1532-1561, 2000.

Sommerfeld, A., Partial Differential Equations, Lecture Notes on Theoretical Physics, Vol. 6, Academic Press, San Diego, California, 1949.

Sousa, F. M., Determinacao da Temperatura da Superficie do Mar com Satelites, Uma Aplicacao ao Oceano Costeiro de Portugal (Evaluation of Sea Surface Temperature with Satellites, An Application to the Portuguese Coastal Ocean), M. Sc. Thesis, 127 pp., Universidade de Lisboa, Lisbon, 1986.

Sousa, F. and A. Bricaud, Satellite-Derived Phytoplankton Pigment Structures in the Portuguese Upwelling Area, *Journal of Geophysical Research*, 97, 11343-11356, 1992.

Wooster, W. S., A. Bakun and D. R. McLain, The Seasonal Upwelling Cycle Along the Eastern Boundary of the North Atlantic, *Journal of Marine Research*, 34, 131-141, 1976.

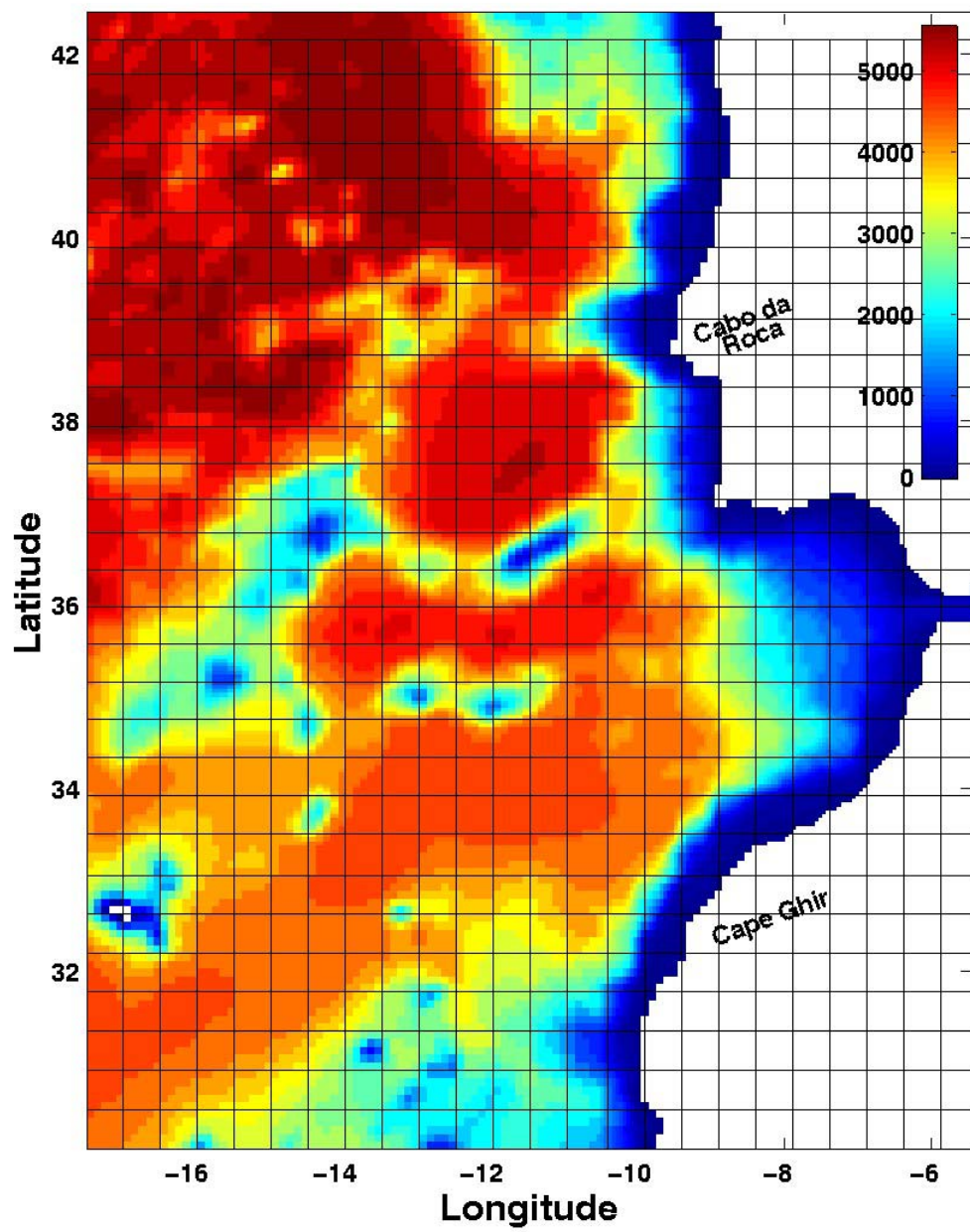


Figure 4.1a. Bottom topography in color, depths in meters. Every fifth grid line for the POP model is represented.

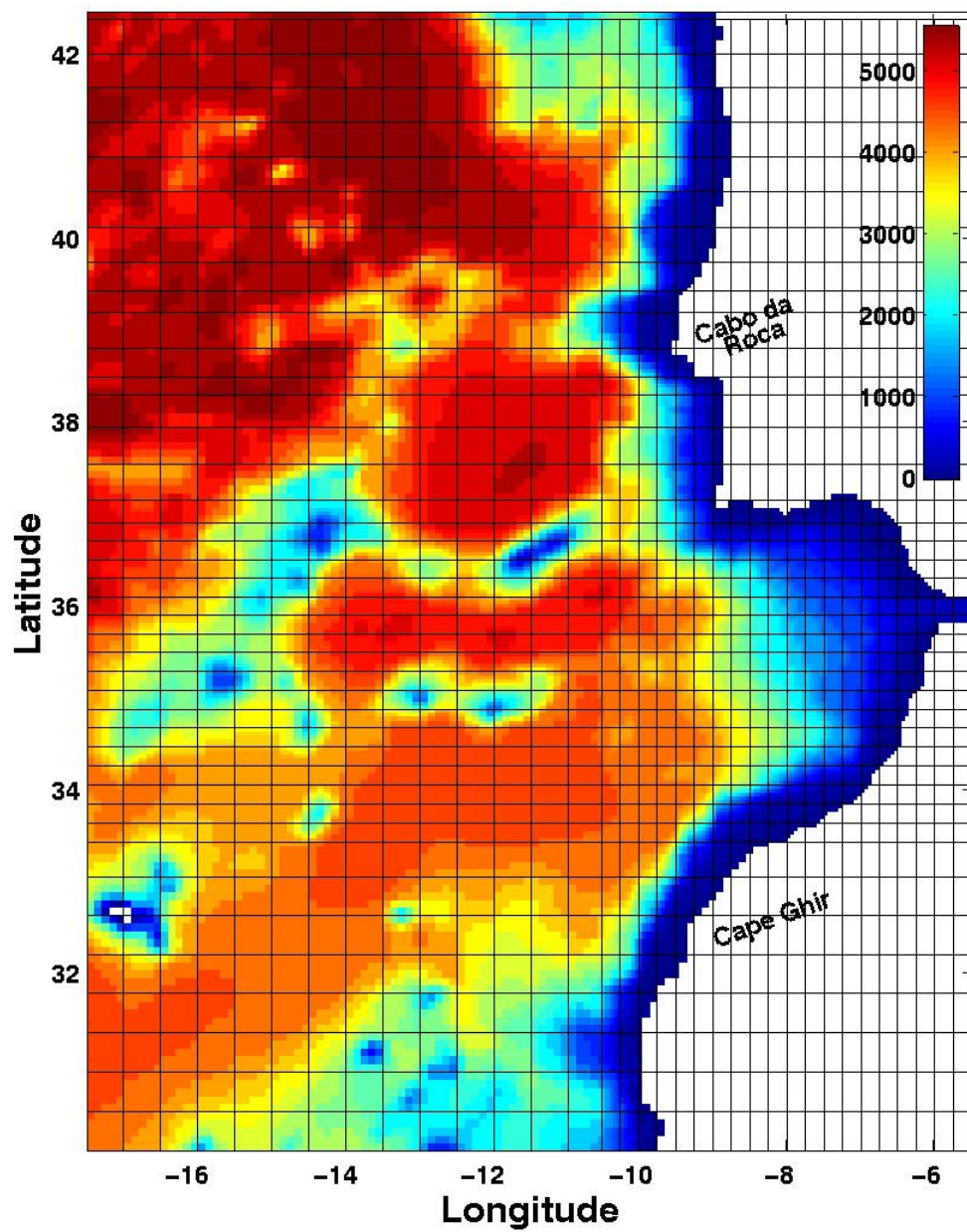


Figure 4.1b. Bottom topography in color, depths in meters. Every fifth grid line for the POM model is represented.

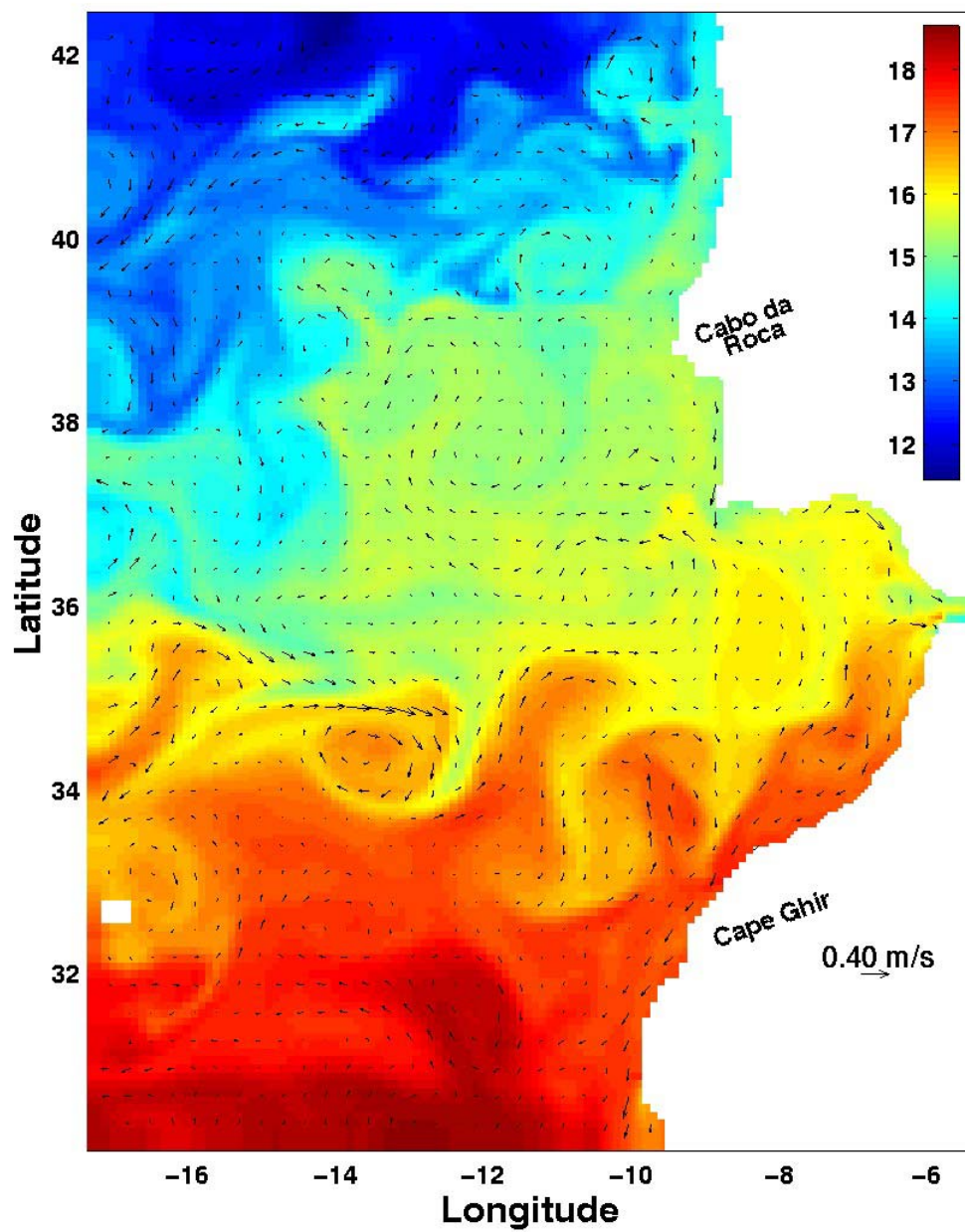


Figure 4.2a. Initial surface temperature ($^{\circ}\text{C}$) fields interpolated for the NCCS POM model. Initial surface velocity (m/s) (arrows).

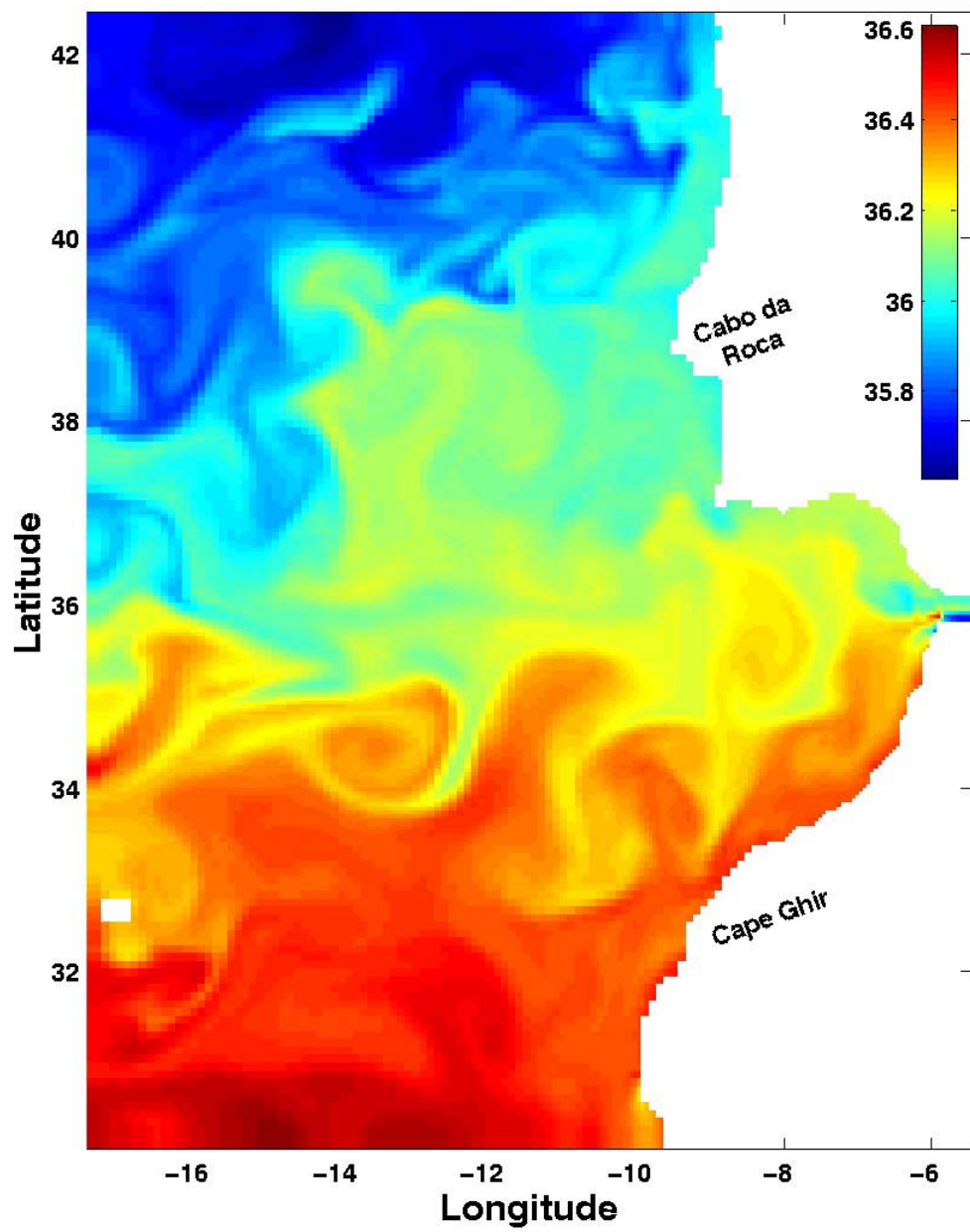


Figure 4.2b. Initial salinity field interpolated to the NCCS POM.

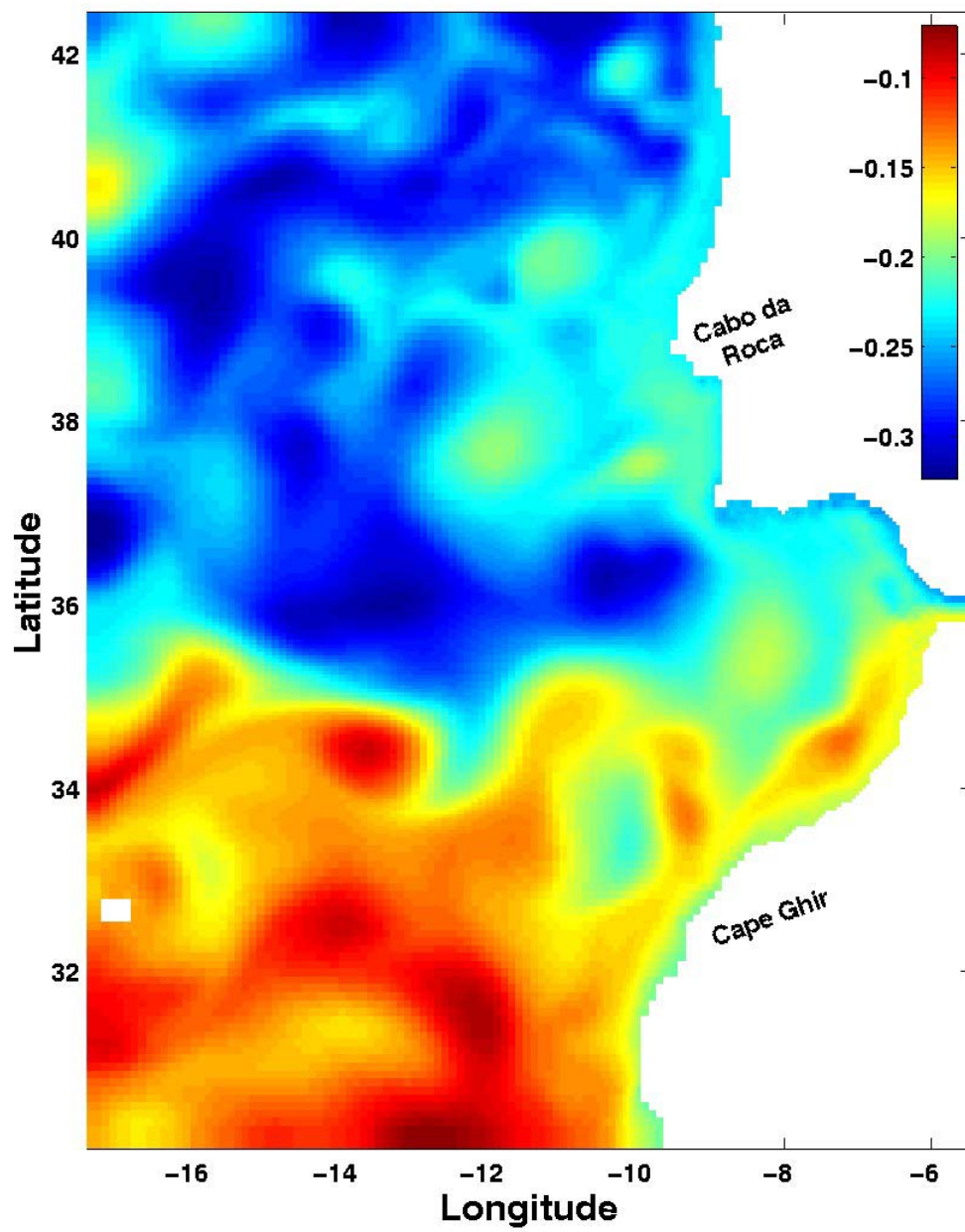


Figure 4.2c. InitialElevation (m) field interpolated to the NCCS POM.

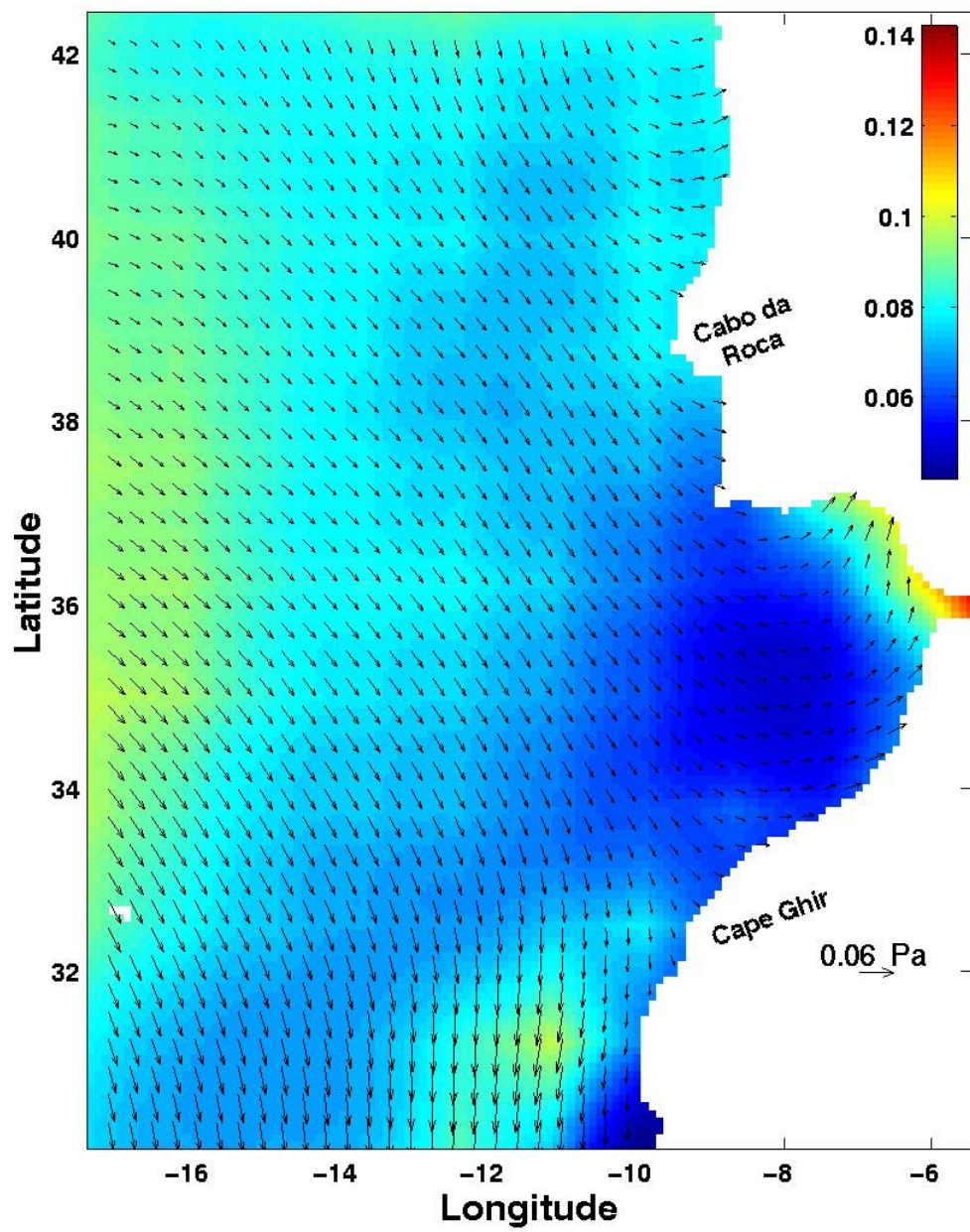


Figure 4.3a Mean wind stress (Pa) from March to May (arrows). Standard deviation of the magnitude of the wind stress from March to May (in color).

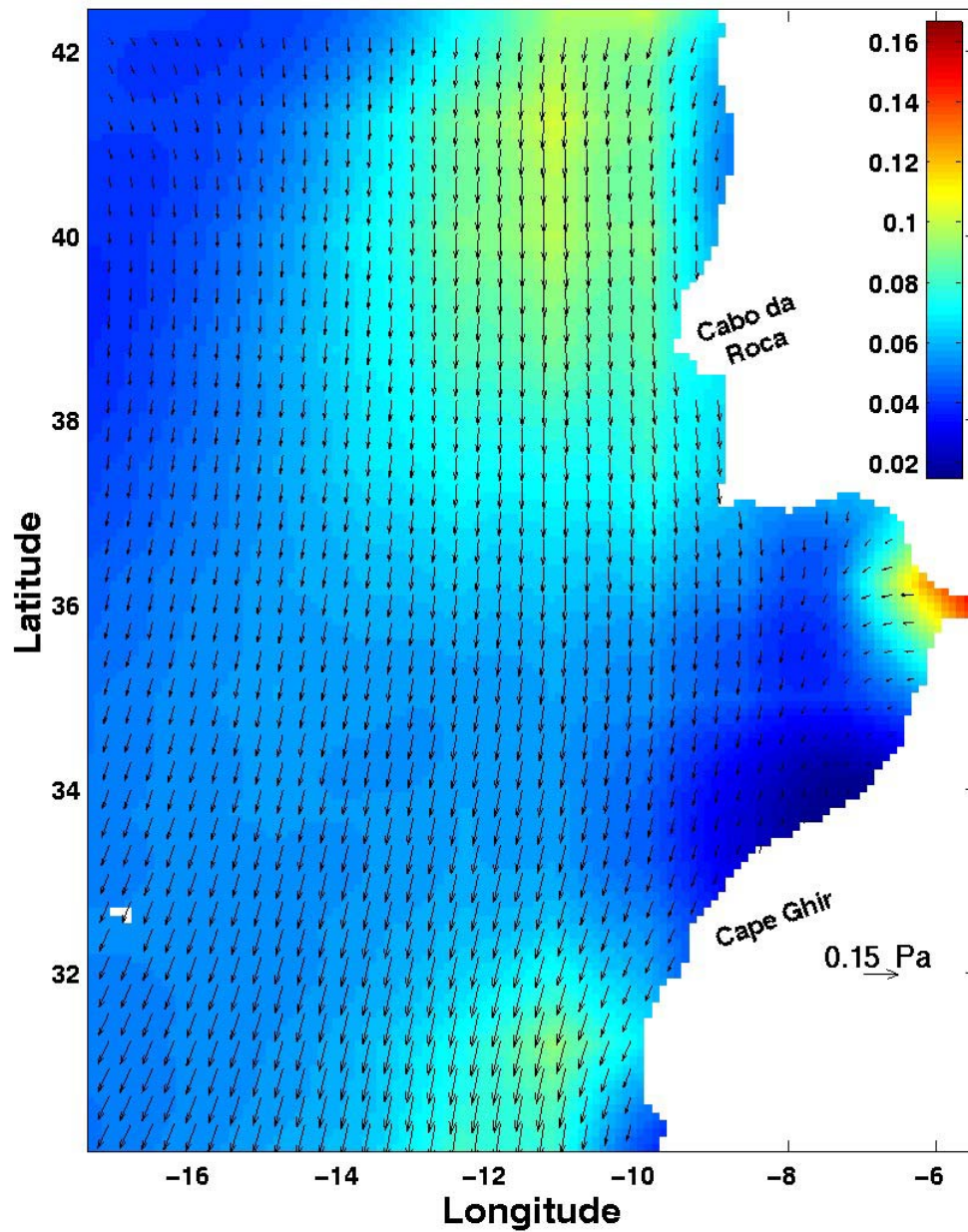


Figure 4.3b Mean wind Stress (Pa) from June to August (arrows). Standard deviation of the Magnitude of the Wind Stress from June to August (in color).

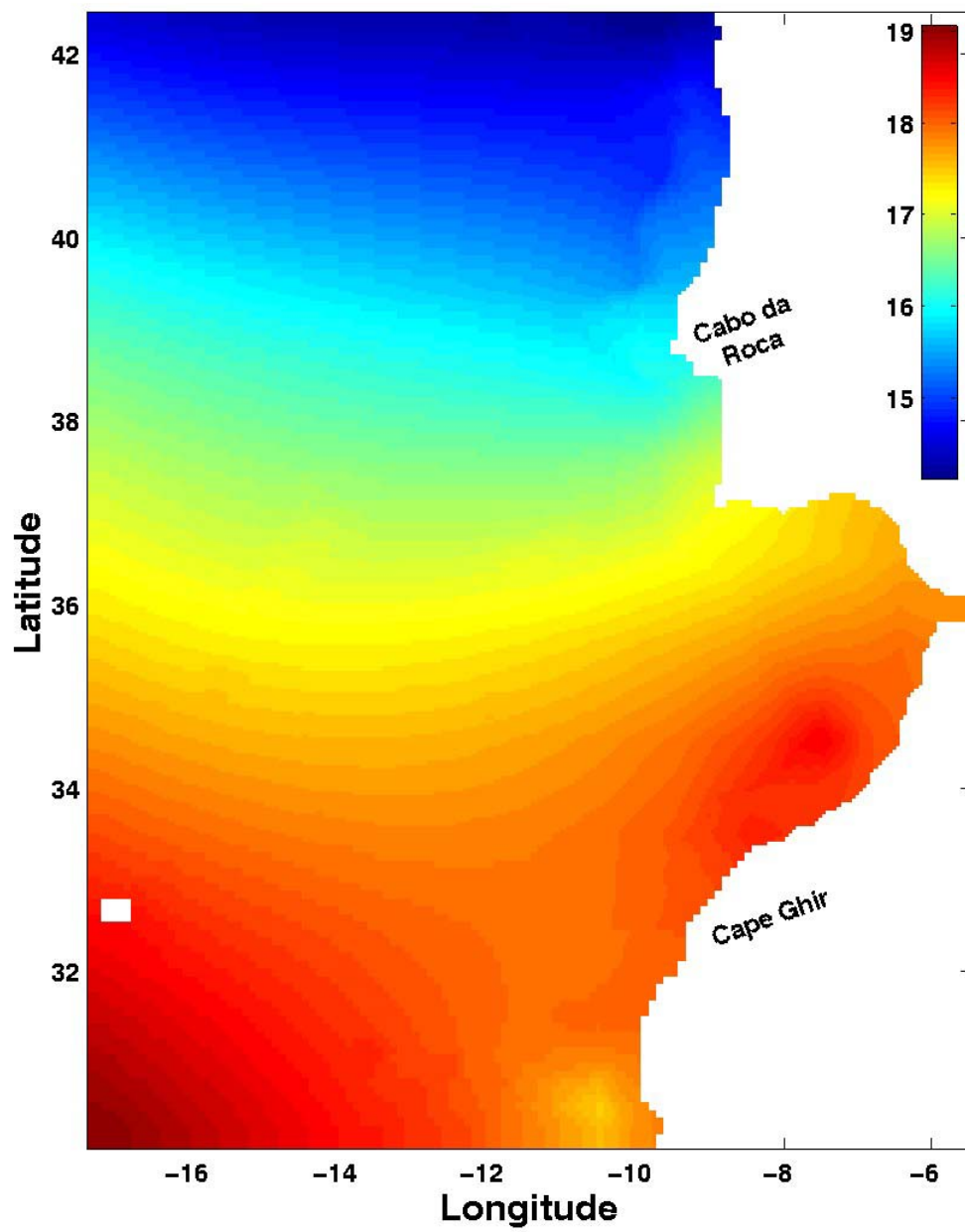


Figure 4.4a Monthly surface temperature (°C) from Levitus 94 on March.

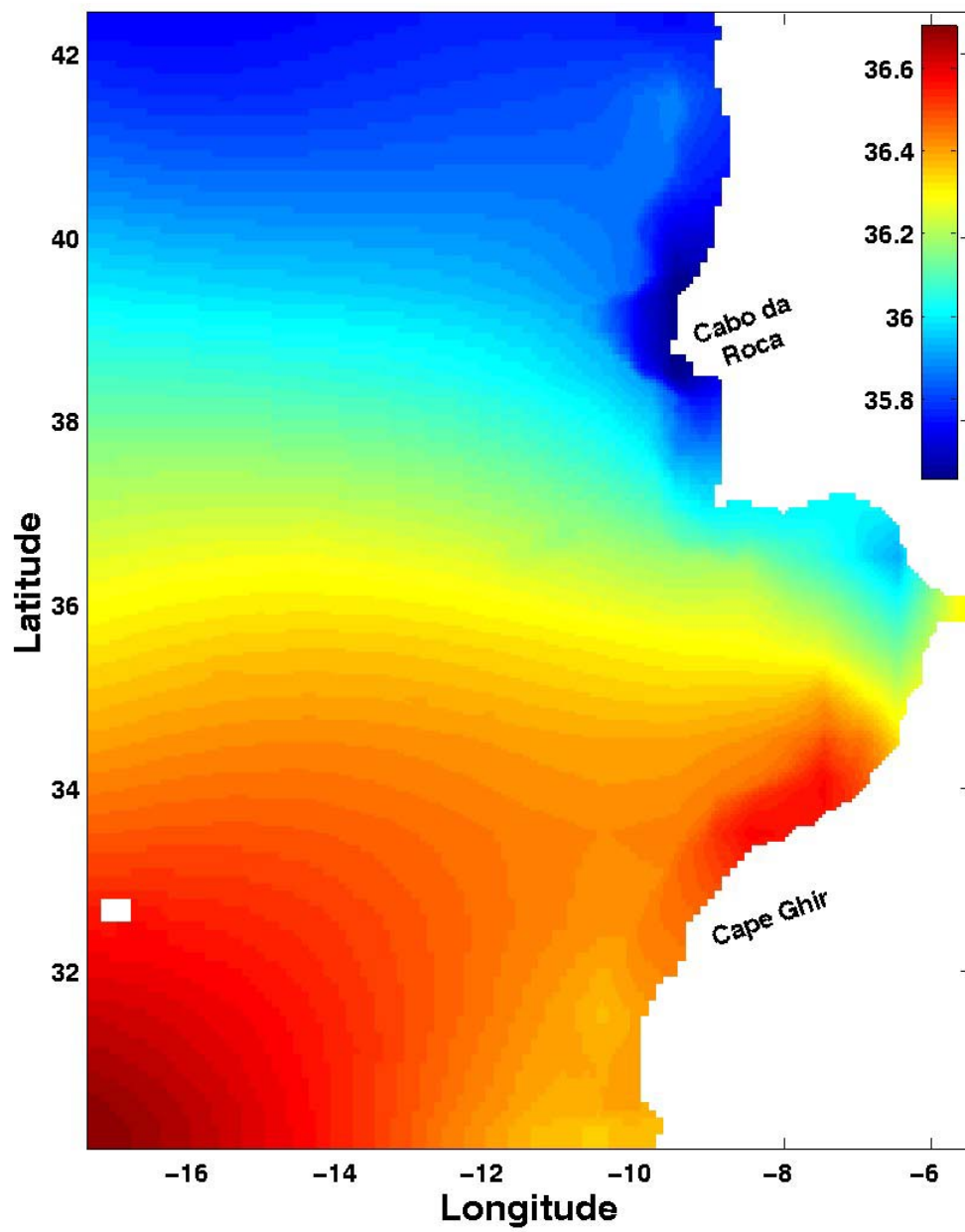


Figure 4.4b Monthly surface salinity from Levitus 94 on March.

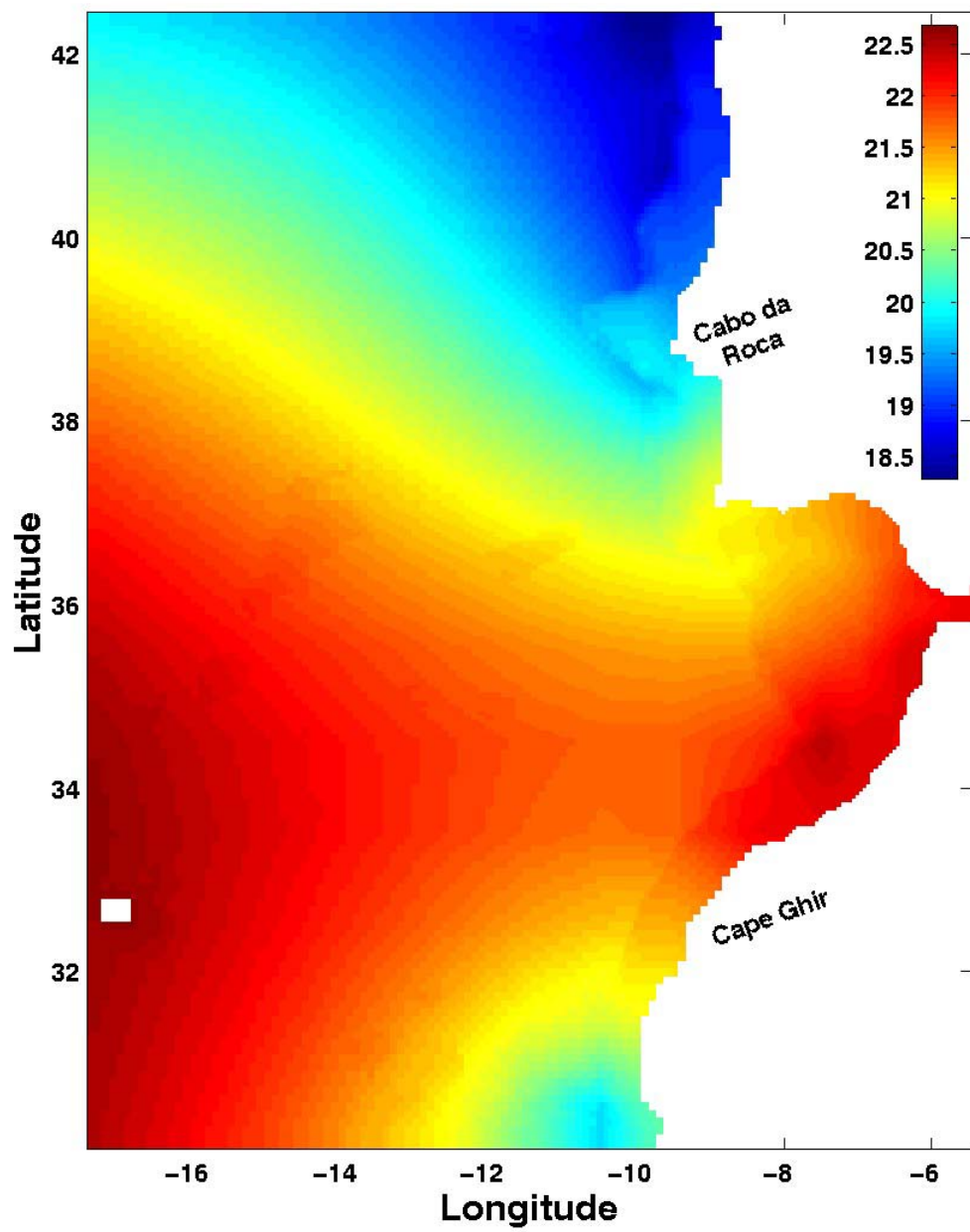


Figure 4.4c Monthly surface temperature (°C) from Levitus 94 on August.

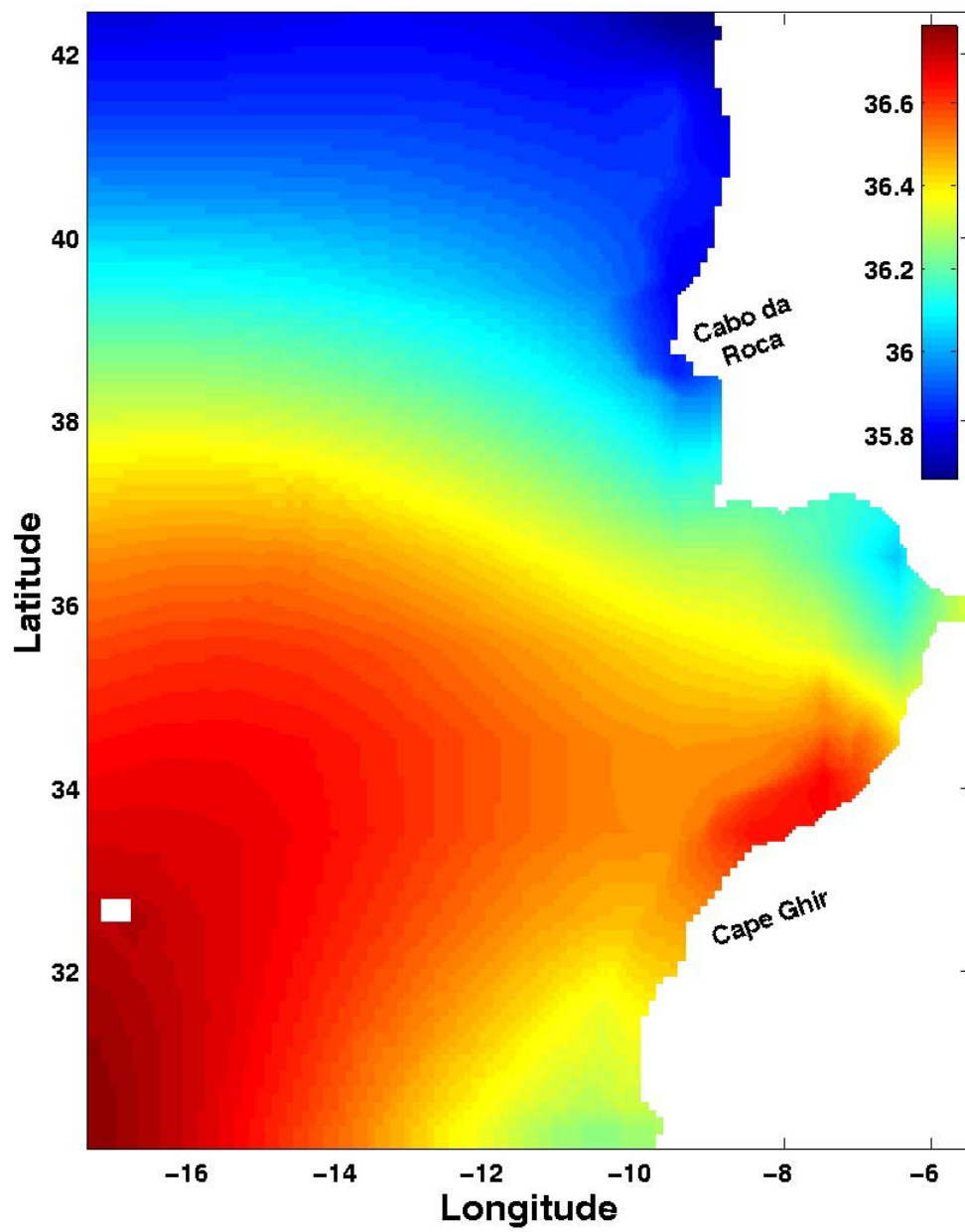


Figure 4.4d Monthly surface salinity from Levitus 94 on August.

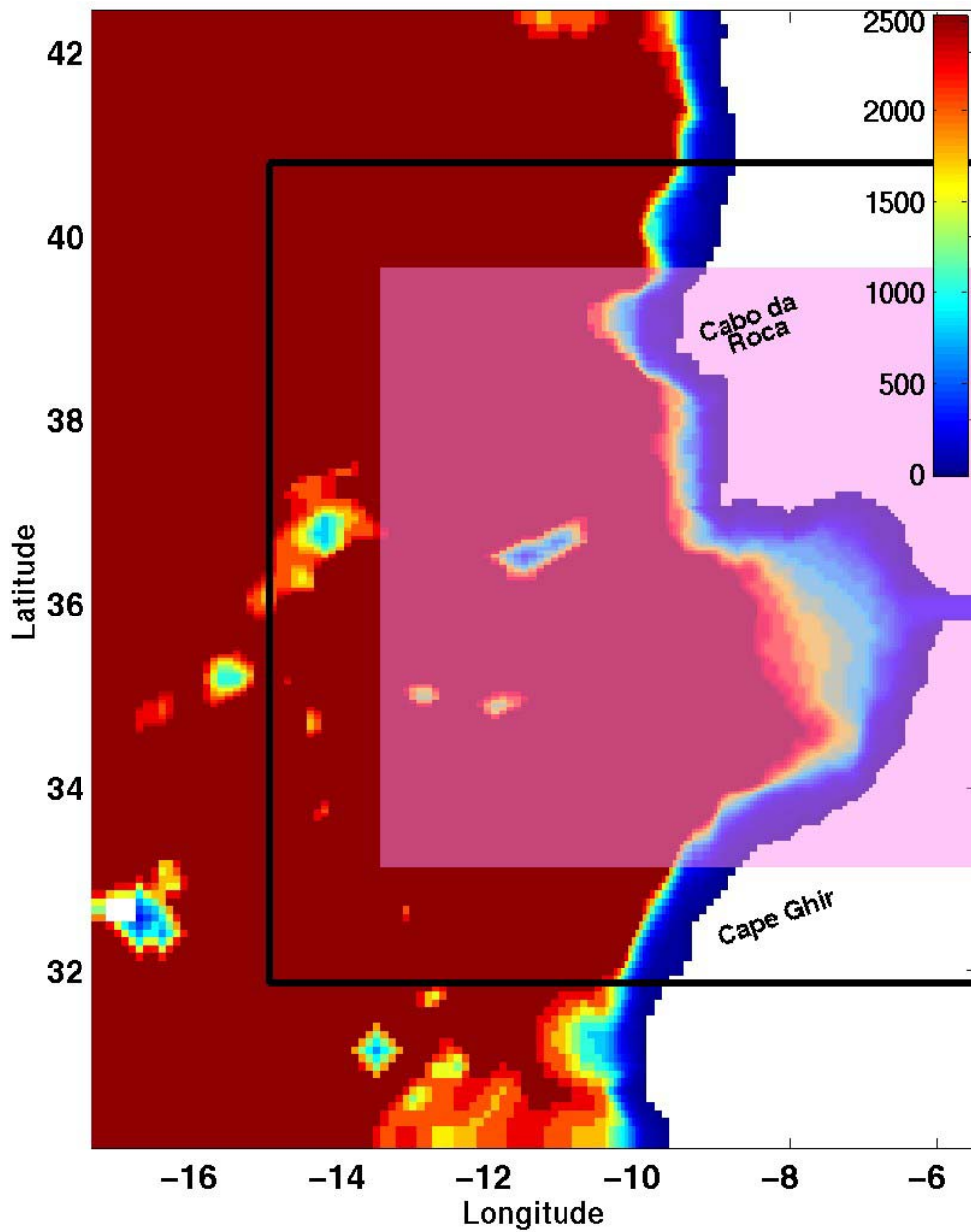


Figure 4.5 Model topography, depths in meters. The largest area (Region A) is the reference model area. The black box (Region B), represents the test model area and is used to study the boundary conditions. The pink area (Region C) is where the results are shown and where the analysis is made. Note that, Region C is outside the sponge layer of both Region A and Region B.

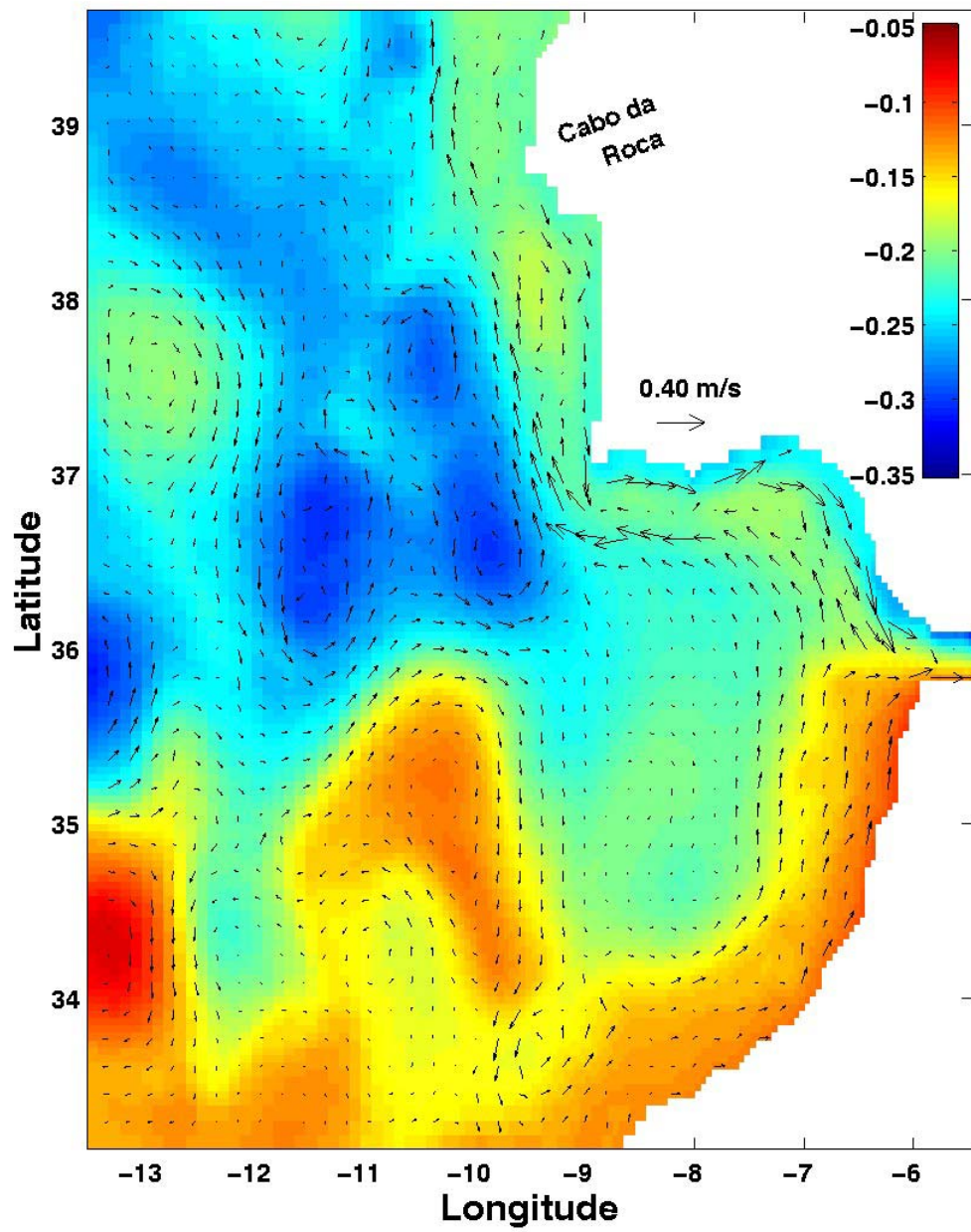


Figure 4.6a. Elevation (m) (in color) and barotropic velocity (m/s) (arrows) at day 30 for the reference model.

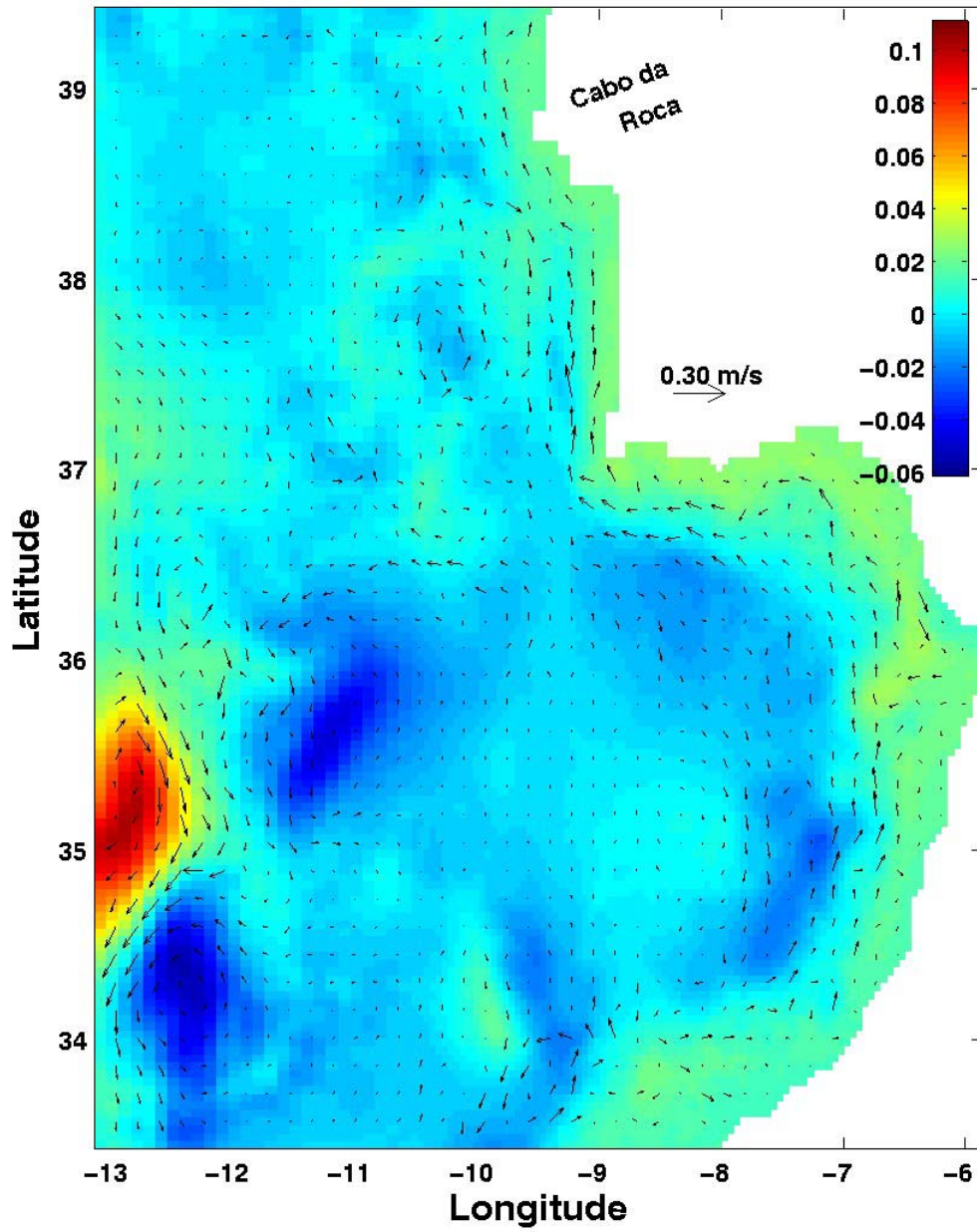


Figure 4.6b. Difference in Elevation (m) (in color) and in the barotropic velocity (m/s) (arrows) at day 30 between the boundary condition study with the inflow nudging time scale for velocities (tracers) equal to 3 (1) days (Experiment 1 in Table 4.4) and the reference model.

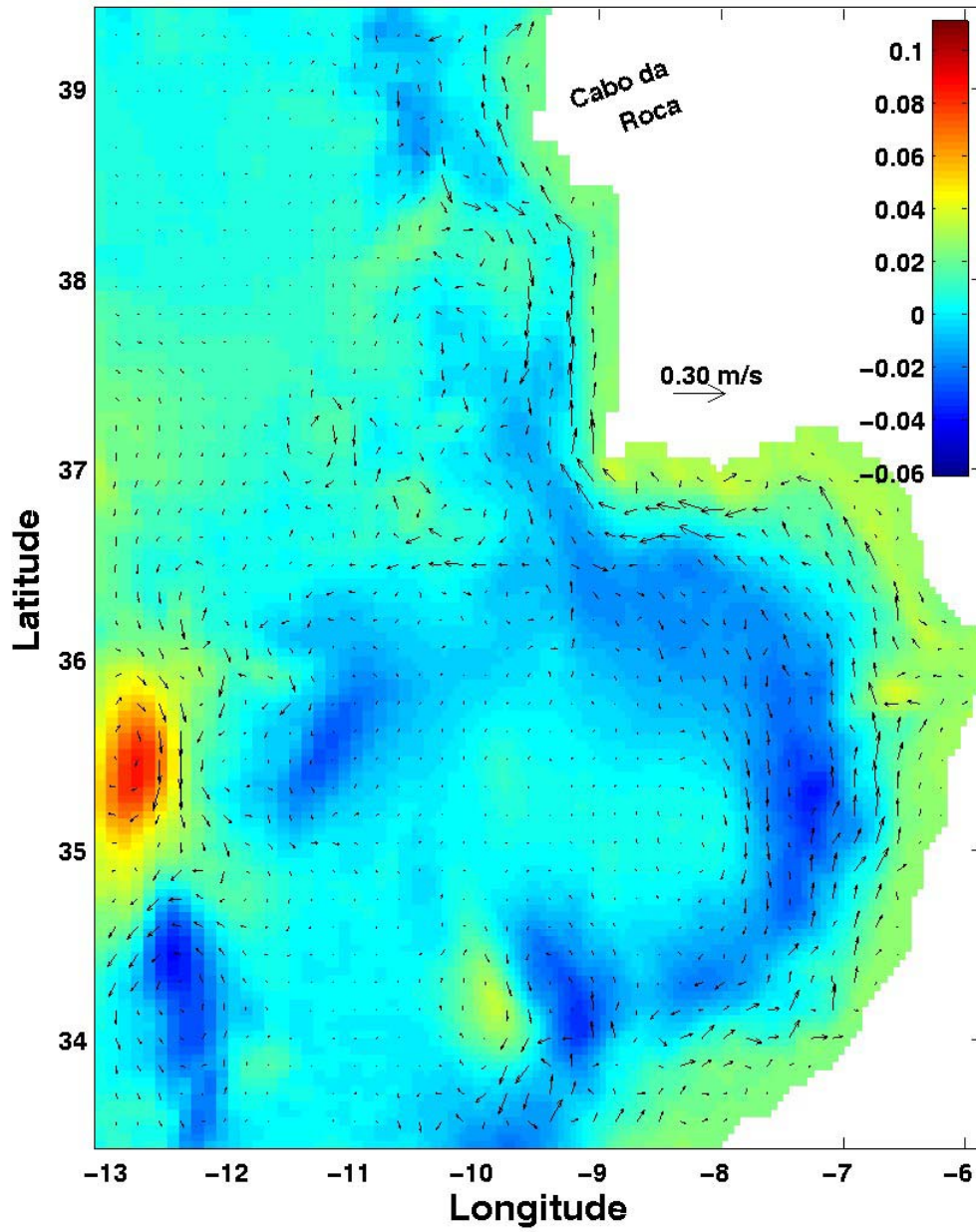


Figure 4.6c. Difference in Elevation (m) (in color) and in the barotropic velocity (m/s) (arrows) at day 30 between the boundary condition study with the inflow nudging time scale for velocities (tracers) equal to 1 (0.5) days (Experiment 2 in Table 4.4) and the reference model.

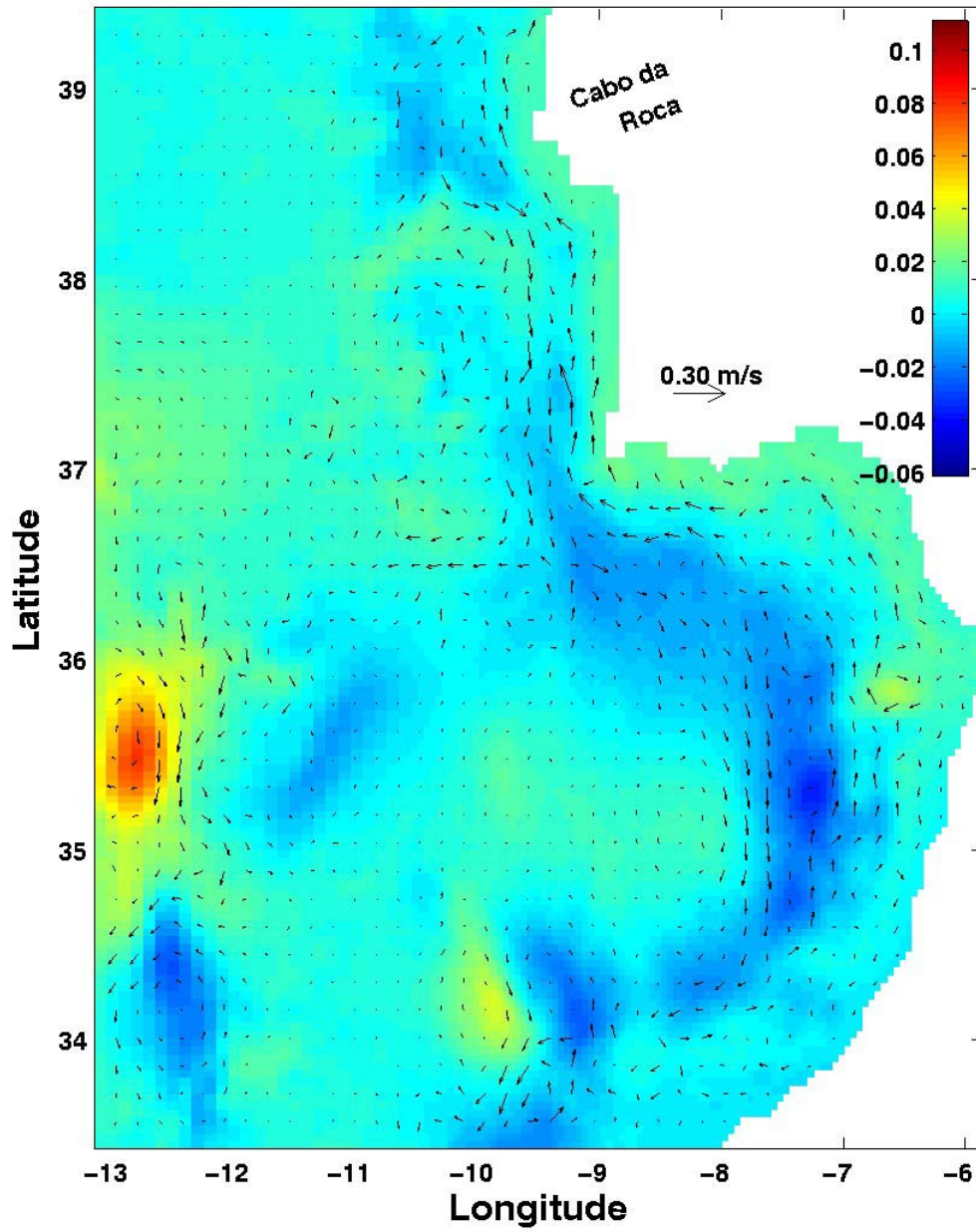


Figure 4.6d. Difference in Elevation (m) (in color) and in the barotropic velocity (m/s) (arrows) at day 30 between the boundary condition study with the inflow nudging time scale for velocities (tracers) equal to 0.5 (0.5) days (Experiment 3 in Table 4.4) and the reference model.

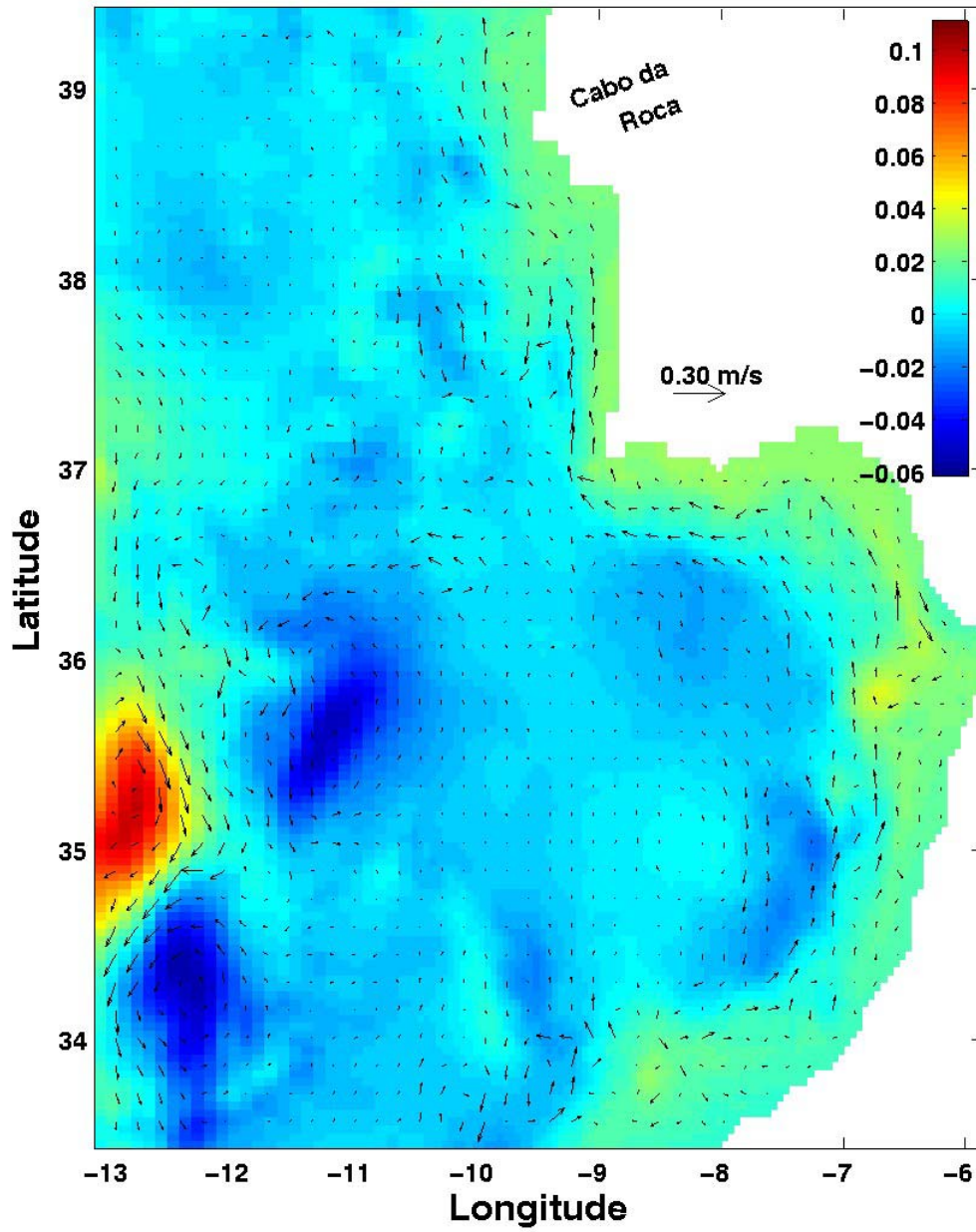


Figure 4.6e. Difference in Elevation (m) (in color) and in the barotropic velocity (m/s) (arrows) at day 30 between the boundary condition study with the inflow nudging time scale for velocities (tracers) equal to 3 (3) days (Experiment 4 in Table 4.4) and the reference model.

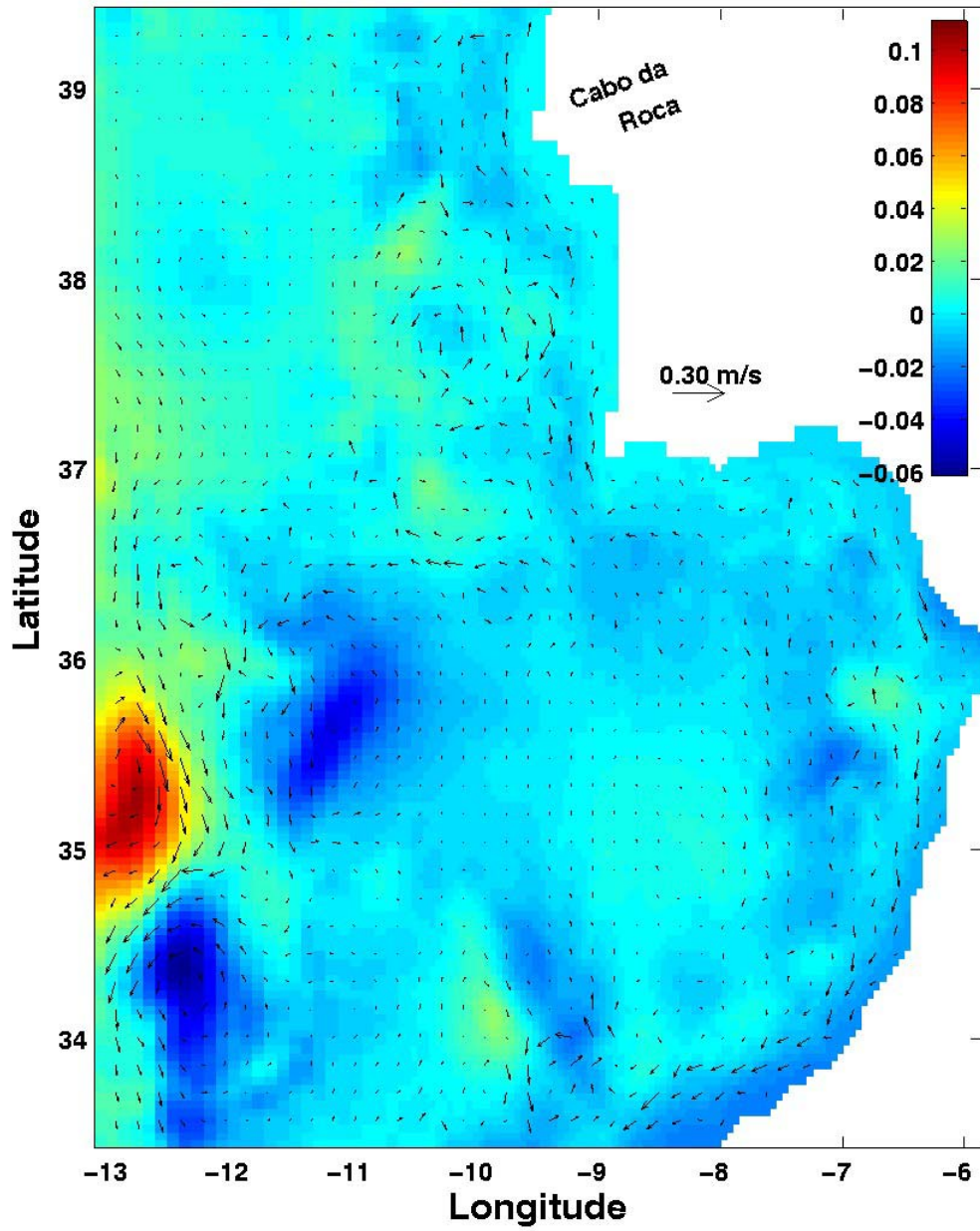


Figure 4.6f. Difference in Elevation (m) (in color) and in the barotropic velocity (m/s) (arrows) at day 30 between the boundary condition study with the inflow nudging time scale for velocities (tracers) equal to 3 (1) days with no active sponge layer (Experiment 5 in Table 4.4) and the reference model.

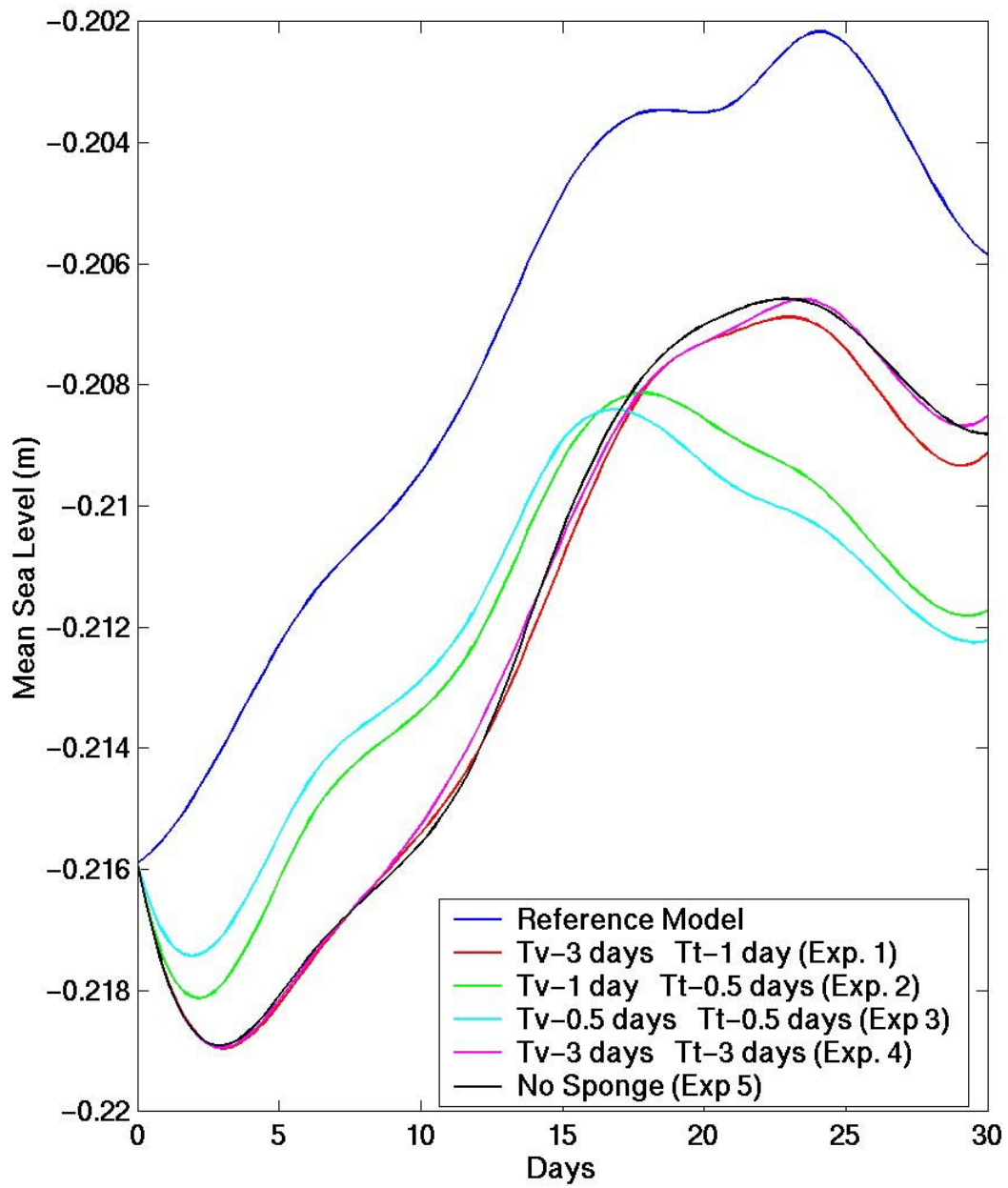


Figure 4.7a. Mean sea level (m) for all the experiments. T_v is the inflow nudging time scale for the velocities and T_t is the inflow nudging time scale for the tracers.

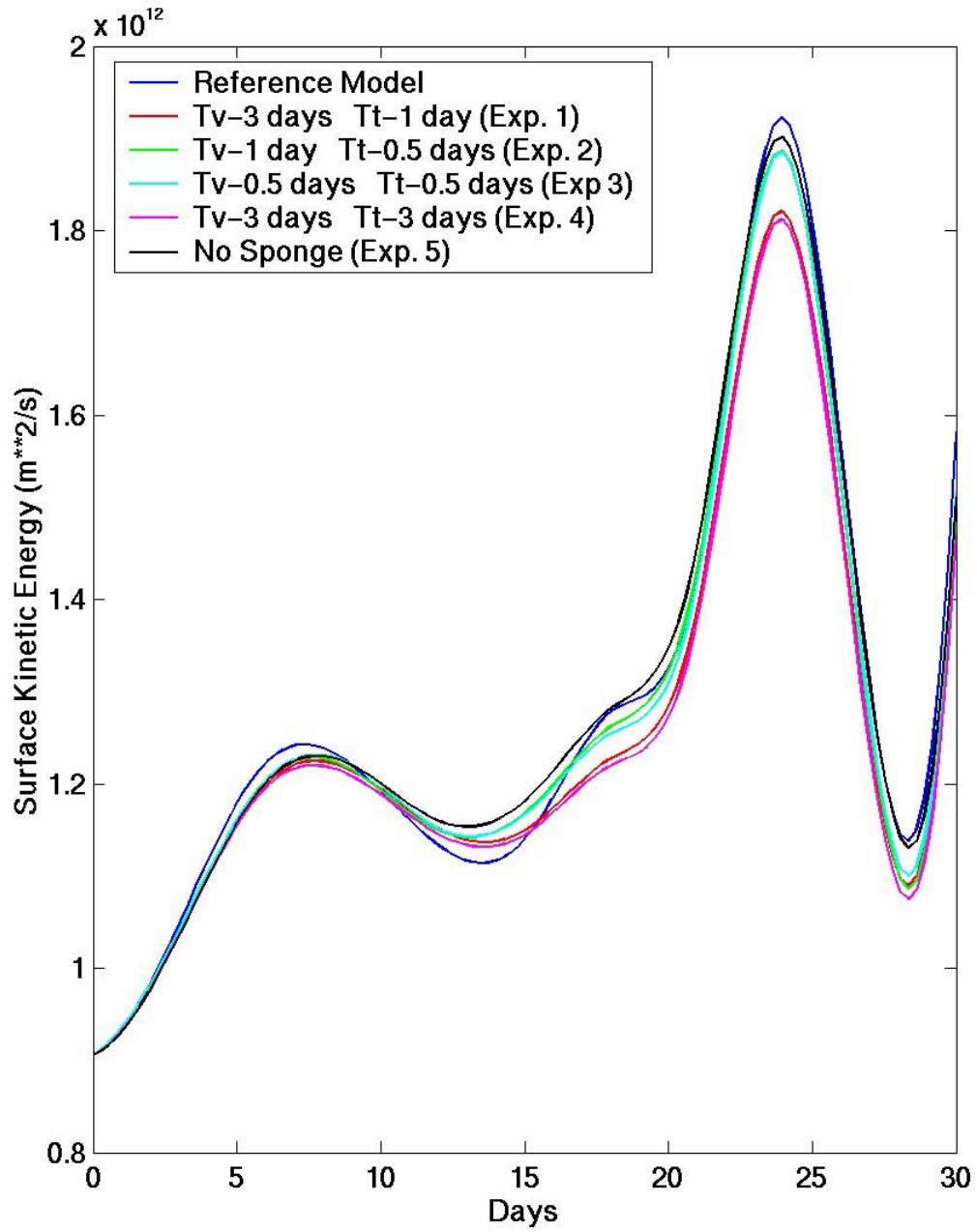


Figure 4.7b. Surface kinetic energy for all the experiments (m^2/s). Tv is the inflow nudging time scale for the velocities and Tt is the inflow nudging time scale for the tracers. Note that Red and magenta lines are almost coincident.

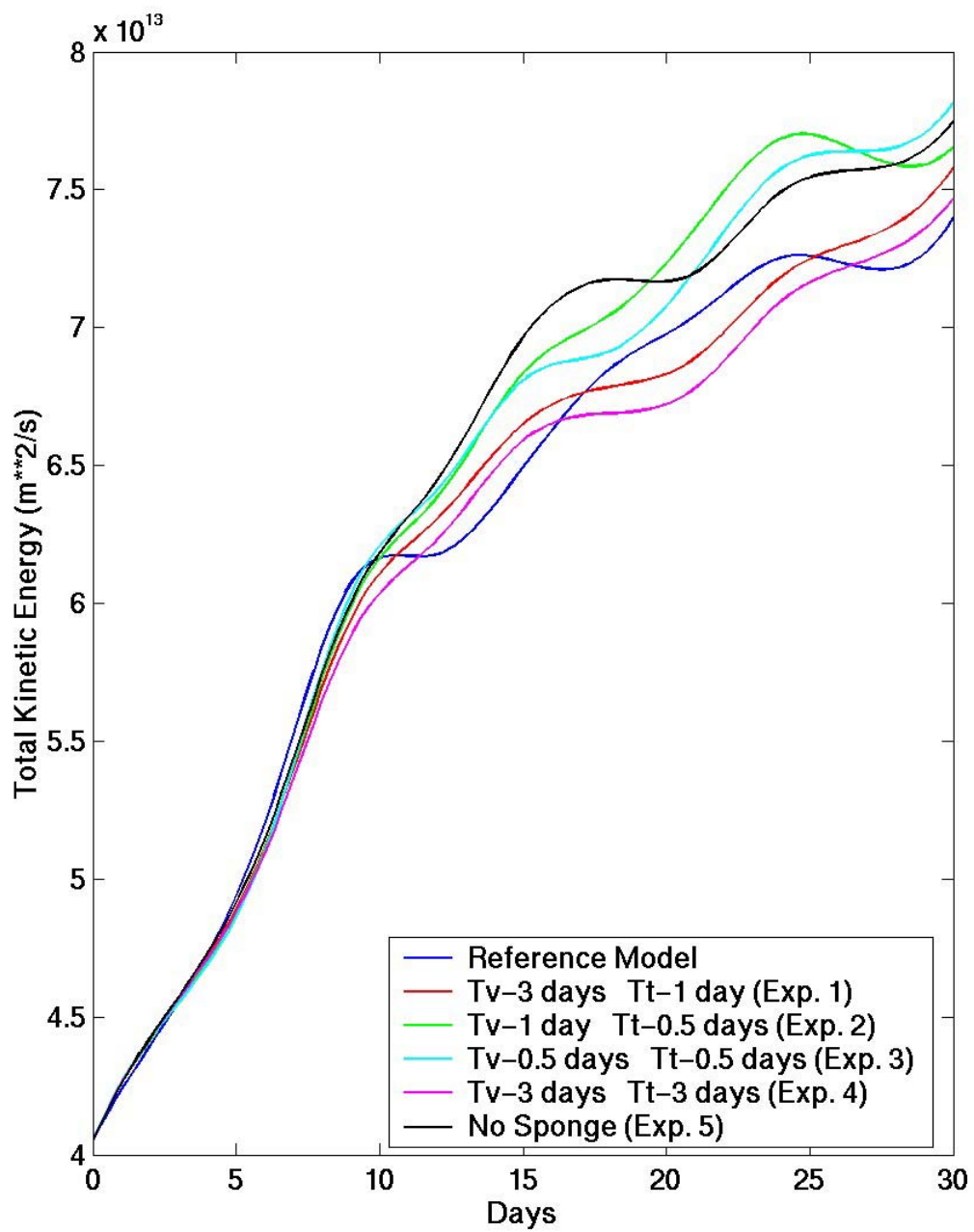


Figure 4.7c. Total kinetic energy (m^2/s) for the 6 experiments. Tv is the inflow nudging time scale for the velocities and Tt is the inflow nudging time scale for the tracers.

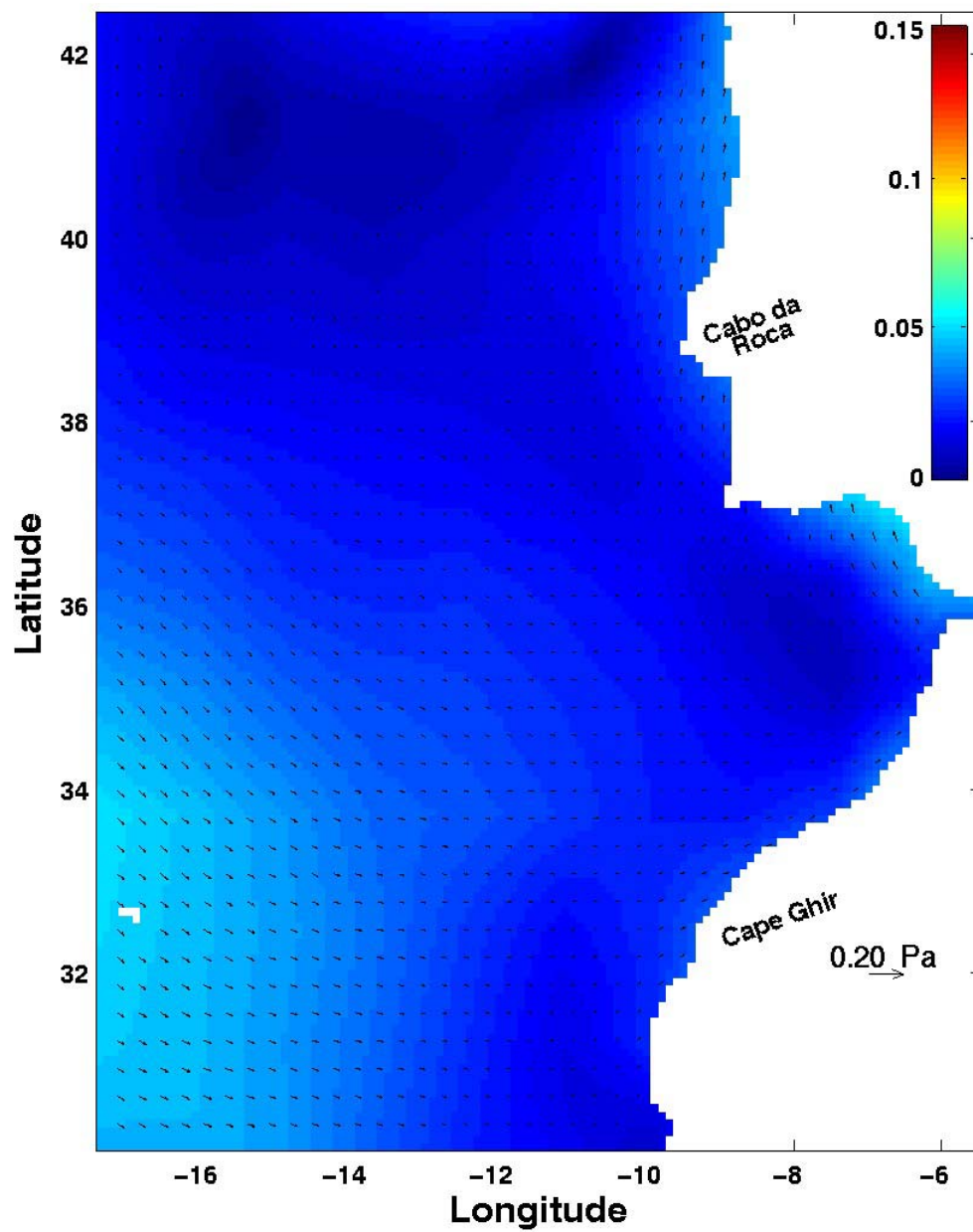


Figure 4.8a. Monthly wind stress vector (Pa) (arrows) and intensity (Pa) (in color) for March 1996.

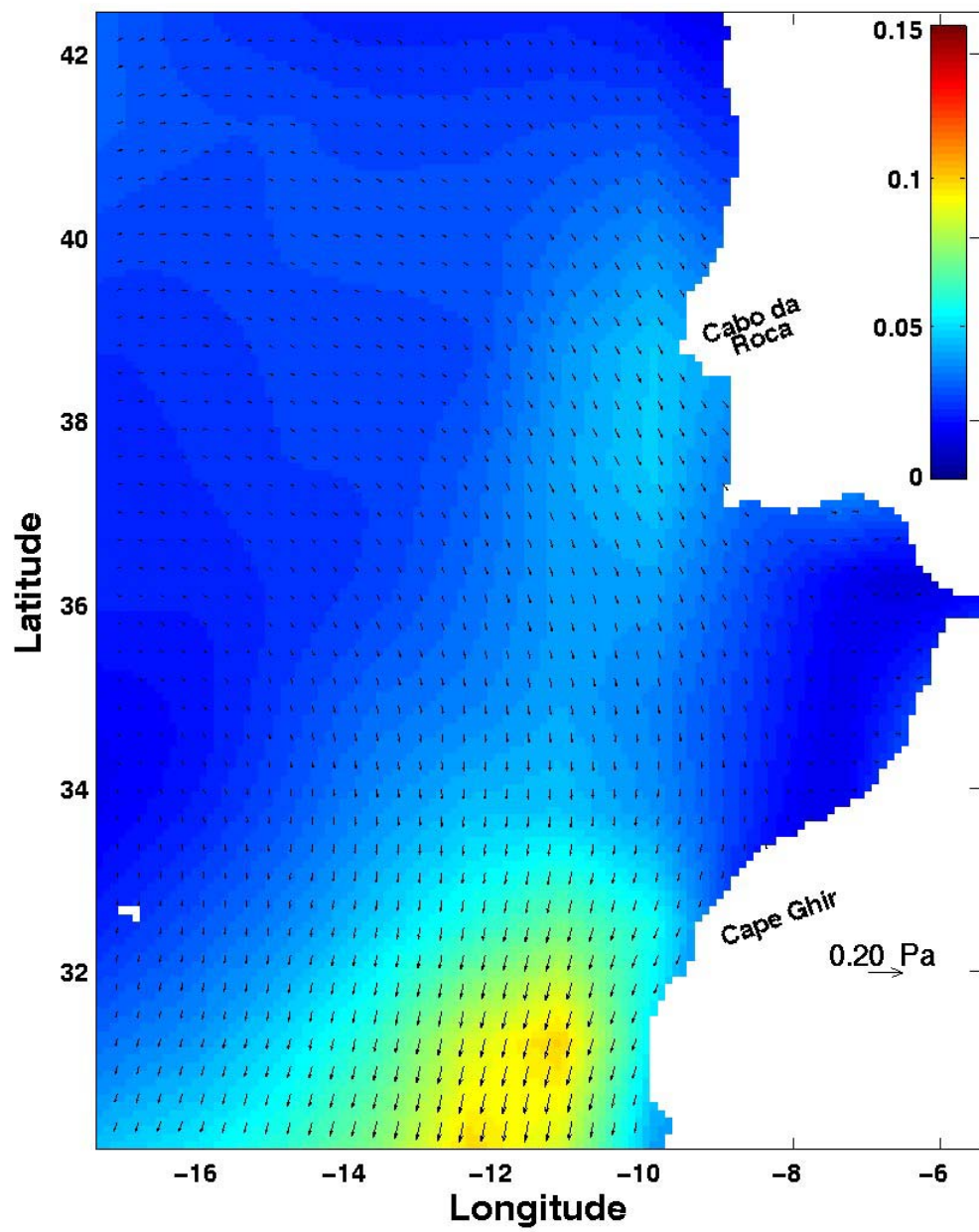


Figure 4.8b. Monthly wind stress vector (Pa) (arrows) and intensity (Pa) (in color) for April 1996.

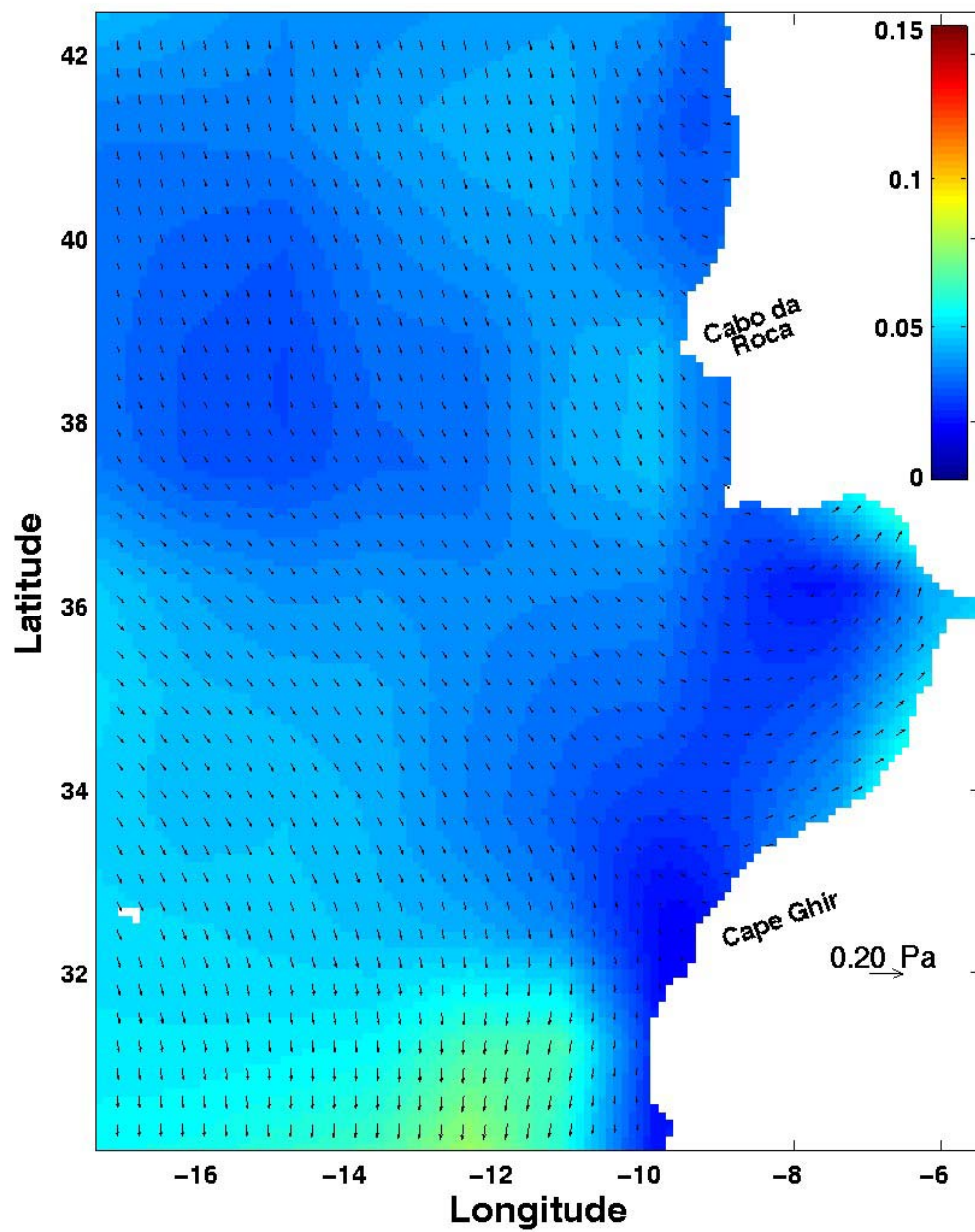


Figure 4.8c. Monthly wind stress vector (Pa) (arrows) and intensity (Pa) (in color) for May 1996.

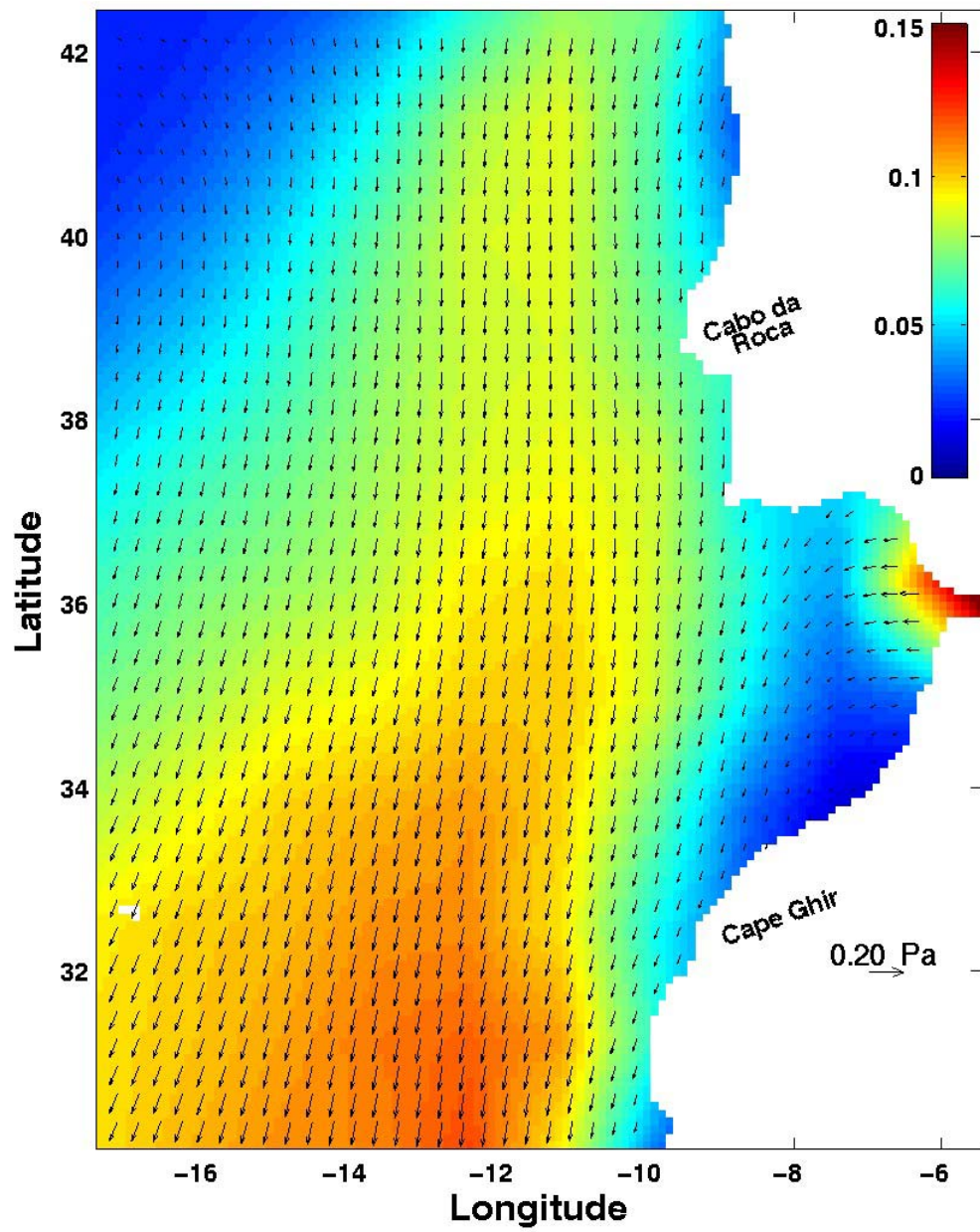


Figure 4.8d. Monthly wind stress vector (Pa) (arrows) and intensity (Pa) (in color) for June 1996.

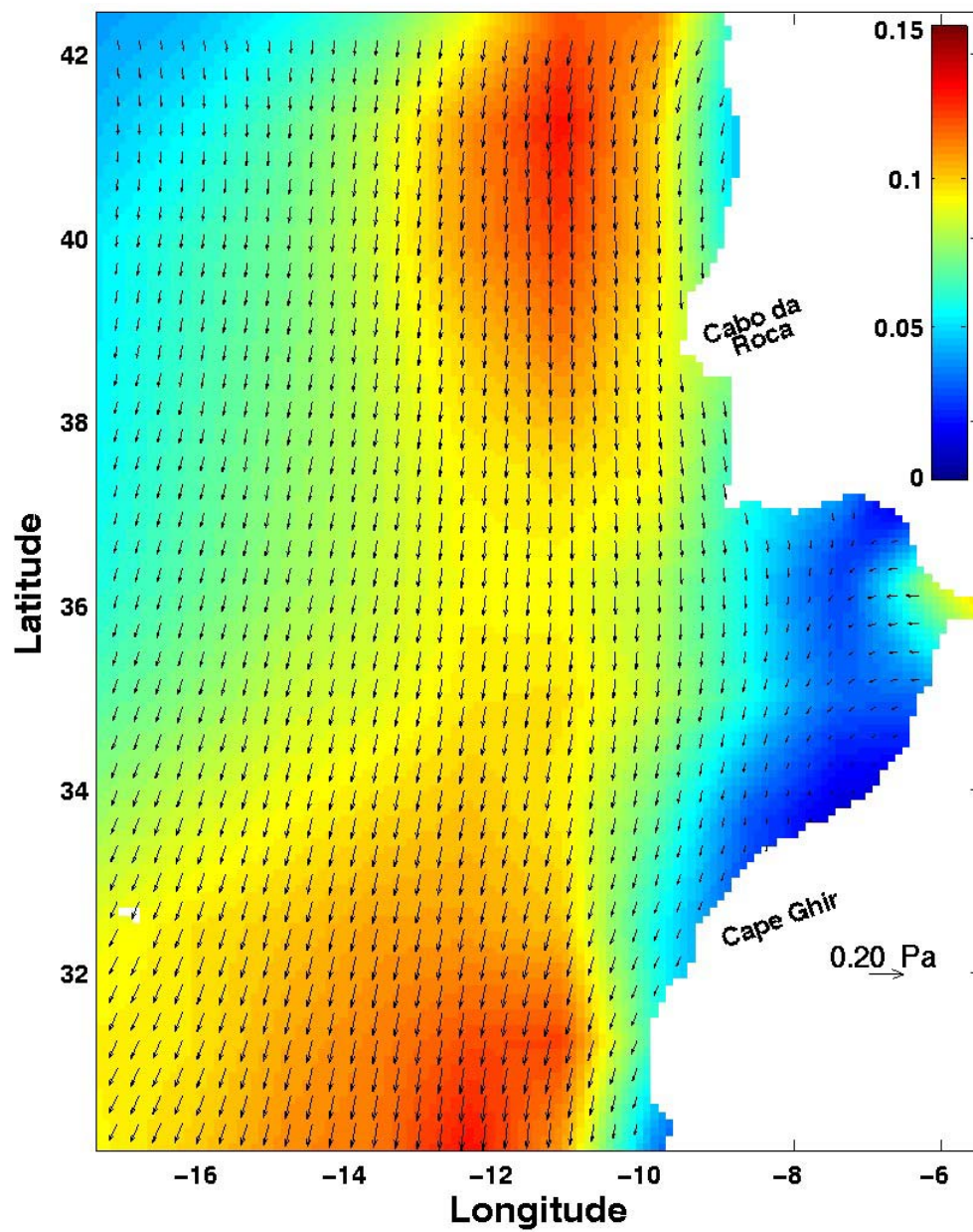


Figure 4.8e. Monthly wind stress vector (Pa) (arrows) and intensity (Pa) (in color) for July 1996.

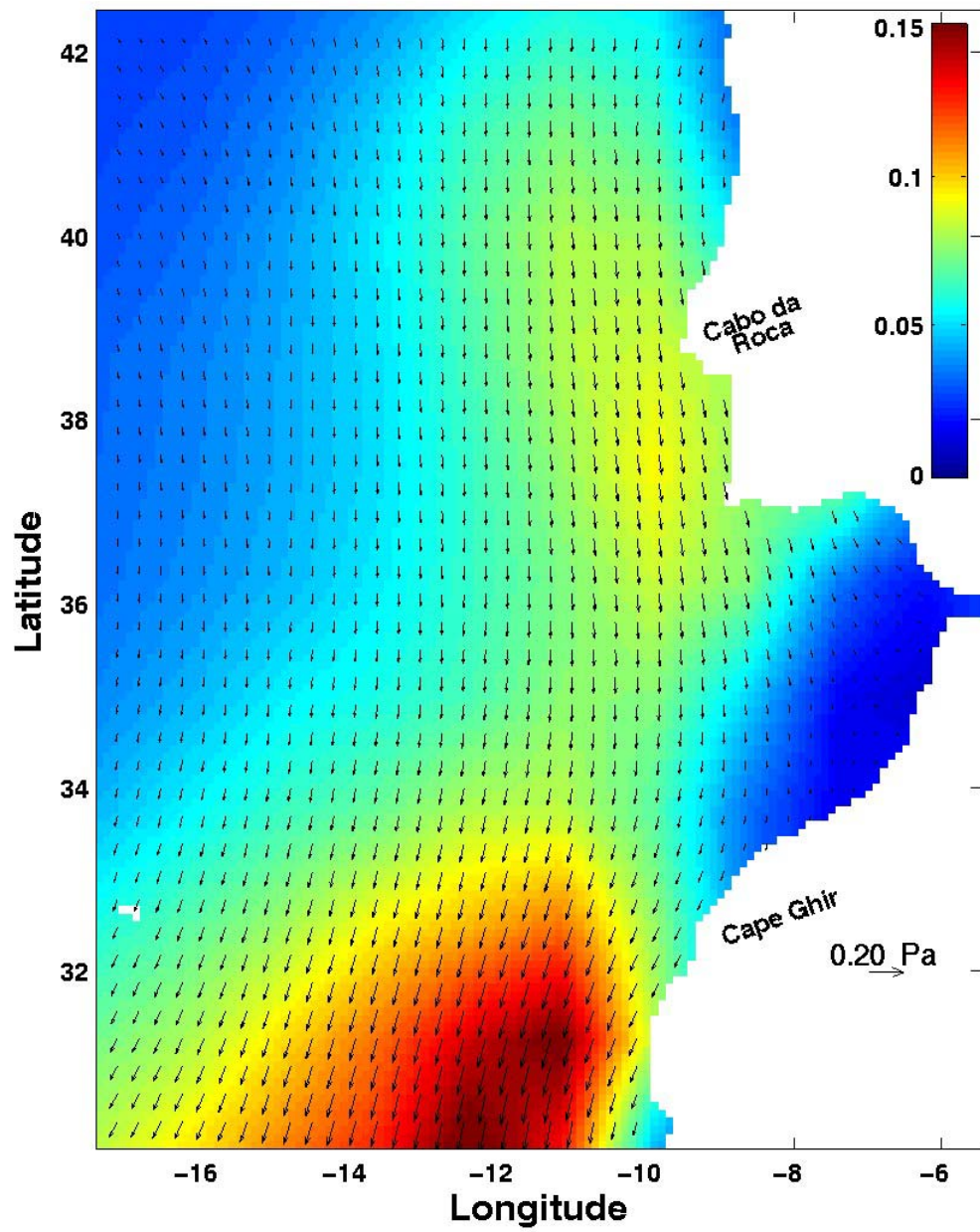


Figure 4.8f. Monthly wind stress vector (Pa) (arrows) and intensity (Pa) (in color) for August 1996.

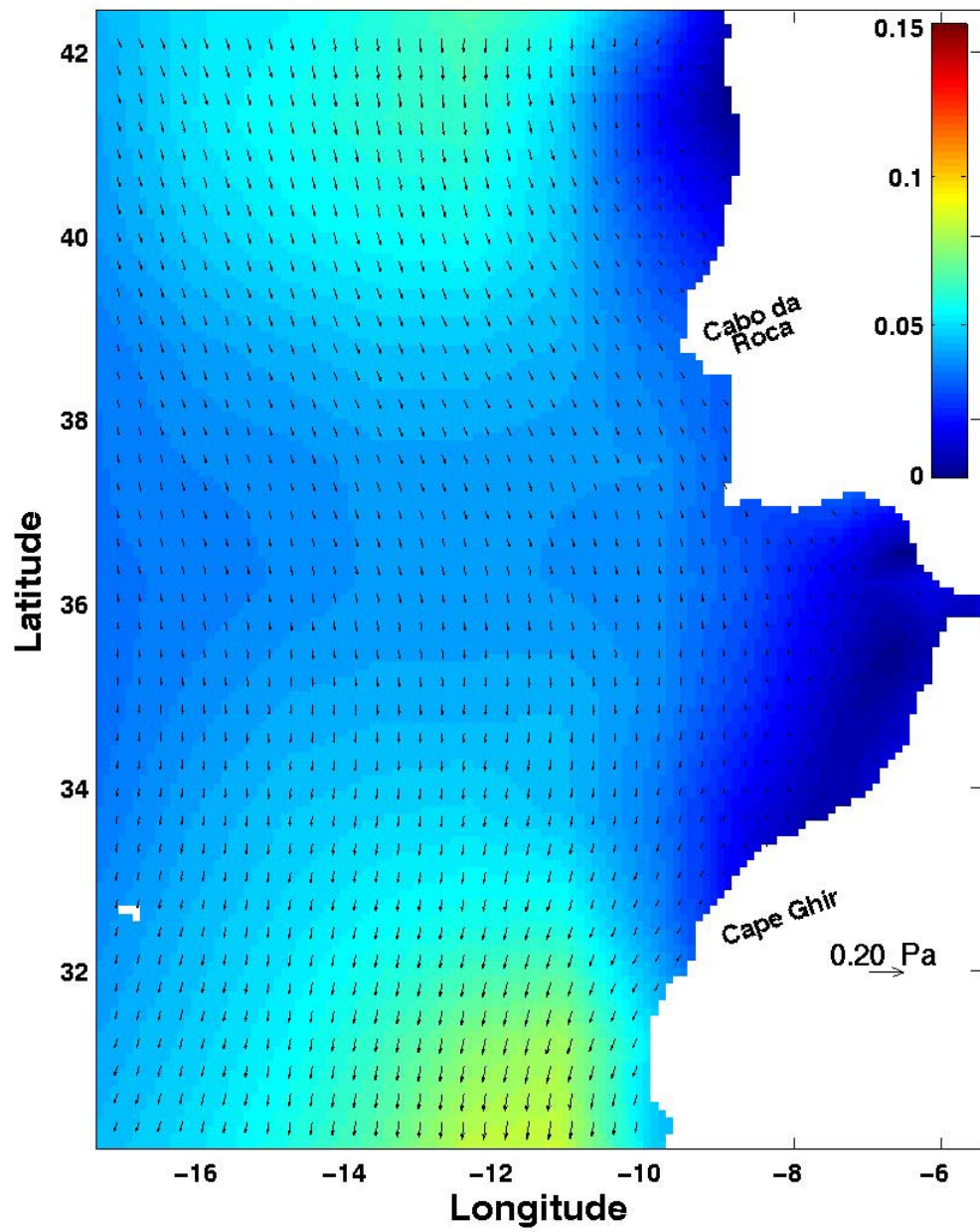


Figure 4.8g. Monthly wind stress vector (Pa) (arrows) and intensity (Pa) (in color) for September 1996.

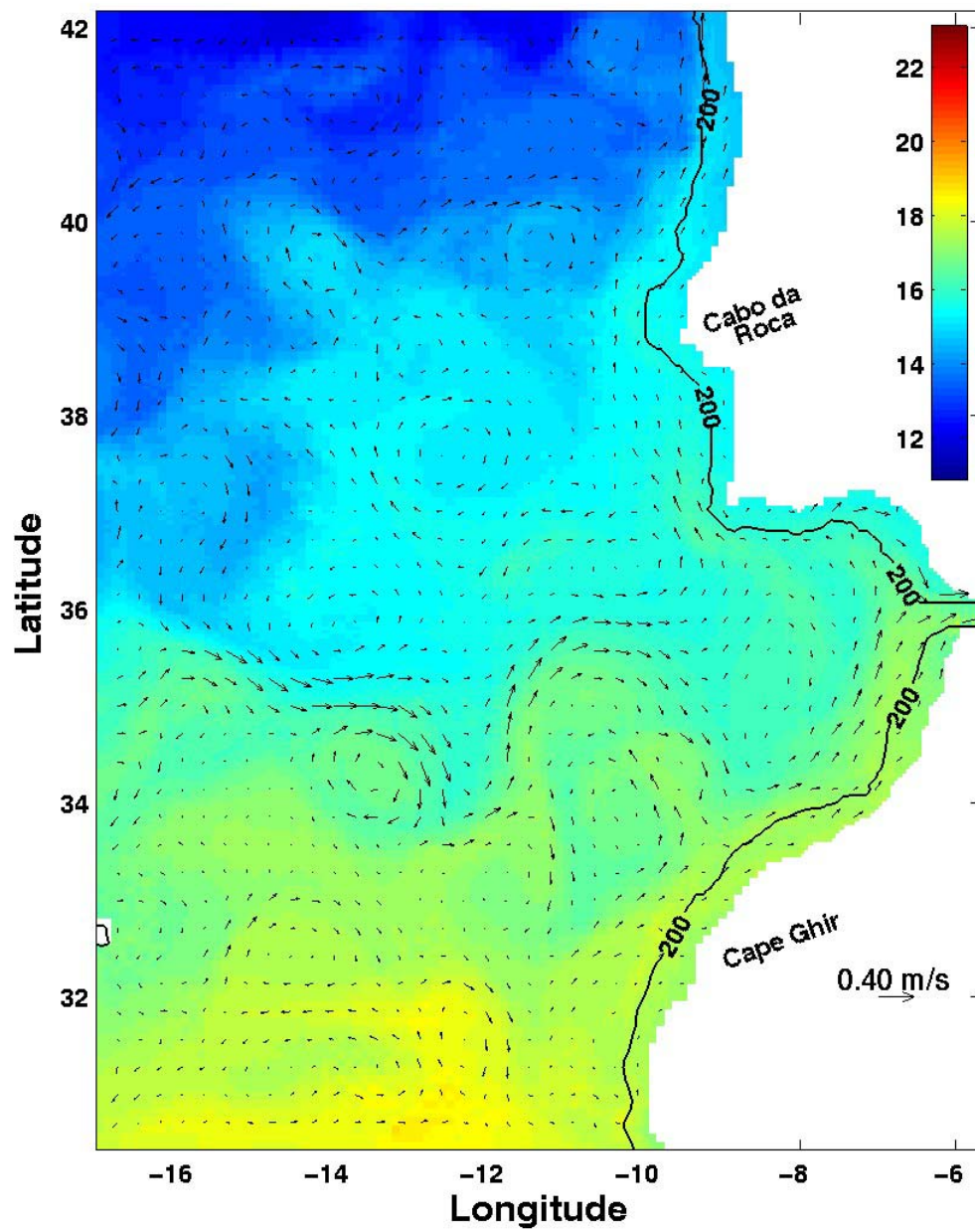


Figure 4.9a. Monthly surface temperature (°C) (in color) and velocity vectors (m/s) (arrows) for March 1996. Contour at 200 m depth is shown.

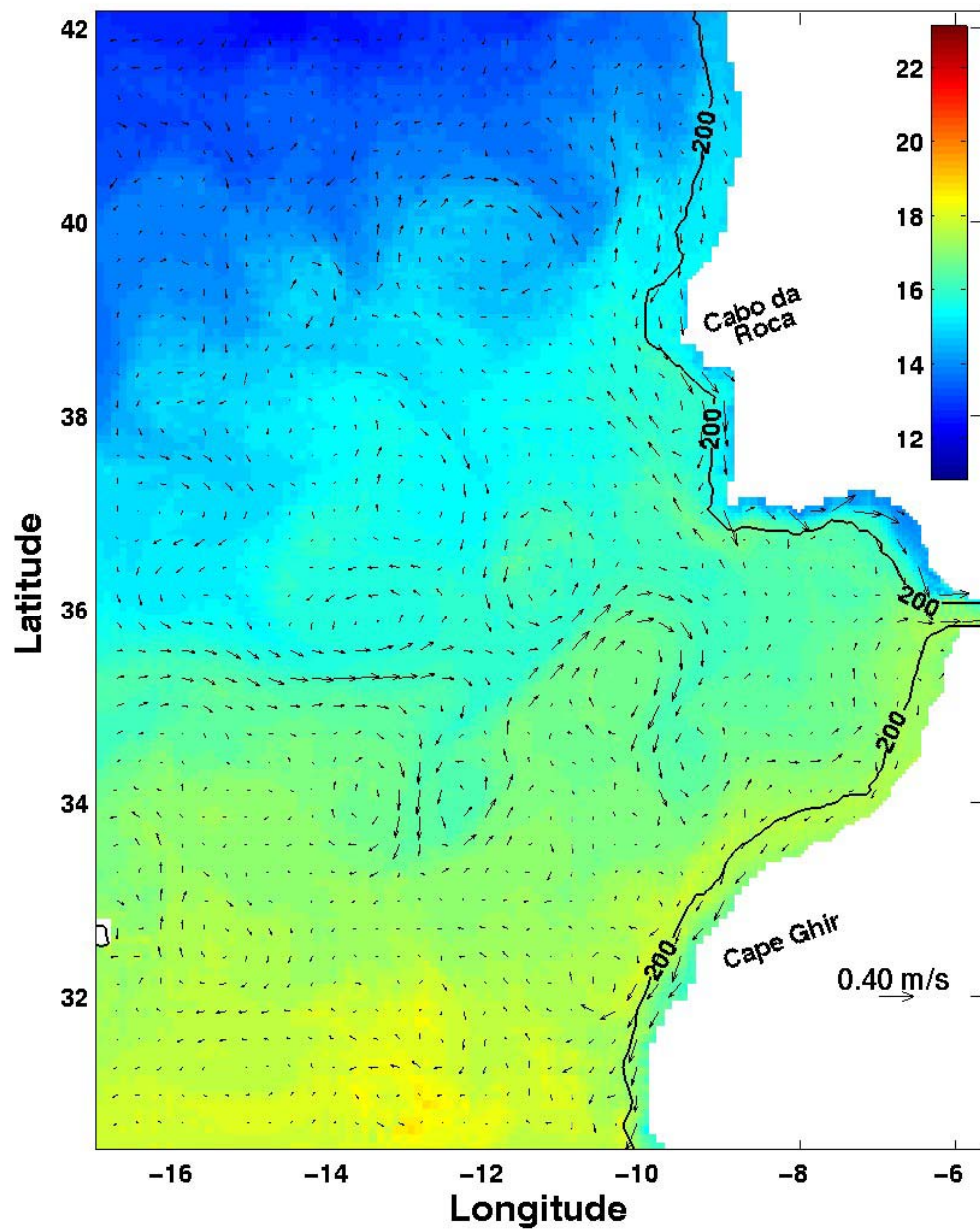


Figure 4.9b. Monthly surface temperature (°C) (in color) and velocity vectors (m/s) (arrows) for April 1996. Contour at 200 m depth is shown.

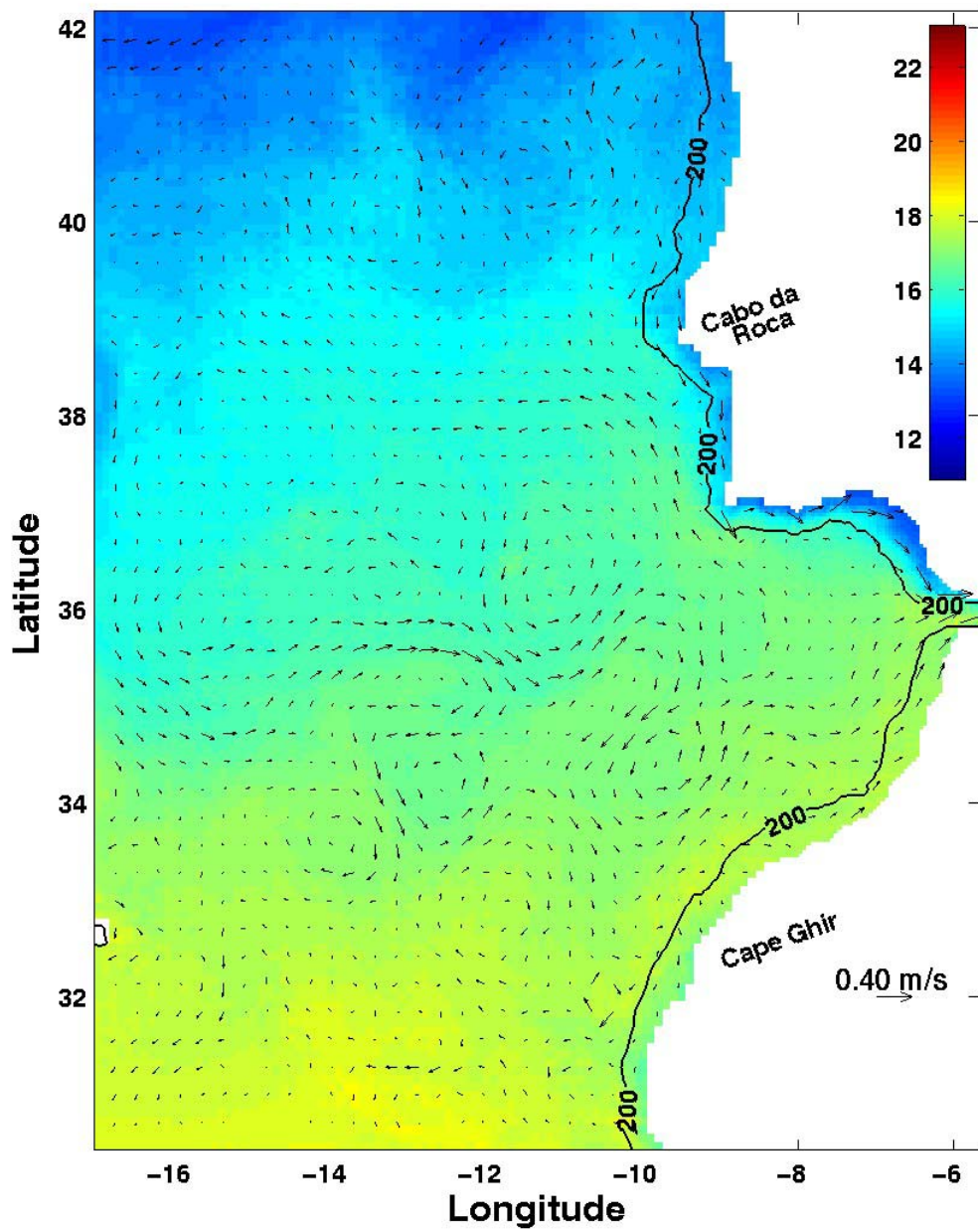


Figure 4.9c. Monthly surface temperature (°C) (in color) and velocity vectors (m/s) (arrows) for May 1996. Contour at 200 m depth is shown.

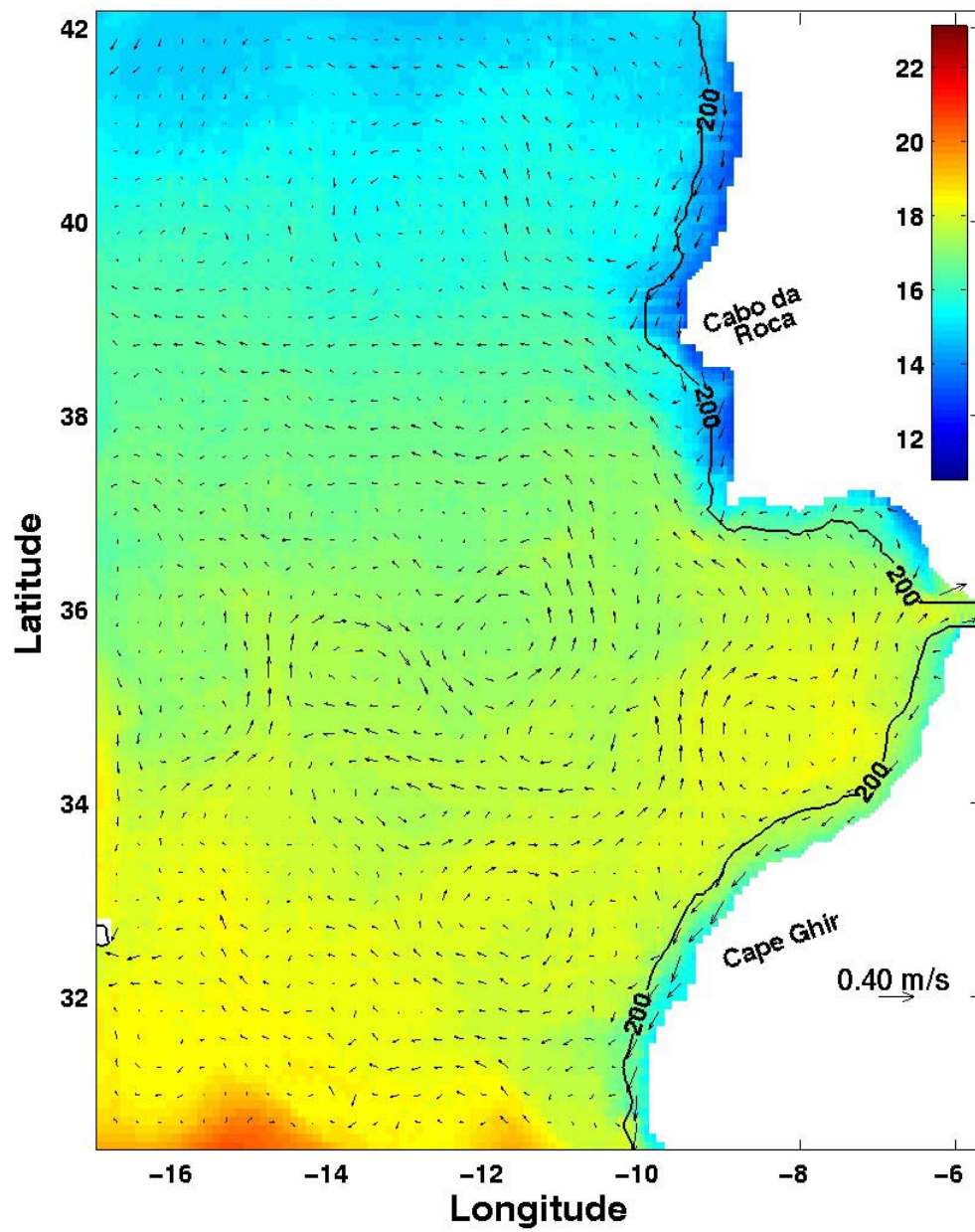


Figure 4.9d. Monthly surface temperature ($^{\circ}\text{C}$) (in color) and velocity vectors (m/s) (arrows) for June 1996. Contour at 200 m depth is shown.

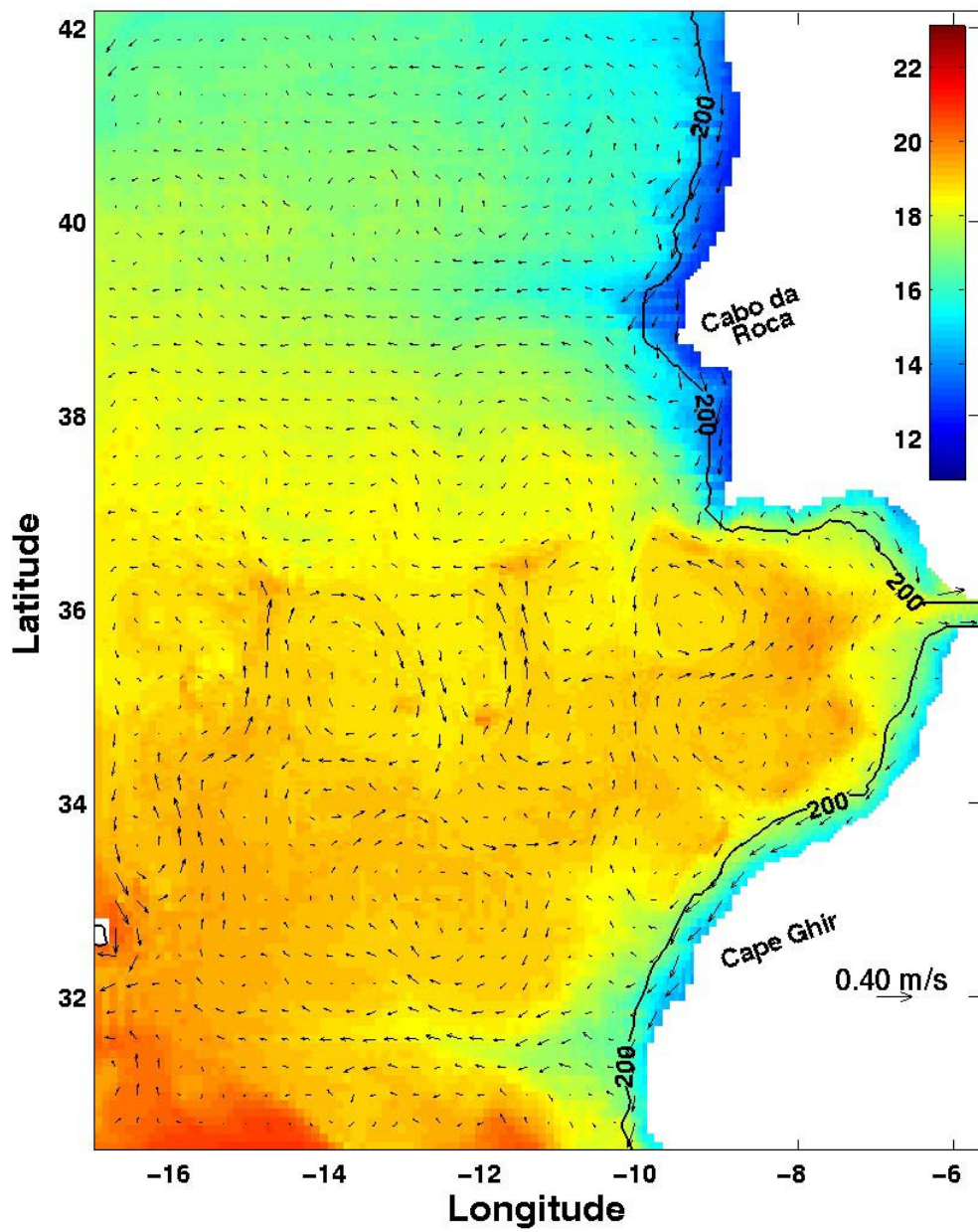


Figure 4.9e. Monthly surface temperature (°C) (in color) and velocity vectors (m/s) (arrows) for July 1996. Contour at 200 m depth is shown.

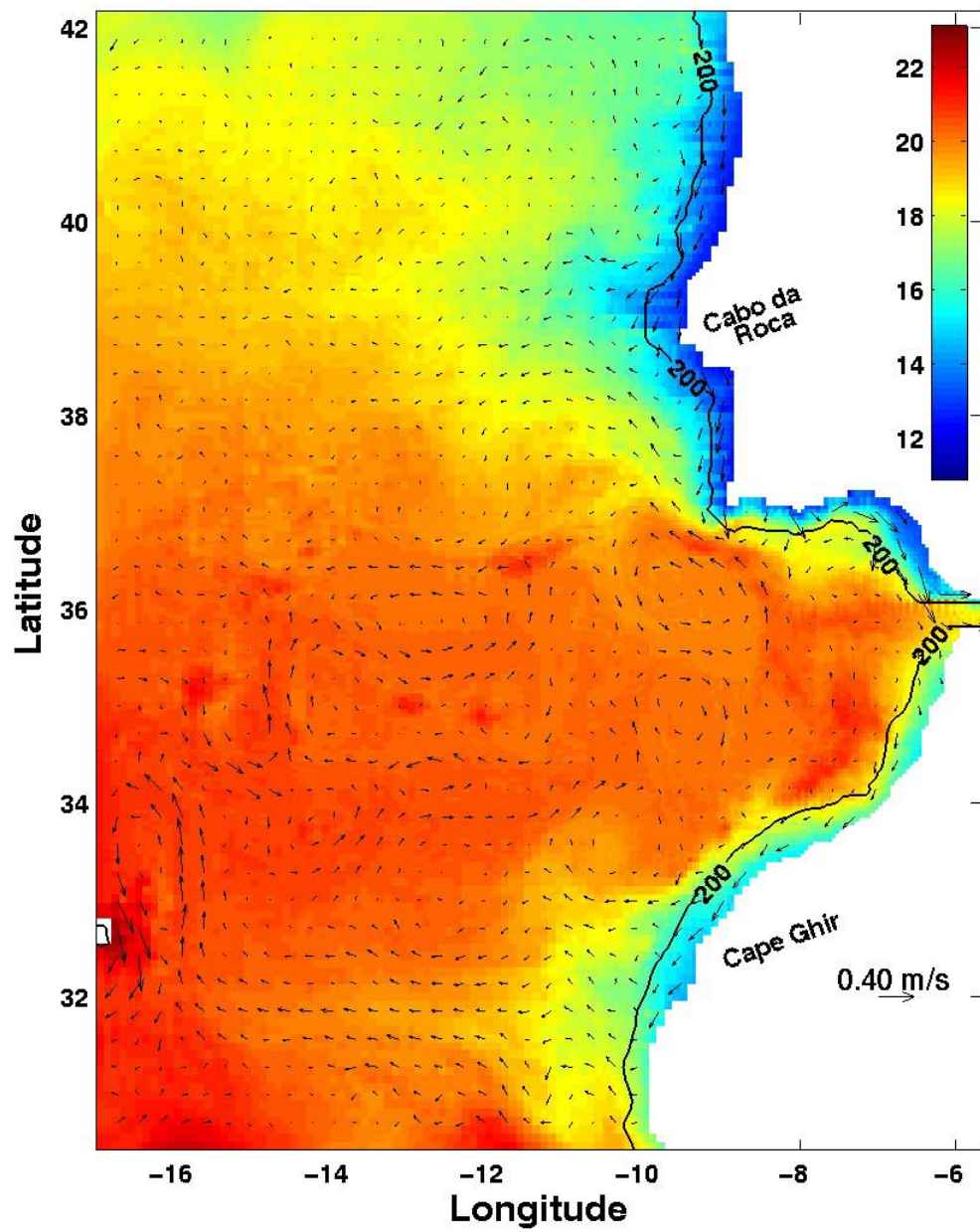


Figure 4.9f. Monthly surface temperature (°C) (in color) and velocity vectors (m/s) (arrows) for August 1996. Contour at 200 m depth is shown.

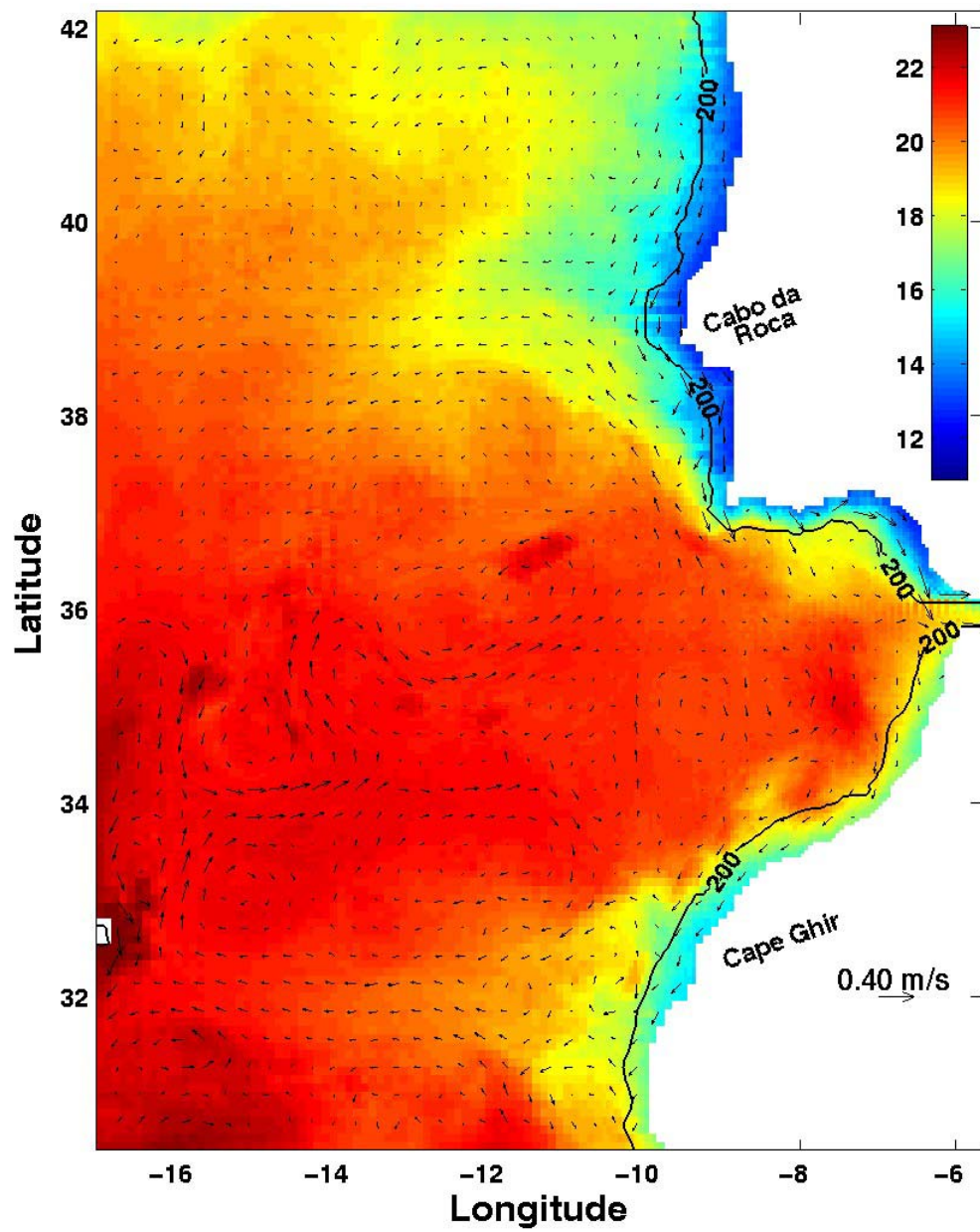


Figure 4.9g. Monthly surface temperature (°C) (in color) and velocity vectors (m/s) (arrows) for September 1996. Contour at 200 m depth is shown.

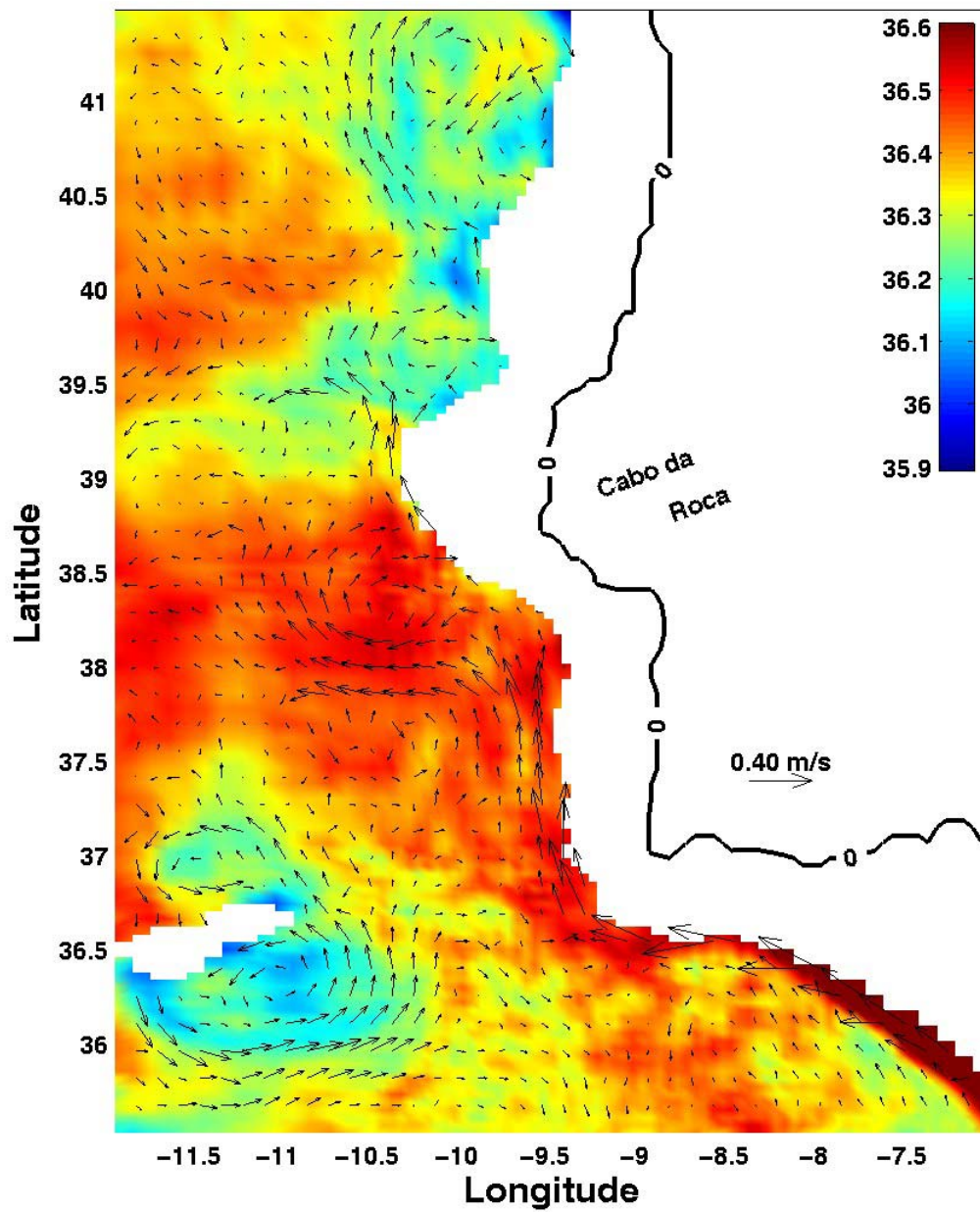


Figure 4.10a. Salinity (in color) and velocity vectors (m/s) (arrows) at 1000 m depth at simulation day 65.

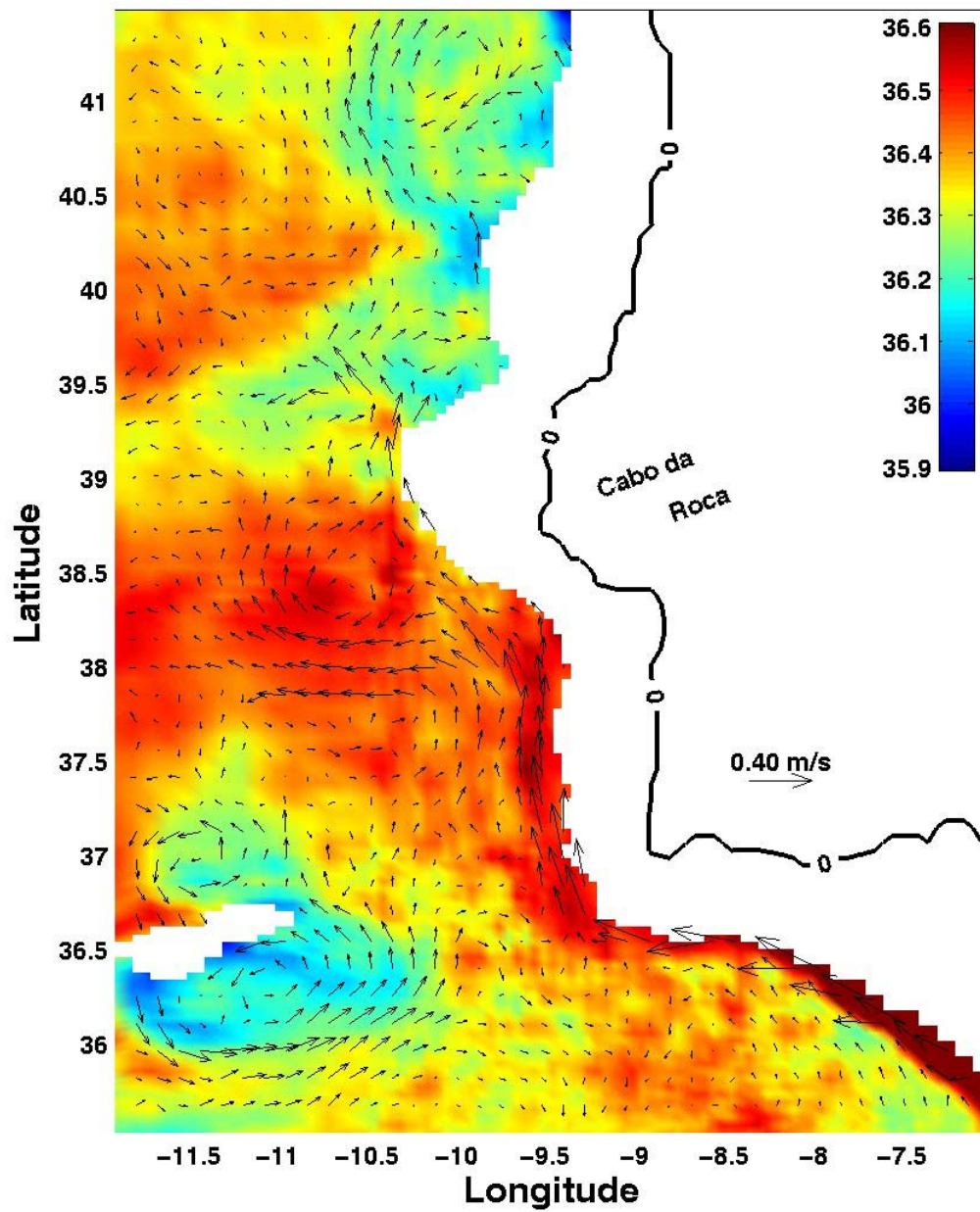


Figure 4.10b. Salinity (in color) and velocity vectors (m/s) (arrows) at 1000 m depth at simulation day 70.

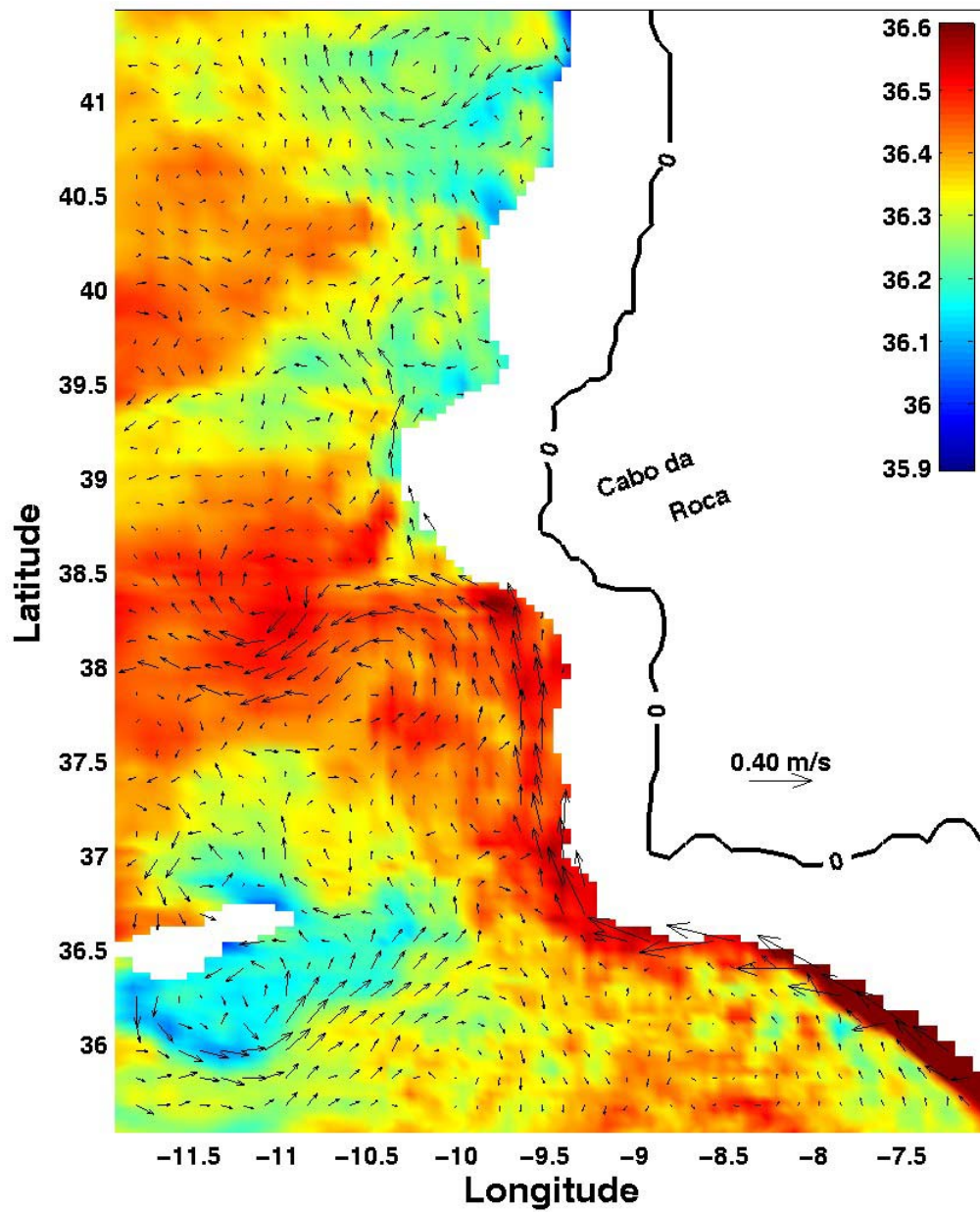


Figure 4.10c. Salinity (in color) and velocity vectors (m/s) (arrows) at 1000 m depth at simulation day 75.

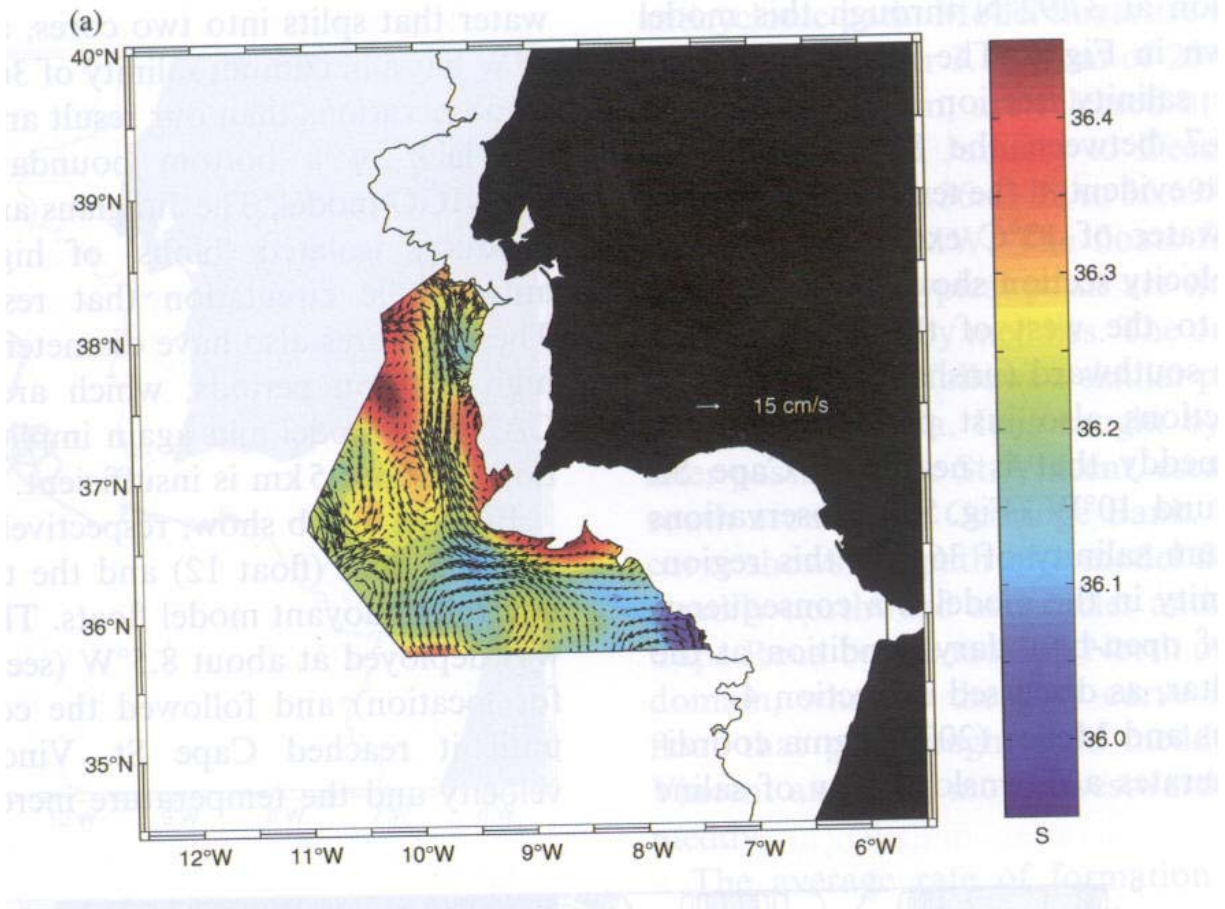


Figure 4.10d. Observed Salinity (in color) and geostrophic velocity (cm/s) field at 1200m referenced to 2000m, September 1997 (from Johnson et al., 2002).

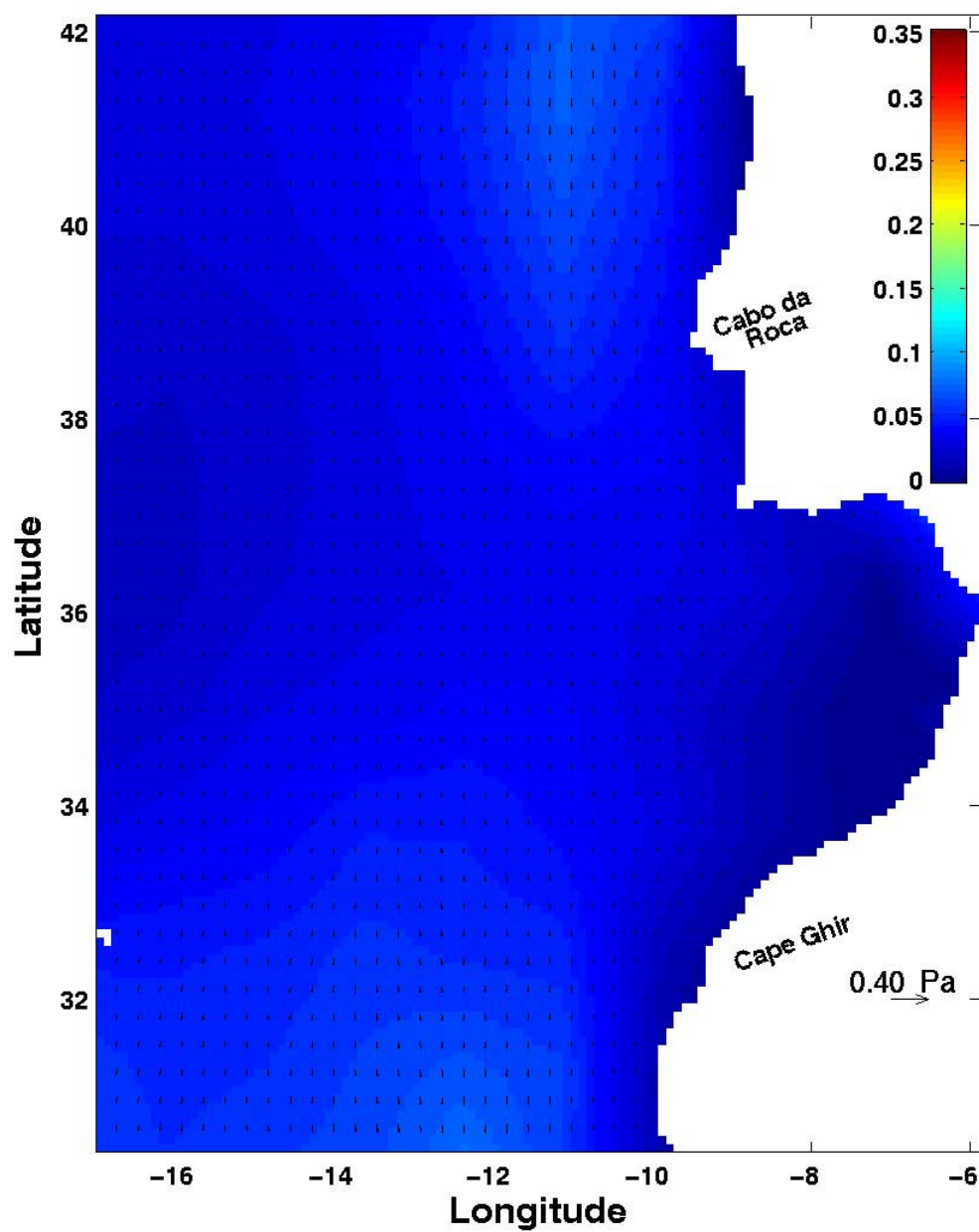


Figure 4.11a. Average wind stress vector (Pa) (arrows) and intensity (Pa) (in color) for 21-24 July.

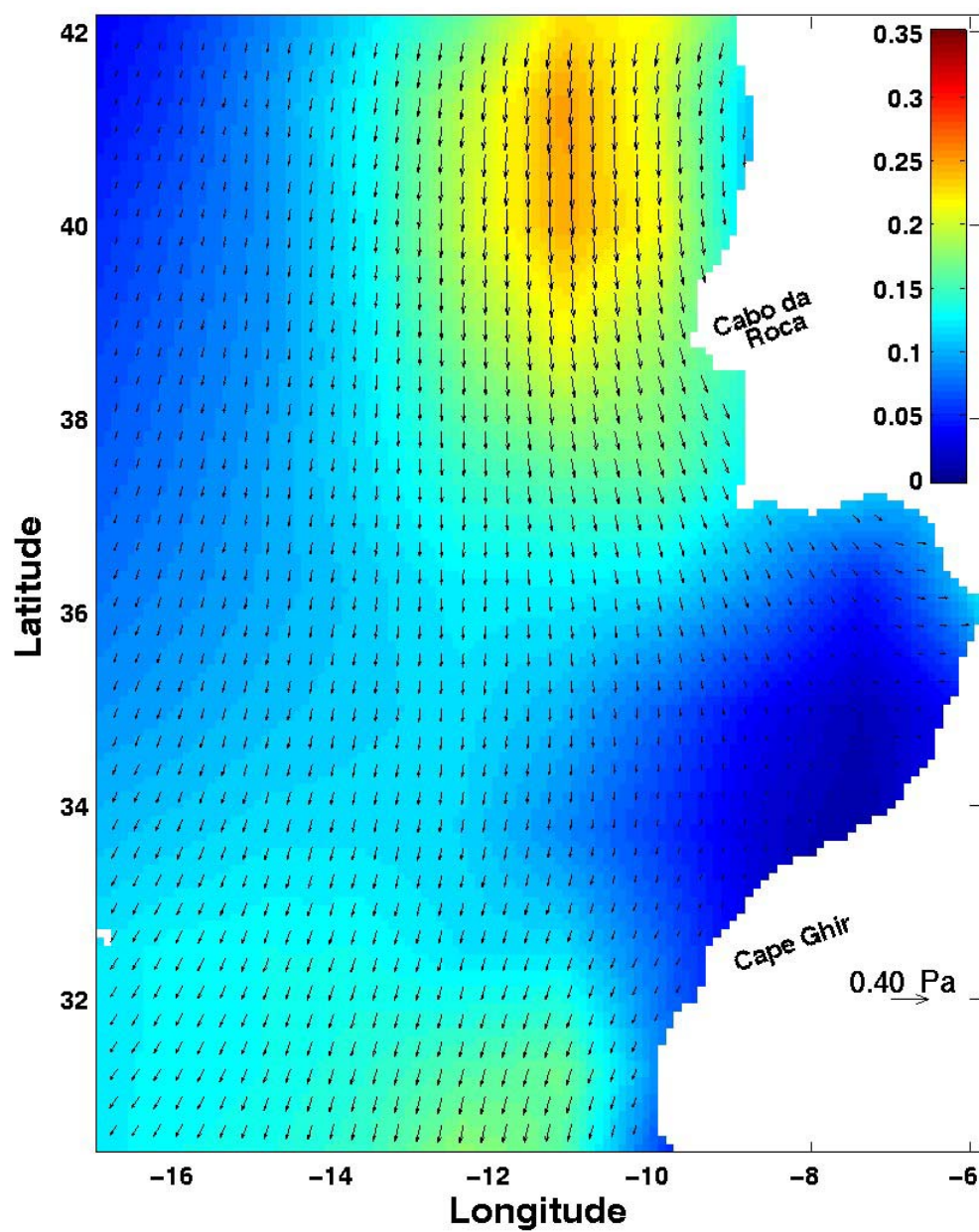


Figure 4.11b. Average wind stress vector (Pa) (arrows) and intensity (Pa) (in color) for 24-27 July.

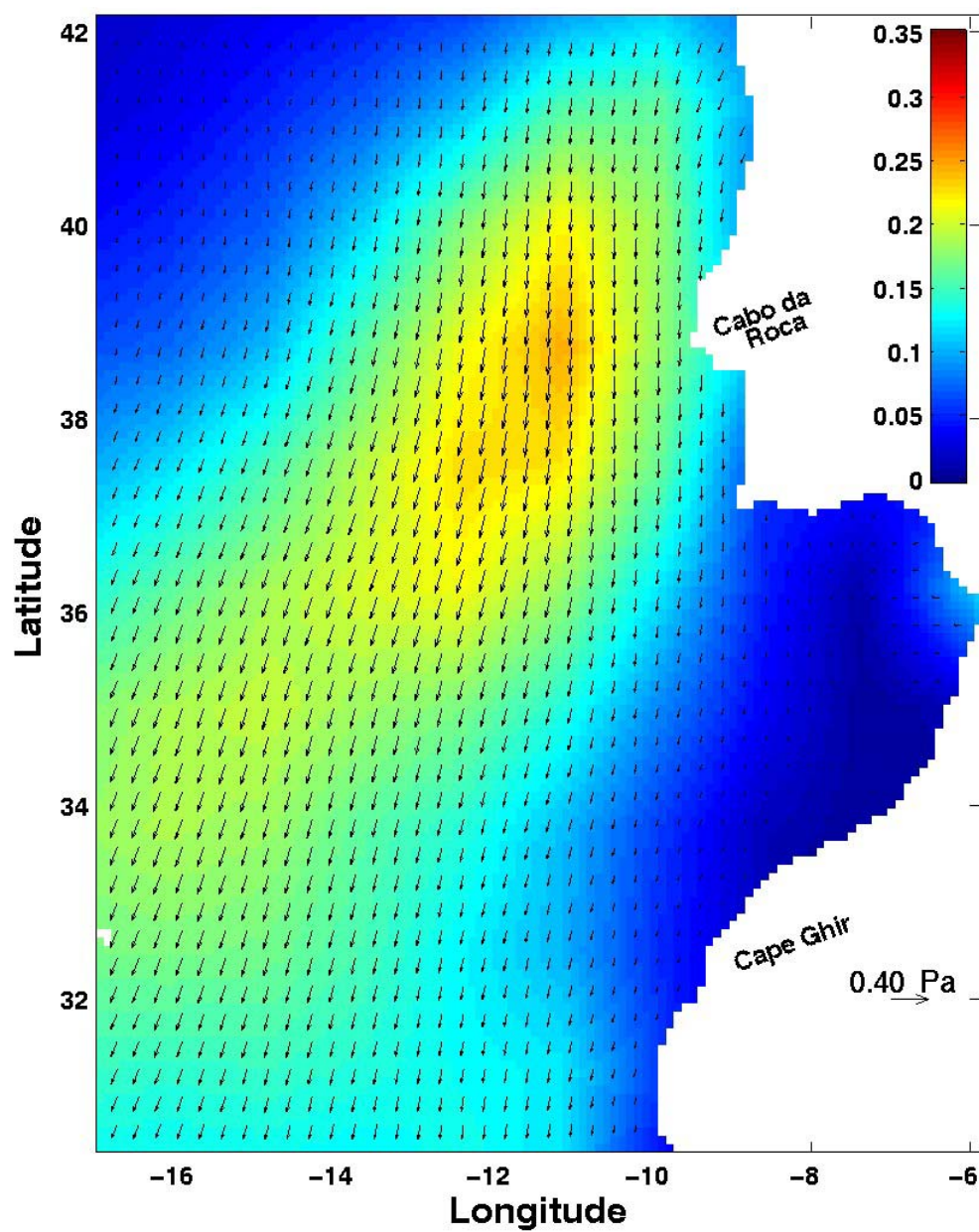


Figure 4.11c. Average wind stress vector (Pa) (arrows) and intensity (Pa) (in color) for 27-30 July.

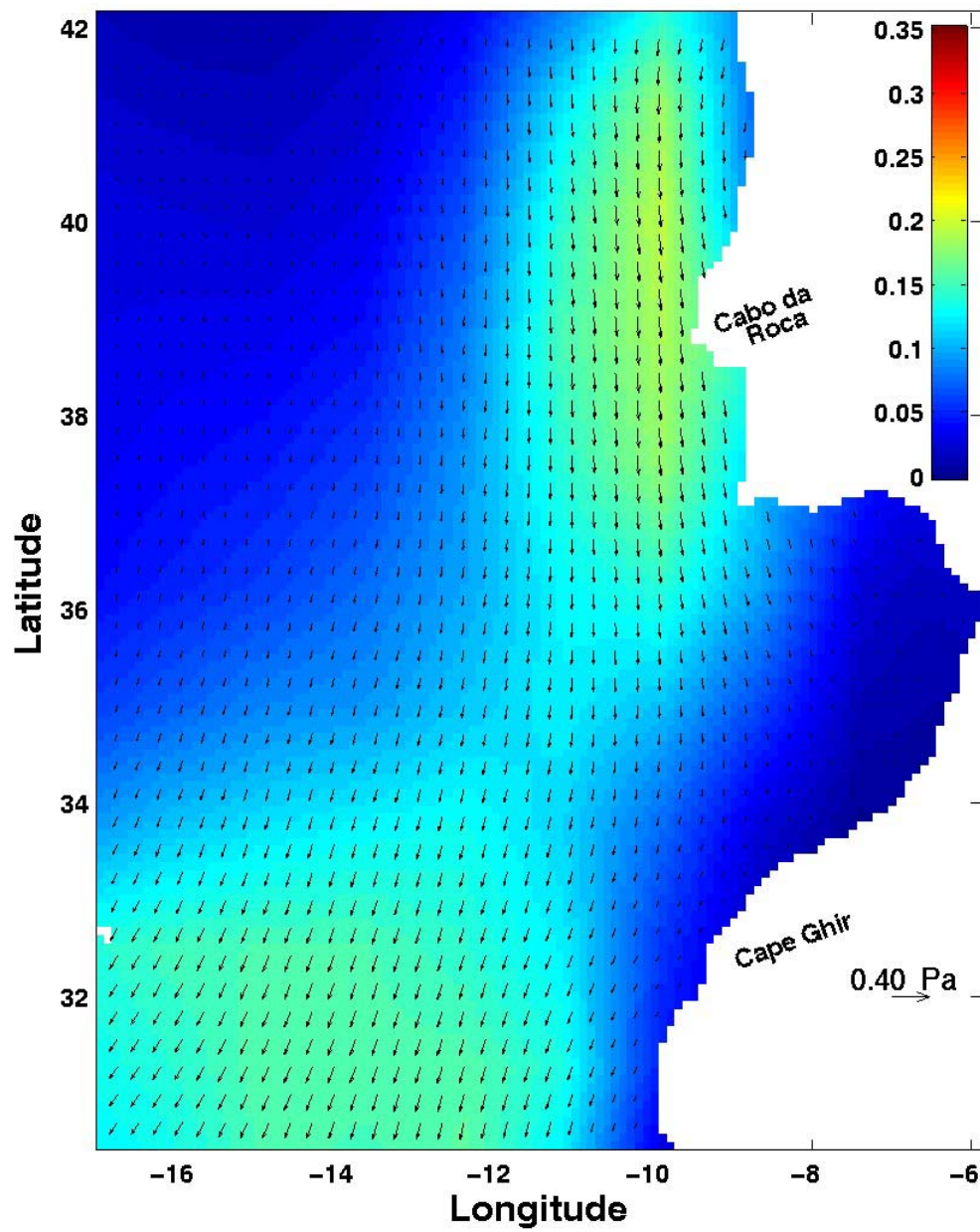


Figure 4.11d. Average wind stress vector (Pa) (arrows) and intensity (Pa) (in color) for 30July-02August.

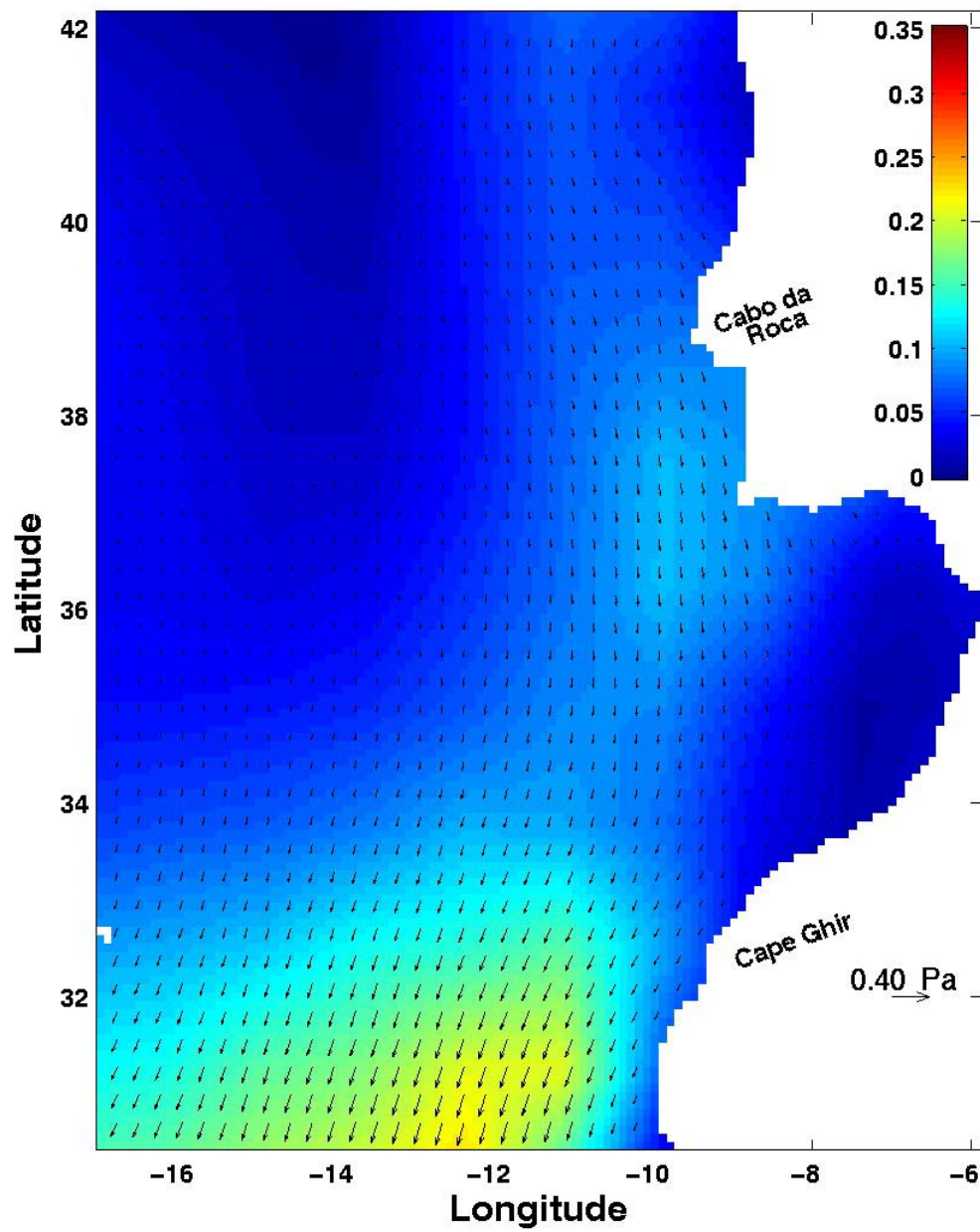


Figure 4.11e. Average wind stress vector (Pa) (arrows) and intensity (Pa) (in color) for 02-05 August.

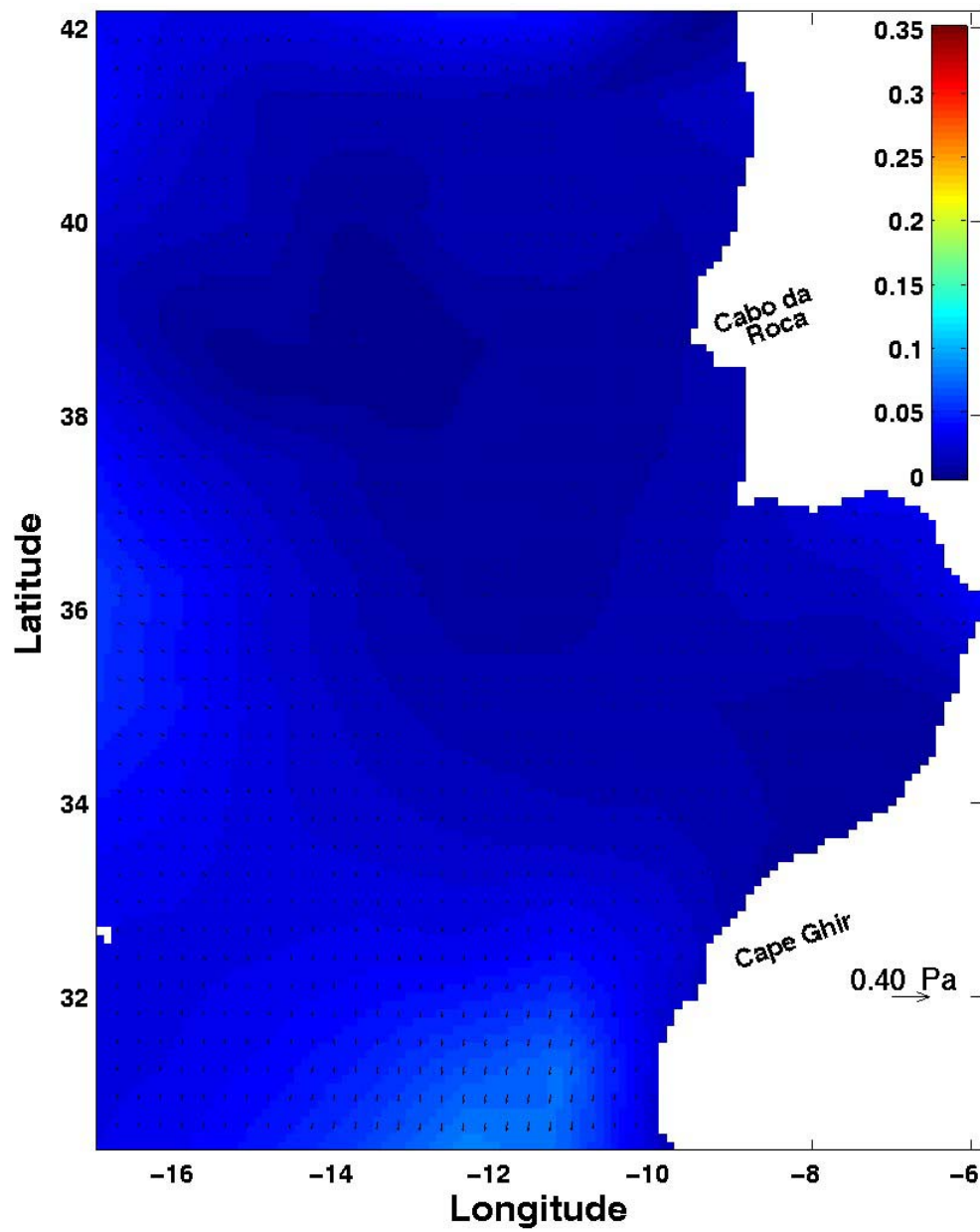


Figure 4.11f. Average wind stress vector (Pa) (arrows) and intensity (Pa) (in color) for 05-08 August.

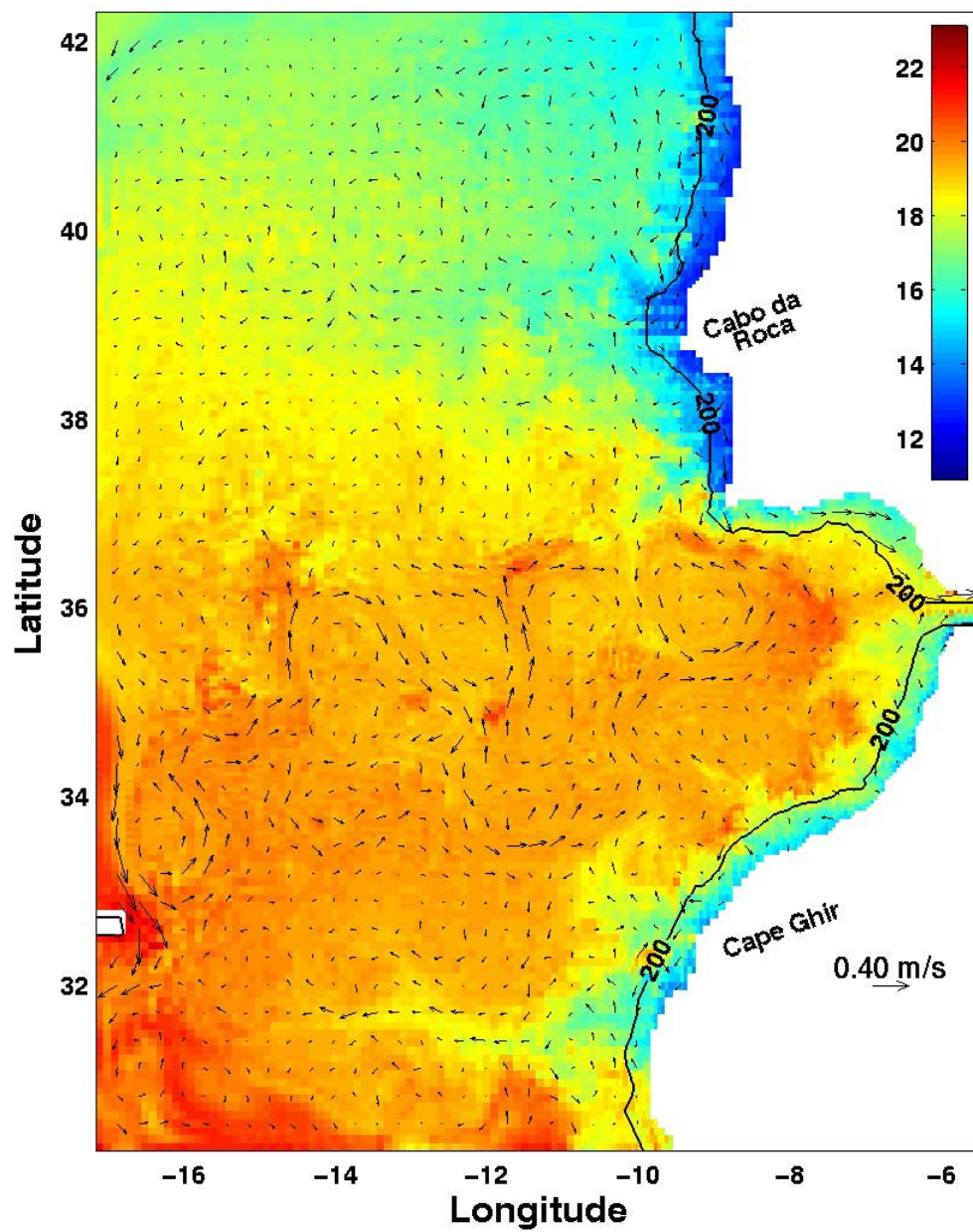


Figure 4.12a. Average surface temperature (°C) (in color) and velocity vectors (m/s) (arrows) for 21-24 July. Contour at 200 m depth is shown.

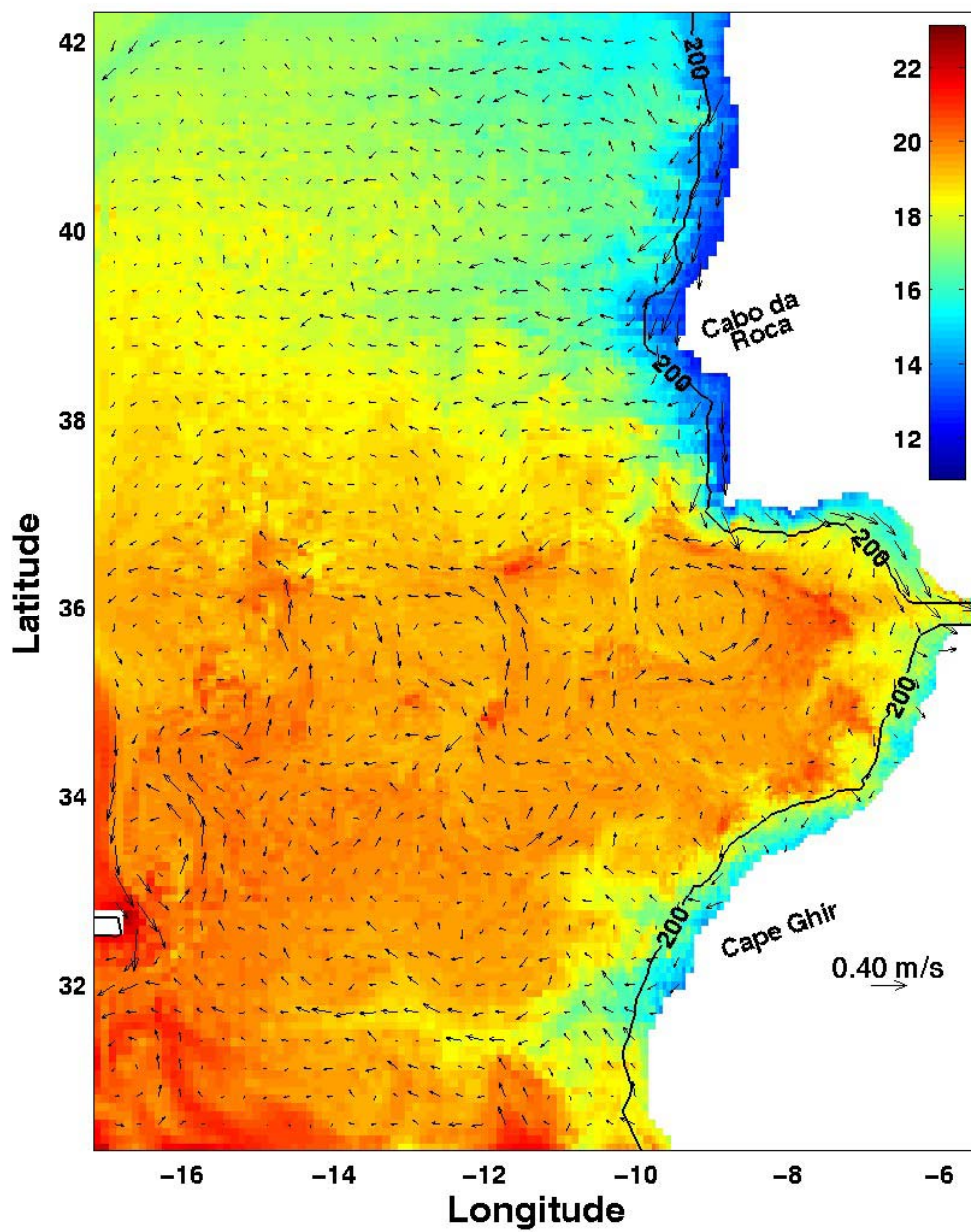


Figure 4.12b. Average surface temperature (°C) (in color) and velocity vectors (m/s) (arrows) for 24-27 July. Contour at 200 m depth is shown.

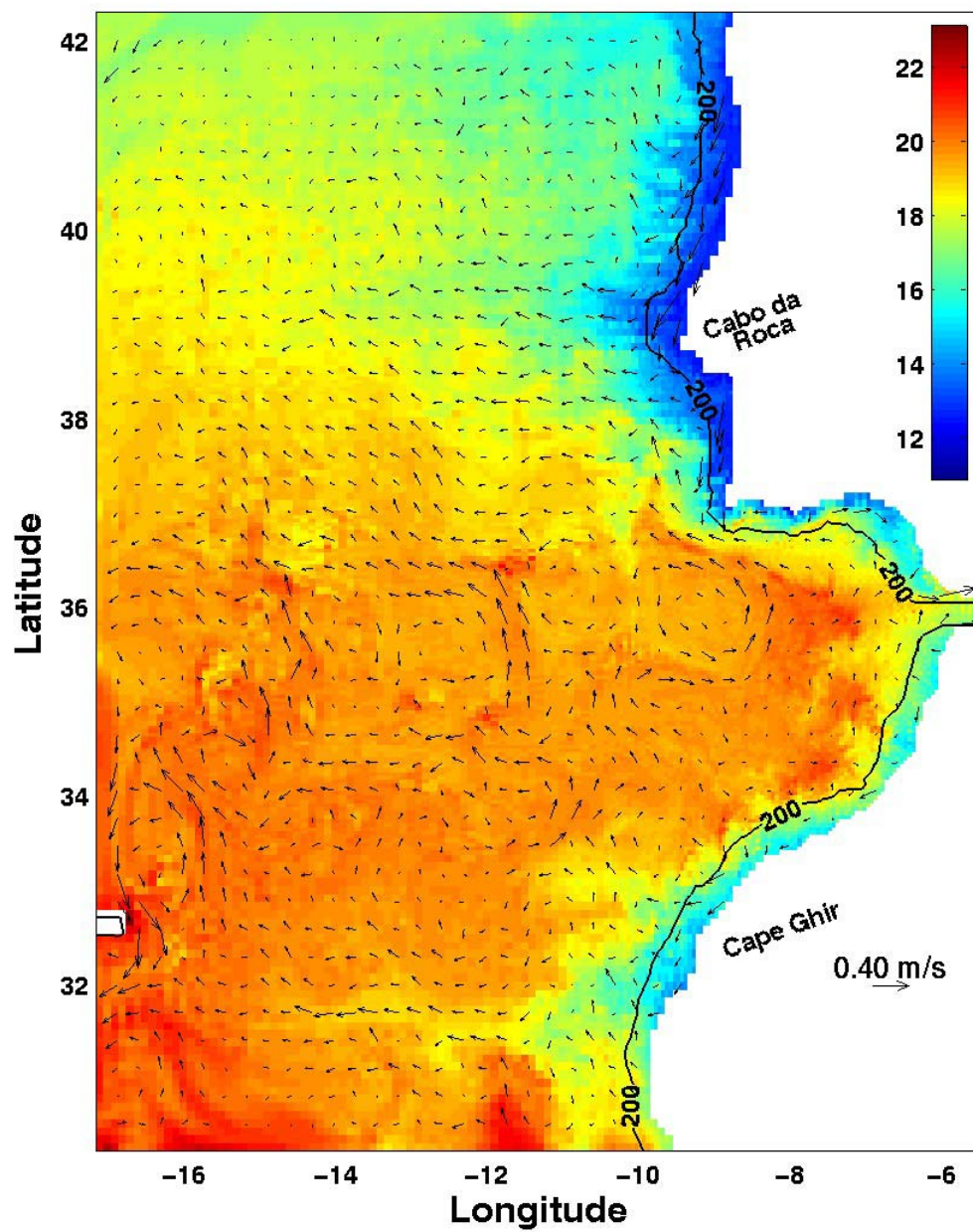


Figure 4.12c. Average surface temperature (°C) (in color) and velocity vectors (m/s) (arrows) for 27-30 July. Contour at 200 m depth is shown.

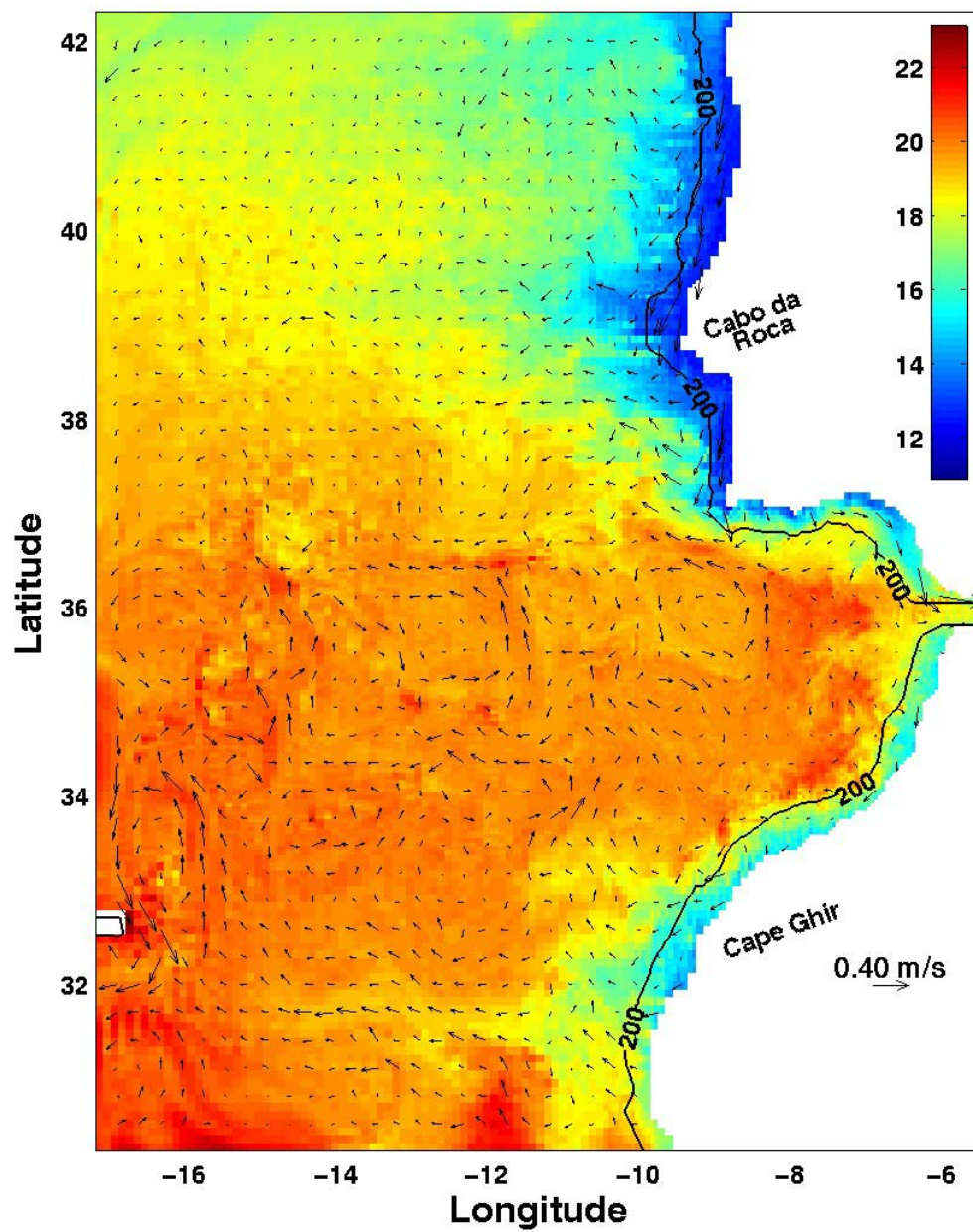


Figure 4.12d. Average surface temperature (°C) (in color) and velocity vectors (m/s) (arrows) for 30 July-02 August. Contour at 200 m depth is shown.

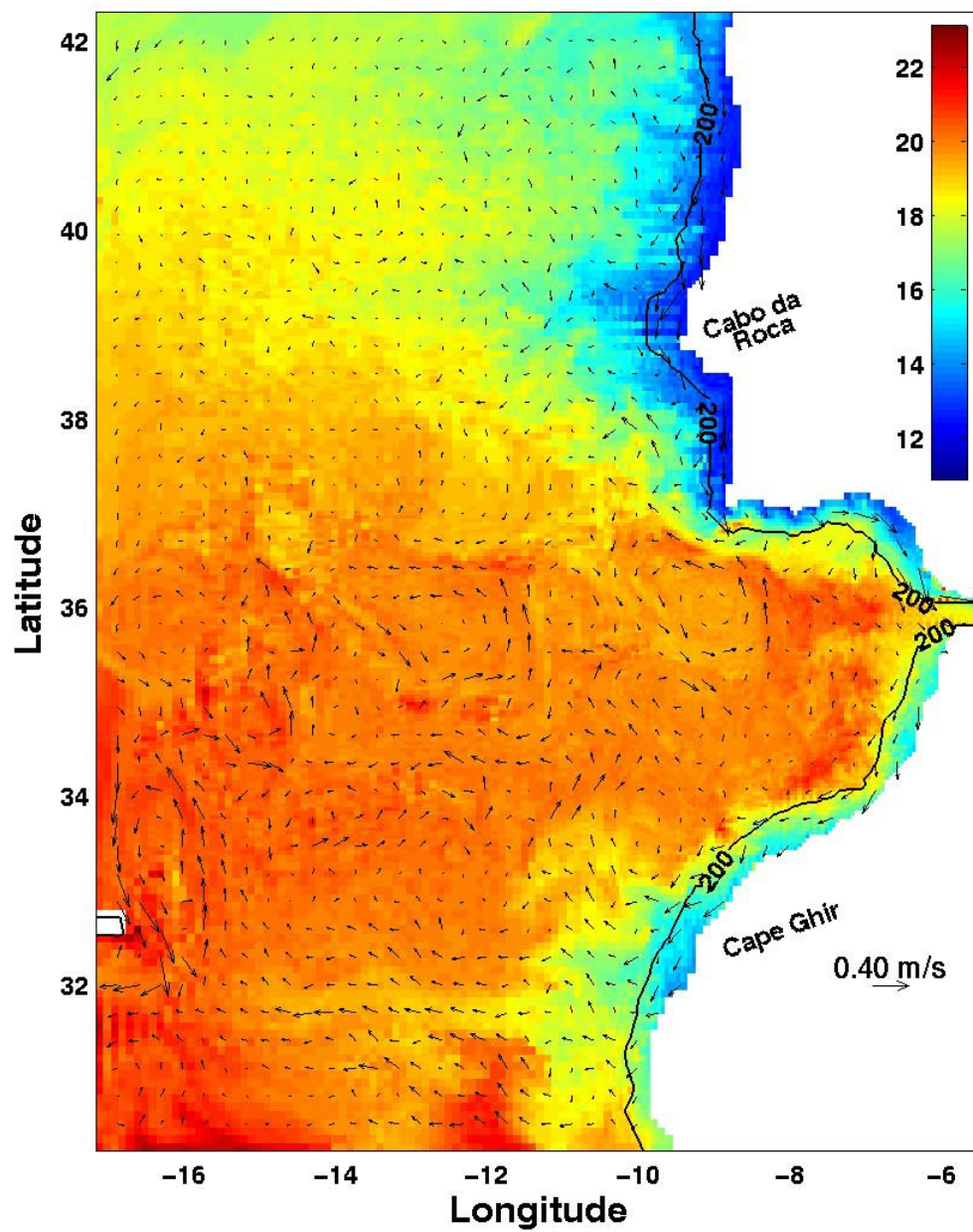


Figure 4.12e. Average surface temperature (°C) (in color) and velocity vectors (m/s) (arrows) for 02-05 August. Contour at 200 m depth is shown.

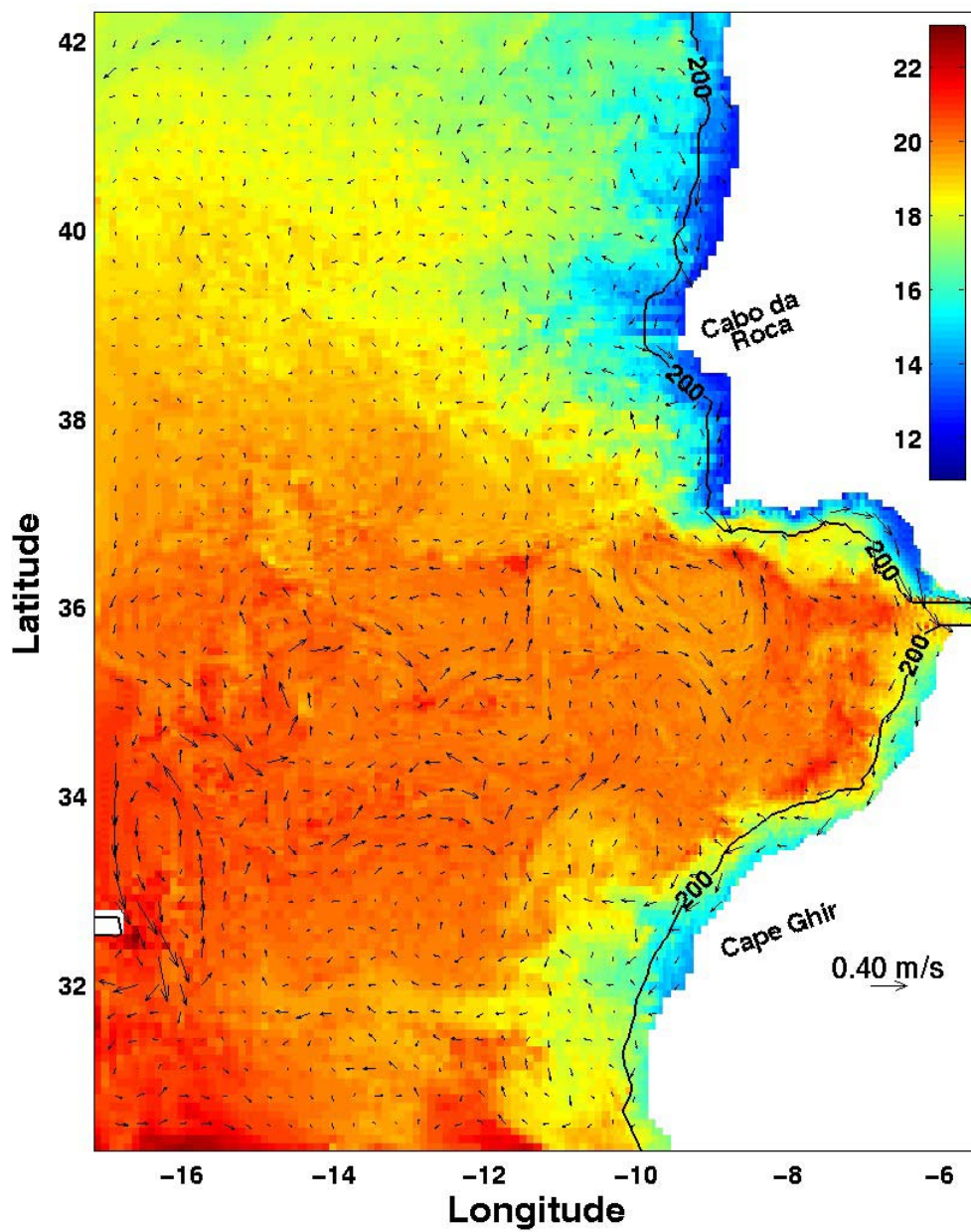


Figure 4.12f. Average surface temperature (°C) (in color) and velocity vectors (m/s) (arrows) for 05-08 August. Contour at 200 m depth is shown.

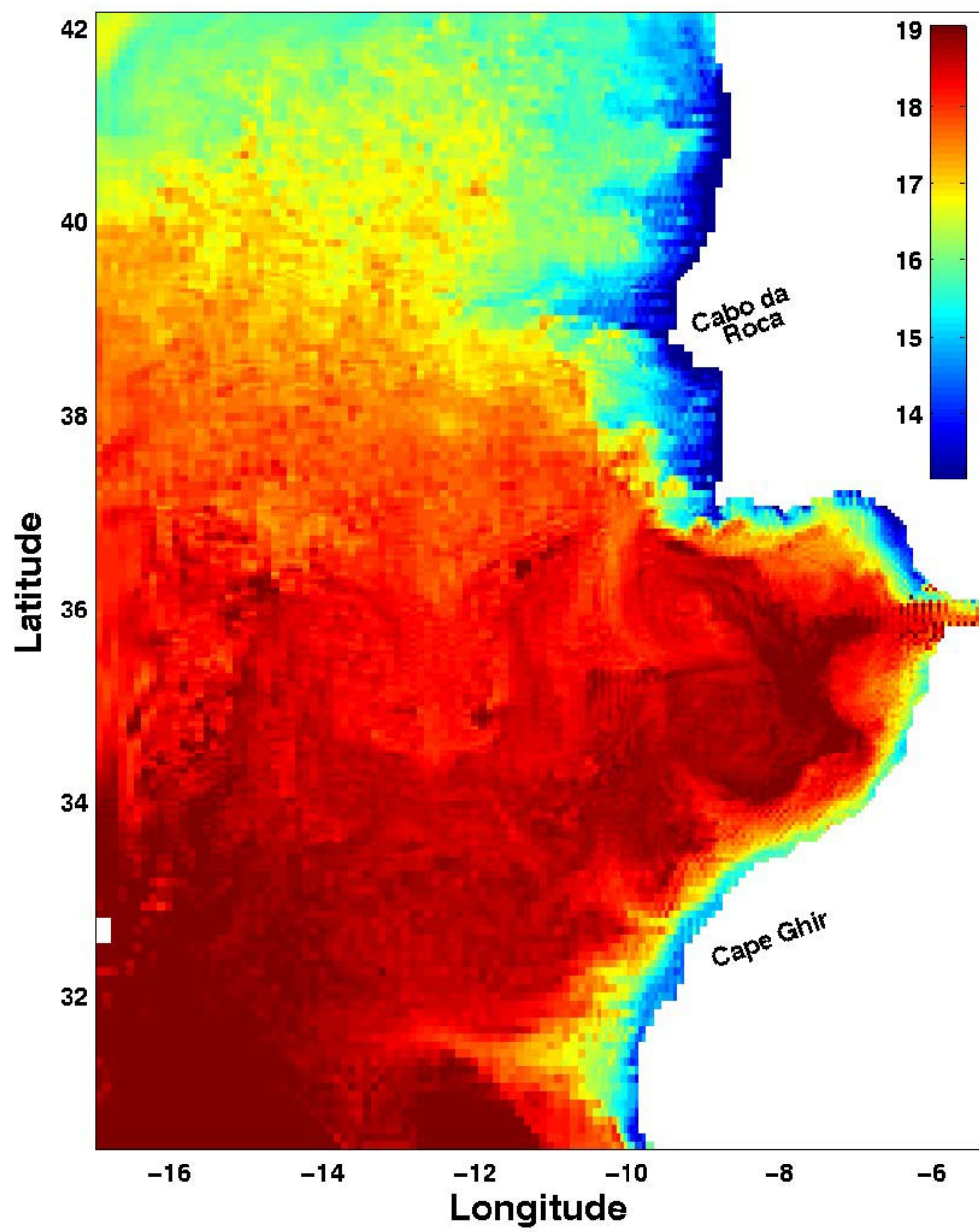


Figure 4.13a. Average surface temperature (°C) (in color) for 03-06 July.

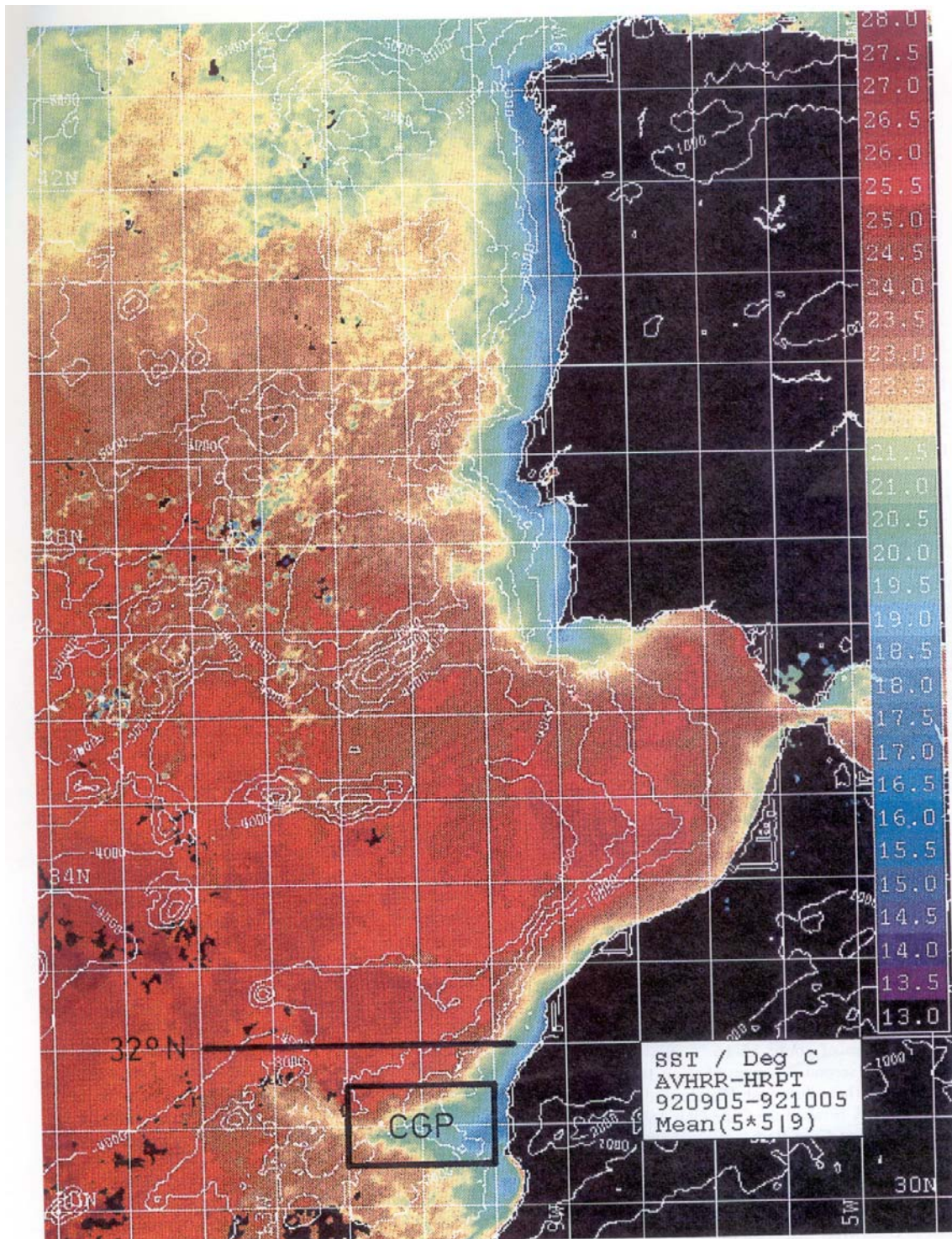


Figure 4.13b. Averaged AVHRR surface temperature for 05Sep to 05 Oct (°C) (in color) and bottom topography contours (m). From Hagen and al., 1996.

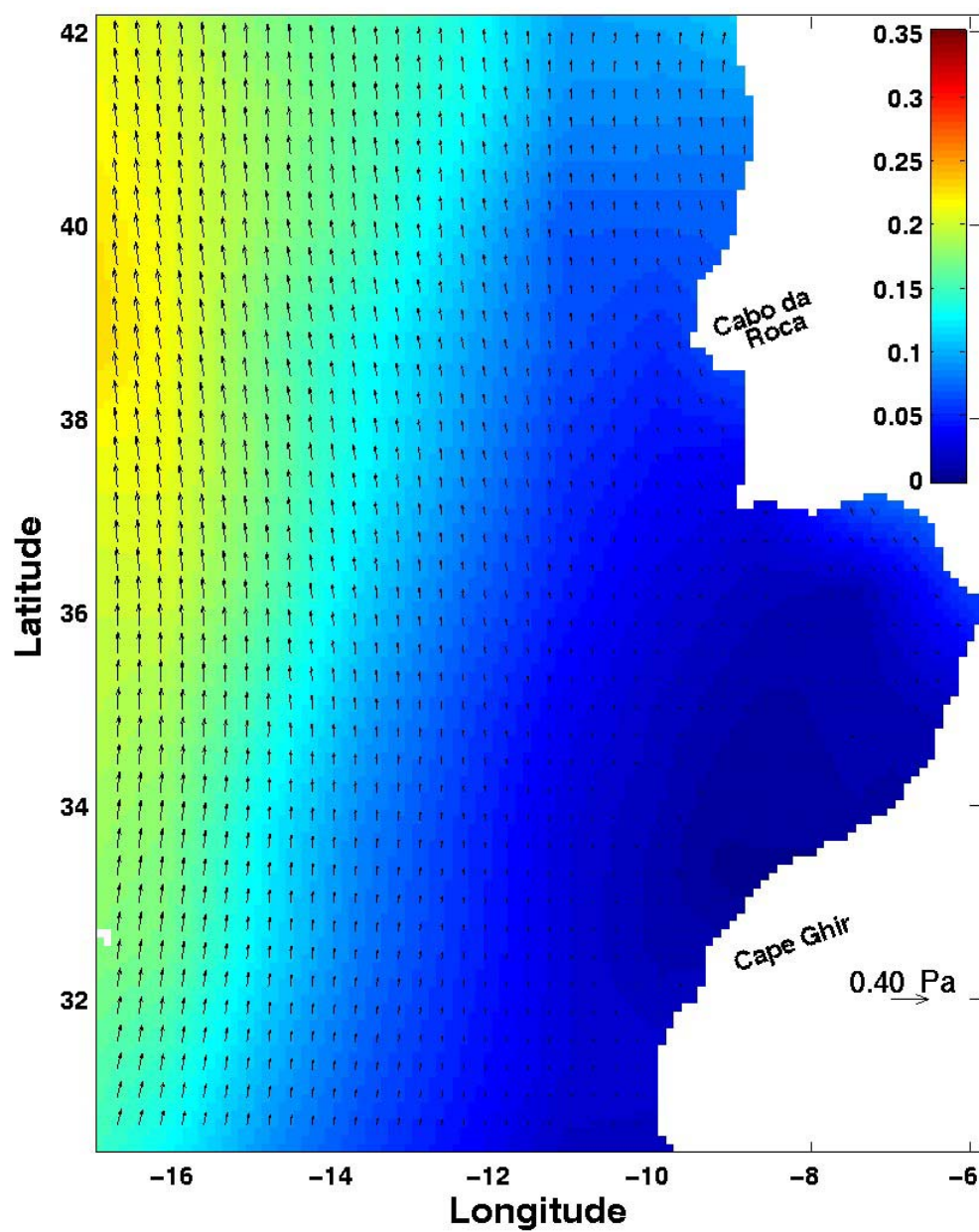


Figure 4.14a. Average wind stress vector (Pa) (arrows) and intensity (Pa) (in color) for 20-23 March.

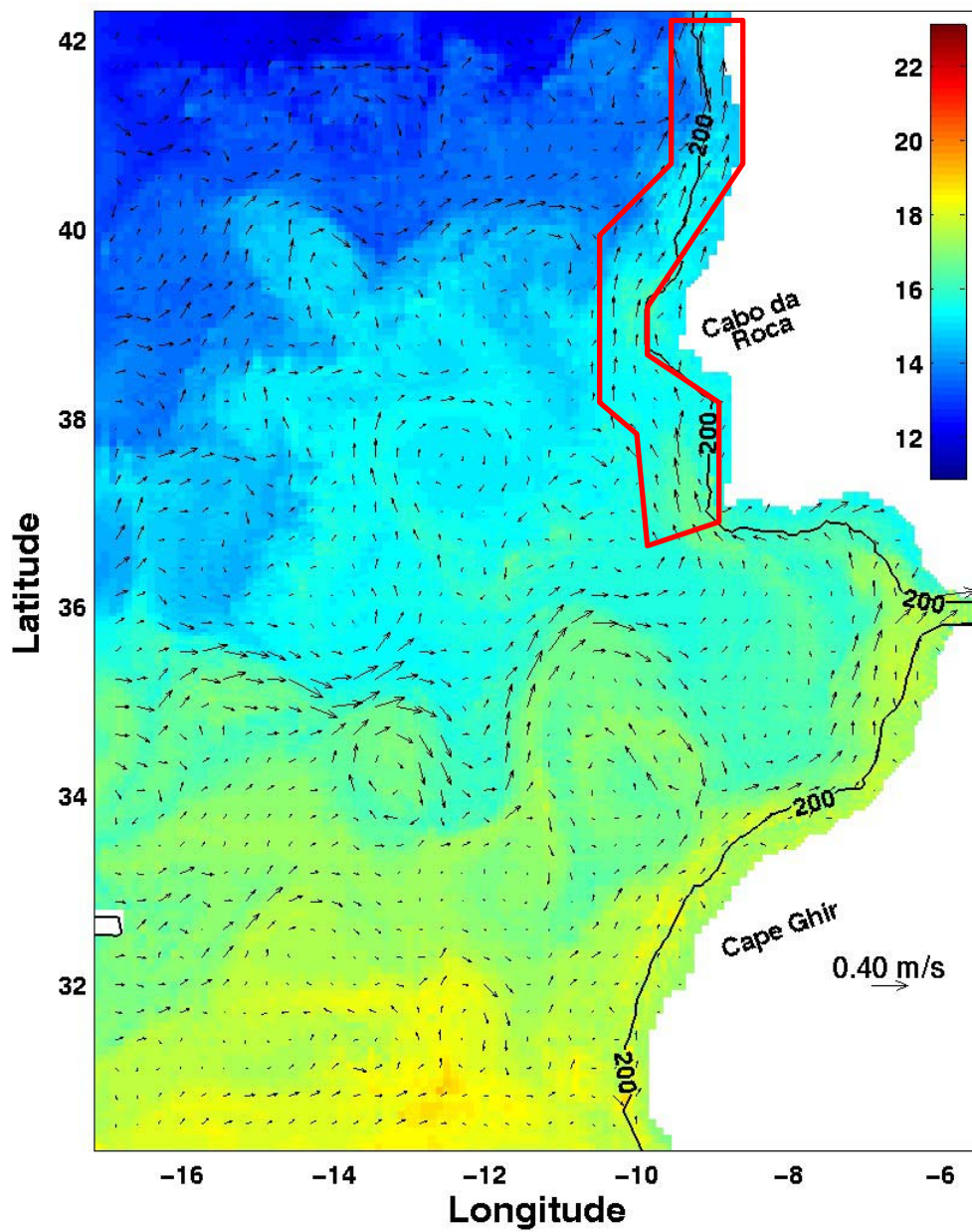


Figure 4.14b. Average surface temperature ($^{\circ}\text{C}$) (in color) and velocity vectors (m/s) (arrows) for 20-23 March. Iberian Current enclosed by red polygon. Contour at 200 m depth is shown.

V. THE DEVELOPMENT OF THE AUTOMATIC PARALLELIZATION OF THE PRINCETON OCEAN MODEL USING THE MULTI-REGION PARALLELIZATION SCHEME WITH MESSAGE PASSING INTERFACE

A. ABSTRACT

A few decades ago, when the emphasis of the computer industry was on the development of powerful vector machines, ocean modelers became interested in developing code that was highly vectorized to take advantage of those machines. Nowadays, because of their low price-performance ratio, the emphasis has switched to the development of Massively Parallel Processors (MPP). As a result many ocean modelers are now interested in the development of highly parallelizable code.

Here, an automatic multi-region parallelization of a typical sigma coordinate bottom-following model, the Princeton Ocean Model (POM), is developed. The multi-region results are shown to give the same results as the corresponding serial model codes. This type of parallelization is shown to have several advantages relative to standard parallelization. A key advantage of the multi-region parallelization scheme is that the sub-regions behave as independent models and only exchange information at a few (rather than hundreds) locations where the boundary conditions would normally be executed. Also, only seven prognostic variables are exchanged between sub-regions compared to the exchange of dozens of variables in standard parallelization. For a small number of processors, multi-region parallelization is shown to have superior performance compared to the standard parallelization. The multi-region parallelization also allows the parallelization of nearly 100% of the code with little modification, while the standard parallelization typically allows parallelization of only 80 to 90% of the code (the latter due to extensive modifications of the code).

B. INTRODUCTION

The development of numerical models with increasingly complex ocean physics higher spatial resolution, smaller time-steps, longer run times and near real-time data

assimilation capability requires significant increases in computational resources. Because of their low price performance ratio, both distributed memory Massively Parallel Processors (MPP), based on commodity chips and more recently Linux clusters have become increasingly important to supercomputing. The increasing use of MPP and Linux clusters makes it imperative to develop and implement parallel codes. Since POM is a serial code, it is necessary to parallelize the code to be able to run simulations in a reasonable time frame.

Here a different and new parallelization approach is implemented, a multi-region parallelization scheme is used, in which the initial domain is subdivided into several sub-domains. Each sub-domain runs on a different processor. All of the calculations are performed as if each sub-region was a completely independent ocean model. After the boundary conditions (BC) are calculated for each sub-domain, data is exchanged between sub-regions using the Message Passing Interface (MPI) library. MPI is a library of Fortran, C, C++ subroutines designed to exchange information in parallel computers, clusters of workstations and heterogeneous networks.

Since the version of the Princeton Ocean Model (POM) used in this study does not allow land masking, there could be a significant increase in the computational speed of the model if multi-regions were used. In particular, careful implementation of a multi-region POM could significantly reduce the number of land points effectively calculated. As a result, reduction in time for running the model would be achieved not only because several parallel processes would be running simultaneously and going through the same code with different data subsets, but also because the number of points calculated over land could be significantly reduced. In the following sections the use of multi-region parallelization is explored with the message passing interface protocol for use in the POM.

C. MULTI-REGION PARALLELIZATION

The standard parallelization is discussed in Appendix C. Here, the multi-region parallelization is used. Instead of having sub-domain models running in different

processors with a halo region for the calculations where data needs to be exchanged for all the variables in each loop (involving usually hundreds of synchronization and transfer points), there are sub-region models running in different processors with a MPI exchange region (MPIER). This is a region common to adjacent processes, where just the basic prognostic variables are exchanged at every time step. For example, for POM there would be only five synchronization and transfer points. In particular, the basic prognostic variables exchanged would be temperature (T), salinity (S), the zonal component of the velocity (u), the meridional component of the velocity (v), elevation (η), the zonal component of the barotropic velocity (UA), the meridional component of the barotropic velocity (VA), and the magnitude (Q2) and length scale of the turbulent kinetic energy (Q2L).

The distinct advantage of this method is that the quantity of data exchanged is significantly reduced (several fold for the number of variables actually exchanged). Also, the number of synchronization and data exchange points is much less, increasing the speed of the processes.

D. MESSAGE PASSING INTERFACE (MPI) DETAILS

All the MPI multi-region runs were made in a double precision mode, after it was determined that the use of single precision induced errors on the order of 10^{-5} for the surface temperature after 30 days in the MPI multi-region mode. This also induced errors on the order of 10^{-4} for the same variable if standard parallelization was used. The MPI variable used to make the exchange was of the type MPI_DOUBLE_PRECISION, which is the equivalent of REAL*8 in Fortran.

Point-to-point and collective communication subroutines were used to execute the transfer between the several processes. The safest point-to-point communication mode, synchronous send, was used in which the send and respective receive commands are synchronized automatically. Since MPI send and receive subroutines only exchange adjacent data in memory, there are two alternatives when exchanging parts of matrices

between two processes, the use of an intermediate vector to where the data is copied and the use of MPI derived data types. Since MPI derived data types do not allow optimization, the intermediate vector option was used. As a result the data to be exchanged is first copied to a vector. Afterwards a call to a MPI send subroutine is executed. A corresponding MPI receive call is then executed on the receiving process that will receive the vector. The data in the vector is then transferred to the destination variable.

Even if synchronous communication methods are used, note that, with more than two processes it is still possible to have deadlocks. Different communicators and barriers are used to avoid this situation. In particular, at some chosen locations in the model, the processes are forced to wait for each other to avoid deadlocks.

E. PRACTICAL DETERMINATION OF THE MESSAGE PASSING INTERFACE EXCHANGE REGION (MPIER)

It is usually not too difficult to determine the dependencies between the different variables, inside each loop in the standard parallelization. Consequently the halo regions are readily determined. For the multi-region parallelization this is not the case since the dependencies have to be calculated for each prognostic variable over hundreds of lines of code. In this case an idealized model can be used to do an experimental determination of the MPI exchange region. The idealized case we use here to calculate north-south (west-east) dependencies calculated independently using a north-south (west-east) channel, with north-south (west-east) winds on an f-plane with cyclic boundary conditions. Note that the size of the cyclic boundary conditions when no instabilities are generated will be the size of the MPIER. Here, only the experiment for the north-south dependencies will be shown.

For this test a simple model is used which has a north-south channel with a wall on the western side and a simulated continental shelf and slope on the eastern side (Figure 5. 2a). The corresponding slope parameter is shown in Figure 5. 2b. While the continental shelf was simulated with a slope parameter of 0.09, the continental slope had

a larger slope parameter of 0.2 (which is the maximum value that should be used in sigma coordinate ocean models, according to Mellor, 1998). The model is initialized with a temperature profile and constant salinity given by

$$T(x, y, z) = 5 + 15 * e^{\left(\frac{z}{1000}\right)} \text{ } ^\circ\text{C}$$

$$S(x, y, z) = 35 \text{ psu}$$

where T is temperature and S is salinity. The model used cyclic boundary conditions for all the basic prognostic variables in the north-south direction. Both the initial velocities and elevation are set to zero, to avoid artificial inertial oscillations induced in the model, the initial wind stress is set to zero. Increasing linearly at every internal time step until the final value of 0.1 Pa is achieved (at ~ 10 days). Afterwards the wind stress was kept constant. Figure 5.3 shows the wind stress at day 10.

Since POM uses an Arakawa C-Grid (Figure 5.4), all the basic prognostic variables have boundary conditions (BCs) at the first and last grid points, except for the meridional (zonal) velocities in the southern (western) boundary where the boundary is located at the second grid point.

In the first experiment the model uses cyclic boundary conditions with three common lines as seen in Figure 5.5a. Because of the use of the Arakawa C-Grid, this is the least number of common lines that can be used to have cyclic boundary conditions. The three common lines are the suggested number for the cyclic boundary conditions according to Mellor, 1996. In Figure 5.5a line 3 is coincident with line 100, line 2 with line 99 and line 1 with line 98. After each time step the basic prognostic variables, instead of being calculated by linear boundary condition formulations, are exchanged between the corresponding points. Because there is no alongshore variation in the forcings, in the topography or in the coastline geometry and the model uses an f-plane. The expected result is that there should be no meridional variation for all the prognostic variables. Unexpectedly, however, an instability does develop slowly over time. By day 23, there is a substantial increase of the instabilities, which happens when the maximum value for the velocity is between 60 and 70 cm/s. Figure 5. 5b at day 25 shows a high variation of the

meridional component of the baroclinic velocity (v) with a variation of about 70 cm/s and a length scale of about 50 km. This instability develops initially over the continental shelf and is seen over the entire coastal water column (not shown). By day 43 these features detach offshore, creating a connecting loop between two different poles of high velocity components (Figure 5.5c). Note that these loops are well defined near the boundaries which is an indicator of instability at these locations. By day 80 the fully developed signal of the meridional component of the baroclinic velocity is discernible (Figure 5.5d) with two different columns of large meridional variation in the v component of velocity. While highly developed areas of convergence and divergence are discernible (Figure 5.5e, coastal zoom) near the coast, they are difficult to detect in the temperature signal (Figures 5.5e and 5.5f).

This experiment shows that it is not possible to use only three common points to have stable cyclic boundary conditions over time. In the next experiment, four common points (Figure 5.6a) are used with exactly the same initial fields and forcing as before. The model results (Figures 5.6-e) show no meridional variation of the values of all the basic prognostic variables which agrees with the expected result.

A comparison of the values of the prognostic variables with similar experiments using five and six common points for the cyclic boundary conditions shows the same results as with the four common points. As a result, it is concluded that four points is the ideal boundary condition length for the cyclic boundary conditions of POM in the north-south direction. Note that the same experiment run in a west-east channel also yielded the same results for the west-east direction.

If some algorithms in the model are changed, for example, if the second order centered in space algorithm for advection is changed for the multidimensional positive definite advection transport algorithm (MPDATA), the same set of tests has to be repeated in order to determine the new dependencies. Note that with this test only the dependencies for the fully calculated non-linear equations are determined (i.e., the boundary condition dependencies are not calculated). Boundary condition formulations can have either wider local dependencies where the MPIER should be changed

accordingly, or global dependencies (e.g., volume constraint) where corrections have to be applied separately. To be sure that all of these BC dependencies are determined, a comparison between the results of the serial model and the corresponding results of the multi-region model should always be done after the initial setup of the model or after changing any of the algorithms. This practical method of determining dependencies should be able to be used in any other model that uses finite difference algorithms.

F. MESSAGE PASSING INTERFACE (MPI) EXPERIMENTS

To verify that the use of the MPI will not induce any instabilities, a test is done with the previous model setting with four cyclic boundary points run in duplicate (with MPI) before starting to divide the model in sub-regions. Here the cyclic boundary conditions will be exchanged between the two different processes (see Figure 5.7).

The results obtained using MPI are the same as the ones obtained in the previous experiment. This shows that the MPI exchange does not induce any new type of error, non-linear interaction or approximation (note that, the MPI variable is also double precision).

The next experiment consists of dividing the initial region in two MPI sub-regions (Figure 5.8a). In this case it is necessary to increase the total number of points in the model from 100 to 104, because four common points are needed to exchange information between the two processes. In Figure 5.8a, the MPIER region between processes corresponds to the points 49 to 52 while the data exchange between points 1 to 4 and 97 to 100 are the cyclic boundary conditions. The results of this are the same as for the previous experiment, which shows that MPI subroutines can be used for the subdivision of POM in sub-regions and without inducing spurious errors.

To determine running times in the standard parallelization and sub-region parallelization, the north-south channel model, described previously was used, with 100 by 70 by 21 grid points with cyclic boundary conditions. The results using this model are shown in Table 5.1. The multi-region models shown in Table 5.1 can be seen in Figures

5.8a-c. In Table 5.2 the results for the model used in Chapter II, the Northern Canary Current System was used. This is a 287 by 241 by 21 grid point model. The several sub-regions using this model are shown in Figures 5.9a-e.

	Increase in Points Calculated (%)	Time (s)	Time in Ideal Parallel (s)	Efficiency* (%)
Serial	---	500	---	---
SP*-2 Threads	0	287	250	87.1
SP*-3 Threads	0	185	166	90.1
SP*-4 Threads	0	156	125	80.1
MR* – 2 Procs. Longitudinal (Figure 5.8a)	4	231	250	108.2
MR* – 3 Procs. Longitudinal (Figure 5.8b)	8	165	166	101.0
MR* – 4 Procs. Longitudinal (Figure 5.8c)	12	146	125	85.6

Table 5.1. Running times for north-south channel (model 1) with 100 by 70 by 21 points and cyclic boundary conditions.

* SP – Standard parallelization

* MR – Multi-region parallelization

* Efficiency – ratio time in ideal parallel (column 4) and time (column 3)

* Ideal Parallel – Same as standard parallelization with zero transfer time and memory allocation between threads (not achievable in real computers).

	Increase in Points Calculated (%)	Time (s)	Time in Ideal Parallel (s)	Efficiency[*] (%)
Serial	---	3008	---	---
SP [*] -2 Threads	0	1560	1504	96.4
SP [*] -3 Threads	0	1094	1003	91.7
SP [*] -4 Threads	0	856	752	87.8
MR [*] – 2 Procs. Longitudinal (Figure 5.9a)	1.9	1520	1504	98.9
MR [*] – 3 Procs. Longitudinal (Figure 5.9b)	3.9	920	1003	109
MR [*] – 4 Procs. Longitudinal (Figure 5.9c)	5.8	820	752	91.7
MR [*] – 4 Procs. Rectangular (Figure 5.9d)	4.3	770	752	97.7

	Increase in Points Calculated (%)	Time (s)	Time in Ideal Parallel (s)	Efficiency* (%)
MR* – 4 Procs. Rect. No Land (Figure 5.9e)	3.5	700	752	107.4

Table 5.2. Running Times for the Northern Canary Current System (model 2) (see Chapter II) with 287 by 241 by 21 Points.

* SP – Standard parallelization

* MR – Multi-region parallelization

* Efficiency – ratio Time in Ideal Parallel (column 4) and Time (column 3)

* Ideal Parallel – Same as standard parallelization with zero transfer time and memory allocation between threads (not achievable in real computers).

The total running time of the program with the standard parallelization and standard ideal parallelization is:

$$T_{SP} = \frac{T_{SR}}{M} + T_{SYNC} + T_{MEM} + T_{EXCH} \quad (5.1)$$

$$T_{ISP} = \frac{T_{SR}}{M} \quad (5.2)$$

where T_{SP} is the running time of the standard parallel program, T_{ISP} is the running time of the ideal standard parallelization program, T_{SR} is the corresponding running time for the serial program, M is the number of threads used, T_{SYNC} is the synchronization time, T_{MEM}

is the time spent in memory allocations due to the parallelization and T_{EXCH} is the time spent in the actual exchange of data between threads. Since in a non-ideal computer, T_{SYNC} , T_{MEM} and T_{EXCH} are always positive, the time to run a standard parallelization program is always larger than the ideal time (T_{ISP}). This is supported by the values in Tables 5.1 and 5.2, which show that for all the standard parallelization cases, values for the efficiency are smaller than 100 %. As the number of threads increases, the amount of data actually exchanged also increases, resulting in increasing synchronization, allocation and exchange times with the respective drop in efficiency. While this is the general trend in the tables, note that for three threads there is an increase in efficiency compared to the two thread result in Table 5.1. This is due to other variables influencing the T_{SP} value, e.g., the size of the bus transfer.

Let us now compare the standard parallelization times with multi-region times. In the later case the time spent to run a model is given by:

$$T_{MR} = T_{BSR} + T_{SYNC} + T_{MEM} + T_{EXCH} \quad (5.3)$$

where T_{MR} is the time necessary to run a multi-region model, T_{BSR} is the time necessary to run the biggest sub-region in one processor, T_{SYNC} is the synchronization time, T_{MEM} is the time spent in memory allocations due to the parallelization and T_{EXCH} is the time spent in the actual exchange of data between processes.

Since the sub-regions are always larger than the sub-blocks (i.e., there are always four common points between two adjacent sub-regions) and there is always time lost in the exchange of data, it seems that the efficiency should be always less than 100%. This expected result is however contradicted by the inspection of the values in Tables 5.1 and 5.2. To understand these largest values for the efficiency, the dependency of the running times must be checked with the total amount of points in the model. Let us use the previous models (i.e., the north-south channel, model 1, and the NCCS, model 2) to illustrate this. The ratio of the total number of points between model 1 (see Table 5.1) and model 2 (see Table 5.2) is 5.03, while the ratio of the serial running times between the

same models is 6.02. This can be interpreted to mean that model 2 takes 18% more time to run than it would take if the numerical schemes solved by the model were linearly dependent on the total number of points N . This shows that there is a non-linear dependency between the number of points and the total amount of time needed to run the POM model. In particular, the algorithms used in the POM are between order N and $N \cdot \log(N)$, where N is the total amount of points in the model. This means that

$$T_{BSR} < \frac{T_{SR}}{M} \quad (5.4)$$

if the size of sub-regions is similar. The time gained because of the non-linearity of T_{BSR} with the total number of points can exceed the summation of T_{SYNC} , T_{MEM} and T_{EXCH} . As a result the efficiency will be higher than 100%.

These results show that for two to four processors, the efficiency is always higher for multi-region models than for those with standard parallelization for the same number of processes/threads (see Tables 5.1 and 5.2). The results of Table 5.2 also show that not only the number of sub-regions affects the efficiency but also their geometry. When four rectangular sub-regions (Figure 5.9d) are used instead of longitudinal ones (Figure 5.9c), the efficiency increases by 6%. The reason for this is that the number of points calculated has been decreased by 1.5% relative to the longitudinal sub-regions (see Table 5.2). The MPIER region is also smaller which results in a corresponding decrease in the data exchange between models.

Another advantage of using sub-regions is that in complex geometry coastline regions, such as in the NCCS the calculations over land points can be greatly reduced. This is the last example shown in Table 5.2 and Figure 5.9e which shows a reduction of 19% in the number of points calculated. However, there is only a gain of 10% relative to the complete rectangular sub-region calculation because this model is a mix of rectangular and longitudinal geometries. As a result, it is not as efficient as a pure rectangular model. Also because of the coastline geometry it was not possible to make all the sub-regions of the same size. If one sub-region is larger than the others, the smaller

sub-regions still have to wait until the calculations for larger regions are executed, resulting in a loss of processing capability.

G. AUTOMATIC MULTI-REGION PARALLELIZATION

In order to be able to run the POM model in different platforms with a varied number of processors, an automatic parallelization of the POM is developed. Four common points are used for the MPIER region. In this version, the sizes and locations of each sub-region are first determined. The grid of each sub-region is subsequently calculated. Because Fortran 77 (the language in which POM is written) does not have true dynamic allocation of memory, only one process is made to read the whole initialization fields in order to avoid going beyond the stacksize limits. The fields are then sent to each sub-region, with each sub-region running a different process in a different processor.

The synchronization between the processes is executed only three times for each internal time step and two times for each external time step (once for the elevation and other for the barotropic velocities). The transfer of data between the different processes is executed automatically based on the previous determination of the sizes and position of each sub-region. An option exists to use cyclic boundary conditions, which can readily be used for test problems.

The transfer of data between the several processes was optimized. Adjacent processes of the same color in Figure 5.10a exchange data simultaneously between themselves. Afterwards, in a second step the adjacent processes of the same color in Figure 5.10b then exchange data simultaneously. With this simultaneous transfer among a high number of processes, both accumulation of latency and transfer times are avoided, resulting in an increase of the efficiency of the multi-region code.

Changes to the POM serial code are minimal. In particular, the subroutines that read the initialization and forcing data need to be altered. Subroutines only needed to be

inserted to make the transfer data between processes following the calculation of boundary conditions for the prognostic variables.

H. CONCLUSIONS

An automatic version of the multi-region POM was developed. The multi-region POM was shown to have several advantages relatively to traditional standardization methods. With the multi-region POM, the changes made to the code were minimal. In particular changes were only made in subroutines that read initialization and forcing. Only a few subroutines were needed to be inserted (and in only five locations) in the code to exchange data between sub-regions, i.e., just after the calculation of the boundary conditions for the prognostic variables. In contrast, the standard parallelization there are substantial changes made to the code and exchange of data is done in hundreds of locations, with increased synchronization and transmission times. The variables exchanged between processes in the multi-region were only seven basic prognostic variables (i.e., potential temperature, salinity, barotropic and horizontal baroclinic components of the velocity, elevation and the turbulent kinetic energy and length scale), while in the standard parallelization every variable with horizontal dependencies needed to be exchanged in every loop. For a small number of processes the multi-region parallelization was shown to always have a better performance than the standard parallelization. Contrary to the standard parallelization, it was shown that efficiency values could be greater than 100% due to the non-linear dependency of the running times with the total number of points. The efficiency was shown not only to be dependent on the number of sub-regions used but also on their geometry. When rectangular instead of longitudinal (compare Figures xx and XX) sub-regions were used, the efficiency of the model increased because the amount of data for transmission and the amount of duplicate points between sub-regions in the MPIER region decreased. This was due to transmission data being proportional to the perimeter of the sub-regions also sub-regions with geometries similar to squares have smaller perimeters (Ayoama and Nakano, 1999). The sub-region parallelization allowed parallelization of almost 100% of the code. Reading

external data turned out to be the most inefficient part of the code. While that does not correspond to the most time consuming part of the code, the problem can be solved with the use of input/output parallel libraries such as MPI 2, Hierarchical Data Format 5 (HDF 5) or NetCDF. In contrast, the standard parallelization only allows the parallelization of 80 to 95% of the code (to obtain values greater than 90% significant changes to the code have to be made), which greatly limits the performance of the POM model.

The biggest disadvantage of the multi-region POM is that there is duplication of calculation in part of the MPIER region between adjacent sub-regions, which artificially increases the total number of the points calculated by the model. This can be partially offset if major changes in the limits of the control variables in the loops are made.

A comparison of the automatic multi-region parallelization with the serial model showed that there is no type of non-linear interactions, approximations (round-off errors) or errors of any other kind induced by this type of parallelization. The results obtained with the multi-region model were the same as the results of the corresponding serial model.

I. REFERENCES

Amdahl, G.M. Validity of the single-processor approach to achieving large scale computing capabilities, In AFIPS Conference Proceedings vol.30 (Atlantic City, N.J., Apr 18-20), AFIPS Press, Reston, Va., 1967, pp 483-485.

Aoyama, Yukiya, and Jun Nakano, RS/6000 SP: Practical MPI Programming, International Technical Support Organization, 1999.

MacDonald, Neil, Elspeth Minty, Tim Harding and Simon Brown, Writing Message-Passing Parallel Programs with MPI, Edinburgh Parallel Computing Center, 1997.

Message Passing Interface Forum, MPI: A Message-Passing Interface Standard, 1994.

Message Passing Toolkit: MPI Programmer's Manual, Silicon Graphics, 2001.

MIPSpro Fortran 77 Language reference Manual, Silicon Graphics, 1999.

MIPSpro Fortran 77 Programmer's Guide, Silicon Graphics, 1999.

Pacheco, Peter, A User's Guide to MPI, 1995.

Pacheco, Peter and Woo Ming, MPI User's Guide in Fortran, 1997.

Parallel Programming with MPI, Ohio Supercomputer Center, 1999

William Gropp, Ewing Lusk and Anthony Skjellum, Using MPI: Portable Parallel Programming with the Message Passing, MIT Press, 1994.

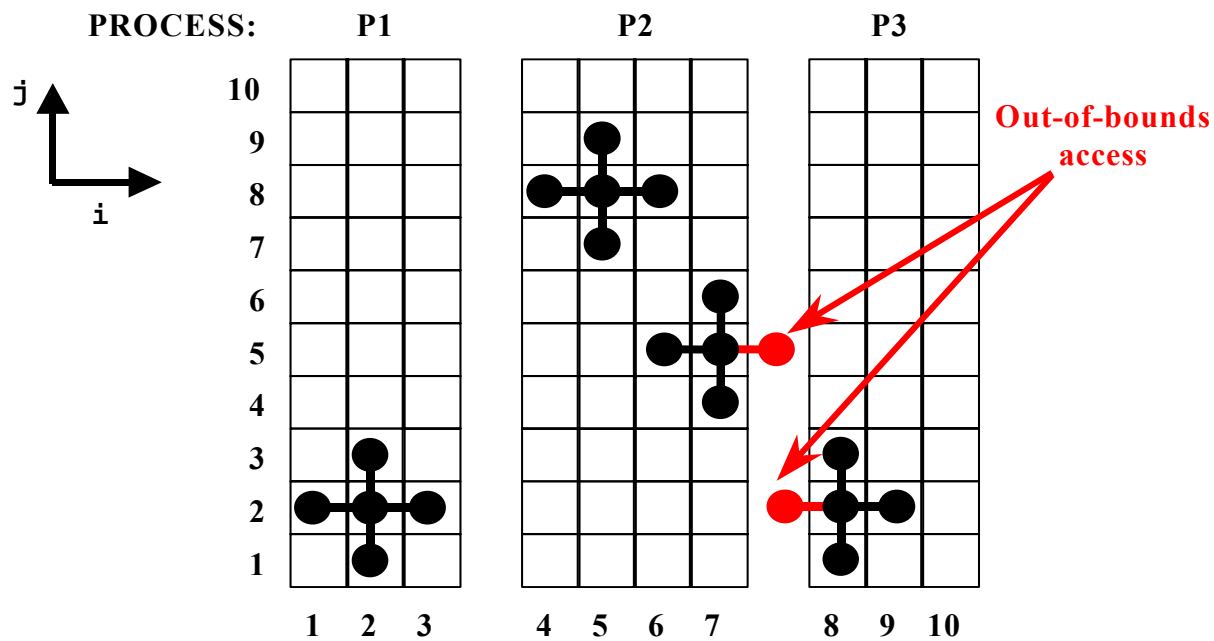


Figure 5.1a. Illustration of how an adjacent dependence causes out-of-bounds data references on processes P2 and P3 (from SMS Users Guide).

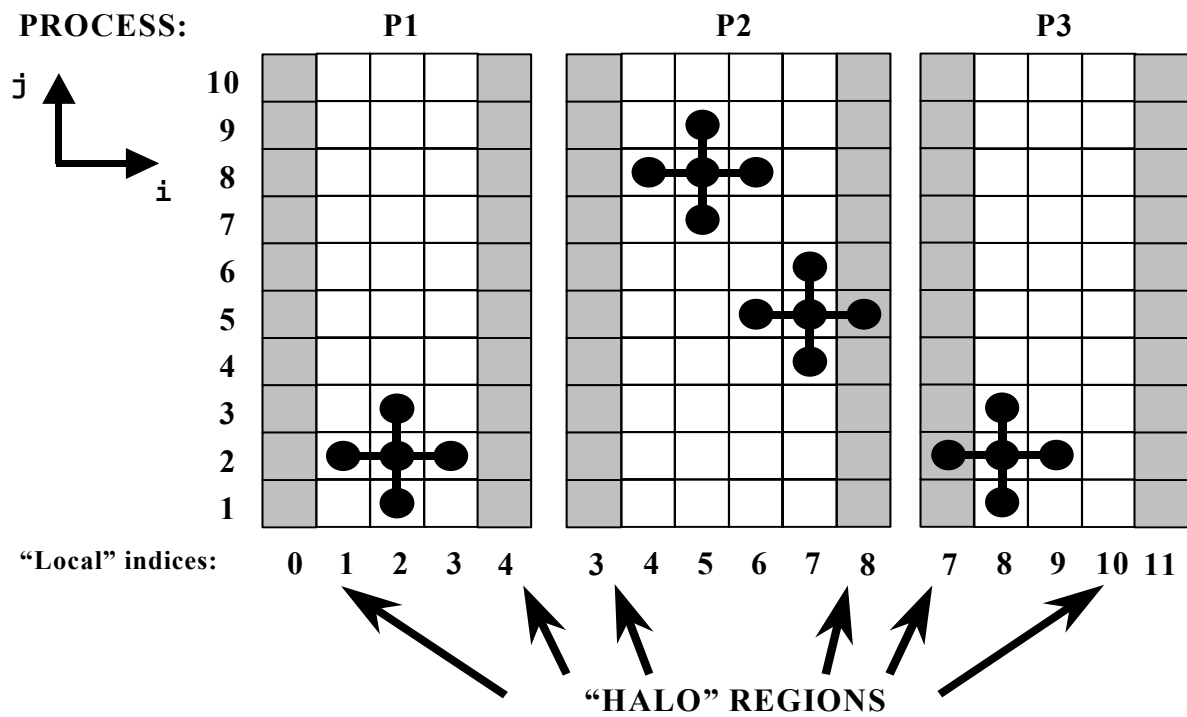


Figure 5.1b. Halo regions eliminate the out-of-bounds array references. Notice the distinction between interior points (in white) and halo points (in gray). The local indices of the halo points on the domain edges actually lie outside the serial domain range (1 to 10). These edge halo points are only used for problems that have periodic boundary conditions (from SMS Users Guide).

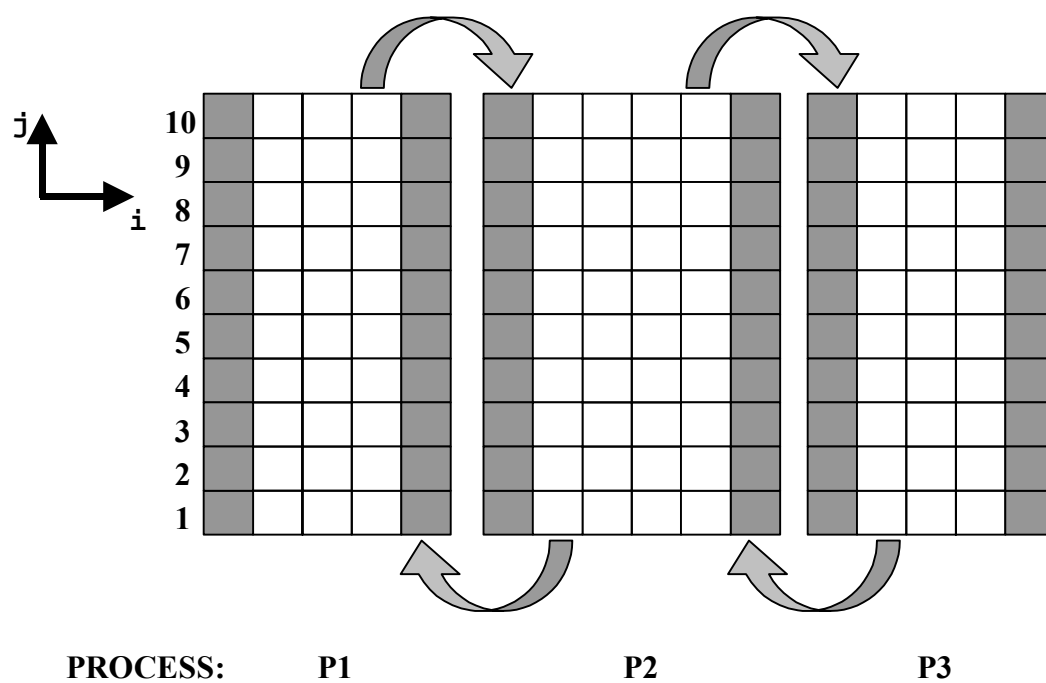


Figure 5.1c. Halo regions are updated by exchanging data between adjacent processes (from SMS Users Guide).

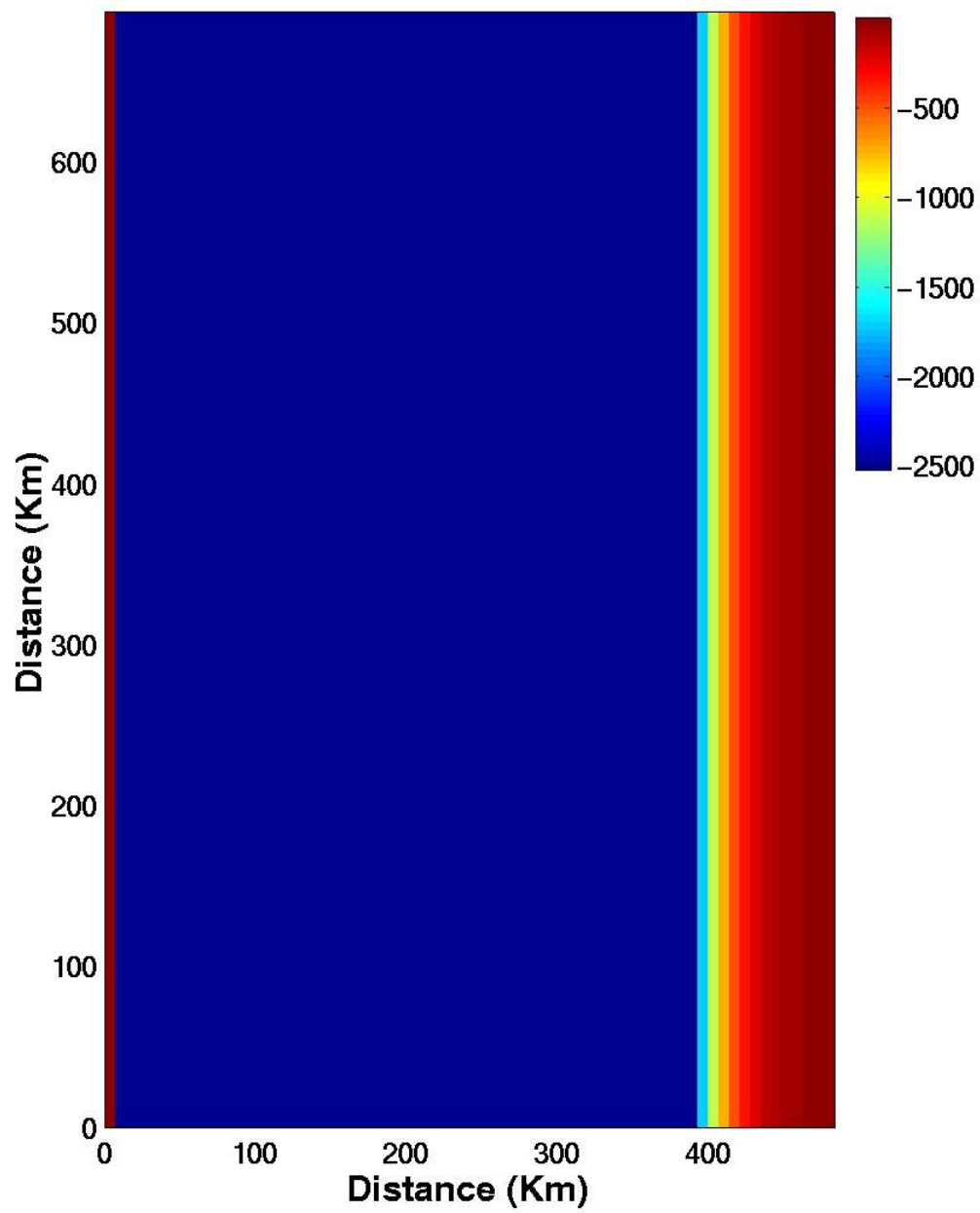


Figure 5.2a. Topography, Depths in Meters.

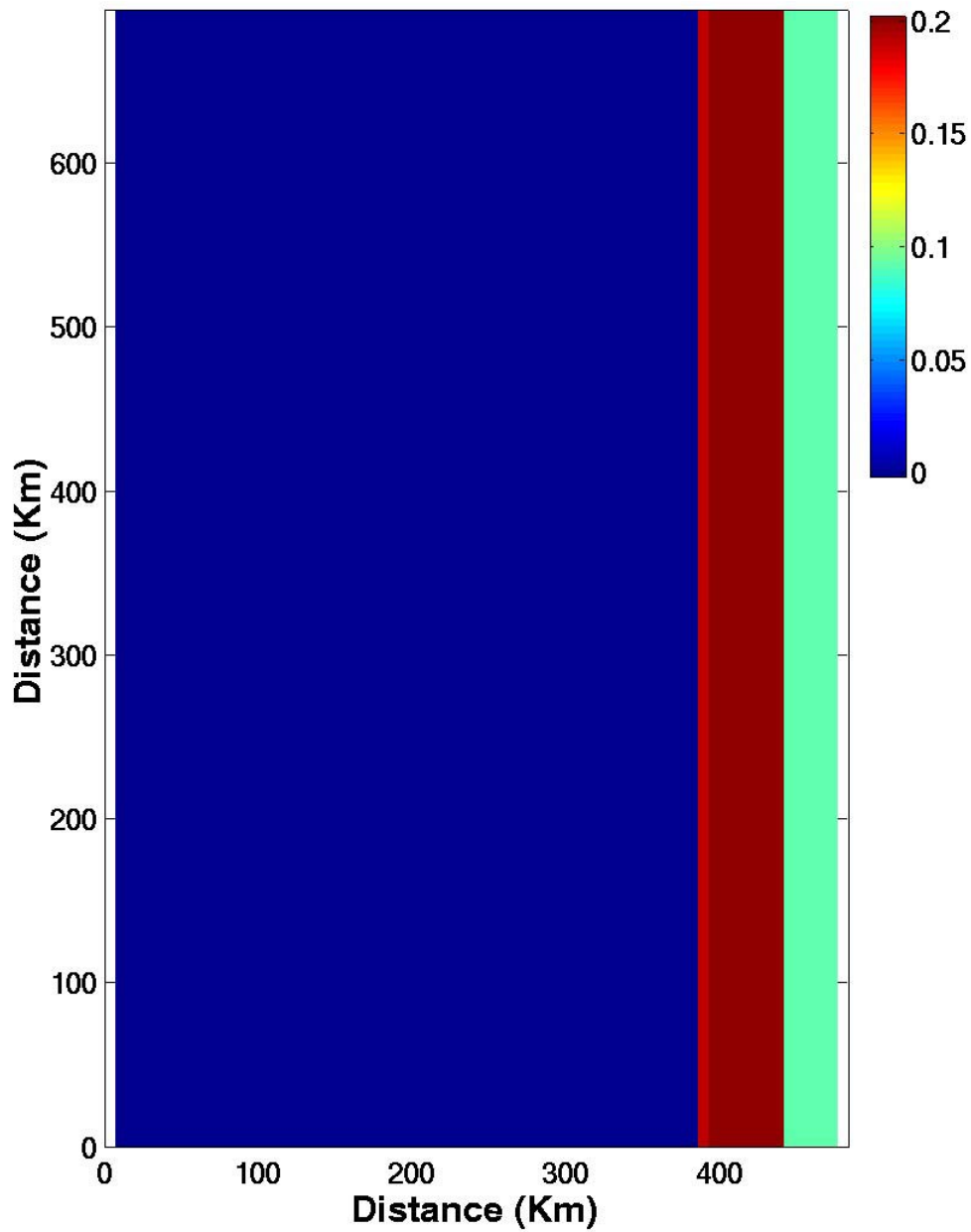


Figure 5.2b. Slope parameter defined as the absolute value of the difference in depths between adjacent points scaled by their mean. In this case it can be seen the simulation of the continental shelf with a slope parameter of around 0.09 and the continental slope with a value of 0.2 (the maximum suggested for sigma coordinate models).

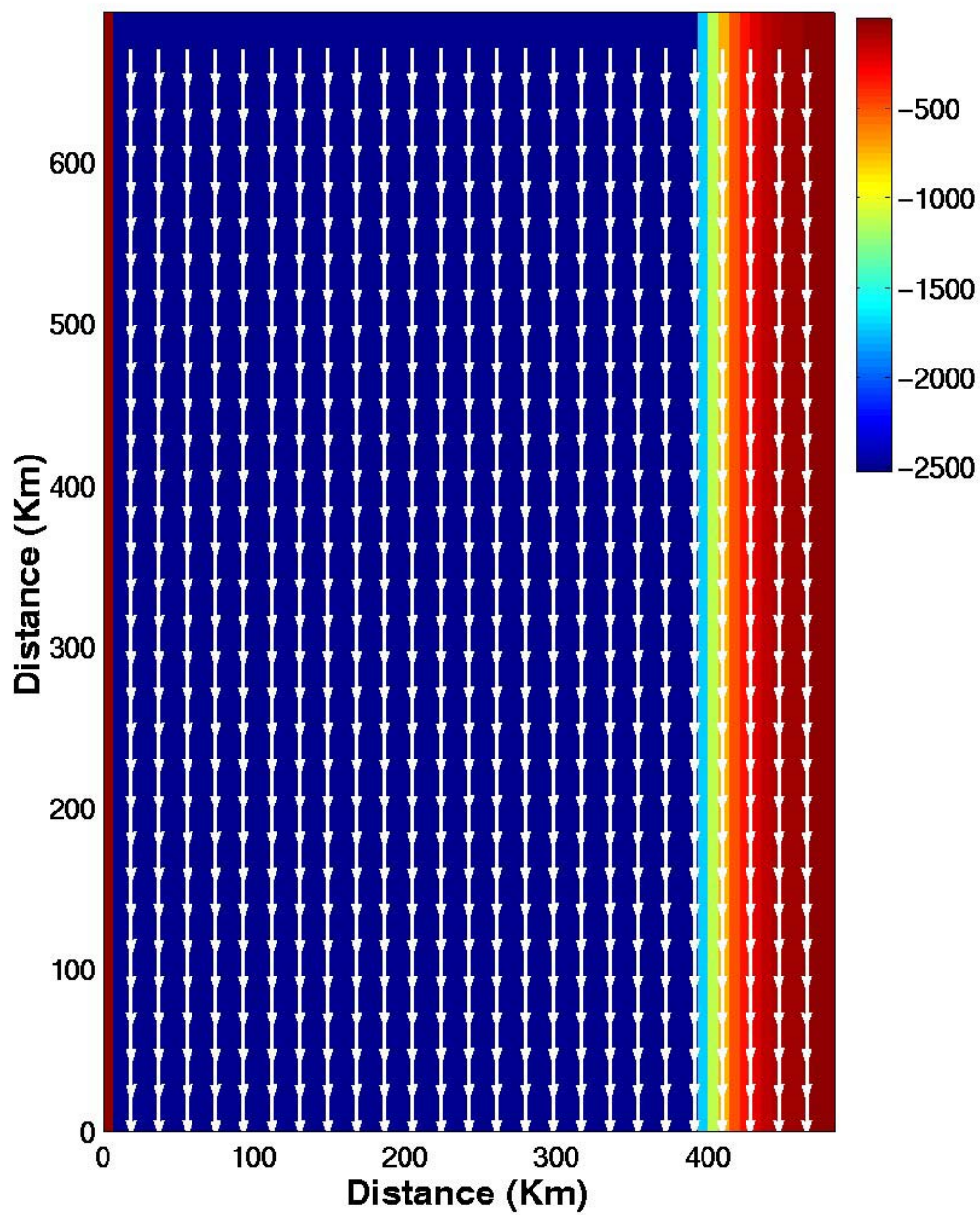


Figure 5.3. Wind Stress (Pa) (arrows) after 10 days over the topography (in color). The length of the arrows corresponds to 0.1 Pa. Depths in meters.

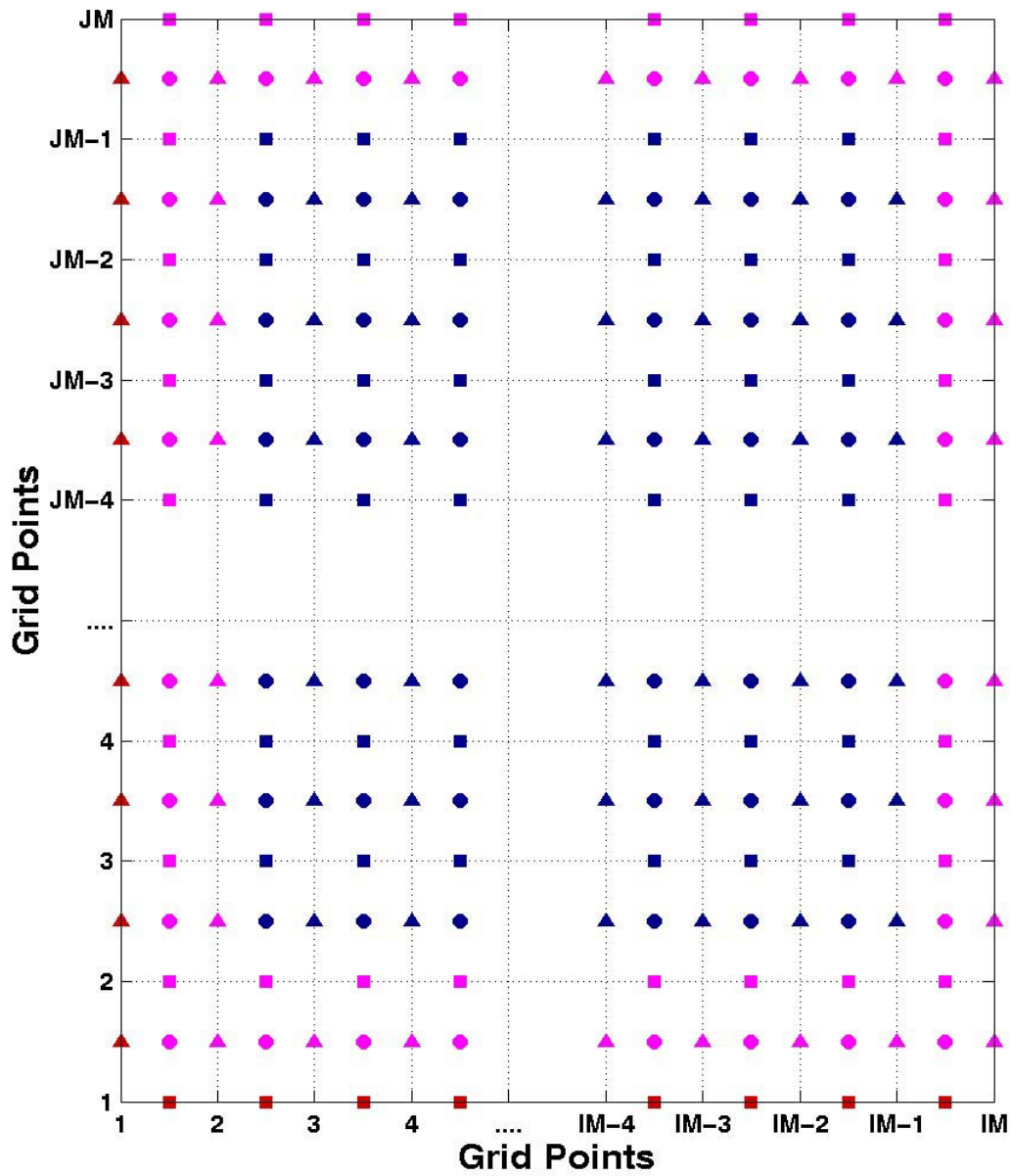


Figure 5.4. Representation of the Arakawa C-Grid. Squares represent the meridional component of the velocities, triangles the zonal component of the velocities and circles represent the elevation, temperature, salinity, and magnitude and length scale of the turbulent kinetic energy. In red, points not used, in magenta, boundary conditions and in blue, points fully calculated by the non-linear equations.

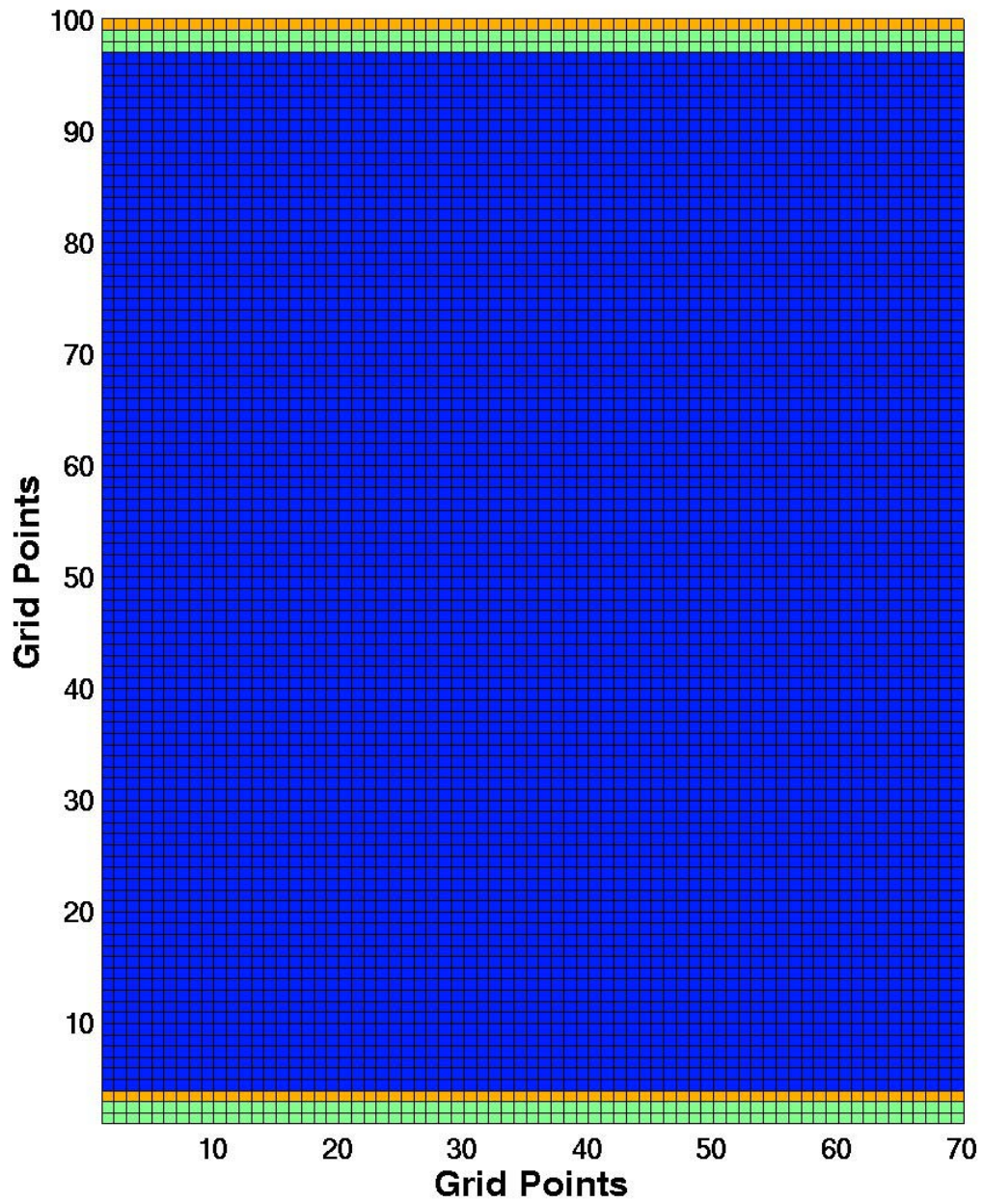


Figure 5.5a. Cyclic boundary conditions with three common points are shown in green and orange. In blue points fully calculated by the non-linear equations.

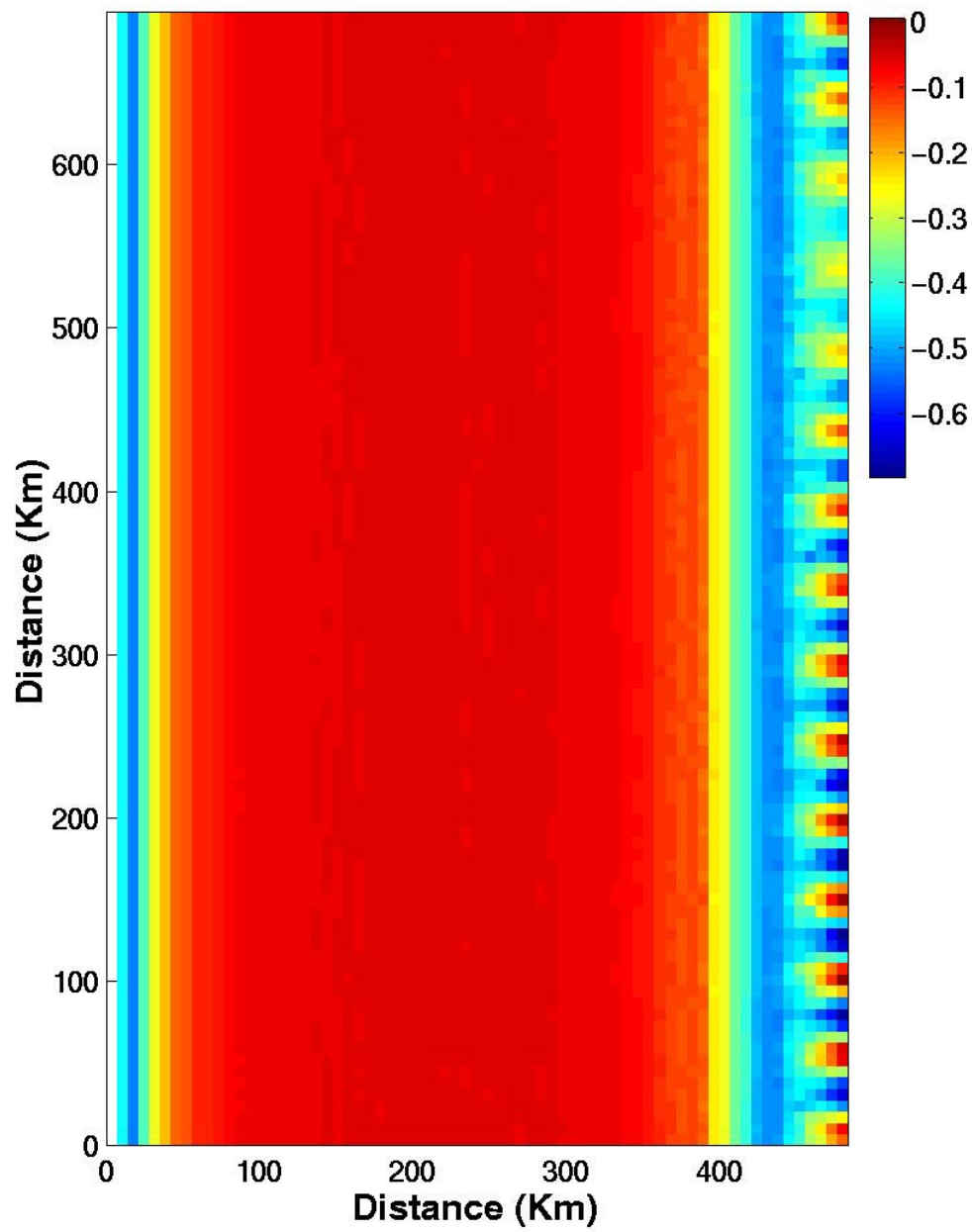


Figure 5.5b. Surface meridional velocity (m/s) component at day 25.

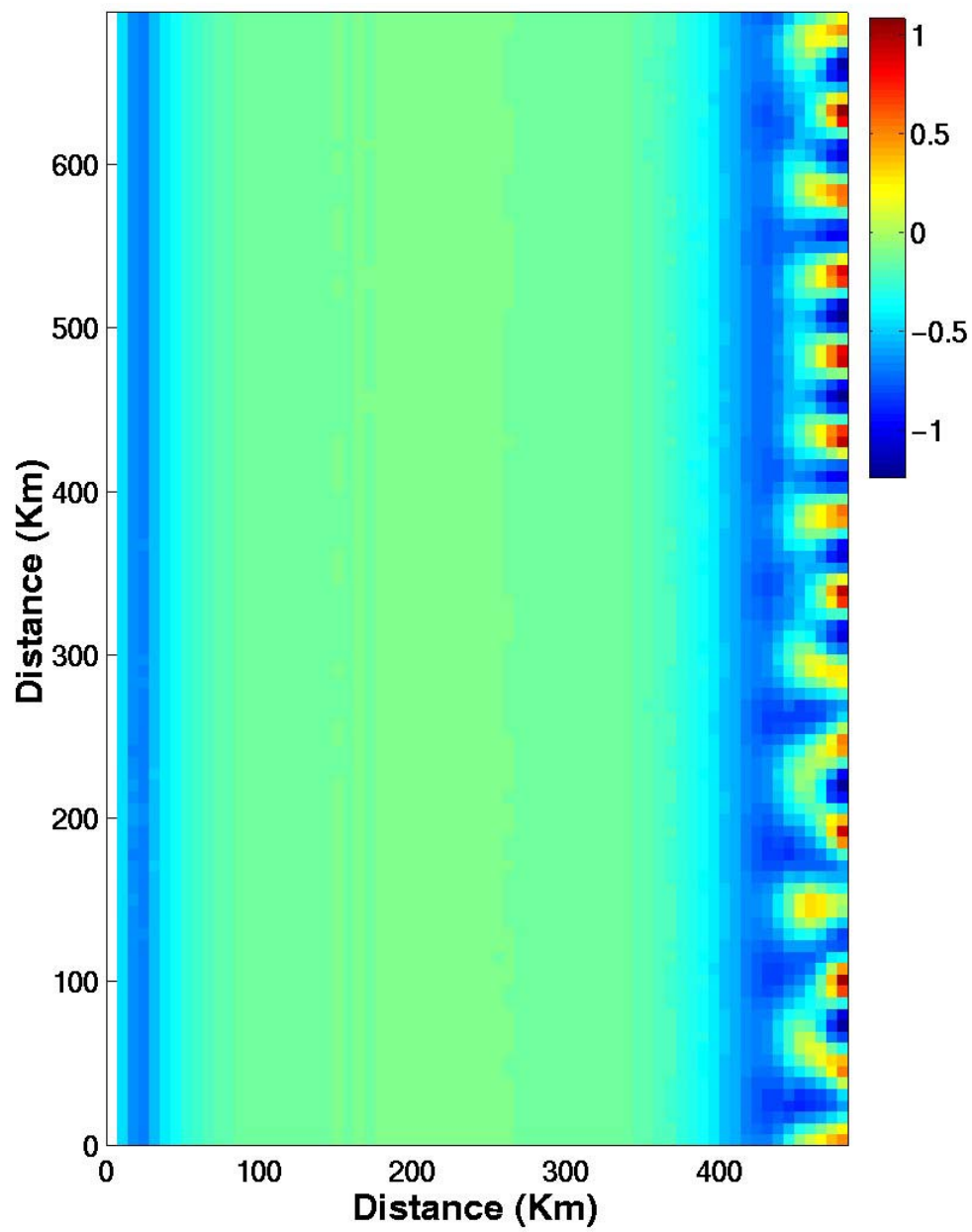


Figure 5.5c. Surface meridional velocity (m/s) component at day 43.

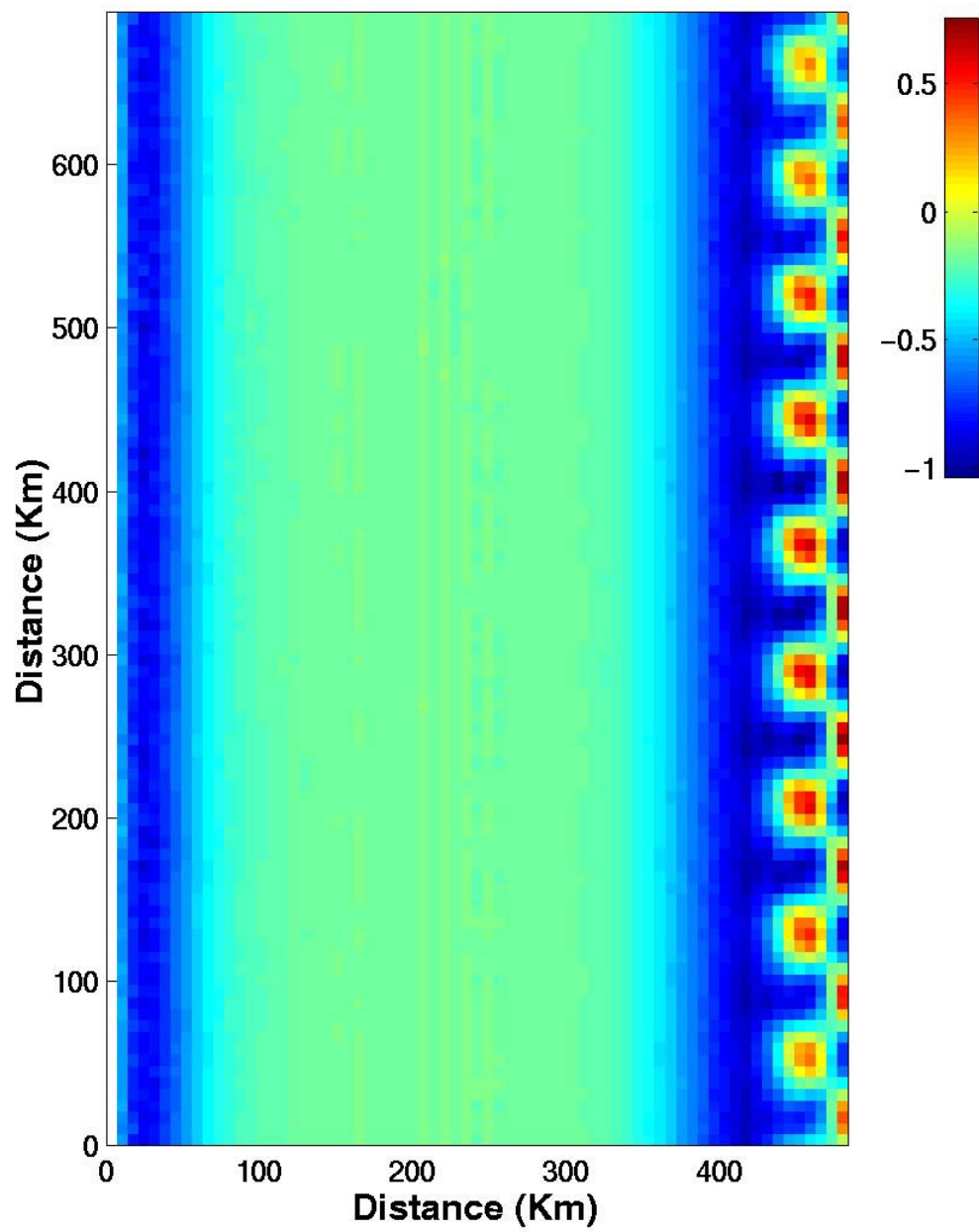


Figure 5.5d. Surface meridional velocity (m/s) component at day 80.

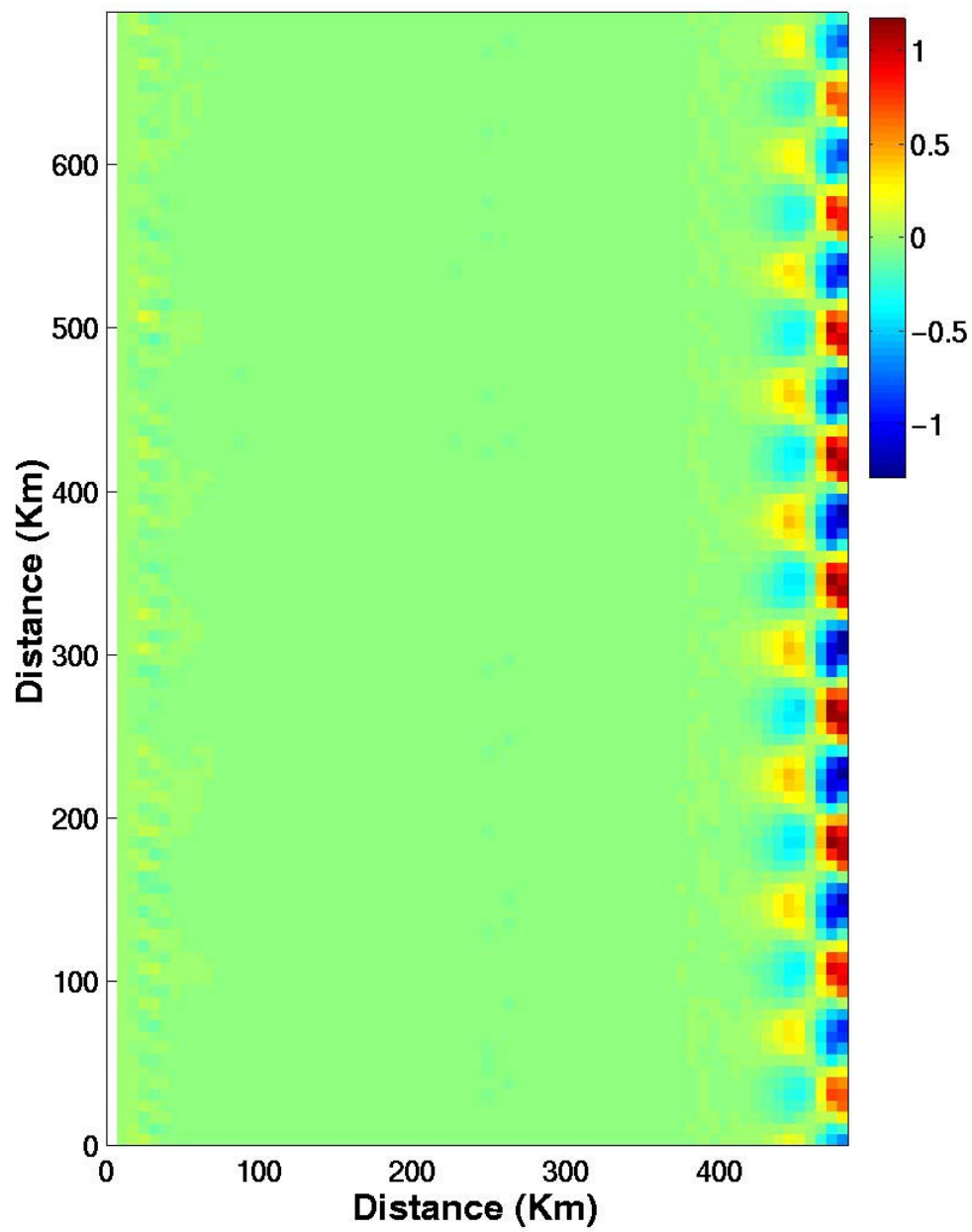


Figure 5.5e. Surface zonal velocity (m/s) component at day 80.

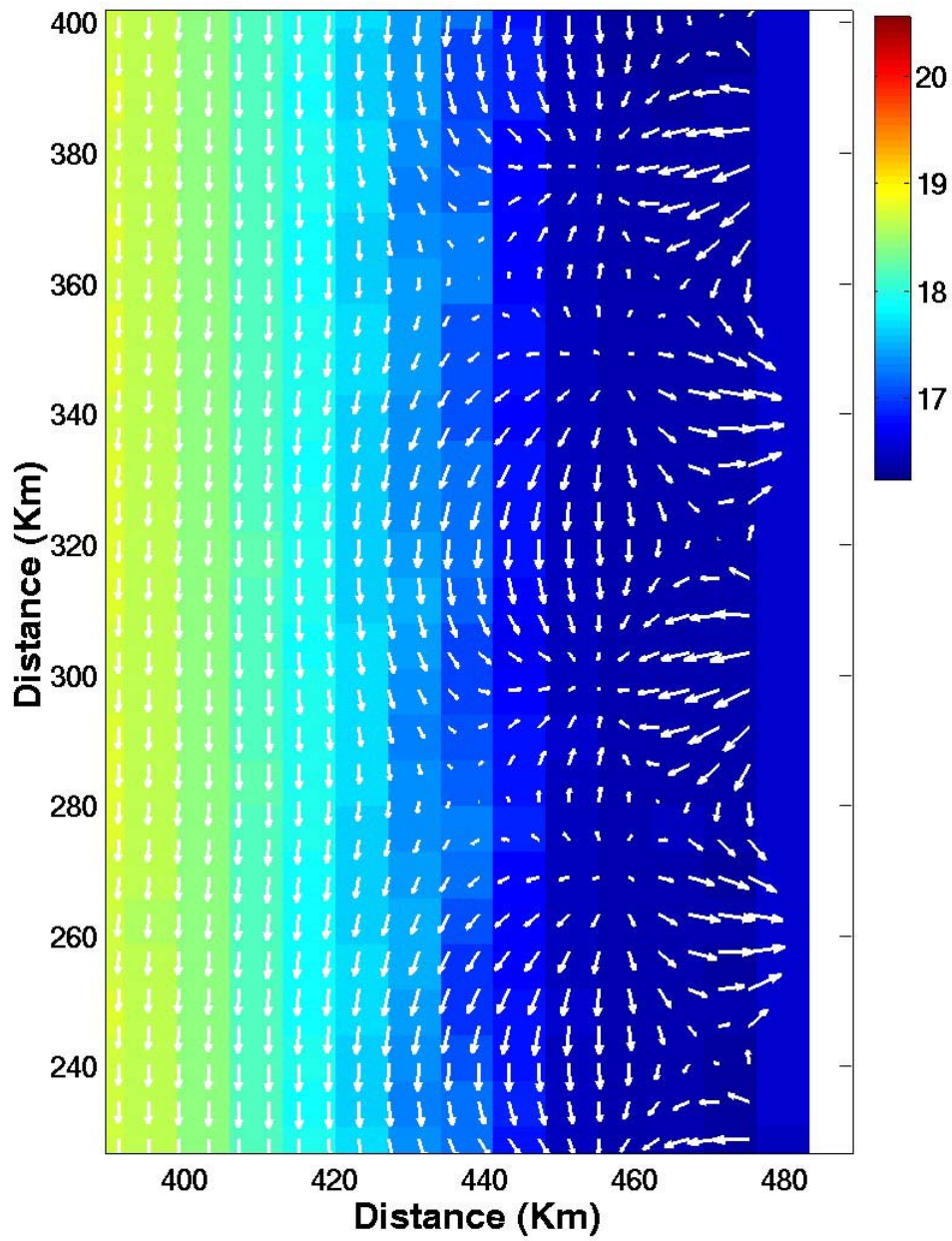


Figure 5.5f. Surface velocity (m/s) (vectors) and surface temperatures (°C) (in color) at day 80. Highest vector magnitude is 1.25 m/s

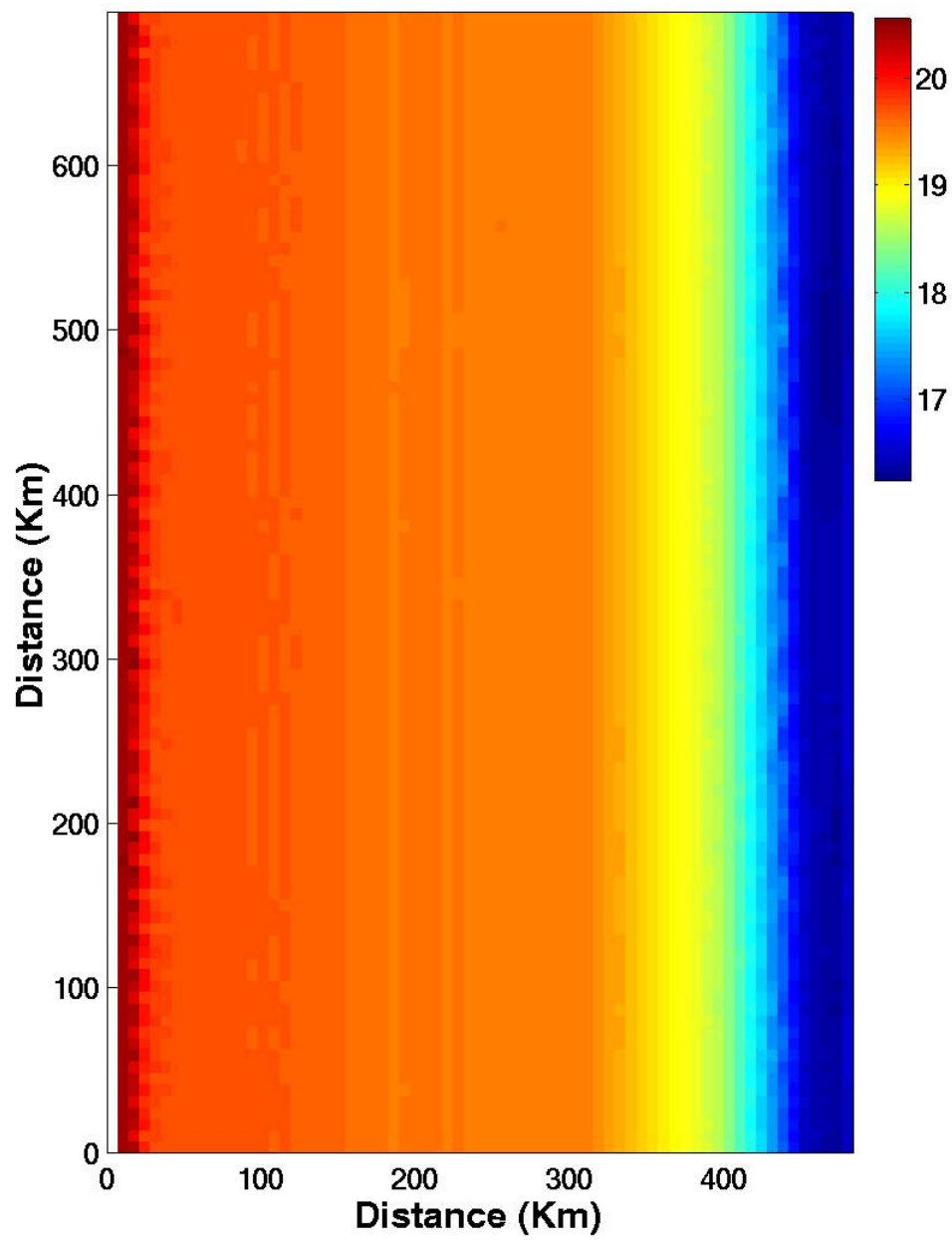


Figure 5.5g. Surface temperature (°C) at day 80.

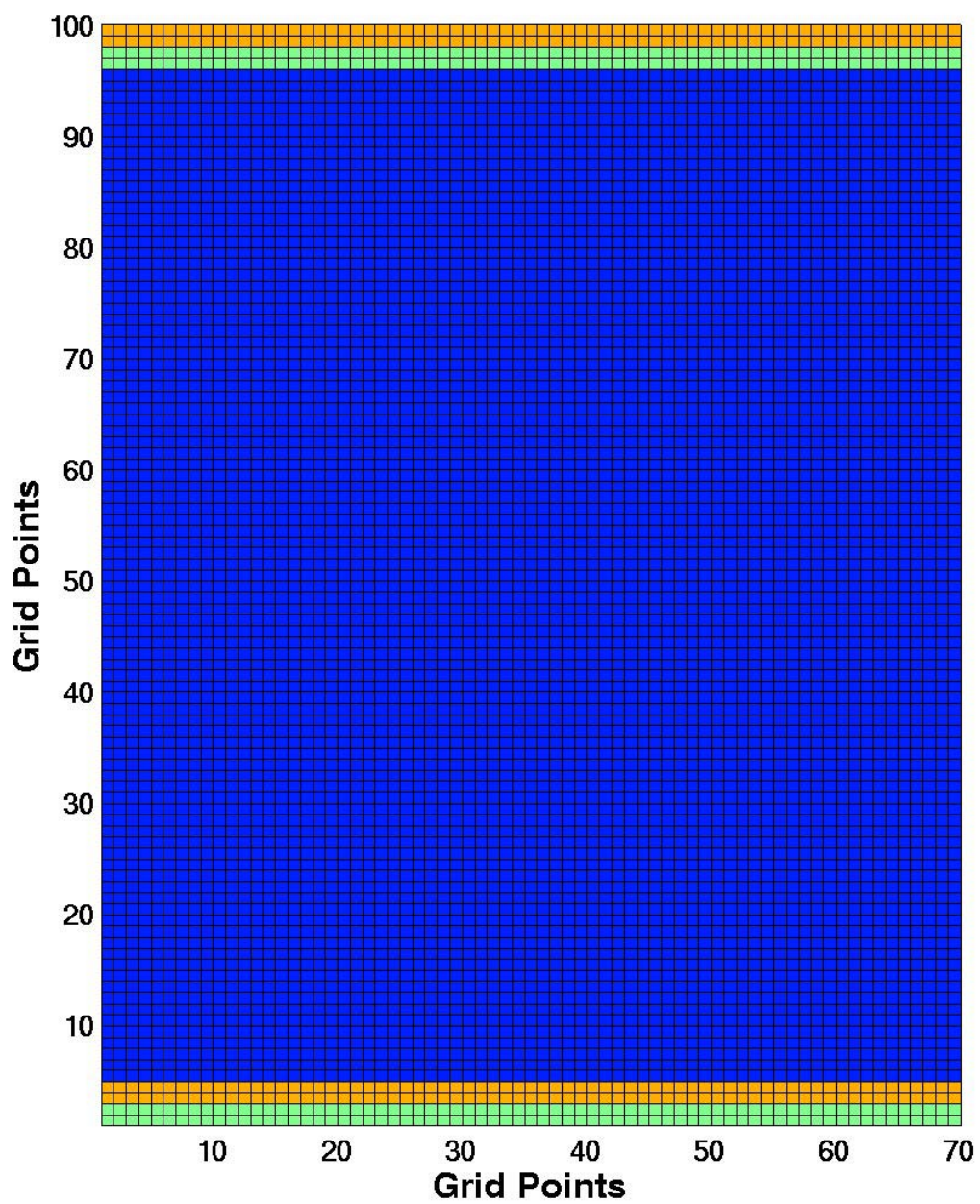


Figure 5.6a. Cyclic boundary conditions with four common points shown in green and orange.

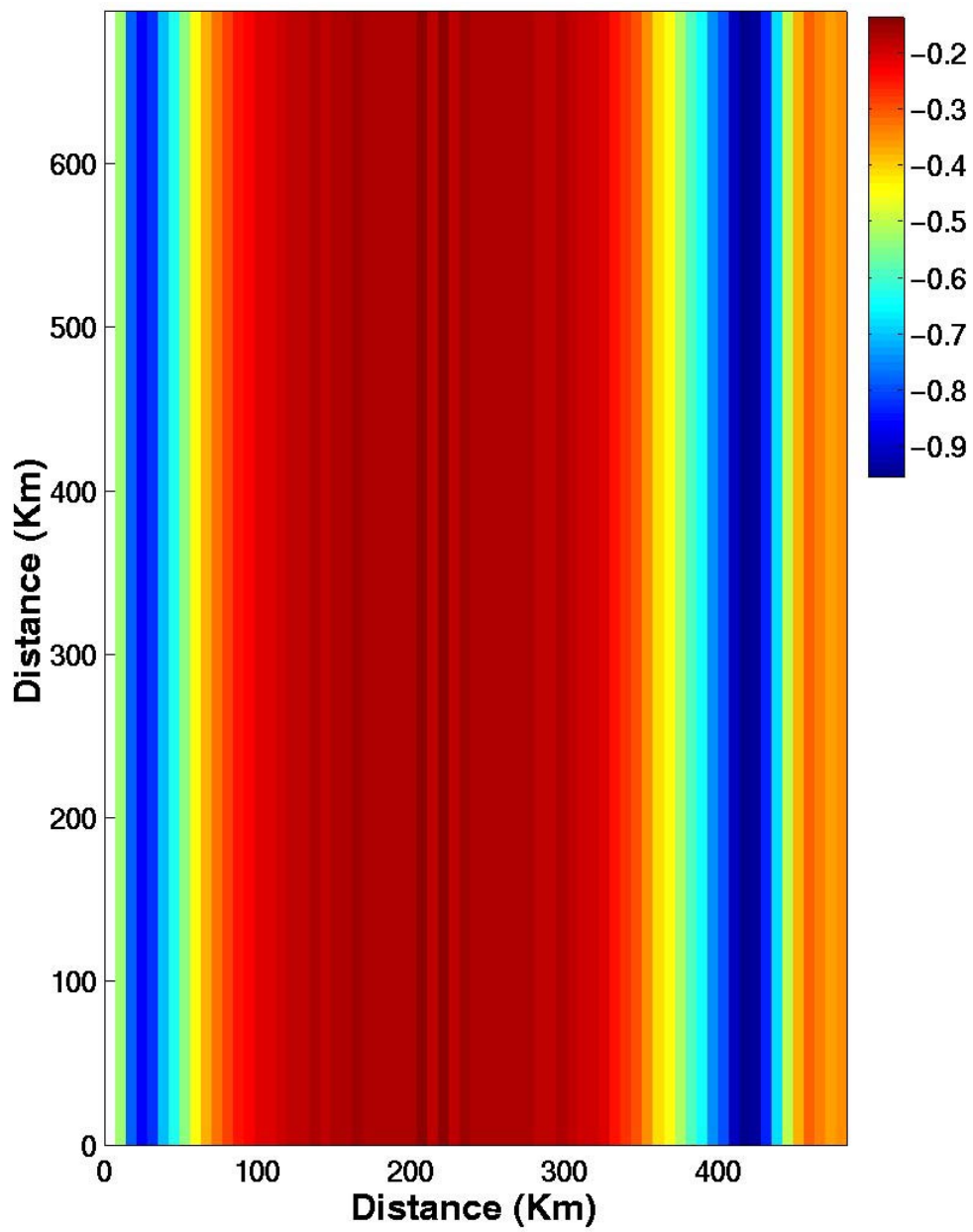


Figure 5.6b. Surface meridional velocity (m/s) component at day 80.

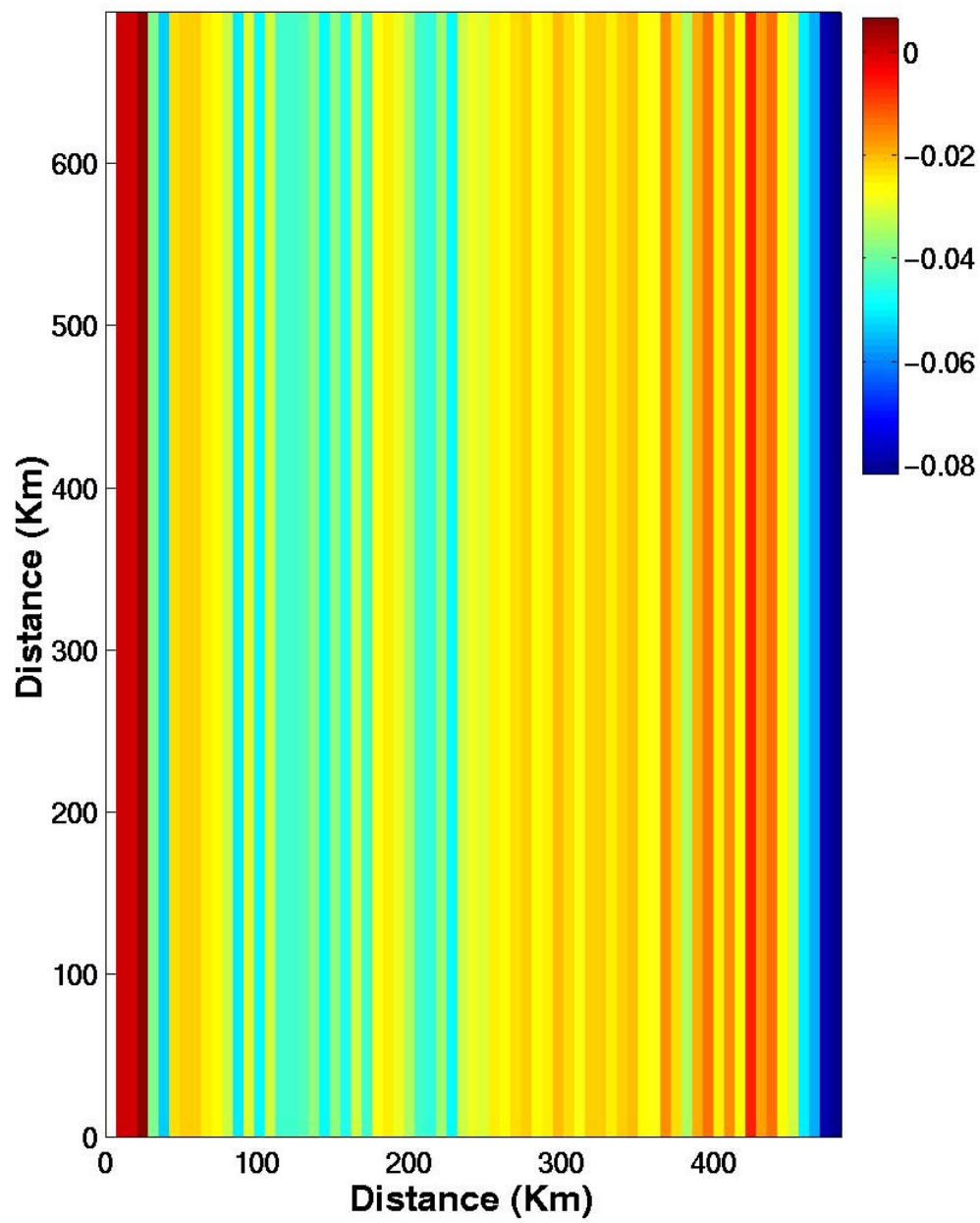


Figure 5.6c. Surface zonal velocity (m/s) component at day 80.

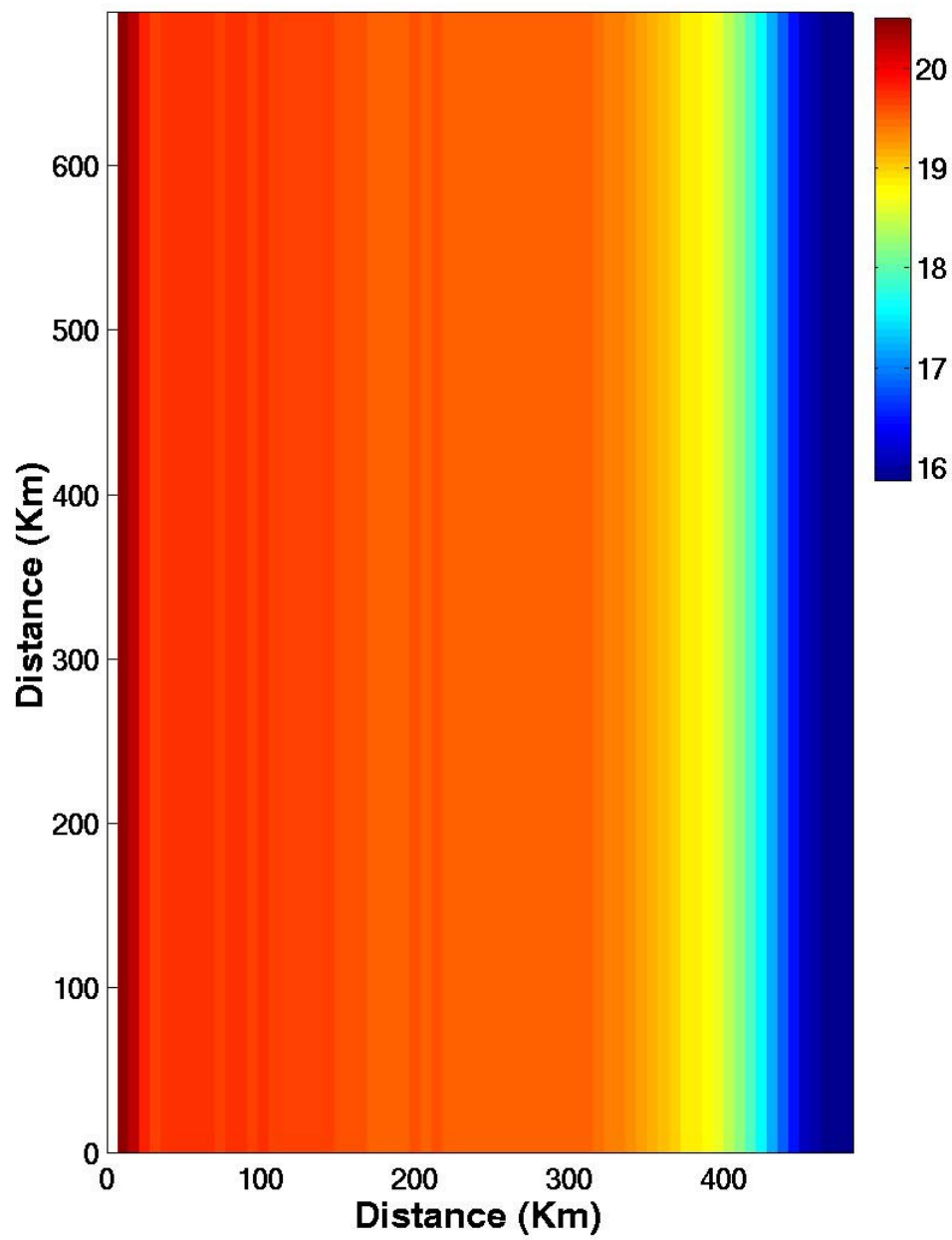


Figure 5.6d. Surface temperature (°C) at day 80.

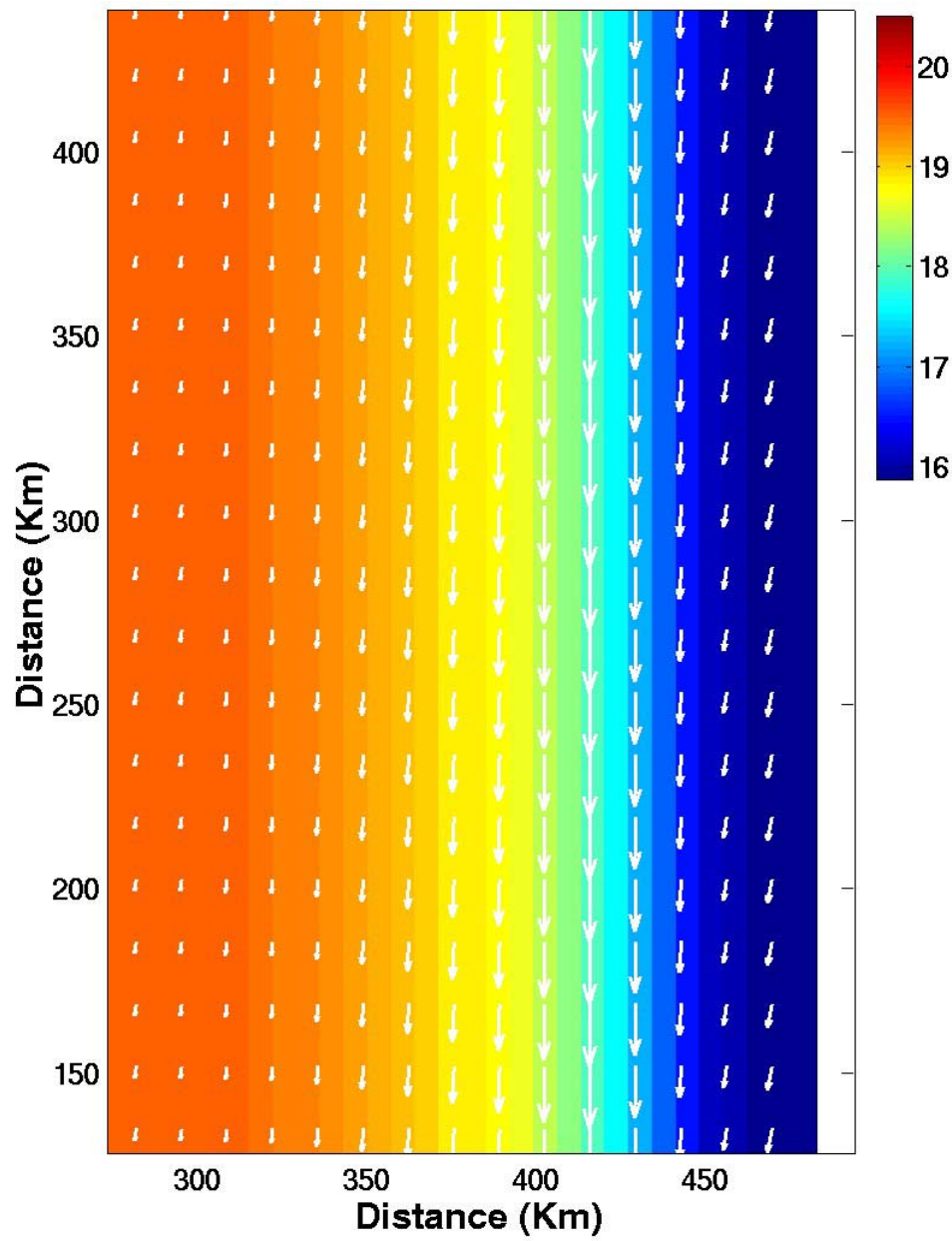


Figure 5.6e. Surface velocity (m/s) (vectors) and surface temperature (°C) (in color) at day 80. Highest vector magnitude is 0.95 m/s.

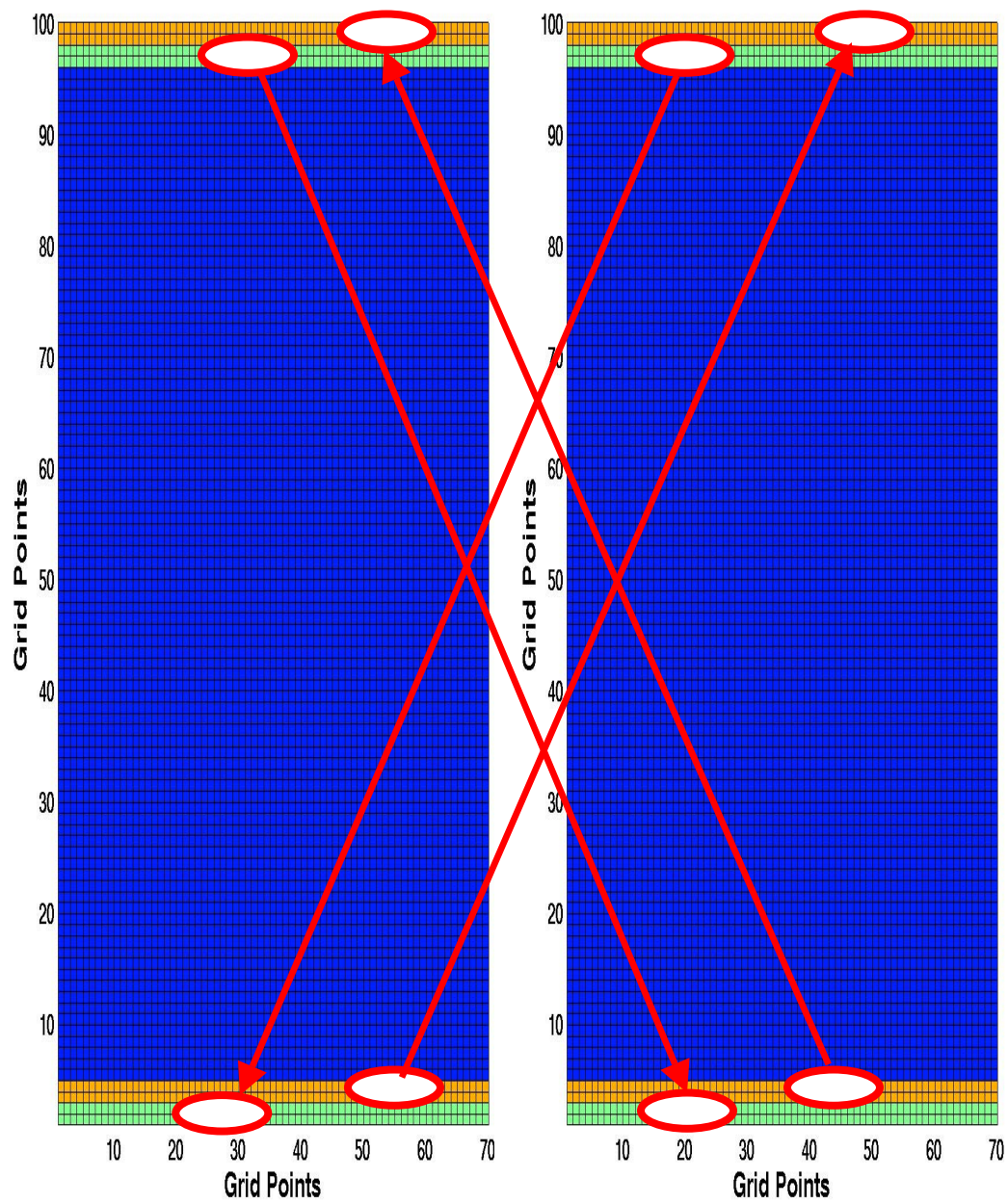


Figure 5.7. Exchange of information between the two processes running at the same time represented by the red arrows.

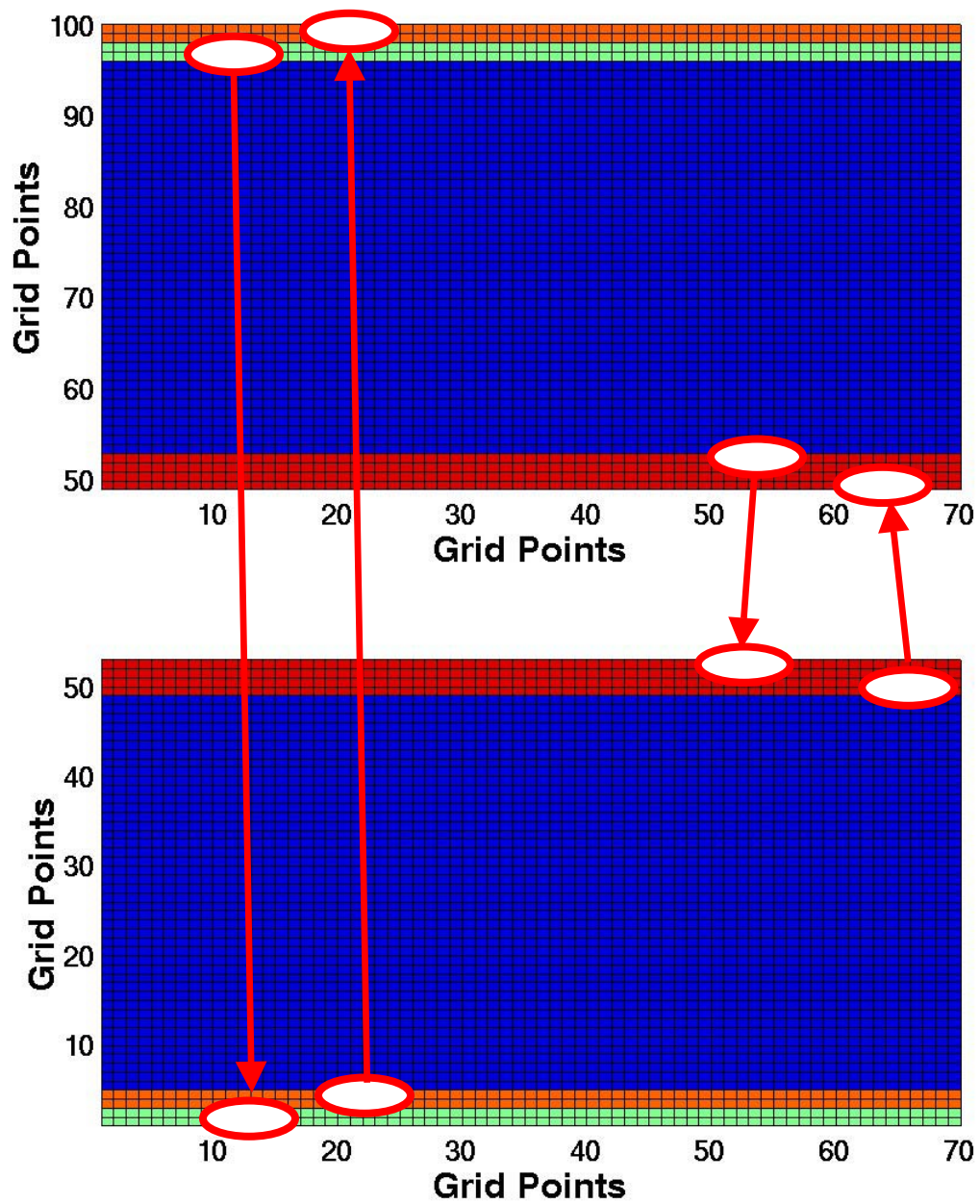


Figure 5.8a. Exchange of information between the two processes running at the same time represented by the red arrows. In green, orange and red the points common to both processes. In green and orange the cyclic boundary conditions.

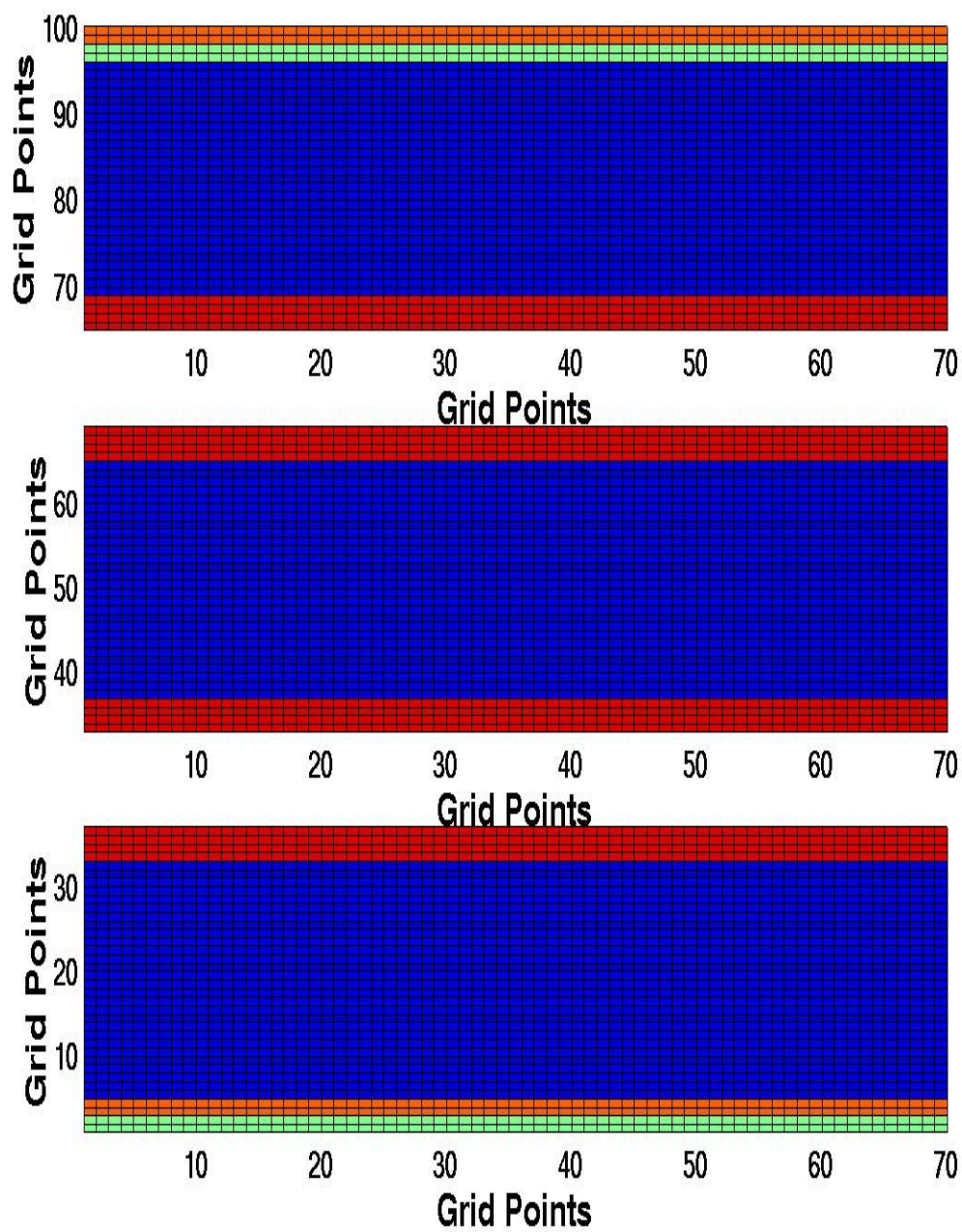


Figure 5.8b. Subdivision of the main region in three zonal sub-regions, running on different processors. Common points between the models in orange, green and red. In green and orange the cyclic boundary conditions. Exchange of data between processes not shown.

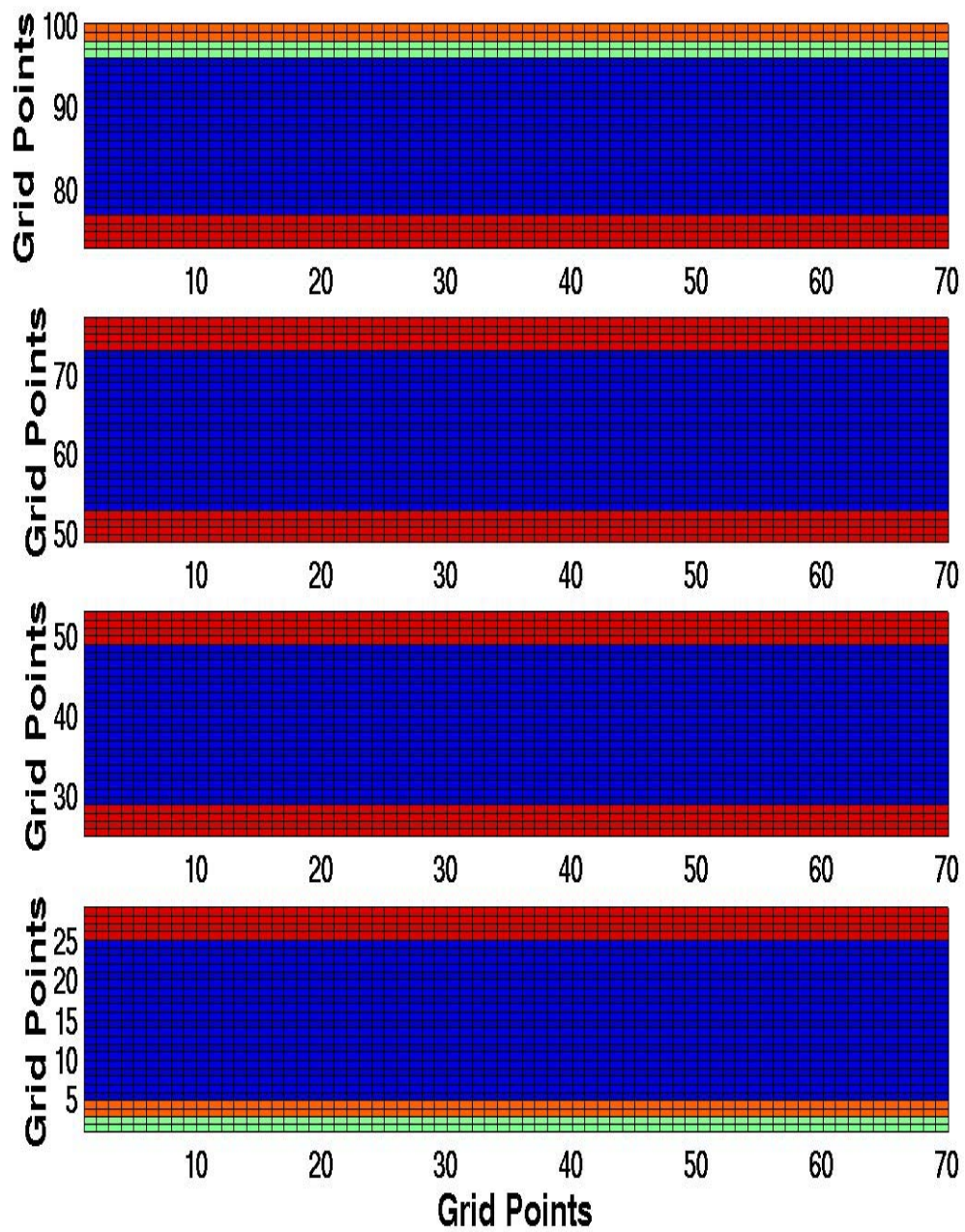


Figure 5.8c. Subdivision of the main region in four zonal sub-regions, running on different processors. Common points between the models in orange, green and red. In green and orange the cyclic boundary conditions. Exchange of data between processes not shown.

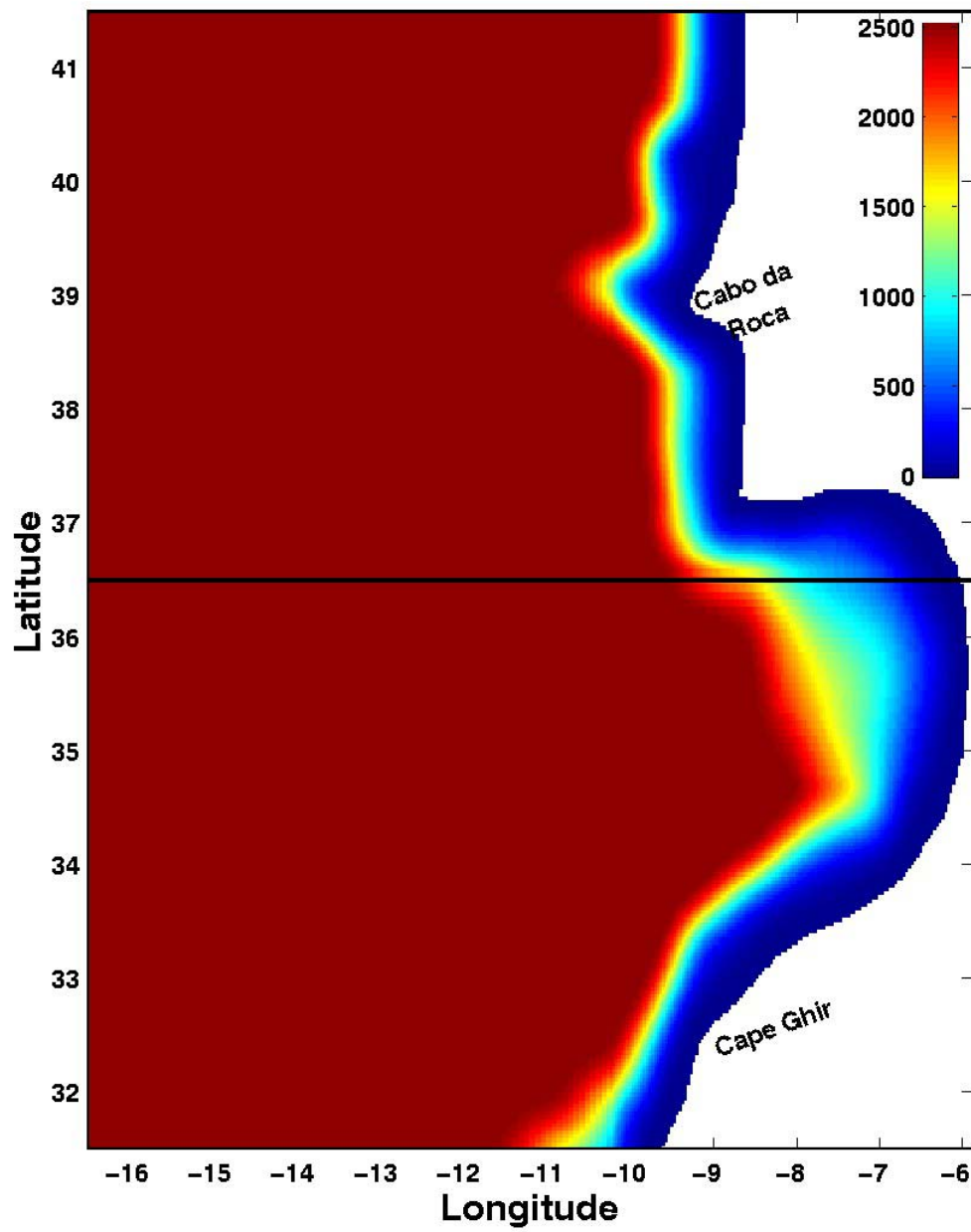


Figure 5.9a. Subdivision of the Northern Canary Current System model in two zonal sub-regions.

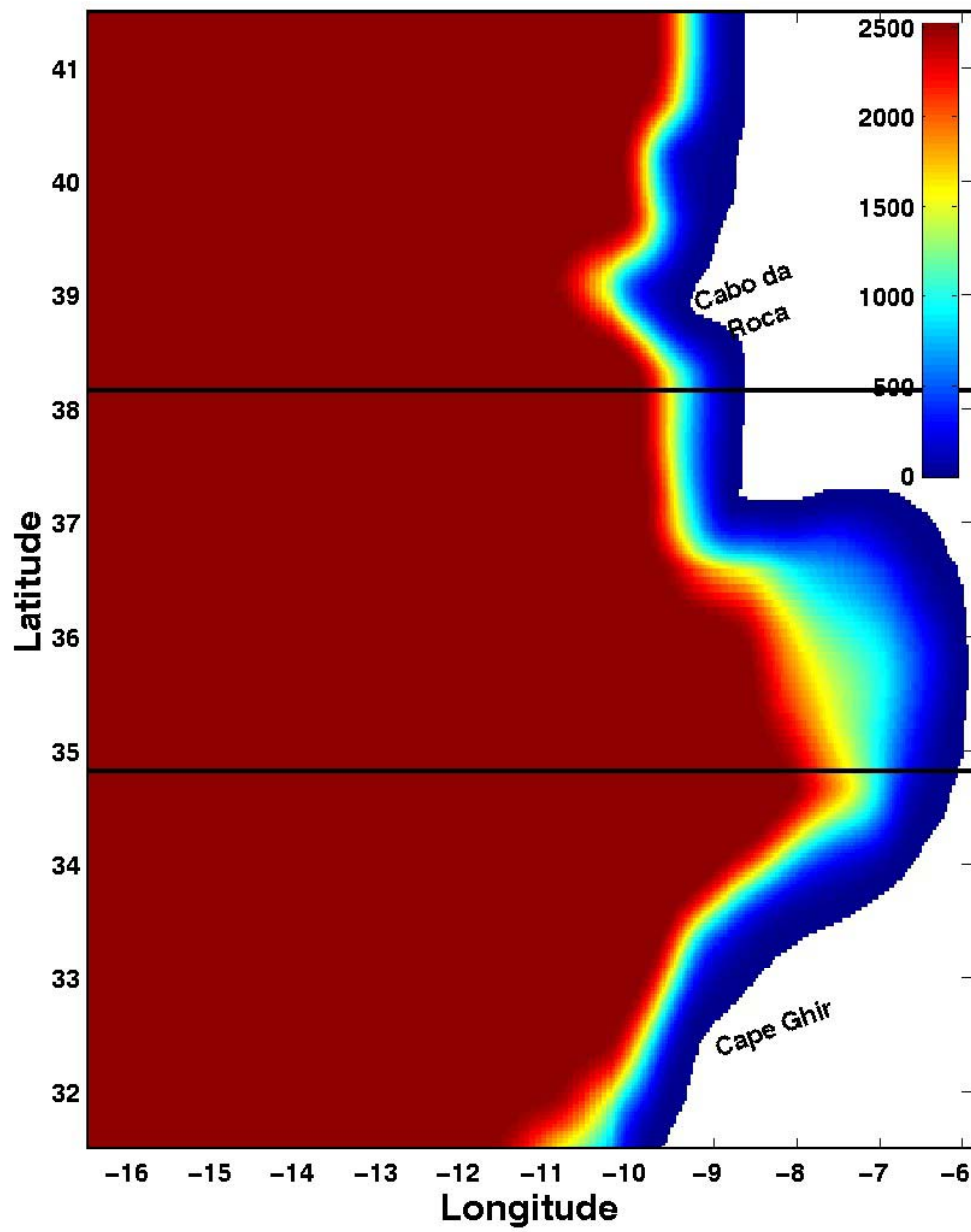


Figure 5.9b. Subdivision of the Northern Canary Current System model in three zonal sub-regions.

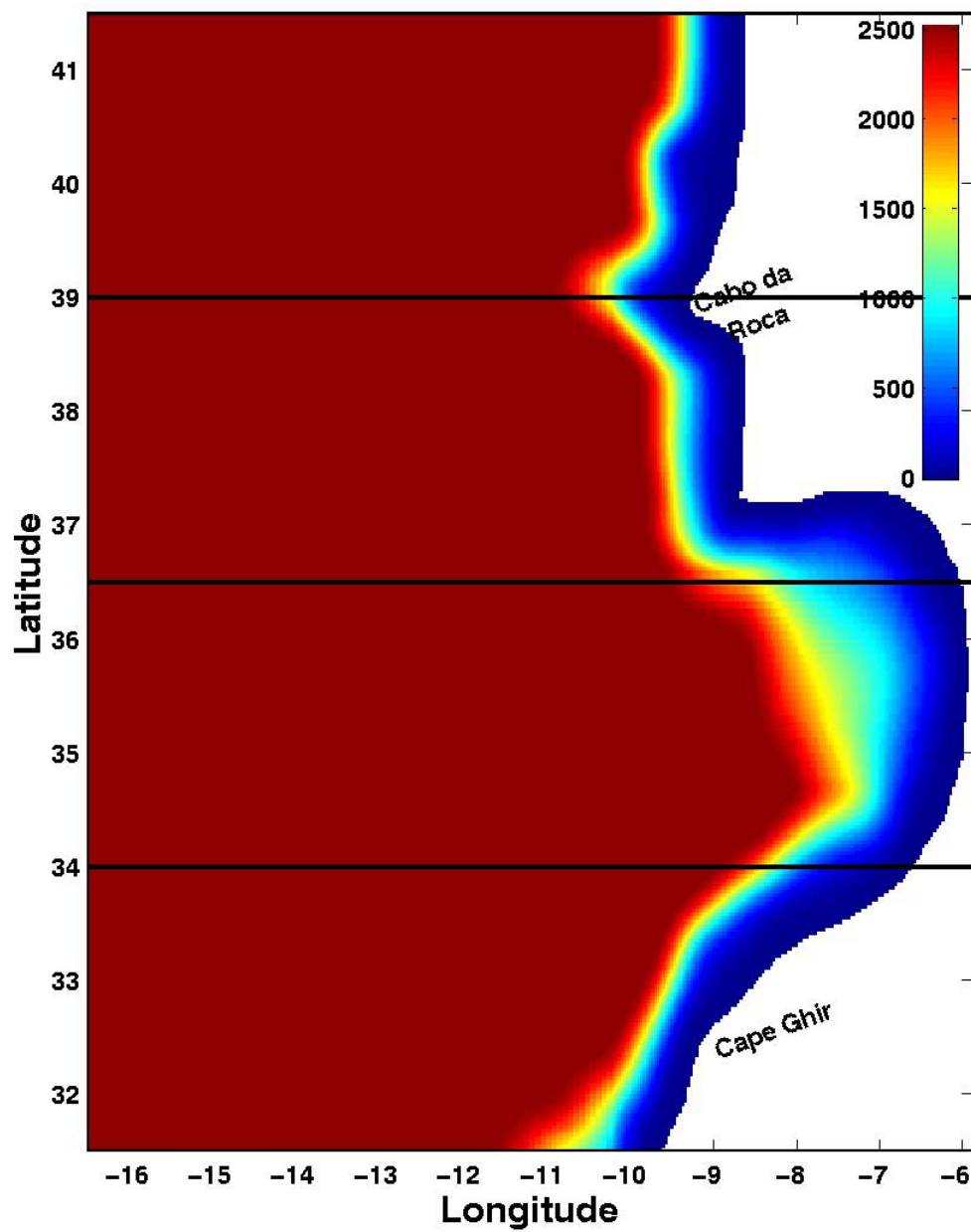


Figure 5.9c. Subdivision of the Northern Canary Current System model in four zonal sub-regions.

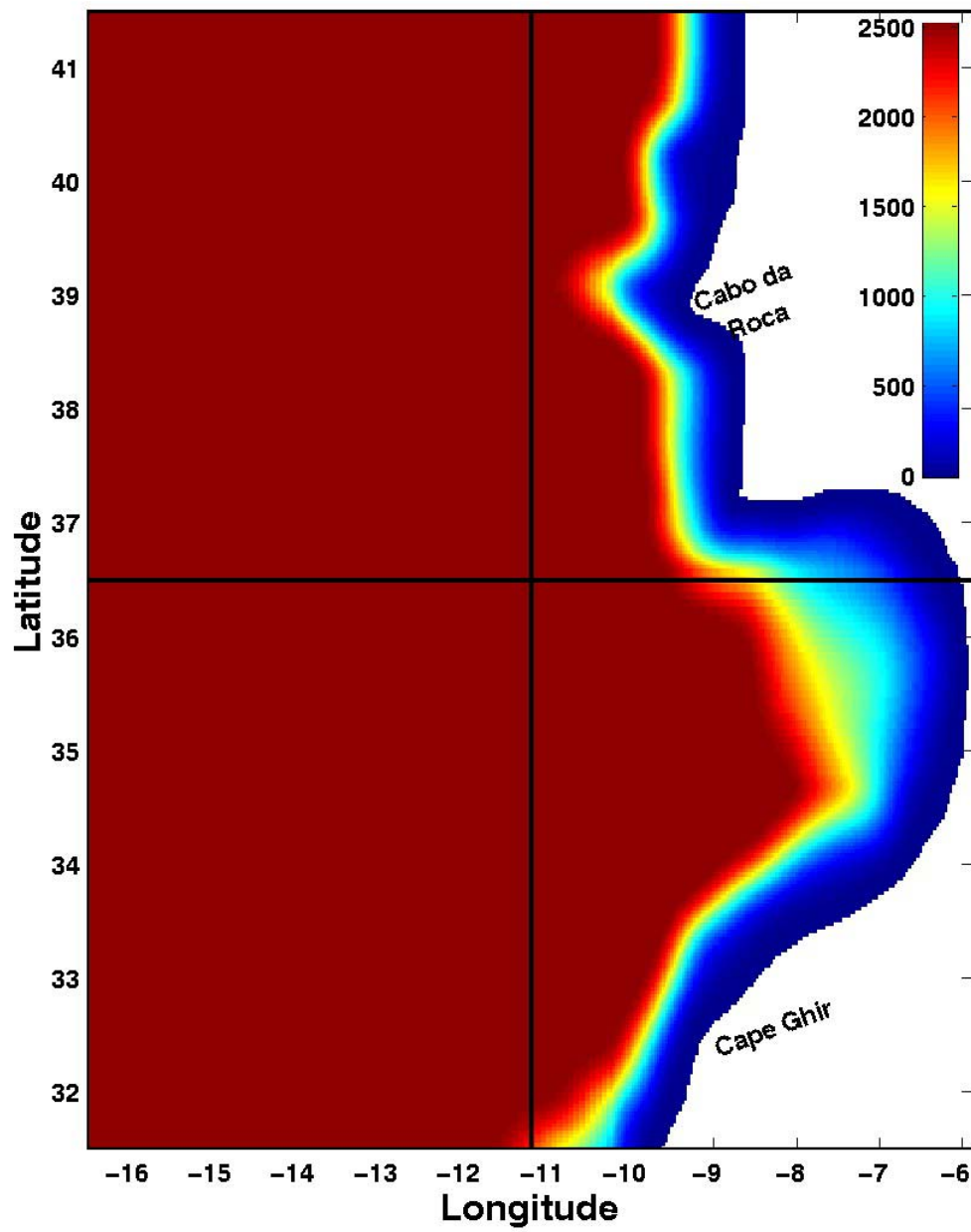


Figure 5.9d. Subdivision of the Northern Canary Current System model in four rectangular sub-regions.

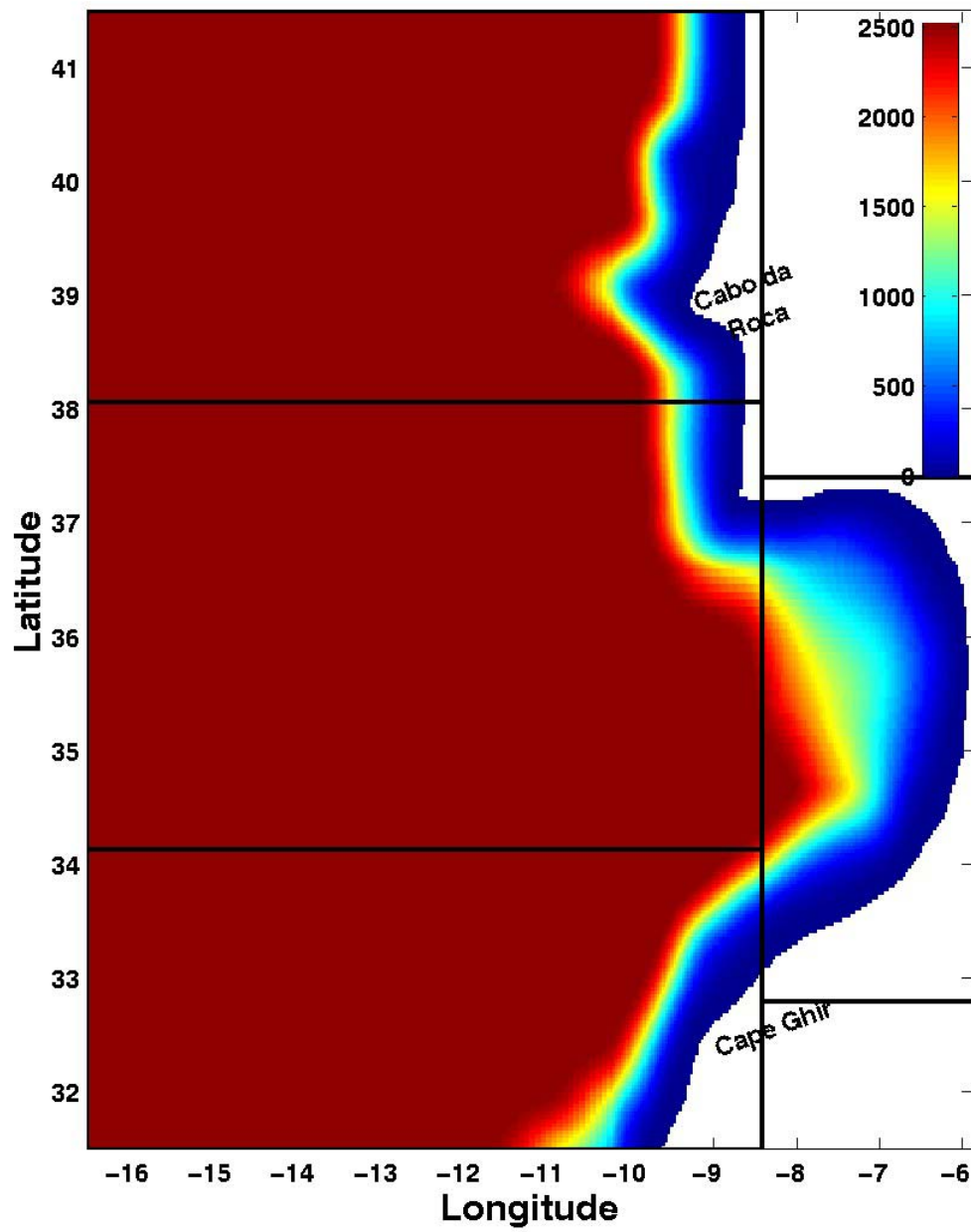


Figure 5.9e. Subdivision of the Northern Canary Current System model in four rectangular sub-regions avoiding most of the land points.

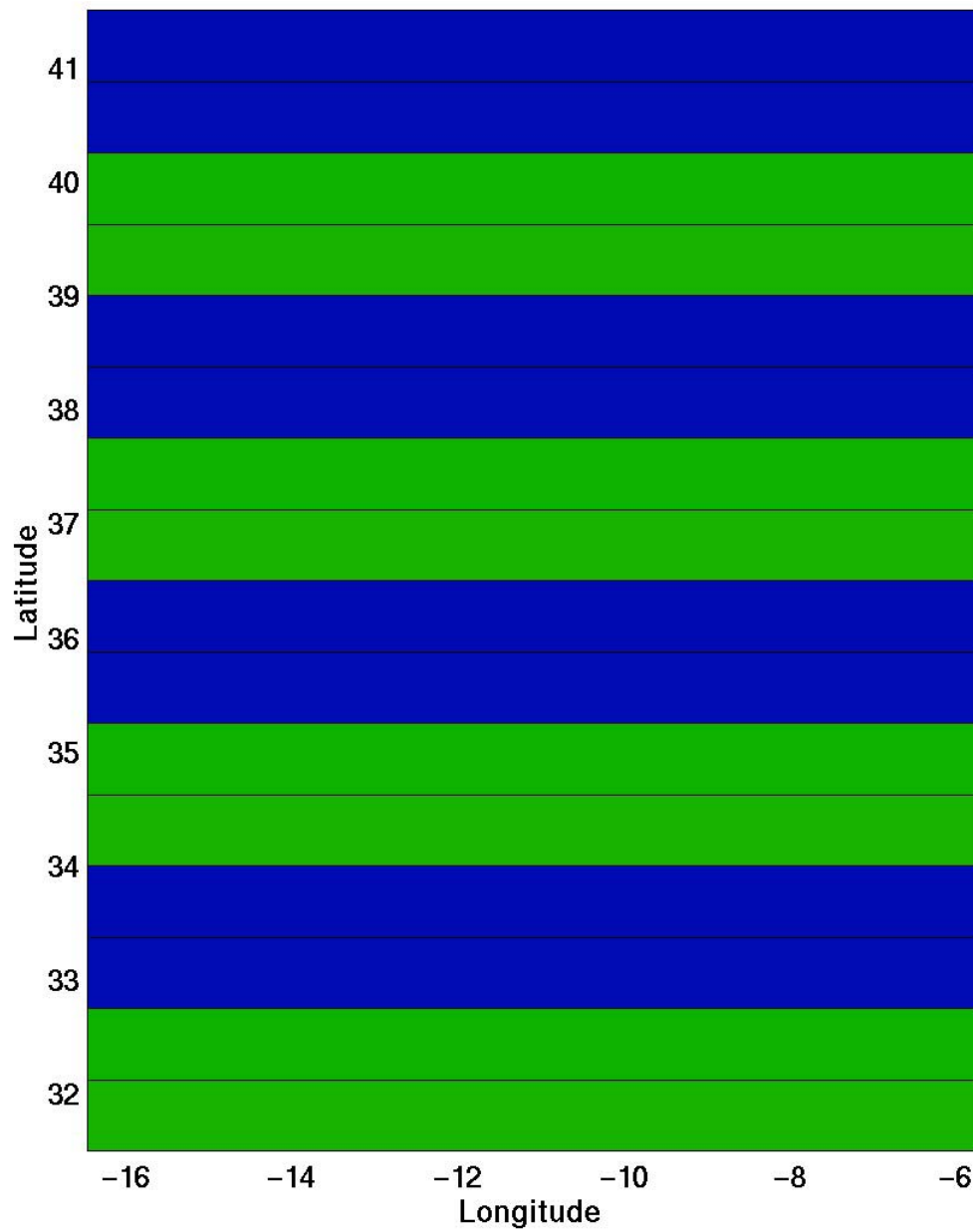


Figure 5.10a. Time step one of data exchange. Representation of a model subdivided in 16 sub-regions with the processes of the same color exchanging information simultaneously.

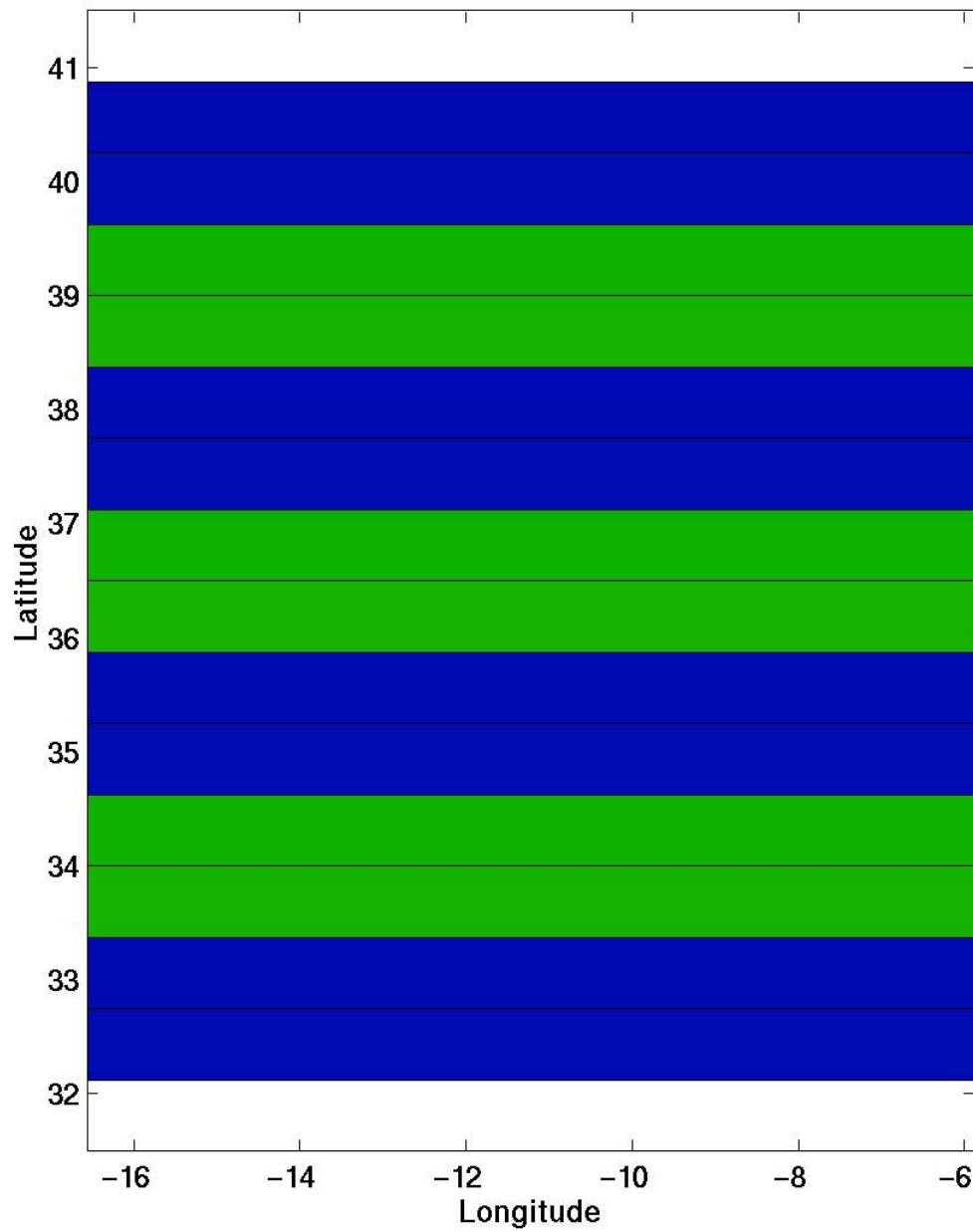


Figure 5.10b. Time step two of data exchange. Representation of a model subdivided in 16 sub-regions with the processes of the same color exchanging information simultaneously.

VI. SUMMARY

In this thesis coastal processes were systematically investigated and new numerical methods were developed in order to improve the capabilities of sigma coordinate bottom-following models, such as the Princeton Ocean Model (POM). Most of the methods were tested in the Northern Canary Current System (NCCS) model. The results should be applicable to other coastal models such as other Eastern Boundary Current (EBC) regions.

In Chapter II coastal processes were investigated in order to explore the role of wind forcing, bottom topography and thermohaline gradients in the NCCS. Several experiments of increasing complexity were conducted with annual forcing and initialization in order to isolate their effects on the generation, evolution and maintenance of classical as well as unique features in the NCCS. In Chapter II, four experiments are conducted with the POM in order to investigate the role of wind forcing, bottom topography and thermohaline gradients on classical as well as unique features in the NCCS. The first experiment investigates the pressure gradient force error, an unavoidable error in sigma coordinate models. It was shown that with a combination of smoothing the topography, increasing resolution and subtracting the area-averaged density before the computation of the baroclinic integral, the error was decreased from ~ 100 cm/s to less than to 1 cm/s. The highest velocities of ~ 0.5 cm/s were found near the shelf break (corresponding to the highest values for the slope parameter). Experiment 2 (annual winds with horizontal averaged climatology) produced the classical features of the NCCS, namely, an offshore surface equatorward meandering jet, realistic subsurface poleward currents, upwelling, meanders, eddies and filaments. In addition, unique features of the NCCS such as, separation of the upwelling regimes between the Iberian and Morocco coasts, poleward spreading of the MO and the development of Meddies off the Capes of Iberia were produced. The additional effect of bottom topography in Experiment 3 showed that topography plays important roles in intensifying and trapping the equatorward current near the coast, in weakening the subsurface poleward current, in

intensifying eddies off the capes of Iberia and in producing eddies off Figueira da Foz. The use of full instead of horizontally averaged thermohaline gradients in Experiment 4 highlighted the development of the Iberian Current off the Portugal west coast, a feature not seen in previous experiments. This shows that thermohaline gradients are essential to the formation of the Iberian Current. Overall, these results show that while wind forcing is the primary mechanism for generating classical EBC features, bottom topography and thermohaline gradients also play important roles in the generation, evolution, and maintenance of classical as well as unique features in the NCCS.

In Chapter III a new numerical method of reducing the slope parameter was developed. This one-dimensional robust direct iterative technique efficiently smoothed the bottom topography so that the pressure gradient force errors, which are common in sigma coordinate models were reduced to acceptable values. Sigma bottom-following coordinate models have an inherent error, the pressure gradient force error (PGFE). The PGFE decreases as the slope parameter decreases. The maximum value suggested to the slope parameter to be used in sigma coordinate models is 0.2. Since raw topographies have typically a maximum value for the slope parameter in between 0.6 and 0.8, it was necessary to smooth and/or increase the resolution in order to achieve the recommended value. In Chapter III a one-dimensional direct iterative method for reducing the slope parameter was developed. The idea behind the development was the observation that when two-dimensional Gaussian filters are used, the topography is quite different than the original topography in coastal areas. With the direct iterative method the minimum amount of change required to reduce the slope parameter to the assigned values is done and the method is maxima conservative. Also, contrary to standard smoothing, all the points with slope parameter less than or equal to 0.2 remain unchanged. This method was tested in three different areas (NCCS, CCS and western and southern Australia) with complex topography. In all the regions the slope parameter was successfully reduced from ~ 0.8 to 0.2. This method has also the unique advantage of maintaining coastline irregularities, continental shelves and relative maxima such as seamounts and islands.

In Chapter IV a regional sigma coordinate POM model (i.e., the NCCS region) was successfully coupled with a basin scale z-coordinate POP model. To achieve this, a new smoothing technique was developed which adds positive corrections to the bottom topography in order to avoid vertical extrapolations of data.

Several experiments were conducted in order to explore different boundary condition (BC) formulations using the high spatial/temporal resolution data forcing of POP. The starting point for the development of this BC was the boundary conditions developed by Marchesiello et al. (2001) (Table 4.1). These BCs were shown to be unstable in this setting. Also, several other BC experiments were shown to be unstable in the high resolution setting (see Table 4.3). A new set of stable boundary conditions was explored (Table 4.2). Several sensitivity experiments were conducted with different values for the inflow time scales for the velocities and tracers. The modified Marchesiello et al. (2001) BC showed fairly good results in the NCCS when compared with a wider reference model. The change in the mean sea level between the test model and the reference model showed that the mean sea level adjustment was more sensitive to the inflow time scales for the velocities than for tracers. The test model with the inflow time scales for the velocities of three days showed initially a slow response but had the best results over time. The surface kinetic energy was the parameter least sensitive to the inflow time scales. The total kinetic energy results showed that the sponge layer, besides absorbing disturbances and suppressing computational noise, also had the effect of helping to conserve the total kinetic energy of the model. Overall the best results were obtained with inflow time scales of three days for the velocities and of one day for the tracers.

In Chapter V, an automatic multi-region parallelization of the POM was developed. In this parallelization scheme, several sub-regions behaved as independent models and only exchanged information after the calculation of the boundary conditions. This parallelization scheme was shown to have several advantages relative to the standard parallelization. The changes made to the code were minimal. In particular, changes were made to the input/output subroutines and subroutines to exchange data between the

processes were inserted in only five locations in the code. In contrast, in the standard parallelization the exchange of code was done in hundreds of locations. In the multi-region parallelization only the seven basic prognostic variables were exchanged while in the standard parallelization dozens of variables were exchanged. For a small number of processors the multi-region parallelization is shown to have better performance than the standard parallelization. It was also shown that it was possible to have efficiency values greater than 100% due to the non-linear dependency of running times with the total number of points. The multi-region parallelization allowed the parallelization of almost 100% of the code while the standard parallelization typically allowed only 80 to 90% parallelization of the code, the latest due to extensive modifications in the code. When four common points were used between adjacent models, the multi-region POM was shown to reproduce the results as the serial model.

APPENDIX A

The robustness of this algorithm is that in each direction only the signed slope parameter (SSP) values less than the negative of the intended slope parameter ($-SP_f$) are targeted. In addition each pocket of high values of the slope parameter is treated separately.

The main steps used in the calculation are the following:

- 1 – Store non-smoothed topography in a matrix (DEP).
- 2 – Determine the land points.
- 3 – Calculate the initial water volume V_i .
- 4 – Calculate the signed slope parameter (SSP) in each line.
- 5 – In each line (LINE) determine the last column (LAST_COL) where $SSP < -SP_f$.
If there are no points with $SSP < -SP_f$, skip to step 10.
- 6 – Construct the line vector SUBS, where the first value is equal to DEP(LINE, LAST_COL+1) and all the points have slope parameters equal to $-SP_f$.
- 7 – Construct the new line vector FLIP_SUBS, that is the horizontally flipped vector SUBS. The last point of SUBS is the first point of FLIP_SUBS.
- 8 – Align FLIP_SUBS with the respective points in DEP. The last point in FLIP_SUBS should be coincident with DEP(LINE, LAST_COL+1). Starting at point (LINE, LAST_COL) and traveling to the left (in direction of the beginning of the row), find all consecutive points in which the depths of the FLIP_SUBS are higher than the corresponding DEP depths and substitute this values in DEP by the values of FLIP_SUBS.

- 9 – Repeat steps 4 to 8 until all the points have $SP \geq -0.2$. This is necessary because each pocket of values is treated separately.
- 10 – Rotate the topography matrix by 90 degrees, repetition of steps 4 through 9.
- 11 – Repeat step 10 two more times.
- 12 – Rotate topography by 90 degrees. By now the topography has the same orientation as in the beginning.
- 13 – Calculate of the final water volume V_f .
- 14 – Multiply of the smoothed topography by the coefficient $K = \frac{V_i}{V_f}$. Note that this volume constraint is slope parameter conservative.
- 15 – Repeat steps 3 through 14 until $SP < SP_f$ in all points of the domain.

It is possible to implement this algorithm without rotating the topography matrix if individual code for each of the four directions is done separately. This is an interactive process because the change in topography necessary to reduce the slope parameter in one direction may change the slope parameter in a perpendicular direction to values greater than 0.2. When this happens another iteration is necessary.

If the volume constraint in step 14 is not applied, the change in volume for the three regions tested applying this algorithm is on the order of 0.5 %. The suggestion is to use this correction if you have initialization data below the raw depth values.

APPENDIX B. SELECTION OF THE MESSAGE PASSING INTERFACE (MPI) LIBRARY

There are several different ways of communicating between different processes/threads. The most commonly used are the OpenMP and the message passing interface (MPI). Since the need to run the model in a cluster of workstations was perceived, MPI was chosen as the most viable communication standard since it allows the transfer of information not only on shared but also distributed memory platforms and clusters of workstations with implementations for Unix, Windows and Linux (e.g., LAM and MPICH). Let us briefly review MPI.

MPI is a message-passing library specification designed to be used in parallel computers, clusters of workstations and heterogeneous networks, allowing the development of portable parallel software libraries. There are several advantages in using the MPI libraries (Maui High Performance Computing Center, 1999):

- Standardization – MPI is the only message interface that can be considered a standard. It is supported in virtually all platforms.
- Portability – There is no need to modify source code when using different platforms.
- Performance – Vendor implementations are available which exploit native hardware features in order to optimize performance.
- Functionality – Over 115 routines available.
- Availability – A variety of implementations available, both vendor and public domain.

- Target Platforms – Massively parallel processors (MPP), symmetric multiprocessor (SMP) clusters, workstation clusters and heterogeneous networks.

For use at the Naval Postgraduate School, the Silicon Graphics (SGI) implementation of MPI (Boney, 1996) was chosen to be used in the SGI Origin 2000 computers.

APPENDIX 5.C. STANDARD PARALLELIZATION

Parallelizing loops in a code is the standard type of parallelization. This is also known as model decomposition parallelization. This type of parallelization results in shrinking arrays, where each process only has in memory a subset of the data, which subsequently requires much less memory in each node than before parallelization. Using this method there is always a part of the code that cannot be parallelized (for example if there is a call to a subroutine that changes variables already in use by the loop). If Amdahl's law is used, we find that the speedup achieved by using parallel processing is given by

$$Speedup = \frac{s + p}{s + \frac{p}{N}} = \frac{1}{s + \frac{p}{N}}$$

where s is the fraction of the code that cannot be parallelized (the serial code), p is the fraction of the code that can be parallelized ($p = 1 - s$) and N is the total number of processes used. It is readily seen that even if we have an infinite number of processes the maximum speedup obtained is only $\frac{1}{s}$. Since ocean models always have a part of the code that is not parallelizable, this is a strong constraint.

Let us suppose that we wanted to do the following calculation in a 10 by 10 point region, $df(i, j) = 0.25 * (f(i-1, j) + f(i+1, j) + f(i, j-1) + f(i, j+1)) - f(i, j)$, where f and df are model variables and i and j are indices. If the initial domain were to be subdivided in, for example three processes we would end up with the sub-domains shown in Figure 5. 1a. Note that each process, cannot by itself (i.e., just with its own data) do the

required calculations. As a result there is the necessity of having some halo regions (Figure 5. 1b), which are regions common to all the adjacent processes that allow each process to do the required calculations. Since the values at these halo regions usually vary with time (e.g, if they are prognostic variables in an ocean model), there is the need to have to constantly update the values of the halo regions (Figure 5. 1c).

This simple example with just the dependency on one variable, i.e., f , was shown. In a real model, several variables would need to be exchanged at each loop. The halo regions, depending on the processes being calculated, could have one or more points. Resulting in a high amount of data exchanged and a code that would have to be substantially changed to account for the transfers of data in every loop and for every variable in the model where there are lateral dependencies between the variables.

INITIAL DISTRIBUTION LIST

1. Defense Technical Information Center
Ft. Belvoir, Virginia
2. Dudley Knox Library
Naval Postgraduate School
Monterey, California
3. Mary Batten
Department of Oceanography, Naval Postgraduate School
Monterey, California
4. Albert Semtner
Department of Oceanography, Naval Postgraduate School
Monterey, California
5. Julie McClean
Department of Oceanography, Naval Postgraduate School
Monterey, California
6. Roger Williams
Department of Meteorology, Naval Postgraduate School
Monterey, California
7. Julie Pullen
Naval Research Lab
Monterey, California
8. Direccao Servico Formacao
Lisboa, Portugal
9. Instituto Hidrografico
Lisboa, Portugal

10. Carlos Ventura Soares
Instituto Hidrografico
Lisboa, Portugal
11. Castro Breno
12. Don Stark
Department of Oceanography, Naval Postgraduate School
Monterey, California
13. Antonio Santos Martinho
Instituto Hidrografico
Lisboa, Portugal